The Dissertation Committee for Robert Douglas Morgan certifies that this is the approved version of the following dissertation:

Colloidal Nanoparticles: A New Class of Laser Gain Media

Committee:

Todd Ditmire, Supervisor

John Keto

Michael Downer

Greg Sitz

Desidero Kovar

Colloidal Nanoparticles: A New Class of Laser Gain Media

by

Robert Douglas Morgan, B.S.

Dissertation

Presented to the Faculty of the Graduate School of

The University of Texas at Austin

in Partial Fulfillment

of the Requirements

for the Degree of

Doctor of Philosophy

The University of Texas at Austin

December, 2009

Acknowledgements

First I would like to thank my advisor Professor Todd Ditmire for not only allowing but encouraging me to pursue such an ambitious topic. Due to its scope, the work herein required perhaps an unusual level of vision, trust, support, guidance, as well as patience from an advisor. I would also like to thank Professor John Keto for providing invaluable guidance, conversation, and insight into the fascinating and often complicated world that exists at the nano-scale. Several fellow students including, but not limited to, Kris Gleason, Manuj Nahar, Ignaciao Gallardo, and David Stoker provided a wealth of knowledge, and willingness to help for which I am grateful. Without the dedication, precision and experience of the machinists in the Physics department including Jack Clifford, Richard Goodwin, Gorge Sandefur, and Allen Schroeder this work would not have been possible. Finally I would like to thank all my family, friends and colleagues for sharing their support and wisdom.

Colloidal Nanoparticles: A New Class of Laser Gain Media

Publication No._____

Robert Douglas Morgan, Ph.D.

The University of Texas at Austin, 2009

Supervisor: Todd Ditmire

Development of high average power lasers has historically been limited by the properties of available gain media. As a result it is either too costly or impractical to employ lasers in many applications for which they would otherwise be well suited. We have synthesized a new type of colloidal laser gain material that should possess many of the advantages of solid state media without their primary disadvantage: poor thermal performance. The colloid consisted of an emulsion of 20% Nd^{+3} doped phosphate glass nanoparticles suspended in nonanoic acid. The spectroscopic properties of the material were found to be consistent with those of bulk Nd^{+3} doped materials and suitable for laser development.

Table of Contents

List of Tables

List of Figures

Chapter 1: *Introduction and Background*

1.1 INTRODUCTION

Since the invention of the laser scientists, engineers, and policy makers have devised ambitious research and technological goals for specialized laser beams, far outstripping the pace of development of systems capable of producing such beams. The numerous applications devised for the laser include manufacturing, defense, communications, metrology, and even nuclear fusion to name just a few. Nearly all nontrivial uses of laser light require both precise control of the radiation field as well as high intensity and respectable average power. However, due to the fundamental macroscopic properties of classical dielectric media (plasmas, gases, liquids, glasses, ceramics, and crystals), practical laser performance is limited a-priori to a highly constrained parameter space and has never really exceeded that of the light bulb in terms of average power radiated. Nevertheless, high performance laser systems can be designed and built, but only at great expense and are typically unstable and unreliable, since normal operation occurs near the damage threshold of many principle components of the system, most notably in or near the amplification medium.

Despite many valiant attempts over the past 30 years, it is not possible to engineer around the constraints imposed by physics. The performance of lasers is fundamentally constrained by the damage threshold of their optics and the atomic physics of gain media. With current dielectric technology the damage threshold sets the upper limit of 10 MW/cm^2 for CW operation and 10 J/cm^2 for a 10 ns pulse[1]. Reaching these limits has not been possible due to the thermodynamic constraints of the host media (often linked to the material's phase). For example, any mechanism that increases the perturbation rate of the excited species will decrease the maximum possible laser performance of a material. Sources of the perturbations can be found by studying the equation for Gibbs free energy,

and affect laser performance through the collisional rate, the concentration of various species, or the temperature of the system. This is not the only role thermodynamic effects can play in constraining the peak performance of a laser system. The effects of heat and complexity creep into the picture through the bulk optical properties and resonator stability criterion as well. Trying to control or engineer around these fundamental problems is like squeezing a balloon in one place only to have it pop in another. The challenge when making scaling arguments about potential laser systems lies in finding the unintended consequences that couple to the various design parameters available to the engineer. A few examples will prove useful when thinking about this problem.

As stated above, producing beams with these intensities requires a system capable of tolerating a significant fraction of the total beam power as waste heat. For gas and liquid lasers the medium can circulate easily removing the excess heat. For solid lasers the only option is to maximize the surface area to volume ratio and hence conduction rate through the material. In solids there are two basic ways of doing this: small CW beams or big pulsed beams (neither of which is well suited to stable laser operation at high power). It should be noted that in general, large diameter CW beams have their own set of thermodynamic difficulties that act to couple heat loads to cavity stability and noise sources. Fiber optic lasers operate near both the damage and nonlinear thresholds and therefore meet a hard ceiling that can't be overcome except by increasing the mode volume, which in a waveguide will also degrade beam quality. Thin disk lasers can operate significantly below the damage threshold of the material but can't beat the ASE/whispering gallery mode limit set by their large transverse path length and typically high ion density. Thus the only way to efficiently scale these lasers is to add more length to the media, decreasing already poor thermal conductivity. Therefore the total volume

of gain media available to a solid state laser as a function of operating intensity is constrained to lie somewhere between these two extremes. Thus for solid materials the heat flow rate sets a hard ceiling on laser operation well below the power density limits of the optics themselves.

Due to their low density, gas lasers require large total volumes to produce high power operation. Thus, the logical knob to tune would be the density. But this increases the temperature and pressure and hence the collision rate in the system leading to an increase in the density of non-radiative terminal states, dropping the lifetime and efficiency. The only way out of this particular corner of the parameter space box is to raise the average intensity of the circulating beam and flirt with the damage threshold. Alternatively a large diameter beam can be utilized with the same caveats governing the disk laser as well as the additional problem of a large mode. Large mode volume and high gain don't mix well. In addition to being vulnerable to ASE, large mode volume lasers also have stability issues due to either resonator design or the ability of the gain medium to act as a noisy amplifier. This may contribute to multimode operation or unstable operation caused by perturbations in the system that do not damp quickly. Such a system is at risk for spiking and hotspots among other undesirable behaviors.

Dye lasers suffer from the problems of short lifetime and high cross sections. The reasons for the short lifetimes can be seen from Fermi's golden rule. Since these molecules are typically complex and can access a large continuum of low energy perturbations caused by the high collision rate in a fluid, the density of states near the ground state is broad and the fluorescence lifetime short. In principle this could be overcome. However, since a laser's efficiency scales with the saturation intensity the damage threshold of the optics prevents effective output coupling of a CW dye system.

Efficient pulsed operation is also not possible since it would be limited by the mismatch in lifetimes of available pump sources and the dye.

Operating a reliable high average power laser will require a gain medium that does not suffer the same thermodynamic limitations as solids, liquids or gasses. A viable high average power gain medium would combine the density and quantum mechanical properties of solid media with the thermal conductivity and mechanical properties of a fluid. A colloid would therefore be the natural middle ground.

1.2 BACKGROUND

Before addressing the problems encountered when attempting to engineer a new type of high power laser material the discussion must be constrained to render it tractable. Thus a brief detour is useful to examine and derive several of the important quantities that govern the operation of all laser systems. The analytical work presented in Appendix A focuses on developing an intuition for the physical processes that determine the fluorescent lifetime, cross sections for absorption and stimulated emission, as well as their relationship to laser operation. The Appendix also presents a concise derivation of Fermi's golden rule which relates the density of states in a manifold to the probability of an optical transition. A clear understanding of these concepts has proven useful in both the engineering aspects of this project as well as during data analysis. The derivation of the laser rate equations presented below follows from the quantum mechanical and thermodynamic origins of the optical processes embodied in the Einstein A-B relations discussed in the Appendix.

Following this work, the basic model for a laser is that of an atomic system with 3 or 4 levels, although many systems with N levels can be effectively treated as a 4 level

system under common operating conditions. The basic diagram uses a notation where the occupation number density of the ground state is N_1. The following rate equations can be written based upon the properties of the interaction of an atom with light developed in Appendix A. The sum of the rates of transitions to and from a given level forms the total rate of population change in that level. The normalization condition and constraints on the radiation fields close the system. The rate equations could also be coupled to the PDE's that govern the spatial distribution of the beam due to the mode structure of the cavity. However, for this work that level of detail is unnecessary.

$$\begin{aligned}
&\frac{dN_i(x,t)}{dt}dx = \sum_{i\neq j}\left(\sigma_{ji}-\sigma_{ij}\right)\frac{I_{ji}(x,t)}{h\omega_{ji}}N_i(x,t)dx + \sum_{k=i+1}A_{ki}N(x,t)_k\,dx - N_i(x,t)f_\tau e^{\frac{-\Delta E_{ki}}{k_B T}}dx \\
&\sum_i N_i(x,t) = N(x,t) \\
&\frac{dI_{ji}(x,t)}{dt} = \frac{I_{ji}(x,t)}{h\omega_{ji}}\sigma_{ij}N_i dx - \frac{I_{ji}(x,t)}{h\omega_{ji}}\sigma_{ji}N_j dx + \frac{dI_{ji}^{external}(t,x)}{dt} - \alpha_{ji}(t)I_{ji}(x,t)
\end{aligned} \tag{1}$$

The external term could refer to a seed beam for the laser, or a pump beam providing the energy source for the gain. The α term accounts for all losses such as scattering from optical surfaces, the fractional transmission of the output coupler, or in pulsed operation the action of a Q-switch. This coupled set of equations though potentially complex is guaranteed to have a unique solution for any physical set of source functions or functionals I(t). Solutions to this problem can be obtained using numerical integration. However, making certain simplifying assumptions will aid in the development of physical intuition about the requirements of a high average power laser. To facilitate such insight, it is useful to look at Figure 1[2].

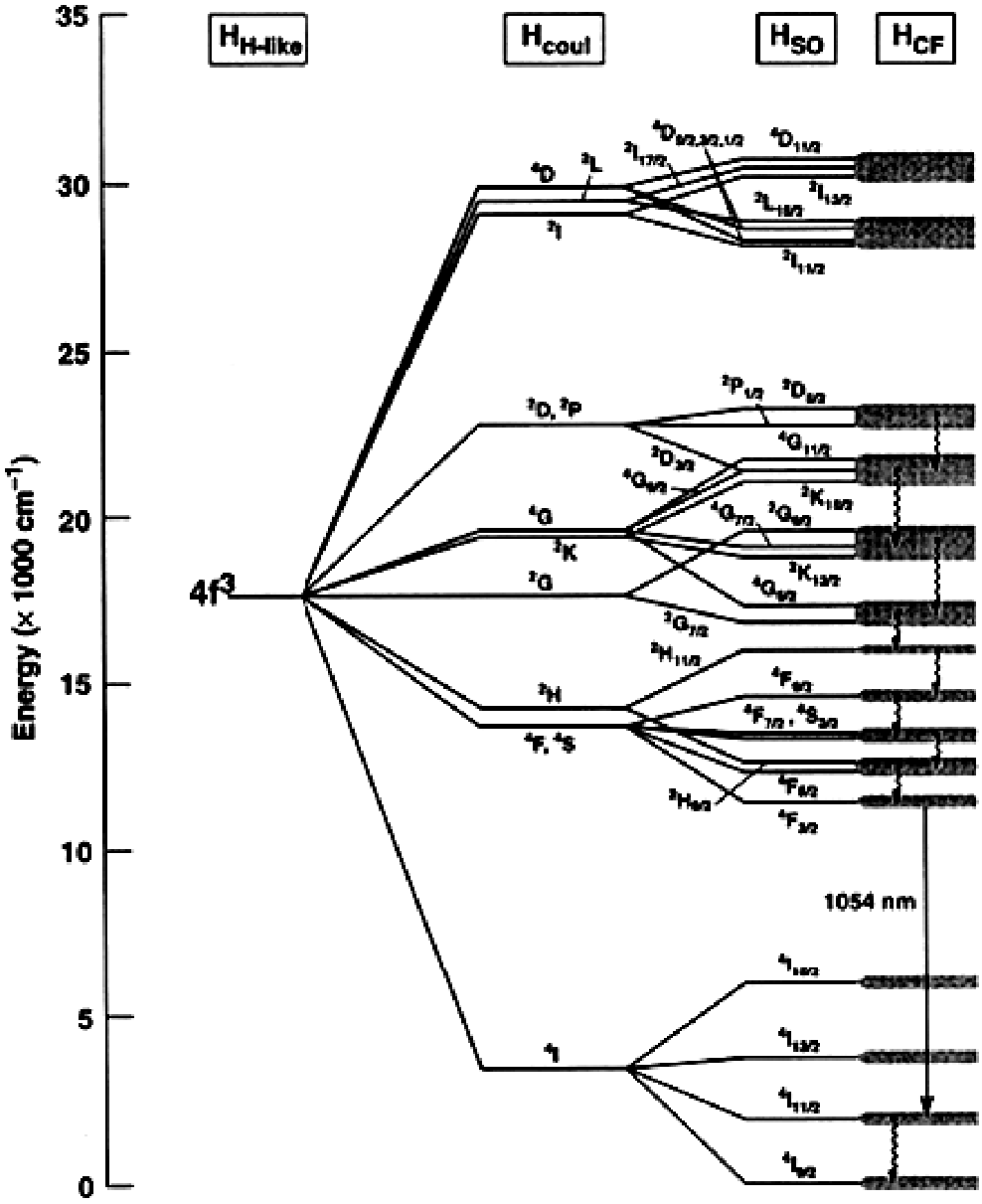

Figure 1. The energy levels of the Nd^{+3} ion in a phosphate glass[3].

This is significantly more complex than a 3 or 4 level system. Depending upon which absorption transition is pumped and what wavelength the laser operates on, it is possible to construct a thermally perturbed, 3 level system by pumping the $4I_{9/2}$ to $4F_{5/2}$

transition and lasing on the $4F_{3/2}a$ to $4I_{9/2}$ transition. The reason for considering this system thermally perturbed is that at room temperature the separation of the $4F_{3/2}a$ and $4F_{3/2}b$ levels is comparable to kT resulting in a macroscopic thermal population of the $4F_{3/2}b$ level. Alternatively, one could construct a 12 level system lasing on the 1316 nm transition between the $4F_{3/2}$ $4I_{11/2}$ levels excited into the $2P_{1/2}$ level by a pump operating in the 420 nm region. Thankfully, the transitions between the $2P_{1/2}$ level and the metastable $4F_{3/2}$ level occur rapidly compared to the metastable lifetime. Thus in Nd^{+3} glass, as is often the case with other materials, the 12 level reality can be ignored, collapsing the excited state decay time into a single transition step as in Figure 2.

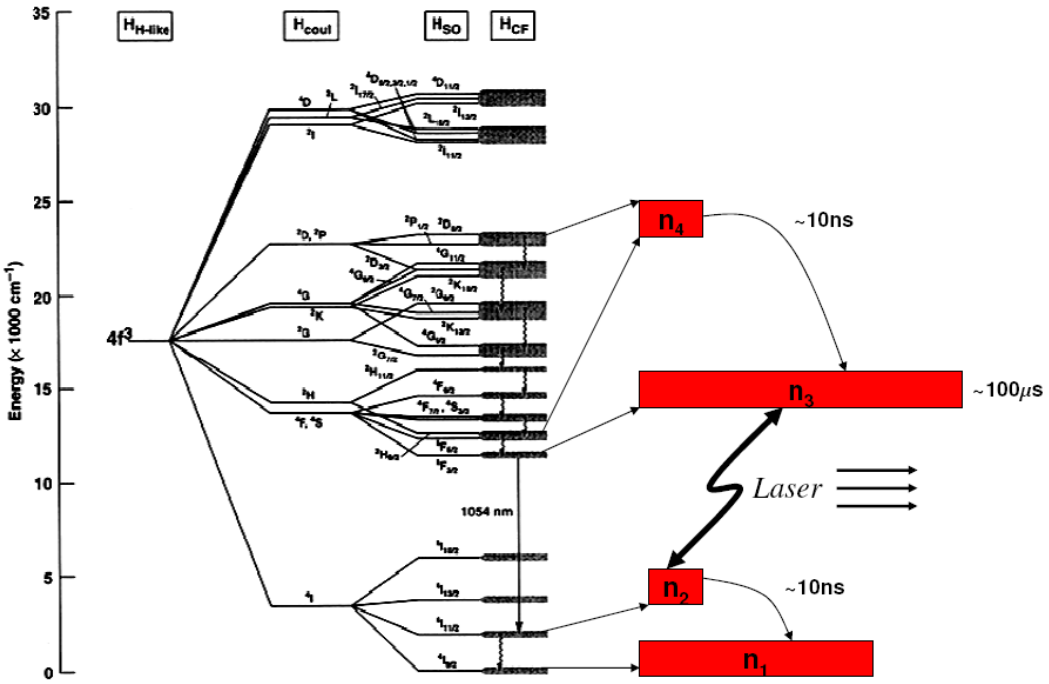

Figure 2. The transition rates among the multiplets allow the manifold to be treated as a 4 level system.

Thus whether a diode laser or flash-lamp pumping system is used or the laser operates at 1054 nm or 1316 nm, the basic rate equation for the system retains approximately the same form and can be further simplified as in Figure 3.

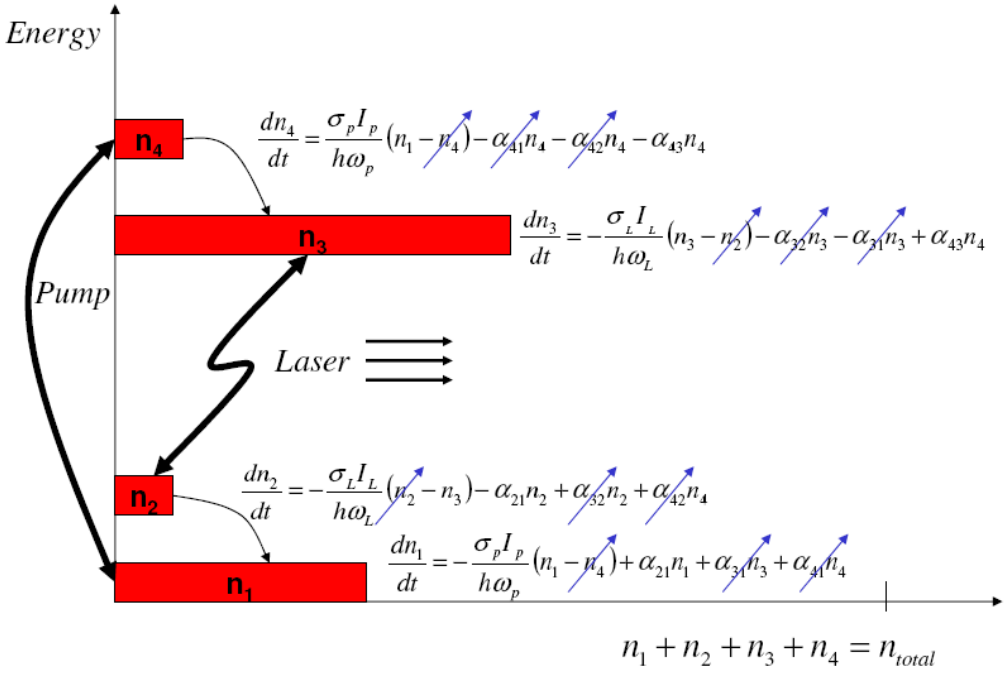

Figure 3. Many of the terms from equation (1) cancel leaving a simplified system of equations to solve.

Applying a similar treatment to a 3 level system operating on the same ion but in the mid 800 nm range produces Figure 4. Canceling all small terms and assuming that the system operates at equilibrium, facilitates the solution of the laser rate equations for a 4 or 3 level system. Solving this system of equations for the pumping rate required to achieve a population inversion in the laser system reveals that for a 3 level system no laser action occurs until a 50% population inversion is obtained between the ground and metastable levels[4,5]. On the other hand, with a 4 level system any pump rate will

contribute to a population inversion and the onset of threshold laser operation will occur once the system's gain exceeds the loss term due to the cavity.

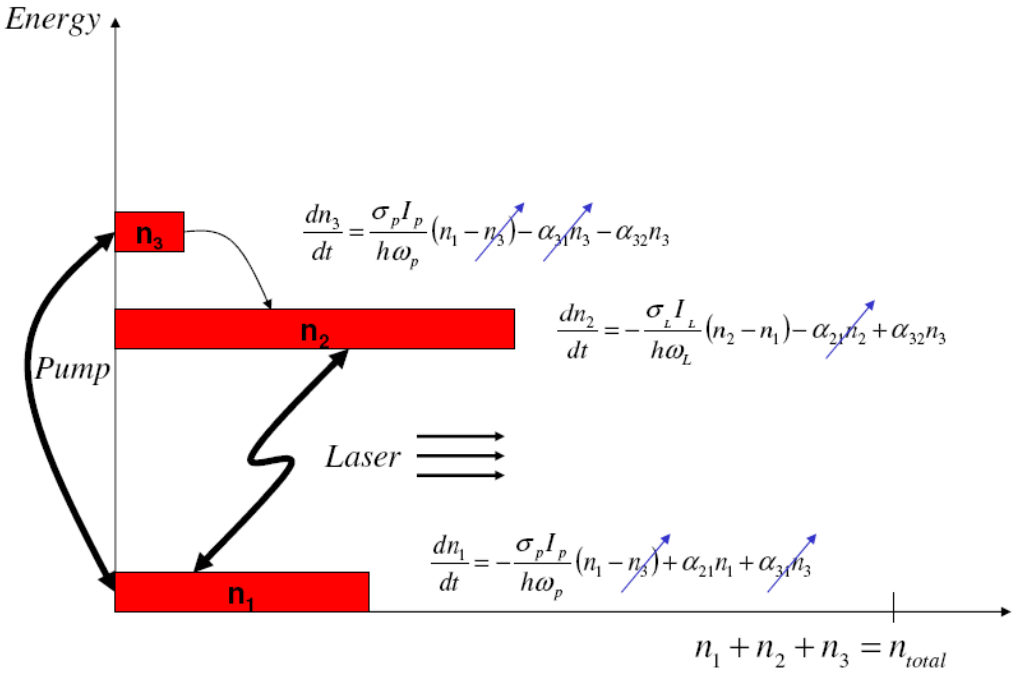

Figure 4. The rate equations for a three level system.

The diagrams and equations above contain several key results for understanding the difficulties in designing a high average power laser. Let's start with gain which according to the above diagrams should depend heavily on the cross section and density. Many people when they first encounter this problem, examine the equations above and conclude that building a high gain system is the best route to follow for high average power operation. However, when designing a real system one must consider the mundane details if they actually wish to build something. It is true that if it were possible to construct and design lasers independent of their physical components that high gain is an attractive starting point. However, I am reminded of a story Prof. Bob Beyer told his

laser class at Stanford about a high power high gain diode pumped laser that one of his graduate students was building at the time. The system's gain was so large that it was possible to achieve threshold operation by removing the high reflector and holding your hand in the beam path several meters from the optics bench. This laser could literally function with someone's hand serving as a cavity mirror. This seems like just a funny story but it serves as a warning to anyone attempting to build a high power laser as we shall see once the discussion has advanced a bit further.

Consider a modern dielectric mirror. If constructed to military specification and operated in a clean environment, this mirror can sustain long term operation at powers in excess of ~1 MW/cm^2 in a CW laser or ~10 J/cm^2 in 10 ns pulsed operation. These numbers set limits on the overall fluence our beam can achieve. Clearly for CW operation modern mirrors can tolerate significant power densities and the limitation of operation falls to the available gain media. However, for pulsed operation, which is arguably of more interest, obtaining significant energy per pulse requires scaling the size of the beam. Thus, amplifying a pulse to 1 kJ with reasonable diffraction limits requires the gain medium to possess a clear aperture of at least 36 cm (using the "Pi D" criterion for retaining 99% of the beam's power in the center spot of an Airy pattern)[6].

Things get interesting since we now have a large radial path length where spontaneous emissions can be amplified inside the gain medium. The walls of the medium form a dielectric interface and at best we can contain any back scatter to no less than .001%. Thus, amplified spontaneous emission (ASE) limits the maximum beam diameter and hence the final energy of a pulse. For example, a 30 cm diameter by 30 cm long 1% Nd^{+3} YAG rod with a cross section of $4x10^{-19}$ cm^2 operating at population inversion of ~1/40 designed to yield 10 J/cm^2 at saturation, assuming minor internal back scattering of ~.001%, would still possess a transverse small signal gain of 32. The large

transverse gain and solid angle with access to this transverse gain combined with the rate of spontaneous emission would rapidly deplete the available excited population. Amplification of large beams at energy densities near 10 J/ cm^2 only becomes possible in materials with lower cross sections such as glass hosts (typical range: $1x10^{-20}$ cm^2 - $5x10^{-21}$ cm^2). A more formal introduction to ASE can be found in Ch 4 of Koechner[5].

A different problem of large beam diameters is encountered when attempting to operate a high gain, gas-based CW system. The energy storage density of a gas is ~1000 times less than that of a solid. If one wishes to store and extract a high power beam from a CW gas system, the active media had better have the storage density necessary to accommodate such high energy flux. To operate near its maximum power density of 1 MW/cm^2 a chemical oxygen-iodine laser (COIL) would need to possess a constant supply of reactants. Given a specific energy density of ~3.5 J/L, it would operate with a flow rate of approximately 250 kL/s (or a linear flow rate of 2500 km/s)[7]. This situation is not very realistic. Thus we must expand the diameter of the beam dramatically to achieve high power operation at reasonable flow rates. Large beam diameters in CW lasers present their own problem as shot noise in the laser beam due to spontaneous emission can achieve threshold in a small neighborhood of the beam, producing local islands of incoherent oscillation resulting in “beam breakup”. Moreover, the larger the beam diameter, the smaller the curvature of the output coupler and the less overall stability present in the laser system[8]. Such systems are known as high finesse cavities. These systems are easily perturbed by physical disturbances such as thermal expansion and vibrations which can also serve as sources of noise in the spatial profile of the beam. This is especially true if the gain of the system is so large that it swamps the effects of cavity diffraction on mode quality that would normally damp out perturbations in a smaller diameter beam. The COIL systems typically have cross sections for stimulated

emission in excess of 100 x greater than that of Nd^{+3}. Thus we can see that high gain is not necessarily a desirable property for high power laser operation, and that Professor Beyer's hand based laser serves as a cautionary tale when developing high-power/high-energy systems.

Systems such as the ABL (COIL-based), and HELLADS (ceramic disk-based) and the HCL (glass plate-based) have been engineered to operate near the maximum possible design specifications for their gain materials and indeed come close to true high average power operation, but nevertheless remain expensive, and somewhat impractical solutions to the problems they were designed to solve.

To fully appreciate why modern laser systems are engineered to operate near their failure points one must understand both the applications that lasers attempt to serve as well as the physical processes that allow a material to serve as a laser amplification medium. Let's begin by examining two extremes for insight into understanding the demands of laser applications: NIF and the Spectra Physics PRO's. The National Ignition Facility is a laser that is designed to achieve breakeven nuclear fusion via compression and subsequent heating of a deuterium target by a highly symmetric semi-spherical set of 192 converging laser beams. Each beam contains approximately 9.4 kJ of third harmonic radiation at 350 nm (generated from Nd^{+3}-doped glass amplifiers operating at 1053 nm). The system is constrained by the process of heat conduction through glass plates to have a repetition rate of about three shots per day. The maximum total power expended by NIF is therefore about 60 W per day in the UV. The spectra physics PRO laser system is a tabletop, Q-switched laser that has found a wide range of applications in both industry and academia. The PRO can deliver approximately 2 J in ~10 ns at 532 nm with a repetition rate of 10 Hz. This works out to be about 20 W of laser light. The scaling is the same for nearly every laser system currently available

whether pulsed or CW. Simply put, lasers are hard pressed to operate reliably above 10 kW much less the 1 MW-GW required for applications such as nuclear power or defense. Tradeoffs can be made, but sacrificing beam quality for total energy, as can be done in high gain gas and plasma systems, or repetition rate for efficiency, as is done in solid state systems, prevents lasers from being suitable for the most conspicuous applications. Effectively, sacrifices in beam quality are sacrifices in spatial uniformity and hence coherent propagation, precisely the property of laser light that makes it useful for applications in defense and energy.

Examining the requirements of the applications for high average power systems namely, defense, energy, and heavy industry gives insight into the performance requirements of high average power lasers. Each of these applications requires efficient robust high average power lasers to perform some specific goal as yet unmet. Lasers lack the power and reliability to shoot down projectiles over a battlefield. They do not have the rep rates, efficiency or economies of scale to be used as machine tools in heavy industry other than in very specialized or very crude applications, and lack the average power and reliability necessary to operate a nuclear fusion power plant. Barring a major technological advancement lasers will never perform any of these roles. Understanding where they fail is the first step toward achieving a desirable breakthrough.

A high intensity high average power laser system requires: optics, gain media, energy source, electronics, and a box to fit in and hold it all together. What constraints does each of these pose on building a laser with arbitrary performance specifications? The optics constrain the total instantaneous power and wavelength of the laser. The energy source places an upper bound on the total energy available to the laser and the efficiency of the system. The electronics and the box shepherd the system and ensure its robustness and reliability as well as fine tune its performance. Thus we are left with gain

medium to finish the job of telling us what type of lasers can be built. We need to search for materials that have the ability to produce pulses near the damage threshold of our optics (10 J/cm^2 in a 10 ns pulse) and that can store and release as much power as we can reasonably generate in a commercial setting or mobile military emplacement (i.e. approximately 1-10 MW CW).

What does this translate to in terms of atomic physics? The answer is simple: long fluorescent lifetimes, gain cross section low enough to minimize ASE but high enough that the saturation fluence is below the damage threshold ($1x10^{-20} – 5x10^{-20}$ cm^2), and high quantum efficiency. The efficiency constraint touches all three of the requirements above. The active ion must not have a significant difference (i.e. $kT << E_{pump} – E_{metastable} < ½ \hbar\omega_{laser}$) between its metastable states and its pump bands that also overlaps with the emission from a useful pump source.

Diodes can operate at up to 70% wall plug efficiency and couple nearly all optical energy into the medium, begging the question: Why not just use the diode lasers themselves? The answer is they have long 300 μs pulse widths and like any very high gain system, poor spatial coherence (they don't focus well) since the tiny emitters cause high levels of diffraction. Moreover, their small volume creates a significant thermal management problem for diode bars operating above 1 kW. Finally, high powered diode arrays are what their name suggests, arrays of individual lasers placed close to each other that emit many overlapping but distinct beams, not a single coherent beam. Thus diodes are useful for bathing a nearby object in light or to propagate a large roughly collimated beam over a large distance without later needing to bring it to a focus.

To achieve efficient storage and transfer of the energy from a diode array to a gain medium, most of the pump must be absorbed by the medium. This can be accomplished by using clever optical engineering and, as such, is not of interest to this

discussion. However, once this engineering dilemma is resolved and an arbitrary amount of energy is stored in a gain medium, efficiently extracting the energy will depend upon both the lifetime and the cross section. First, the cross section for stimulated emission must be large enough so that the energy stored can all be extracted by a laser field with low enough intensity to pass through the optics without damaging them. However, the cross section must also be small enough so that spontaneous emission not captured by the laser oscillator (end mirrors), yet still traverses the medium, doesn't find sufficient gain to deplete a significant amount of the energy stored in the medium (Amplified Spontaneous Emission or ASE and whispering gallery modes must be minimized or prevented). Additionally, the medium must have a large enough density to store sufficient energy inside a volume accessible to optics of a reasonable size (i.e. storage density of order 0.1-10 J/cm^2). Finally, in the case of CW operation, the lifetime must be long enough to saturate the gain without damaging the optics, while for a pulsed system the diode pumping rate must not exceed the loss rate due to spontaneous emission. Diode lasers have been engineered to have pulse lengths of hundreds of microseconds which is not surprising since electrical pulses significantly shorter than this require complicated infrastructure to efficiently transport their energy. Thus, an efficient system must be designed to accumulate and store energy on timescales comparable to this (fluorescence lifetime ~100 μs). These constraints as well as practical engineering difficulties inherent in handling corrosive chemicals and plasmas have tended to lead the field of optical engineering away from gas, liquid, and chemical lasers toward solid state systems. However, despite their "no muss no fuss" appeal and general suitability, from an atomic physics perspective, solid state systems are plagued by a major problem: transparent solids, with diamond being a notable (but thus far not useful) exception, do not conduct heat well!

The ability of the solid state material to shelter the optically active ions is limited by any temperature response of the mechanical or optical properties of the host. For example thermal lensing, birefringence and fracture are ultimately caused by thermal gradients in the solid hosts that cause differential rates of expansion and hence strain[9,10]. Moreover, as temperatures increase, the volume of phase-space will also increase and per Fermi's golden rule, transition rates will also increase. According to this simple result laser performance in all systems (solid, gas, liquid, plasma) degrades as degrees of freedom become accessible whether thermally or through some other mechanism such as an increase in density or pressure as seen in liquid and gas systems or by introduction of impurity species. Statistical mechanics ensures that any novel compound, chemistry, or quantum effect that exists in a conventional phase of matter will meet with the same scaling problems when attempting to utilize it in a high average power application. What is needed to solve this problem is a conventional gain material that exists in a thermodynamic phase capable of minimizing these types of effects so that they impose a higher ceiling to laser performance than the bound dictated by atomic processes.

Thus the current problems in building high average power solid state systems exist at the level of fundamental physics, preempting engineering considerations that serve only to further constrain the problem (such as pumping sources, geometry, cooling requirements, efficient transmission of high voltage, reagent availability and purity, quality of optics/availability of optics at specific wavelengths and diameters, etc.). For example, the discovery of the perfect high average power novel thermodynamic gain material could be rendered useless for military applications if it required flashlamp pumping. The reasons for this are simple to understand: A highly efficient flashlamp pumped laser will only convert 2% of the total power it consumes into laser light[11]. Thus a mobile 1 MW average power laser would require a system with excess power

generation capacity of 50 MW and could probably only find service in the Navy, assuming one can figure out how to effectively dissipate the remaining 49 MW stored in the system as heat. Therefore, any material considered must also meet other engineering constraints as well.

An early candidate solution to these scaling problems was developed by Jason Zwiebeck et al. at General Atomics in the form of a suspension of crushed Nd^{+3} doped laser glass. The idea was to circulate laser glass particles suspended in index matched fluid through a heat exchanger and to operate the system at an average power determined by the rate of circulating volume and the cooling equilibration time of the average suspended particle. This idea worked at low power despite some difficulty in exactly index matching the fluid and glass. However, when operated at high power the index of refraction of the heated glass would deviate from that of the background fluid to such a degree that scattering losses from the glass would grow, distorting beam quality, and eventually dominate over the gain from the material[12]. The solution to the heat equation is plotted in figures 5 and 6 as a function of particle size and time, demonstrating the limits on a solid state laser as well as the colloidal micro-particle laser due to the timescale of cooling processes.

$$c\rho\frac{dT}{dt} = -\nabla\cdot\left(\kappa\nabla T\right) \tag{2}$$

$$T(r) = T(r_0) + \frac{Q}{3K}\left(r_0^2 - r^2\right) \tag{3}$$

$$T(r,t) = T_{ext} + \frac{2T_0 r_0}{\pi r}\sum_0^\infty\left[\frac{1-(-1)^n}{n}\right]\left[\sin\left(\frac{n\pi r_0}{r}\right)e^{-\left(\frac{n\pi r_0}{r}\right)^2\frac{t}{\alpha}}\right] \tag{4}$$

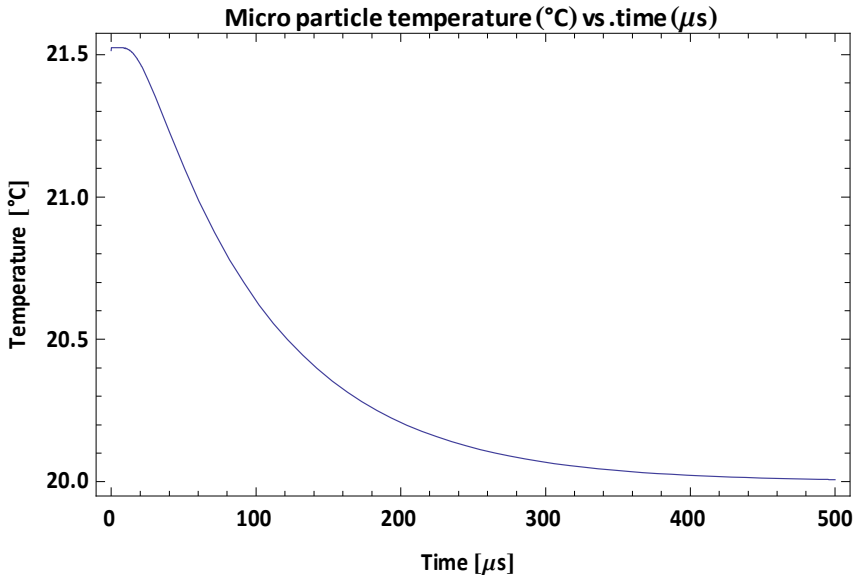

Figure 5. The cooling time of a 10 μm micro-particle.

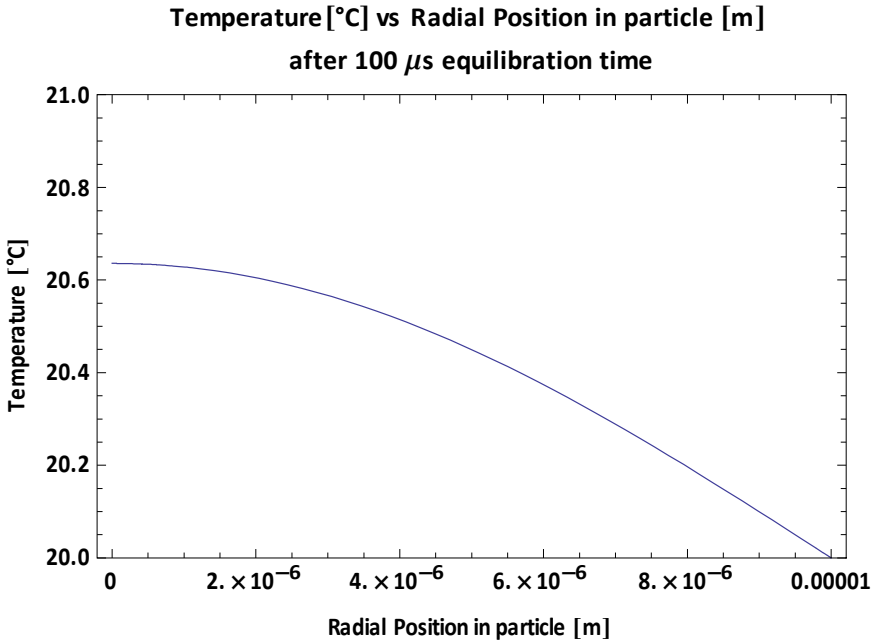

Figure 6. The radial distribution of temperature in a spherical 10 μm micro-particle after 100 μs.

Figures 5 and 6 reveal that the equilibration time for a micro-particle with a 10 μm diameter is approximately 100 μs which means that on the timescales of laser operation it is possible for significant gradients in temperature to exist between the fluid and particulates. Therefore, any mismatch in the change in index of refraction with temperature between the fluid and the micro-particles will result in scattering events that randomly distribute perturbations in the phase front of any wave propagating through the material. By contrast, particles of a few nanometers in diameter equilibrate on nanosecond time-scales with their surroundings, but also scatter light as a result of any dielectric index mismatch. However, their significantly smaller diameter results in a scattering cross section that scales like r^6. Integrating over the large number of particles required to populate a fluid with the same ion density as the micro-particle colloid results in a medium with a total scattering cross section that scales like r^3. Therefore, by utilizing 10 nm nanoparticles instead of 1 μm particles in our colloidal gain material, we could expect a reduction in scattering of at least 10^6. The transmission through a nanoparticle-based colloid can be calculated utilizing Beer's law

$$I_f = I_0 e^{-N(r)\sigma(r,\varepsilon_r)l} \tag{5}$$

where σ is the scattering cross section for a small dielectric sphere[13]

$$\sigma(r,\varepsilon_r) = \frac{8\pi}{3} k^4 r^6 \left| \frac{\varepsilon_r - 1}{\varepsilon_r + 2} \right|^2 \tag{6}$$

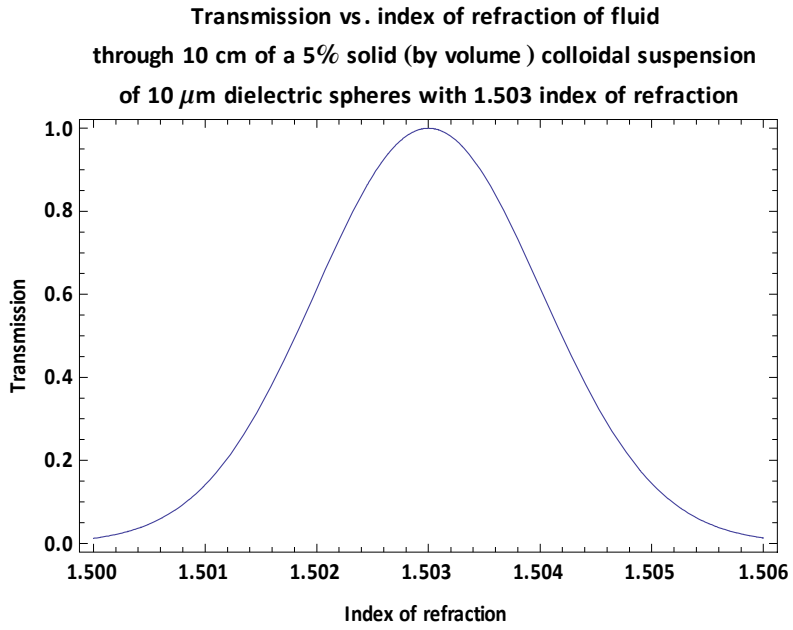

Figure 7. The transmission of a colloidal suspension of micro-particles n = 1.503 vs. the index of refraction of the fluid.

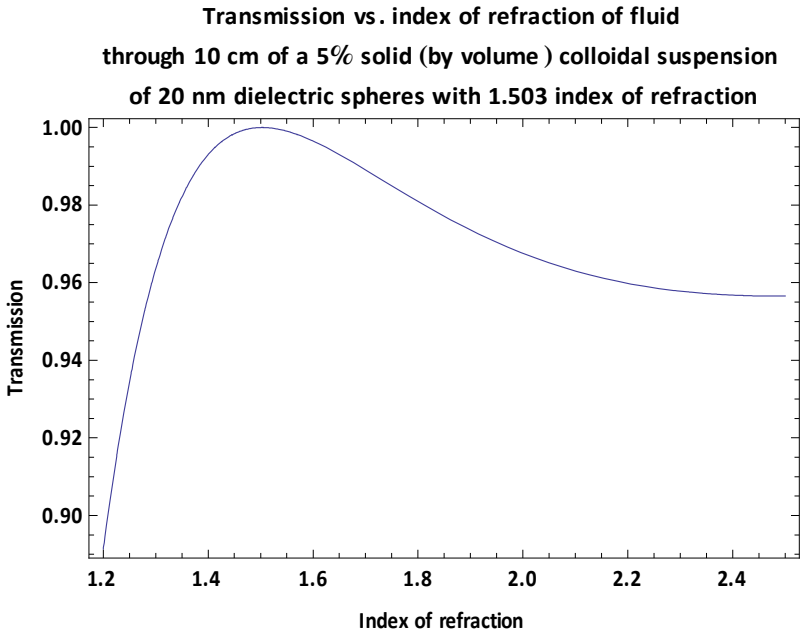

Figure 8. The transmission of a colloidal suspension of nanoparticles n = 1.503 vs. the index of refraction of the fluid.

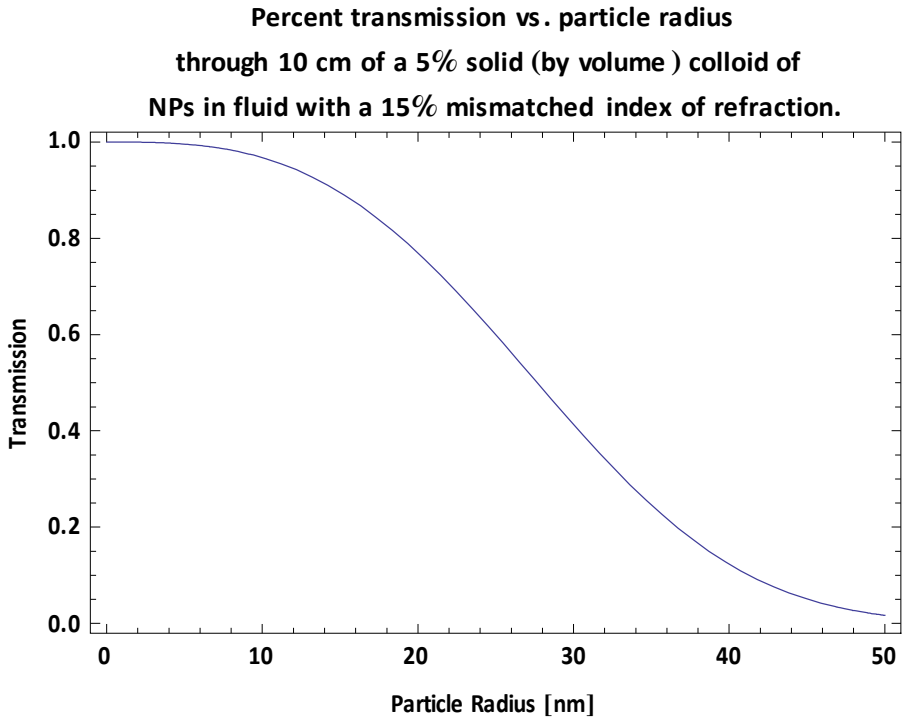

Figure 9. The transmission through a colloidal suspension of nanoparticles as a function of particle radius.

Comparing the transmission through the nanoparticle based colloid to the micro-particle colloid reveals that nanoparticles can tolerate a significant index mismatch without distorting propagation (Figures 7 through 9). This result will be used in the following chapter to calculate the loss term due to scattering in a gain medium for specific laser and amplifier designs. Moreover, this type of material possesses all the advantages of a solid with the thermal properties of a fluid. As will be demonstrated later, the performance of such a gain media is limited only by the atomic processes and not geometric or thermal considerations.

Chapter 2: *Laser and Amplifier Design Using Nanoparticle Based Colloidal Gain Media*

The general overview of atomic physics that resulted in the derivation of the laser rate equations and a discussion of the performance constraints limiting the average power of lasers can be augmented to design laser systems using colloidal nanoparticles as a gain material. Once a laser design is specified its performance limitations can be explored, revealing the advantages this new type of material should possess when operating at high average power. However, it will be useful to start off with a low power design accessible to more practical experiments and capable of verifying the assumptions underpinning a high power design.

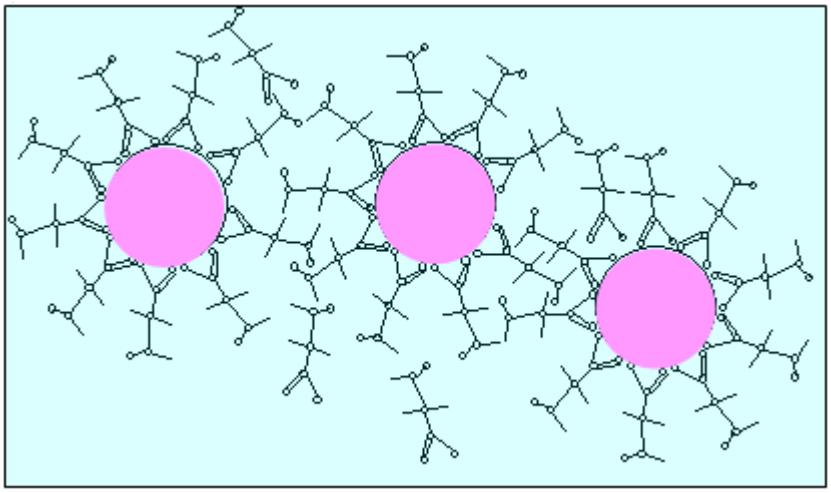

Figure 10. Colloidal nanoparticles encountering a steric barrier to the formation of a flock.

A colloidal laser material has three basic components, the optically active ion, the host material and a surfactant to prevent agglomeration and floccing (Figure 10). The active ion should have optical properties that satisfy the constraints on high average power operation. The requirements for high average power operation can be summarized in terms of energy storage density, absorption cross sections, emission cross sections and

the quantum efficiency of suitable pump wavelengths including any nonradiative transitions which lead to excess heating of the material. First, the energy storage density of a useful material must allow for a compact laser design. This usually means having a storage capacity of at least 1 J/cc or ~10^{19} ions/cc. As discussed in the previous chapter large gain volumes can lead to less robust performance of the system as a whole. For efficient operation the saturation fluence must not exceed the damage threshold of the optical surfaces in the system. In the near IR and visible range the practical limit on saturation fluence is 10 W/cm^2 for a 10 ns laser pulse which sets a lower bound on acceptable cross sections of the laser transition.

Additionally, the laser design and pumping source must deposit energy at a rate greater than losses incurred by the fluorescence lifetime. For materials with short lifetimes, the energy deposited by the pump must be rapidly extracted by the laser. Thus a short lifetime makes pulsed operation tricky, something akin to trying to rapidly fill a leaky bucket before dumping it all out at once. The issue of lifetime in laser engineering arises from the difficulties of efficiently transforming electrical power into optical energy. The time scales over which flashlamps and diode lasers can discharge are on the order of hundreds of microseconds. Therefore efficient operation of high power systems usually requires long lifetimes. Successfully matching the laser design to the pump source and the fluorescence lifetime is essential for efficient operation. Finally, the difference between the pump wavelength and laser wavelength sets the maximum efficiency of the laser.

In addition to the correct quantum mechanical properties, the ion needs to possess a robust chemistry and stable optically active electronic configurations. The need for chemical stability is due to the fact that the highly curved surface of the nanoparticle can strain bonds in the particle increasing reaction rates[14, 15, 16]. In the present work the

chemical stability requirement was relaxed for practical reasons and phosphate glass selected due primarily to its quantum mechanical properties. A discussion of some of the chemical and surface properties of phosphate glass can be found in the literature[17, 18]. Strained bonds can also influence the strength of the external potential that acts to perturb the wavefunctions of the optically active electrons[16]. If the ion is sensitive to its external environment the unpredictable fields present in the nanoparticle may affect the optical properties of the ion and alter the performance of the ion in a laser[19].

A potential host material must also be compatible with the manufacturing process and suitable for laser applications. The surfactant must interact with the host without disrupting the chemical stability of the nanoparticle. The ideal surfactant would attach to the particle surface forming an effective micelle that provides a steric barrier preventing particles from forming agglomerates or reacting with other species present in the system. The surfactant must also possess decent thermal properties, a reasonable viscosity and not be significantly toxic or hazardous.

Neodymium phosphate glass fulfills the above requirements in terms of the properties of host material and the ion. The Nd^{+3} ion in phosphate glass typically has a cross section between 2-6 x 10^{20} cm^2 and a lifetime of 100-400 μs with high densities (ranging between 10^{19} – 10^{21} ions/cm^3)[20]. This material has several transitions suitable for laser operation, the most famous occurring near 1050 nm. A suitable transition for diode pumping occurs near 800 nm with a similar range of cross sections as the laser transition (0.4-6 x 10^{-20} cm^2)[20]. Thus the upper bound on the efficiency of the laser is capped at approximately 76%. With the wall-plug efficiency for diodes including cooling requirements approaching 40%, the maximum efficiency from Nd^{+3} operating at this wavelength becomes ~30%. The relatively low cross section of this material means that the diameter of the glass can be quite large before ASE begins to contribute

substantially to the loss rate. Thus this material has the ability to capture and store a significant fraction of the light from a pump source. Other rare earth ions such as ytterbium possess similar properties making them good candidates for colloidal nanoparticles. However, neodymium uniquely meets all of the above requirements. For example, ytterbium makes a very efficient laser material due to its small quantum defect, but it is a three level system and therefore more difficult to work with at low power. Moreover, its transitions even in crystalline hosts are broader than neodymium indicating that it may interact more strongly with its environment. Finally, due in part to its low quantum defect, it experiences decreased operating efficiency under higher heat loads[21, 22].

The valence configuration of the Nd^{+3} ion is xenon-like (4f3 5s2 5p6) where the optically active 4f electrons orbit well inside the 5s and 5p shells[2, 23]. This configuration allows Nd^{+3} to serve as a dopant ion in a large variety of materials without significantly altering its quantum mechanical properties. For this reason Nd^{+3} makes a good candidate ion for a nanoparticle colloid. Phosphate glass was chosen as the host material because of its favorable laser properties. However, the suitability of this type of glass as the host for Nd^{+3} doped nanoparticles is dependent upon the future discovery of a surfactant capable of stabilizing the particles.

Placing the above discussion on a slightly more quantitative footing will permit the design of a simple laser system that is within reach of the particle production capabilities of the LAM reactor. From this vantage the suitability of this material for high average power operation can be explored. A good starting point for designing a laser is calculating the expected small signal gain. This is accomplished by solving the rate equations for a transition between the metastable state and the first excited state. A complete discussion of the derivation and solution of the laser rate and cavity equations

can be found in a number of comprehensive books on the subject and will not be thoroughly discussed here for the sake of brevity[24]. Assuming the pumping source changes on time scales that are slow compared to the metastable state lifetime, the rate of absorption into the excited state will equal the rate of decay from that state:

$$\frac{d}{dt}n_{ms}(x,t)=\eta\frac{I_p(x,t)}{h\omega_p}\sigma_0 n_0(x,t)-\frac{n_{ms}(x,t)}{\tau_{ms}}-\frac{I_{ms}(x,t)}{h\omega_{ms}}n_{ms}(x,t)\sigma_{ms}=0$$

$$I_p^{sat}=\frac{h\omega_p}{\tau_{ms}\sigma_0},\quad I_{ms}^{sat}=\frac{h\omega_{ms}}{\tau_{ms}\sigma_0} \tag{7}$$

$$\eta\frac{I_p(x,t)}{I_p^{sat}}n_0(x,t)=n_{ms}(x,t)\left(1+\frac{I_{ms}(x,t)}{I_{ms}^{sat}}\right)$$

$$n_0(x,t)+n_{ms}(x,t)\approx n$$

$$n_0\left[1+\frac{I_{ms}(x,t)}{I_{ms}^{sat}}+\eta\frac{I_p(x,t)}{I_p^{sat}}\right]=n\left(1+\frac{I_{ms}(x,t)}{I_{ms}^{sat}}\right)$$

$$n_{ms}(x,t)\left[1+\frac{I_{ms}(x,t)}{I_{ms}^{sat}}+\eta\frac{I_p(x,t)}{I_p^{sat}}\right]=\eta\frac{I_p(x,t)}{I_p^{sat}}n \tag{8}$$

$$n_0=\frac{n\left(1+\frac{I_{ms}(x,t)}{I_{ms}^{sat}}\right)}{1+\frac{I_{ms}(x,t)}{I_{ms}^{sat}}+\eta\frac{I_p(x,t)}{I_p^{sat}}},\quad n_{ms}(x,t)=\frac{n\eta\frac{I_p(x,t)}{I_p^{sat}}}{1+\frac{I_{ms}(x,t)}{I_{ms}^{sat}}+\eta\frac{I_p(x,t)}{I_p^{sat}}}$$

The distribution for the excited states as well as intensity of the radiation fields is found by solving the following coupled system of differential equations.

$$\frac{d}{dx}I_p(x,t)=-I_p(x,t)n_0(x,t)\sigma_0$$
$$\frac{d}{dx}I_{ms}(x,t)=I_{ms}(x,t)n_{ms}(x,t)\sigma_{ms} \tag{9}$$

The solution to this equation is nontrivial for all but the simplest cases. For example, when the pump beam is below the saturation intensity the beam is exponentially

attenuated. If the pump intensity is greater than the saturation intensity and contains sufficient power to remain above saturation intensity throughout the material, the population inversion will be uniform and the power in the beam will decrease linearly through the material. The solution to a real system of equations lies somewhere between these two extremes and is easily calculated numerically by solving the above ODE during steady state operation. To precisely account for transient behavior, the system must be treated as a PDE coupled to propagating pulse envelopes which will be dependent upon the specifics of a laser design. However, for the purposes of understanding the rough characteristics of laser materials or classes of designs, this level of precision is generally unnecessary. Thus, the distribution of excited states in the gain medium can be approximated using the average population inversion density which is obtained by integrating the system of equations for the appropriate limiting case. For example, if both the pump and amplified transition are operating below the saturation intensity, then to first order the following approximations to the above population equations hold which leaves:

$$\begin{aligned} n_0 &= n\left(1-\eta\frac{I_p(x,t)}{I_p^{sat}}\right) \\ n_{ms}(x,t) &= n\eta\frac{I_p(x,t)}{I_p^{sat}} \end{aligned} \tag{10}$$

Substituting equation (10) into equation (9) the rate equations for the intensity can be simplified:

$$\begin{aligned} \frac{d}{dx}I_p(x,t) &= -I_p(x,t)n\left(1-\eta\frac{I_p(x,t)}{I_p^{sat}}\right)\sigma_0 \\ \frac{d}{dx}I_{ms}(x,t) &= I_{ms}(x,t)n\eta\frac{I_p(x,t)}{I_p^{sat}}\sigma_{ms} \end{aligned} \tag{11}$$

Solving for the intensity of the pump beam yields:

$$\frac{d}{dx}I_p(x,t) = -n\sigma_0 I_p(x,t)\left(1-\eta\frac{I_p(x,t)}{I_p^{sat}}\right)$$
$$I_p(x,t) = \frac{I_p^0 I_p^{sat}}{\eta I_p^0 + \left(I_p^{sat} - \eta I_p^0\right)e^{\eta n\sigma_0 x}} \quad \textbf{(12)}$$

Performing the obvious substitution for $I_p(x,t)$ and simplifying:

$$\frac{d}{dx}I_{ms}(x,t) = I_p^0 n\eta\sigma_{ms}\frac{I_{ms}(x,t)}{\eta I_p^0 + \left(I_p^{sat} - \eta I_p^0\right)e^{\eta n\sigma_0 x}} \quad \textbf{(13)}$$

Integrating the expression yields:

$$I_{ms}(x) = I_{ms}^0\left(\frac{1}{1-\eta\frac{I_p^0}{I_p^{sat}}\left(1-e^{-\eta n\sigma x}\right)}\right)^{\frac{1}{\eta}} \quad \textbf{(14)}$$

An analytic approximation can also be derived since the pump intensity was assumed to be less than the saturation intensity:

$$I_{ms}(x,t) \approx I_{ms}^0\left(1+\frac{I_p^0}{I_p^{sat}}\left(1-e^{-\eta n\sigma x}\right)\right) \quad \textbf{(15)}$$

Thus in the small signal case where the intensity of both the amplified beam and the pump beam are significantly lower than their respective saturation intensities, the solution takes the familiar form of exponential gain.

Using this expression for steady state pumping at low intensities, a simple laser can be designed. The first step is to specify the loss terms in a resonator. Threshold operation will occur when the pumping rate creates a small signal gain that exceeds the losses in the cavity. The cavity round trip time c/2L is the decay time constant for the

cavity. Therefore the power stored in the resonator as a function of time can be written in terms of the reflectivity of the mirrors and the transmission through the remaining cavity optics. At the threshold of laser operation the circulating intensity is effectively zero and the round trip loss balances the round trip gain calculated above.

$$\begin{aligned} \alpha_{loss} &= -\ln\left(R_{HR}R_{OC}T_c\right) = 2G_{ss} = 2\left(1+\frac{I_p^0}{I_p^{sat}}\left(1-e^{-\eta n\sigma x}\right)\right) \\ I_p^{th} &= I_p^{sat}\left(\frac{-\ln\left(R_{HR}R_{OC}T_c\right)}{2}-1\right)\left(1-e^{-\eta n\sigma x}\right) \end{aligned} \tag{16}$$

Above threshold, the effects of the loss terms must be accounted for in the gain equation. Moreover, the approximation that the circulating intensity in the resonator is less than the saturation intensity may no longer hold. The equations derived above must then be modified and solved numerically[24].

$$\begin{aligned} \frac{d}{dx}I_p(x,t) &= -I_p(x,t)n_0(x,t)\sigma_0 \\ \frac{d}{dx}I_{ms}(x,t) &= I_{ms}(x,t)n_{ms}(x,t)\sigma_{ms} - \alpha_{loss} \end{aligned} \tag{17}$$

Rigrod analysis produces an expression for the output power as a function of the output coupler by considering the gain loss equations for the counter propagating beams in the cavity as a function of the small signal single pass gain modified by a saturation parameter that is determined roughly by the circulating intensity required to deplete the excited state population and hence round trip gain by half[24].

$$\frac{d}{dx} I_{ms}(t) = I_{ms}(t)\left(\frac{G_{ss}}{1+\frac{I_{ms}(t)}{I_{sat}}} - \alpha_{loss} \right)$$

$$I_{sat} \approx \frac{\lambda_p}{2\lambda_l G_{ss}} \left(I_p(0,t) - I_p(L,t) \right) \quad \textbf{(18)}$$

$$I_{out} = I_{sat} \frac{1-R_{oc}}{\left[1+\left(\frac{R_{oc}}{R_{hr}} \right)^{1/2} \right]\left[1-R_{oc}R_{hr} \right]} \left[Log\left(G_{ss} - \alpha_{loss} \right) \right]$$

This simplistic example does not account for the mode structure present in the cavity during operation. However, for determining the rough performance limits of a colloidal gain medium, mode considerations can be neglected as they contribute only a geometric factor to the estimates and will be substantively equivalent to those already found in the solid state laser literature. Thus, to solve for the circulating power in the cavity, the only parameter that must be specified is the reflectivity of the output coupler. This parameter must be optimized in concert with the pump power to maximize the output power from the laser.

In applying this analysis to the problem of building a small laser from the nanoparticle colloid the primary challenge is estimating the losses. Since both the particle density of the colloid and the cross section for stimulated emission are low, a long optical path length is required to attain threshold. The path-length required dictates the spot size on the resonator mirrors and the minimum waist in the gain medium. For the case of a 1 m cavity, the product of the spot size of the pump and the fluence needed to achieve a population threshold results in an unrealistic >10 W requirement of the pump laser as well as a significant volume of the colloid. Moreover, at these intensities, volumes, and flow rates the temperature of the fluid would also be difficult to control. The solution to all these problems takes the form of a capillary tube capable of acting like

a liquid core waveguide. This is basically just a thin capillary tube coated with a polymer enabling the tube when filled with a suitable material to act like an optical fiber. This allows the pumping area to remain small compared to free space designs. However, the relatively large diameter of the core combined with a flat pump profile results in an almost fully excited fiber and a highly scrambled mode. Thus the contribution of the mode structure to the population inversion is ignored. However, the tradeoff with this type of system is insertion loss. The capillary tube can't directly abut an optic since the fluid needs to be able to freely flow from the tube. Thus a window must be placed near the end of the tube and optics selected to mode match the pump beam and the resonator mirrors with the liquid waveguide. Scattering from the nanoparticles, though minor, must also be considered when calculating the oscillation threshold.

The derivation of Rayleigh scattering is a simple matter of computing the scattering cross section of a small particle from classical E&M and then integrating over the density of particles in the sample[13]. The insertion loss for a re-entrant beam in large core multi-mode fibers is complicated by spherical aberrations and coma from the resonator optics[25, 26, 27]. Investigation of this problem using commercial ray tracing software was not possible due to the complicated mode structure present in this type of waveguide. Thus a ray-tracing program was written that was capable of simulating the output of the fiber and calculating the insertion loss through an aplanat available from CVI laser.

The insertion loss was then calculated as a function of NA, beam diameter and lens position. Comparisons were made between the aplanat and a singlet to establish the magnitude of the insertion loss for a simple design. Some of the conditions from Baker et al. were reproduced to verify that the code was functional[26]. It should be emphasized that they assume axial symmetry across the entire beam wavefront and therefore under-

report insertion loss in a fully excited fiber. However, for their purposes, this approximation sufficiently captures the relevant behavior and dramatically simplifies their computation.

For the calculation reported here no assumption of symmetry was made when specifying the source conditions. Diffraction effects on the relevant length scales are negligible compared to other loss terms and are therefore ignored. A useful discussion of the topic can be found in Born and Wolf[28]. The ray tracer was built with a simple interface similar to commercial ray tracers. The code is an implementation of the refraction problem and does not calculate the solution to the full Fresnel's equation. The program is available in Appendix B.

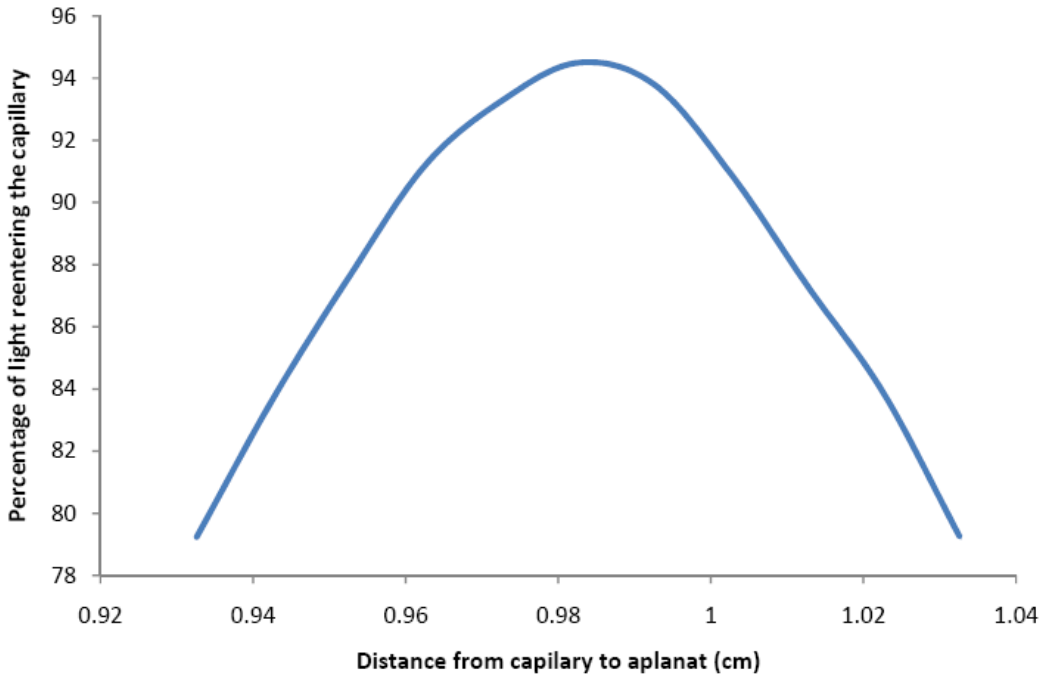

Figure 11. The efficiency of coupling for re-entrant light through an aplanat lens as a function of distance between the aplanat and the Liquid Waveguide Capillary Flow Cell (LWCFC).

Plotted in Figure 11 is the coupling efficiency for re-entrant light into the capillary tube. To make this plot using the ray-tracing software, the exit plane of the liquid waveguide capillary flow cell LWCFC is placed at a variable distance from an aplanat. The beam is then retro-reflected off a mirror positioned one focal distance from the tube forming an image at the entrance of the capillary tube. Rays with the correct numerical aperture that fall within the diameter of the tube are accepted, all others rejected. Though imperfect, the performance is significantly better than a singlet lens or curved mirror, the best of which only reached 70-80% coupling efficiency.

The performance of a simple laser of this type requires knowledge of the nanoparticle concentration, lifetime, and cross section of the laser transition. These parameters can't in general be calculated a priori[23]. For Nd^{+3} these parameters can be calculated roughly using Judd-Olfelt analysis which is a phenomenological model that sets a fit parameter for each rank tensor in the spherical expansion of the wavefunctions to specify the relative scaling of transition strengths[23, 29]. This analysis requires a measurement of the absorption spectra in several regions of the spectrum. Thus, for the purposes of laser design the relevant parameters must be determined in one way or another through direct measurement of the material's spectroscopic properties.

Assuming that it would be possible to manufacture a material with properties similar to the bulk, the effect of any small departure from these values on laser performance can be mapped out. In this manner and in conjunction with iterative experiments, a design for a low power laser that might achieve threshold with this material is presented, given the current limits of the nanoparticle manufacturing process. The cavity consists of an end pumped capillary waveguide with optics determined by the ray tracer. A fiber coupled diode pump laser is mode matched and then coupled through a dichroic high reflector into the cavity. The output end of the cavity is identical to the

input side except that the transmission of the output coupler is chosen to optimize the output power.

The output power as a function of output coupler transmission was found for this laser design, assuming 5 W pump power, a 1 m long capillary tube with an inner diameter of 250 μm, 20 nm diameter particles with a 60 μs lifetime and absorption and emission cross sections of approximately 6 x 10^{-20} cm^2. The single pass gain for this system is approximately 10%. The scattering loss from the particles is 2.3%, the insertion loss is approximately 4.5 %, the high reflector is 0.5 % and the output coupler is ~2%, yielding a 45 mW beam (Figure 12) with a circulating power of ~2 W.

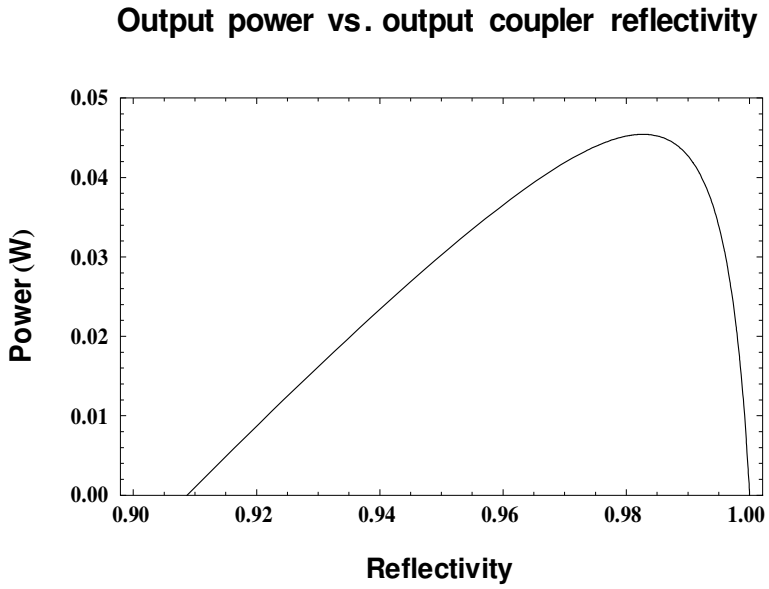

Figure 12. Output power as a function of output coupler reflectivity.

Assuming it is possible to manufacture useful quantities of a nano colloid, and that the optical properties of the material are similar to those of bulk material, a rough analysis of the potential performance of lasers made from this material can be attempted. First, sufficient power, supplied by an intermediate storage and generation system must

be available to operate the system. In this case it will be assumed that at least 1.5 MW of continuous power is available with an intermediate storage system such as a capacitor bank capable of delivering at least 10 MW for up to 1 ms. Also, sufficiently compact multi kW diode laser array capable of QCW pulsed operation at approximately 800 nm must be available. Finally a suitable surfactant must be found to passivate the nanoparticle surface with a heat capacity comparable to common hydrocarbons (i.e. at least 1.8 kJ/kg °K) and a viscosity greater than ethanol but less than glycerin (between $1x10^{-3}$ and $1x10^{-2}$ Pa·s). With these constraints satisfied, scalability of a colloidal gain medium to 10 MW burst operation with 1 MW average power is theoretically possible.

First it should be noted that General Atomics, Lockheed, and Boeing, have all independently verified that reaching the constraints specified above is a practical engineering goal. Additionally, Lockheed designed excess power generating capacity on the Joint Strike Fighter of 1 MW for the purpose of deploying a high average power laser. Finally, Boeing has produced compact micro-channel liquid cooled thin ceramic diode pumped disk lasers capable of operating in the 100 kW range[21, 22]. The advantage a colloidal nanoparticle based laser would have over these other systems would allow convenient scaling to much greater average power operation with designs operating well below their engineering limits.

A colloidal nanoparticle solution operating at 1 MW average power in 10 MW bursts would require no active cooling. In the case of an aircraft based laser, a passive heat exchanger utilizing jet fuel as the heat sink would permit sustained operation of the system. The maximum heating rate of the gain medium is determined by the difference between the pump laser and the extracted beam and the ratio of optical to nonradiative transitions. By utilizing an oscillator amplifier design that operates at a repetition rate significantly greater than the rate of nonradiative transitions, which extracts its energy

from a power amplifier at or near the saturation fluence, the efficiency of the system from the perspective of thermal losses can be maximized. For example, a colloid made from 20% Nd^{+3} Q-X laser glass with 1% solid volume fraction can store 4 J/cm^2. Through a combination of converging edge and end pumping schemes it should be possible to produce a reasonably uniform 7-9% population inversion in 10 μs meaning that the effective storage density is ~0.1 J/cm^2 capable of overlapping with at least 80% of the amplified beam. If the fluorescence lifetime of the material is ~100 μs, then the excited state should not be allowed to persist for more than 10 μs to maintain the criterion that the ratio of radiative losses to non-radiative losses >> 1. However, QCW diodes have typical pulse widths ranging from 250 μs to 1 ms. Extracting most of the energy supplied to the gain material would require at least 100 seed pulses at the saturation fluence. This would require a slicer or Q-switch in an oscillator section of the system to fire at 100 kHz. This level of performance is commercially available. The final engineering challenge requires setting the expansion rate of a beam propagating through the amplifier such that the rate of increase in the beam diameter allowed the fluence in the beam to maintain a near constant value. These design requirements set the performance specifications for the system allowing the beam diameter, heating rate and pump laser requirements to be specified. The amplifier would need to function in a multi stage configuration. The first stage would amplify a 1-100 mJ Gaussian 10 ns pulse to 500 mJ-1 J in 2-4 passes. The next 4 stages would consist of the power amplifiers, each approximately 10 cm long, operating near saturation. The entrance beam diameter would be 5 mm and the exit 5.5 cm. The total pumping volume of fluid would be 380 ml, given a 7% population inversion and a density of ~1 g/ml. Given the amount of waste heat generated by the pumping defect, the ability to achieve ~80% pump overlap, and assuming a 7% upper bound on nonradiative processes (determined by the fraction of the fluorescent state

lifetime elapsed during the pumping process), an upper bound for the total heating rate of the fluid during a 1 ms burst can be established at ~6 MW. This corresponds to depositing 6000 J in the fluid during each burst. Given the heat capacity of 1.0 - 1.8 kJ/(kg °K) and the above values for energy deposition and fluid volume, the maximum temperature change in the fluid during a 100 pulse burst would be 5°-10° K. Matching the fluid velocity to twice the heating rate would only require a flow rate of ~10 m/s and with a modest number of index matched transparent dielectric partitions, the flow could remain laminar (Reynolds number <2000)[30]. Sustained operation at 10 MW would require linear flow rates of ~100 m/s or a more dilute colloid with a longer interaction region. At these flow rates and small thermal gradients, it should be possible using AR-coated index matched thin glass partitions to satisfy the requirements of laminar flow through the interaction region. Though the beam diameter is only 5 cm, the clear aperture of the system at the exit would need to be 30 cm to prevent clipping from degrading beam quality, but overall the dimensions are very reasonable for a laser capable of operating at 10 MW average burst power with 1 MW average power. The duration of a burst is approximately 1 ms. This configuration would deliver 100 kJ to a target in 0.1s. To put this in perspective, the firing rate of a 50 caliber machine gun is at best 20 rounds per second, each delivering at most ~20 kJ. Combining the cooling of the gain media with the cooling of the diodes would mean that with a half full fuel tank (~3500 kg) the Joint Strike Fighter could continuously fire the laser for 12 minutes and only increase the temperature of its onboard fuel by 50°-100° C. In a passively cooled system, firing time would be determined by the heat capacity of the heat sink utilized. Thus, keeping all numbers constant except for the population inversion density allows for the heating problem to scale. Were a larger power source available, increasing the fluid volume utilized while decreasing population inversion density in concert with an increase

in the transverse fluid velocity would permit 10-100 MW average power operation without increasing the beam diameter. However, increasing the average energy per pulse would require a larger beam, and ASE would eventually become problematic for compact designs. Additionally, at worst this amplifier's ASE as a fraction of saturation intensity is approximately 2%. Each amplifier stage has a small signal gain of approximately 1.83 with the total system gain being approximately 11. Scaling to a 1 kJ pulse under the same conditions would require a 1 m long amplifier supporting a 15 cm diameter beam at the output and a ~10 m/s flow rate. Such a system would emit ASE at approximately 13% of saturation intensity.

Beyond the gain medium the main requirement limiting the implementation of the above design is its power consumption. To operate at 1 MW the amplifier as specified above would at best possess a wall plug efficiency of 10% - 15% meaning that the power system would need to supply 7-10 MW continuously in bursts of 70-100 MW. The laser described above operating off a 1 MW generator with no secondary storage system could at best hope to operate at 160 kW. This is near the 150 kW solid state CW laser under development for the JSF. This system is based upon thin, edge-pumped, ceramic disks that operate at approximately 70° K leaving limited head room for increasing the power of the system[21, 22]. Thus compared with solid state systems, a laser of this type has a healthy engineering margin especially since the component technologies have already been proven in other systems. The assumptions in the above scaling argument that remain untested are that nanoparticles possess qualitatively similar optical properties to bulk materials, they can be manufactured at industrially useful rates, and they can be collected in a practical surfactant. The bulk of the work presented here attempts to resolve the questions surrounding the optical properties of the nanoparticles. However, some effort was invested in addressing the production and collection issues. In general,

the results are promising. The optical properties appear to be similar enough to bulk glass for the above analysis to apply. The problems in production rate can be addressed through improvements of the existing manufacturing technology.

Chapter 3: *Manufacturing Nanoparticles via the Laser Ablation of Micro-particle Aerosols*

A flexible technique for the creation and collection of nanoparticles from the laser ablation of aerosolized micro-particles (LAM) was developed at UT by Professors Keto, Kovar, and Becker[31]. The prototype LAM reactor entrains an aerosolized powder in a thin collimated laminar flow. A 300-400 mJ, 200 Hz, 8 ns, KrF excimer laser is focused on the aerosol column using a cylindrical lens. The flow rate of the powder is matched to the length of the beam times the laser's repetition rate to provide uniform continuous ablation of the powder stream. Figure 13 shows a schematic of the LAM production and collection apparatus. The nanoparticles are created in the "horn cell" and proceed to flow over a virtual impactor and then into a supersonic nozzle to be collected by impaction into a fluid. The fluid should ideally stabilize the nanoparticles both chemically and physically, preventing them from interacting with other particles or their container.

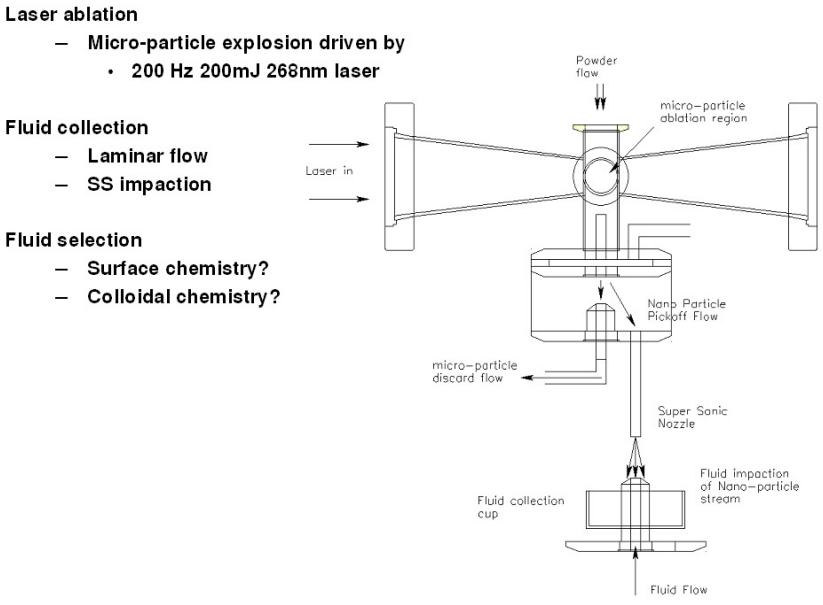

Figure 13. A schematic of the production and collection process and apparatus.

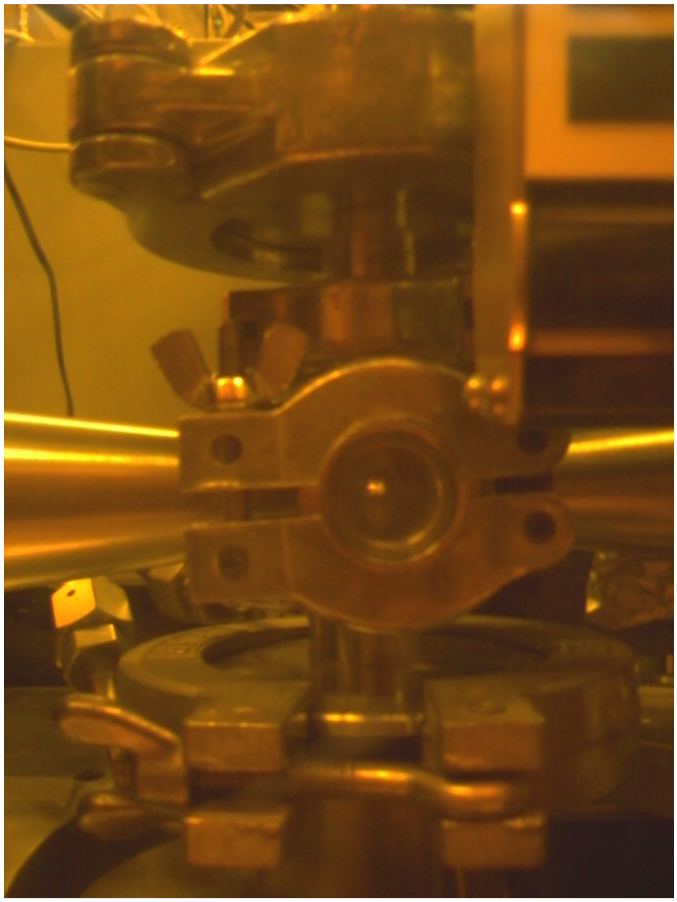

Figure 14. The ablation of a micro-particle aerosol.

Figure 14 shows the LAM reactor in operation. A thin orange plume is visible in the center of the horn cell's window. Micro-particles (in this experiment 20% Nd^{+3} Kigre Q-X phosphate laser glass) in the ablation region absorb a small portion of the laser energy through photo-ionization on their surface creating plasma that rapidly expands. As shown in Figure 15, the expansion of this plasma drives a shock wave through the micro-particle that causes it to explode forming a saturated vapor cloud[32]. One can see how the geometry and absorption characteristics of the material could affect this process. In a transparent sphere, for example, light would focus on the back surface, increasing the fluence and hence the probability of achieving breakdown, as well as the total energy

driving the shockwave. By attending to these details it should be possible to maximize the area of the beam that is above threshold for nanoparticle production and hence the total volume of powder ablated.

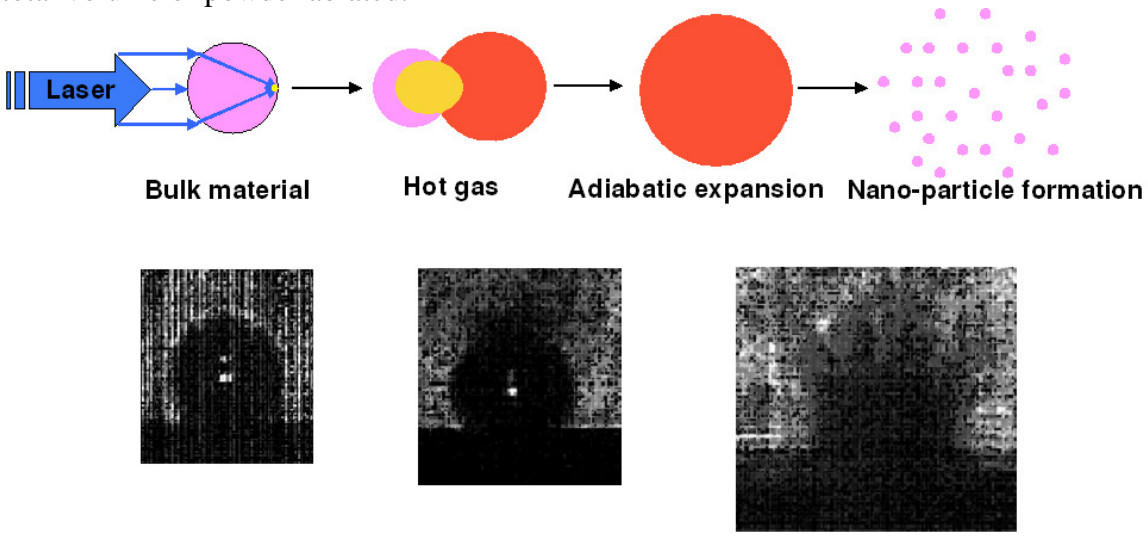

Figure 15. The laser ablation of a micro-sphere and formation of a debris cloud[32]. Images of the exploding micro-spheres from work by J. Keto et al.

Once sufficient adiabatic expansion and hence cooling of the cloud occurs, the saturated vapor condenses forming nanoparticle droplets that rapidly cool in the ambient gas. The droplets continue to grow until the saturated cloud sufficiently expands and cools. By controlling the conditions present during ablation, the LAM production technique has the ability to tune particle sizes over a wide range, 1 nm -100 nm, and is compatible with a large variety of materials.

However, in the case of transparent, amorphous, dielectric materials like the laser glass used in this experiment, the laser fluence is insufficient to break down the entire aerosol flow, resulting in a depressed yield and a large percentage of partially ablated or agglomerated micro-particulates entrained in the aerosol. The micro-particles are separated from the nanoparticles by allowing the gas column to expand into a larger

volume that flows over a "virtual impactor" permitting larger particles to settle upon the surface. The gas and remaining particulates then flow through a supersonic nozzle into a vacuum chamber (~200 mT) imparting sufficient momentum to the particles for them to cross stream lines and impact on a surface coated in a fluid[33]. The fluid, driven off the impactor surface by the pressure from the supersonic jet, drains into a reservoir where a pump then circulates it back to the impactor; continuously increasing the concentration of the nanoparticles.

Chapter 4: *Producing a Powder Suitable for LAM*

The first problem to overcome in manufacturing a useful sample of nanoparticles was simply producing a uniform powder capable of supplying the LAM with an aerosol of reasonable particulate density. A useful powder is simple to define. The ideal powder for the LAM process would have a small enough average diameter such that its terminal velocity was less than the flow rates encountered in the LAM process and wouldn't stick to itself or the internal surfaces of the LAM reactor. The former condition is easily satisfied since calculating the terminal velocity of a particle as a function of its diameter is straightforward (see Figure 16)[34]. The latter condition is a bit more difficult to achieve and requires that the powder be carefully produced. (Note that these conditions are specific to this apparatus particularly the powder feeder used.)

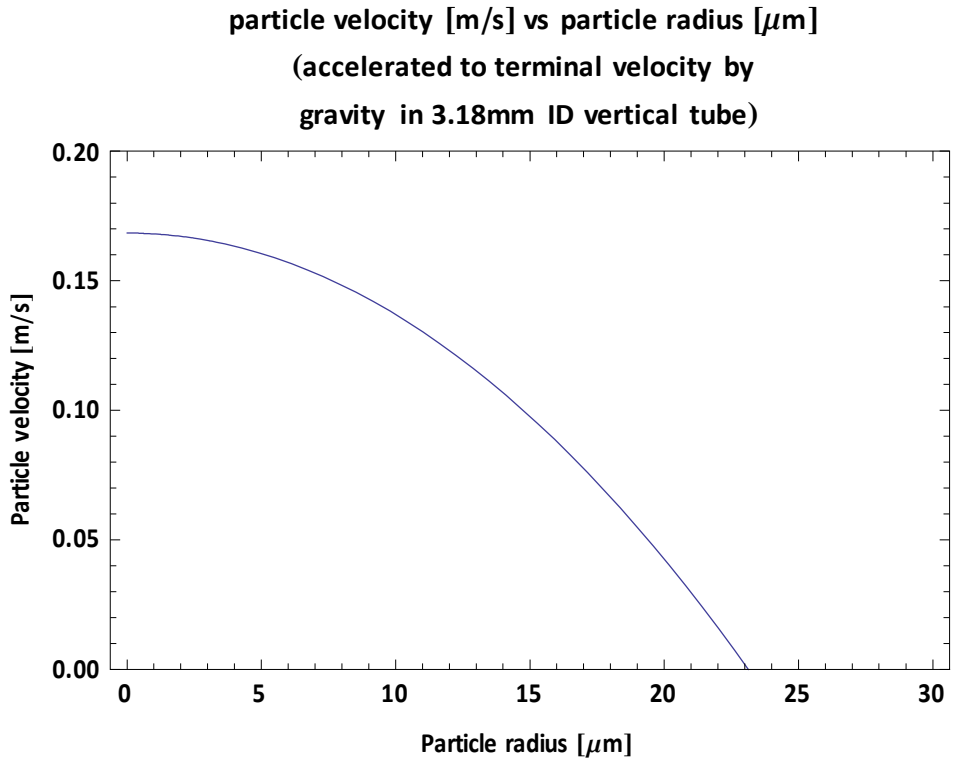

Figure 16. Average particle velocity in an aerosol flowing through a vertical pipe as a function of particle size.

The equation for the terminal velocity of a spherical particle is:

$$V_t = \frac{2gr^2\left(\rho_{particle} - \rho_{fluid}\right)}{9\eta} \quad \textbf{(19)}$$

where η is the viscosity of the fluid, r the particle's radius, and ρ_{particle} its density. Provided that the velocity of an upward flow through a vertical section of tubing exceeds the terminal velocity of a particle, the particle will advance upward with the flow. This condition sets the maximum particle size that can be fed into the LAM reactor. Thus any diameter particle with a positive relative velocity in Figure 16 would be ablated.

The process of turning a block of glass into a useful powder (as defined above) was not trivial to discover. Automatic machine based methods such as crushing, ball milling and grinding were investigated and all found to be unsuitable or impractical, given our resources. A brief review of grinding revealed it to be unworkable due to the high likelihood of introducing significant concentrations of impurities into the material. Crushing ultimately served as an intermediate step in producing our powders, but was not capable of producing uniformity in the particle size. Ball milling though at first promising tended to produce powders with high concentrations of the ball mill media and poor size control (Figure 17).

Ultimately a multi-stage method for preparing useful powders was developed. The glass rod was broken into flakes with a hammer, the flakes then crushed with a hydraulic press, and finally the coarse powder ground in a sapphire mortar and pestle. After grinding, the powder was size sorted by suspending it in a fluid and decanting the powder after giving it sufficient time to settle. Several stages of the grinding and sorting process were necessary to obtain a powder of somewhat uniform size. The smallest

particles would take several minutes to settle and were discarded as they caused agglomeration. This process of sorting and grinding would continue until a powder was obtained that would produce a visible flowing dust cloud in the fume hood when agitated but would not agglomerate when stored in a sealed jar overnight.

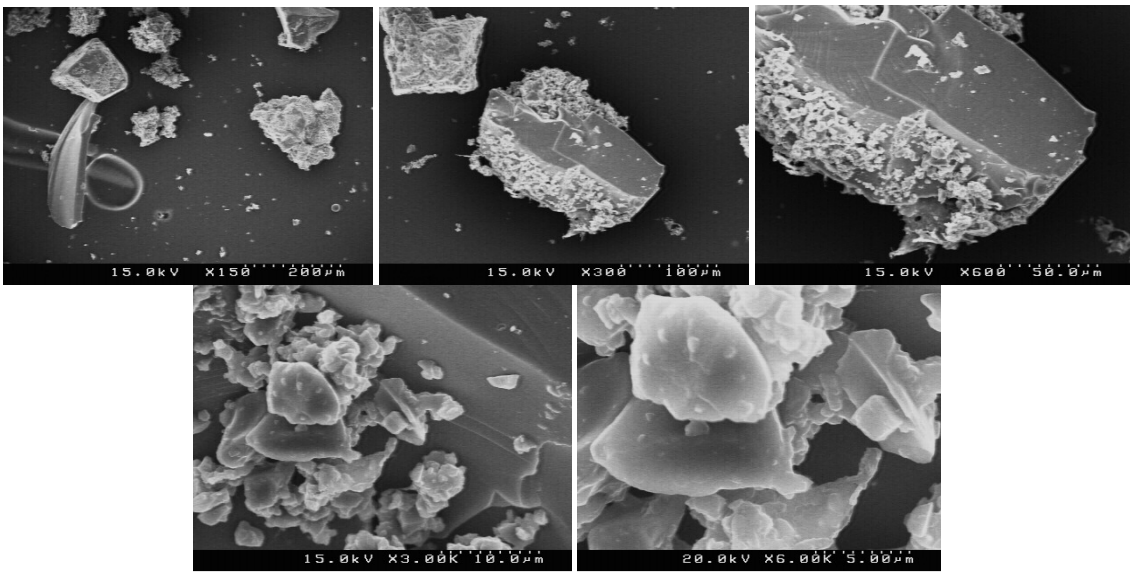

Figure 17. SEM images of ball milled powder after one round of size separation.

First I will discuss the details of what didn't work, to prevent future excursions into blind alleys. All attempts at ball milling proved unsuccessful, producing undifferentiated results. The ball milled powders tended to have a high propensity to agglomerate and contained large contaminant concentrations. The balls lost significant mass during the process, approximately 10-20%, visibly changing size and shape. The procedure for ball milling was to smash a 50-100 g section of glass with a hammer, or crush it in a press and then briefly grind it in a mortar and pestle before adding it to a plastic jar with either zircon, or alumina balls and placing it on the ball mill. The velocity

of the mill was then set so the balls would climb the jar's inner surface before falling as they neared the apex.

The mill would usually be set up during the morning and checked 10-12 hours later that evening. It was found that 10-12 hours was insufficient time to produce a high quality sample. It usually took at least 16-24 hours of milling to produce a fine powder capable of aerosolizing, even after applying a size separation technique to the powder. Visual inspection of the powder was the primary diagnostic utilized, although SEM work was conducted on several samples. In addition to contamination, all ball milled samples usually had a large quantity of both large particle fragments and fine particles (Figure 17), both of which are undesirable, and tended to agglomerate more readily than hand ground powders.

It was hypothesized that the average surface energy was greater in the ball milled samples causing them to have increased inter-particle attraction. To address this concern several samples were prepared and heated to near the glass transition temperature in an inert environment to allow any surface defects to repair themselves. A variety of temperatures were tested on small samples ranging from 350° C to 500° C. The hottest conditions re-melted the glass into a sheet while the lower temperatures showed no changes from the control. SEM images and visual inspection confirmed the onset of particle deformation and flow at about 420° C. Based upon these results we heated a large quantity of powder to 400° C in a helium environment for 16 hours. The powder showed initial improvement resisting agglomeration but subsequently clumped just as easily as the control. This combined with the results contained in Amy Barnes' dissertation led us to conclude that the problem with agglomeration was simply that of surface area and hydration[17]. Particles colliding at oblique incidence experience shear forces proportional to their mass and approximate diameter. If the shear they experience

is greater than the surface potential then they scatter. If the shear is less than the surface potential they stick and rotate about their new center of mass. Thus, it is apparent that the smallest particles will have less inertia in a collision in addition to having larger relative surface potentials and therefore more readily agglomerate. The results described above follow naturally from the expectation that the action of a hydration layer serves to increase both the footprint and strength of the interaction between two glass particles. Therefore, the two remedies that best reduce the tendency of the micro powder to form agglomerates are to remove the very smallest particles and then heat the powder before using it, removing as much of the hydration layer as possible.

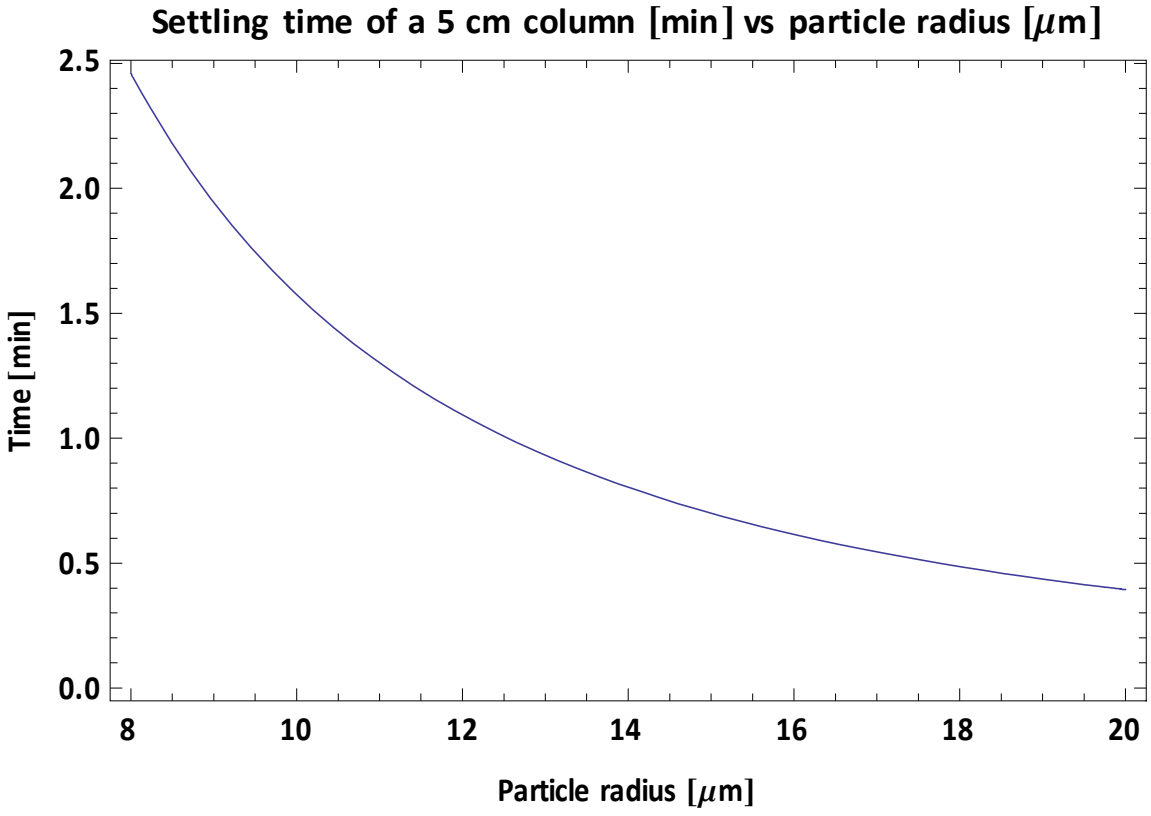

Figure 18 Settling time as a function of particle radius in ethanol.

Unfortunately, despite many attempts to refine the process, ball milling produced an over abundance of the very smallest particle sizes compared to hand grinding. This effect was observed by using a column of ETOH to suspend and then decant the micro particulates. The smallest particles would remain suspended for 5-10 minutes after shaking a covered cylinder containing ETOH and glass powder. From the graph in Figure 18 it is clear that if a 10 cm column of fluid containing micro-particles is allowed to settle for 2 min there will be no particles present with a radius larger than ~13 μm but a significant concentration of particles still in suspension below that cut[34]. This could be directly observed by watching the sedimentation process. During the first few minutes of settling several different color layers would form. If allowed to completely settle, a process taking hours, the final layer would be white, while the various other levels would transition gradually from white to pink and finally at the bottom a substance resembling purple sand.

This purple sand would be harvested and re-ground while the white substance would be removed by shaking and decanting after a few minutes of settling had occurred. To eliminate the fine particles and obtain a useful powder it is necessary to agitate and decant 3-4 times. In ball milled samples this process produced several grams of material compared with a few tens of milligrams for the hand ground powder. The purple sand would then be separated from the usable powder by agitating the powder and then rapidly decanting the solution. The remaining powder in the column would typically need to be re-ground and separated at least 2-3 times to complete the process. The yield of useful powder from a 100 g starting sample was typically in the range of 60-70 g.

After a few years of trial and error a reasonably successful procedure for producing useable powder was devised. The current version of this procedure is straightforward if time consuming.

1. Wearing proper safety gear (safety glasses, puncture resistant nitrile gloves, particle filter breathing mask) break off sufficient glass from the puck, 50-100 g.
2. Wrap the glass in several layers of aluminum foil.
3. Crush the glass/foil in a hydraulic press.
4. Open the foil package in a laminar flow fume hood designed specifically for working with particulates (Standard RLM chemical fume hoods offer insufficient flow rates and hence inadequate protection from the powders produced during this process).
5. Remove any large chunks of glass from foil and repeat steps 2-5.
6. Place a small amount of powder (1-2 g) in a sapphire or agate mortar and pestle, and grind in smooth circular motions using moderate downward pressure (should take 1-2 min/g).
7. Once a uniform consistency is achieved place powder in an airtight non breakable storage vessel. Repeat steps 6-7 until all powder appears uniform.
8. Place 10-20 g of ground powder in a graduated cylinder partially filled with ethanol. Agitate until cloudy.
9. Rapidly decant all fluid and suspended solids into a beaker.
10. Add fresh ethanol to the cylinder and repeat steps 9-10 until the agitated solids settle almost instantly.

11. Wash the remaining powder from the cylinder with a spray bottle and collect in a large beaker. Repeat steps 8-11 until all powder is consumed.
12. Evaporate the ethanol from the coarse powder in the large beaker and re-grind it in a mortar and pestle as per steps 6-7.
13. Take the beaker containing the medium and fine consistency powder and stir it vigorously. Pour the contents into a graduated cylinder and allow it to settle for 2-5 minutes.
14. Decant the liquid from the cylinder discarding the fluid and any fine particles still suspended. It is interesting to note that if the ethanol is allowed to evaporate from the fine particles, the powder that remains readily sticks to nearly any available surface. Samples of the fine powder stored for a few days eventually harden into hard brittle clumps that are difficult to remove from glass and plastic surfaces without significant mechanical action and solvents. Powders that were made via the Ball mill tended to have a larger fraction of this ultra-fine product.
15. Add ethanol to the cylinder and repeat step 14.
16. When the solution has a settling time of 2 minutes, perform the separation again with a settling time of 20 seconds, discarding the large powder into a separate beaker for further grinding. It is important to note that a super-saturated slurry of powder will settle faster than a solution of lower concentration. Thus if there is any doubt be sure to iterate.

The powder will perform best when it achieves a settling time between 30 sec to 2 min. Powders of this size when heated and dried can be seen to waft out of a bottle under ambient air currents. It should be noted that producing a significant quantity of useful powder from this method can take several weeks to months. This procedure crudely resembles a commercial process Missouri-Scientific (Mo-Sci.) uses to produce the uniform frit that they feed into a machine that forms micro-spherical glass beads in a flame spray aerosol. However, instead of using an ethanol column to decant their particles they use a machine with different size mesh to sort the frit by size. It is also worth noting that Mo-Sci also used a mortar and pestle to grind their powders to uniform size.

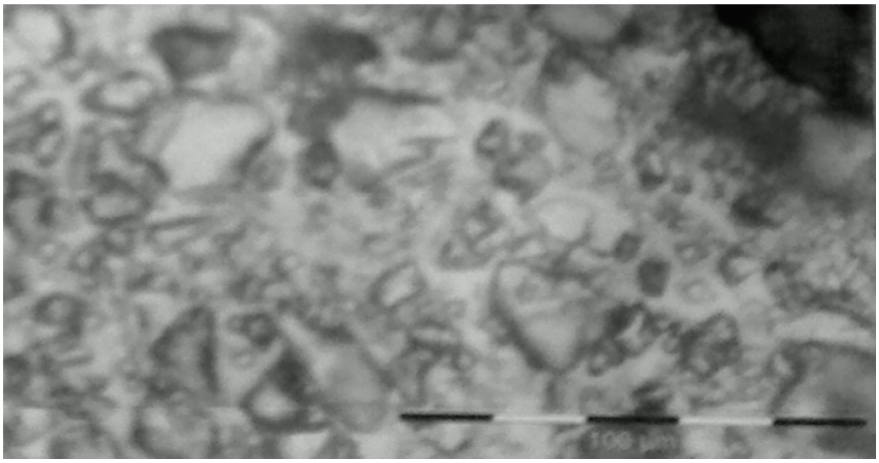

Figure 19. Image of Er^{+3} doped Q-X glass frit prepared by Mo-Sci. Inc. as the starting material for their micro-sphere production process.

The frit obtained from their process behaves in a similar manner to the powder we produced at UT using the above procedure (Figure 19). A \$5000 20% Er^{+3} doped phosphate glass boule was donated to us by Kigre and then Mo-Sci agreed to test run their process for phosphate glass at cost (\$3500) to produce 10g of frit and 1g of spherical

micro-particles (Figure 20). Thus while the optimum materials to produce our nanoparticles exist, they are not available to us on our current research budget. In an optimized LAM reactor at our current estimated level of efficiency, producing 1 g of nanoparticles from micro-spherical particles would likely cost between $15k and $100k.

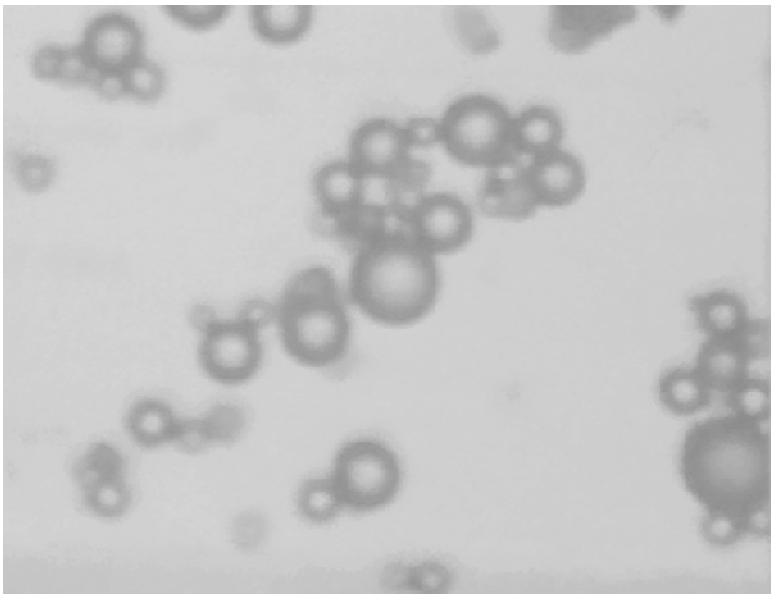

Figure 20. Micro-spheres manufactured from Er^{+3} doped Kigre Q-X phosphate glass by Mo-Sci. Inc. average diameter ~20 μm.

Chapter 5: *Designing and Building a Collection Chamber for the LAM Process*

As discussed in Chapter 3, the process used to make nanoparticles for this experiment is the Laser Ablation of Micro-particles (LAM). Due to their size, collecting these particles is challenging and requires a carefully designed apparatus. Though other means of collecting nanoparticles have been developed and operate successfully, for the purposes of these experiments the only method used was the direct supersonic impaction of particles on solid and liquid coated surfaces[35]. The basic theory of supersonic impaction is to accelerate aerosolized particles through a supersonic nozzle into a chamber at low pressure where they collide with a surface. The high density of gas near the nozzle allows drag forces to act on the particles accelerating them with the flow. The drag forces that act on a particle are proportional to the aerodynamic diameter of the particle as well as the density determined by the mass diameter[33, 36]. When the particles leave the region of expansion and approach the impaction surface they encounter a region of decelerating gas at approximately the ambient chamber pressure. To impact on the surface they must possess a stopping distance greater than the thickness of this boundary layer[37, 38, 39, 40]. This is the underlying principle behind inertial impaction. Thus designing a chamber requires a solution to this impaction problem, optimized as a function of particle mass, diameter, density, chamber pressure, nozzle characteristics, impactor position, and geometry among other variables[40].

By briefly summarizing the production process discussed in Chapter 3, insights into the design requirements of a collection chamber can be gained. To review, powder is entrained in a laminar gas flow and ablated by an excimer laser. The micro-particles explode into a vapor cloud and then condense into nanoparticle droplets.

The process starts with a powder being agitated in a vessel through which gas is flowing at a rate matched by the vertical extent of the laser beam times its repetition rate. This powder feeder results in an aerosol that is fed into the "horn cell". The cell is designed to inject the flowing aerosol into a buffer gas moving at the same velocity allowing the aerosol to remain well collimated and turbulence free. The laser pulse then hits the powder and is absorbed. The absorption process ionizes a portion of the surface and the expansion of the vaporized material drives a shock wave through the material that heats and vaporizes the micro-particle.

Once a micro-particle is shock heated it will rapidly expand and hence work against the background gas. Initially this process is adiabatic allowing the gas to cool, producing a saturated vapor which condenses into droplets[41]. The high surface tension of the droplets pulls them into a spherical shape as they rapidly equilibrate with the background gas.

The newly formed nanoparticles remain entrained in aerosol and are slightly positively charged due to the residual effects of photo-ionization during the laser pulse. The aerosol then flows through a skimmer nozzle that directs the gas flow over a virtual impactor allowing any un-ablated micro-particles to settle out of the gas before it flows into a supersonic nozzle and into a vacuum chamber. Once the nanoparticles are accelerated into the vacuum chamber they possess sufficient momentum to cross the laminar flow lines and boundary layer that exists near the surface of the fluid impactor[40]. The fluid impactor has a small hole at its tip where a gradual flow of surfactant is forced down the surface of the impactor by the pressure of the supersonic gas. The nanoparticles that reach the surface of the impactor are captured by the fluid which is collected in a reservoir. The theory of nanoparticle impaction was worked out by de la

Mora et al and the conditions of our chamber are designed to be well within the high probability region of the impaction curves that they measured[40].

Figure 21. Original fluid impactor and collection cup with glass splatter guard.

Many challenges were encountered in adapting this process to ablate and then collect low density transparent dielectric materials. A chamber and impactor (Figure 21) adapted from a system originally used to collect silver nanoparticles was refitted for collecting lower density glass nanoparticles. The samples collected in this chamber tended to possess larger than expected diameters (~40 nm) and lower density colloids than were detectable using spectroscopic techniques. The ideal chamber would need to be able to operate at high efficiency with particle diameters as small as 1.5 nm. Thus, once it became clear that the collection apparatus was not performing optimally a new collection chamber was designed and built to address the reliability and repeatability problems encountered in the original system.

The first step in producing the new chamber design was to review the literature on hypersonic impactors. The work of de la Mora, Loscertales and Temmet proved to be the most experimentally relevant to the LAM system. Throughout the 1990's de la Mora et al. conducted a systematic exploration of hypersonic impactors. They built a machine capable of producing particles of known size standards and a collection system capable of detecting the impact of these particles with a substrate[40]. The basic design of the experiment was to create small nanoparticles of known size or mass, typically via an electrospray process. The particles would then pass through a neutralization chamber where they were all given a single charge. Next, a portion of the flow would be diverted into a differential mobility analyzer which measures the aerodynamic diameter as a function of charge and density. Finally the particles were diverted to a supersonic nozzle where they would be accelerated by the gradient in pressure between an impactor chamber and the nozzle stagnation pressure.

The particle's mass and diameter were deduced from their bulk density and measured electrical mobility. Since the nanoparticles were charged when they collided with the metallic impactor they produced a current. The impactor efficiency could be measured by monitoring the current through the impactor plate as well as the escaping current. With the DMA data and the response of the impactor, the total impactor efficiency could be measured as a function of particle size, and the ambient physical parameters such as the pressure ratio between the impactor chamber and the stagnation pressure in the nozzle, or the ratio of nozzle diameter to the distance of the nozzle from the impactor.

This work produced the useful result that the particle impaction probability was dependent upon only two dimensionless parameters, the Stokes number at the stagnation point and the Stokes number in the impactor chamber. For a specific impactor design,

this curve would allow for particles to be collected according to their sizes based upon the known theoretical dependence of the particles' aerodynamic properties on the experimental parameters that control the flow through the supersonic nozzle.

The theory behind this result is based upon the result of the Milliken experiment that the mobility of a particle is given by the equation[36]:

$$Z_0 = qB_0 = \frac{q}{6\pi\mu r}\left(1+\frac{\lambda}{r}\left[a+be^{-\frac{cr}{\lambda}}\right]\right) \quad \textbf{(20)}$$

where a, b, and c are the slip factors, λ is the mean free path in the gas, μ is the viscosity, and r is the aerodynamic radius. For small particles the aerodynamic radius differs from the actual radius due to the nature of collisions on short length scales. Intuitively this can be understood as an effect of the particle beginning to behave like a large molecule instead of a macroscopic object. For example, the potential a nanoparticle sees has the ability to influence the motion of the particle at a larger distance than for macroscopic matter just due to the relative inertia of the systems. Moreover, the molecular description also fails, since as the particle becomes larger the energy separation in internal degrees of freedom decreases as well, so that it becomes possible for the particle to absorb energy from an incoming molecule resulting in an inelastic collision. Tammet proposes an approximate formulation for the particle aerodynamic radius that corrects for these issues allowing the particle's aerodynamic radius to be treated as the average collision distance which is simply the sum of the particle (r_p) and gas molecule (r_g) radii and a correction term for the effects of the inelastic collision on the minimum approach distance (h_c)[42].

$$\delta(T) = r_{np} + r_g + h_c(T) \quad \textbf{(21)}$$

For neutral particles with a diameter above ~2 nm it is sufficient to consider only the effect of the molecular radius on the effective aerodynamic radius. Given our current chamber parameters and experimental goals it is unlikely that we would wish to produce

particles in this regime and corrections to the theory were omitted in the design. However, straightforward calculations of the aerodynamic mobility of small particles are presented by Tammet et al. should the reader wish to consider adapting the chamber to collect particles in the sub 2 nm regime[42].

With Tammet's modified theory of electric mobility, the measured value of Z_0 from the DMA data was used to calculate the particle radius allowing the mass of the particle to be obtained from the particle's solid density. Thus for even the smallest particles the behavior of an arbitrary impactor was explained by Loscertales et al. using data from de la Mora et al.[36]

The work by de la Mora combines a theoretical treatment of the impactor problem from the perspective of particle mobility. In their 1990 paper they present a formula for understanding the operation of an impactor using the characteristics of the supersonic flow, as well as several useful design constraints. They then produce a calibration curve that plots the critical Stokes number S_{crit} for 50% collection efficiency at the impactor surface against the initial Stokes number S_0 in the nozzle at the stagnation point. For a supersonic nozzle the Stokes number at the stagnation takes the simple form[36]:

$$S_0 = \frac{\tau_0 c_0}{d_n} \tag{22}$$

where τ_0 is the particle stopping time c_0 is the speed of sound and d_n is the nozzle diameter. The stopping time is related to the particle mass diffusivity coefficient D_0 and the mechanical mobility by[36]:

$$\tau_0 = \frac{m_p D_0}{kT}$$
$$B_0 = \frac{D_0}{kT} \tag{23}$$

Thus we can compute the Stokes number from the ambient gas parameters in the supersonic nozzle. The impaction criterion as presented in the work by Loscertales et al was derived first by de la Mora[33,43]:

$$S_{crit} = S_0\left(\frac{2}{\gamma_n - 1}\right)^{\frac{1}{2}} \frac{p_0}{p_2}\frac{d_n}{\delta} = \frac{1}{\xi} - \frac{1}{4\xi^2},$$
$$\xi = 1 - 2S_0^{\,12/17} \qquad \textbf{(24)}$$
$$\xi = \frac{v_{bow}}{v_{term}} > 0.5$$

where p_2 is the post-shock stagnation pressure and δ is the distance from the recompression shock near the impactor (bow shock) and the impactor surface. Thus for sufficiently large values of ξ (the ratio of the gas jet terminal velocity to the particle's velocity ahead of the bow shock wave) the theoretical critical value of the Stokes parameter for particle impaction is well defined. Using the following relations where p_0 is the ambient pressure in the impactor chamber, the system can be solved to provide the calibration curves for an impactor or yield the characteristic impaction probability for a particular Stokes number and thus provide design constraints for an impactor[36].

$$\frac{p_0}{p_2} = \frac{(\gamma_n - 1)(\gamma_s + 1)}{4 s_n \gamma_n}\left[\frac{4\gamma_s}{(\gamma_s + 1)^2}\right]^{\frac{\gamma_s}{\gamma_s - 1}} x_s^2 \qquad \textbf{(25)}$$

$$s_n = 0.4225\left(\frac{\gamma_n - 1}{\gamma_n + 1}\right)^{\frac{\gamma_n + 1}{2(\gamma_n - 1)}}\left(\frac{2}{\gamma_n - 1}\right)^{\frac{1}{\gamma_n - 1}} \qquad \textbf{(26)}$$

$$\frac{d_n}{\delta} = \frac{1}{x_n F},\ x_s = x_n(1 - F),\ F \approx \frac{\gamma_n - 1}{2(\gamma_n + 1)}$$
$$x_s \approx \frac{L - \delta}{d_n},\ \ for\ \ \eta = \frac{L}{d_n}\sqrt{\frac{p_0}{p_1}} < 1 \qquad \textbf{(27)}$$

In the above equations one of the variables that must be known to specify the design of an impactor is the overall ambient pressure in the chamber. Thus the impactor design depends upon the total flow through the chamber and vacuum system. Here we

write the basic relationship that relates our pumping speed to the pressures we can expect to find in various sections of the vacuum system[44].

$$P = \sqrt{\left(\frac{Q}{S_p}\right)^2 + 2Q\left(\sum_{i=1}^{n}\frac{1}{C_i}\right)} \quad \textbf{(28)}$$

The pressure is a function of three parameters, the speed of the pump [Vol/time], the quantity of gas the pump draws, and the inverse sum over the conductance of the N components downstream from the point of measurement. Fortunately the conductance of a tube (i.e. the constant relating the pressure drop across the tube to velocity of the gas) is simple to calculate depending only on its cross sectional area and its length[44].

$$C_i = 2.92 \cdot 10^5 \frac{A^2}{l}\left[\frac{1}{m^2 \cdot Pasc \cdot s}\right] \quad \textbf{(29)}$$

Calculating the actual amount of gas flowing through the system is also straightforward if more involved. The expression for the velocity of a gas freely expanding into vacuum from a nozzle is just:

$$v_e = \sqrt{\frac{\gamma k_B T_e}{m_g}} \quad \textbf{(30)}$$

$$T_e = \frac{T_0}{1+\frac{\gamma-1}{2}} \quad \textbf{(31)}$$

where m_g is the mass of the gass and T_0 is the ambient temperature before the nozzle. The density of gas at the nozzle exit is given by:

$$\rho_e = \frac{P_0}{k_B T_e\left(1+\frac{\gamma-1}{2}\right)^{\frac{1}{\gamma-1}}} \quad \textbf{(32)}$$

Thus the flow rate is simply the product of the nozzle area with the gas velocity and density at the exit. With the ideal gas law and conservation of mass we can relate this to the pumping speed and the pressure measured at the entrance to the pump.

$$Q = P\frac{\Delta V}{\Delta t} = \rho_e v_e \pi r^2 k_B T \quad \textbf{(33)}$$

This expression has units of [J/sec] or [Pa m^3/s] and thus represents the pumping power required to drive the expansion.

These expressions were used to develop estimates of the flow rates at various points in the system. Choke points were thus identified and eliminated. For example, the pressure in the chamber was nearly halved by increasing the diameter and conductance of the manifold connecting the pump to the chamber as well as the flow characteristics of the chamber itself.

As noted by de la Mora et al. the above description of an impactor should hold provided that $\eta > 0.4$ where η is defined by[43]:

$$\eta = 0.67\frac{L}{L_D} = \frac{L}{d_n}\sqrt{\frac{p_1}{p_0}} \quad \textbf{(34)}$$

L_D is the distance to the Mach disk and L is the distance from the nozzle (diameter d_n) to the impactor. The zero crossing in the plot of η - 0.4 vs. impactor height (in nozzle diameters) sets the limit on the qualitative shape of our impactor efficiency curve. In theory, beyond the zero crossing, the behavior of the impactor will no longer resemble a step function. Continuing to increase the distance to the impactor beyond this limit should result in decreased collection efficiency since particles approaching the Mach disk will begin to lose velocity. The distance to the Mach disk in a freely expanding gas is given by:

$$L_D = \frac{2}{3}\sqrt{\frac{P_0}{P_f}} \quad \textbf{(35)}$$

where P_0 is the pressure backing the nozzle and P_f is the ambient pressure in the chamber supporting the flow. The performance of actual impactors does not quite match the theoretical predictions. Good performance defined by a sharp cut and a flat collection

plateau beyond the critical distance only is achieved for $\eta < 0.13$. At values of $\eta < 0.3$ the slope of the cut becomes pronounced. At distances corresponding to $0.3 < \eta < 0.4$ sub-optimum collection will occur including a 10-15% decrease in maximum collection efficiency[43].

Given the parameters of the new chamber and a 300 μm nozzle, the Mach disk is located approximately 30 nozzle diameters ~1 cm from the nozzle. Therefore, data taken by de la Mora indicate that the collection efficiency given our pumping speed should closely resemble a step function for impactor nozzle separation distances less than 10 nozzle diameters. Between 6 and 14 nozzle diameters the knee in the step function grows less sharp with a significant loss of resolution in the particle cut. At 16 nozzle diameters the step should become significantly sloped and we can expect to collect less than 50% of the smallest particles as well as slightly depress the collection efficiency of the larger particles due to deceleration in the flow approaching the mach disk.

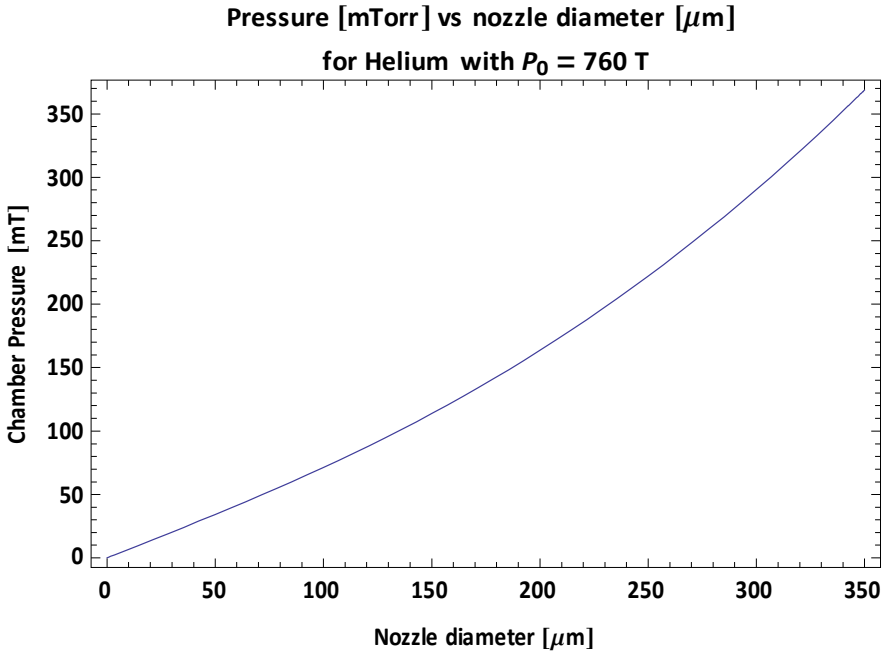

Figure 22. Chamber pressure vs. nozzle diameter for helium.

In Figure 22 we see a graph of chamber pressure vs. nozzle diameter. The theoretical values agree well with those measured during normal operation. Larger nozzle diameters are preferable since it minimizes the potential of a clog interrupting operation. When high density aerosols flood the chamber or sudden transient discharges of powder erupt from the feeder they can overwhelm the virtual impactor occluding the supersonic nozzle with un-ablated micro-particles as well as nanoparticles. When this occurred in the past it required the disassembly of the experiment and thorough cleaning of the system before collection could resume. Thus in addition to designing the chamber to operate at larger nozzle diameters, the nozzles themselves are precision machined to unscrew and then relocate to within <10 μm of their original position vertically and horizontally facilitating rapid turnaround in the event of a clog without significantly changing the parameters of an ongoing experiment.

Ablating in helium, with a target operating pressure of approximately 350 mT for a nozzle diameter of 350 μm and ~220 mT for a 250 μm nozzle, we can compute the cutoff curve for the impactor as a function of particle size and distance between the impactor and supersonic nozzle (Figure 23 through Figure 26). Comparing these curves reveals a decrease of approximately 2 nm in the cutoff diameter by using the 250 μm nozzle. This result can be understood intuitively, since decreasing the flow rate through the nozzle decreases the density of the gas in the chamber as well as the ambient pressure, which increases the pressure ratio, thereby extending the distance to the Mach disk.

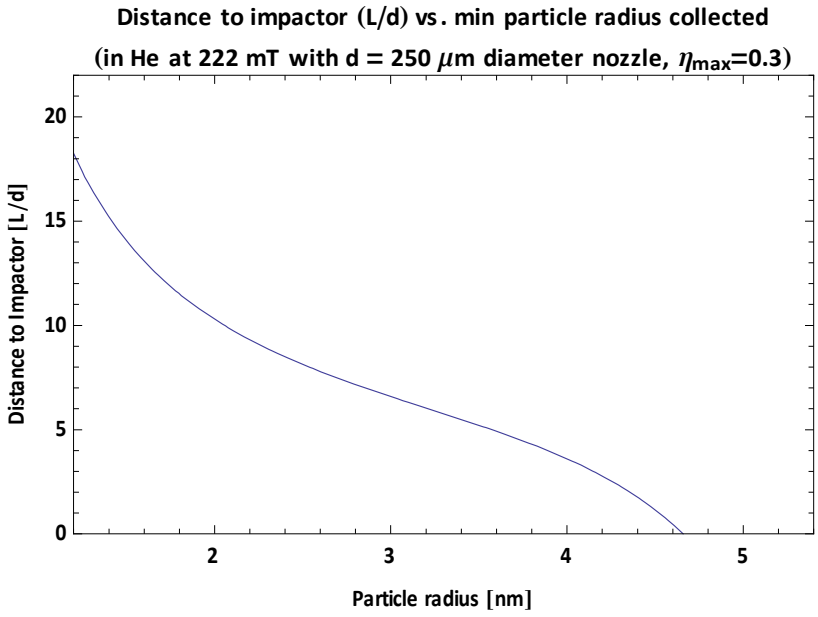

Figure 23. Distance from nozzle to impactor for 50% collection as a function of the critical particle radius. At a fixed distance particles to the right of the curve have greater than a 50% probability of impacting the surface.

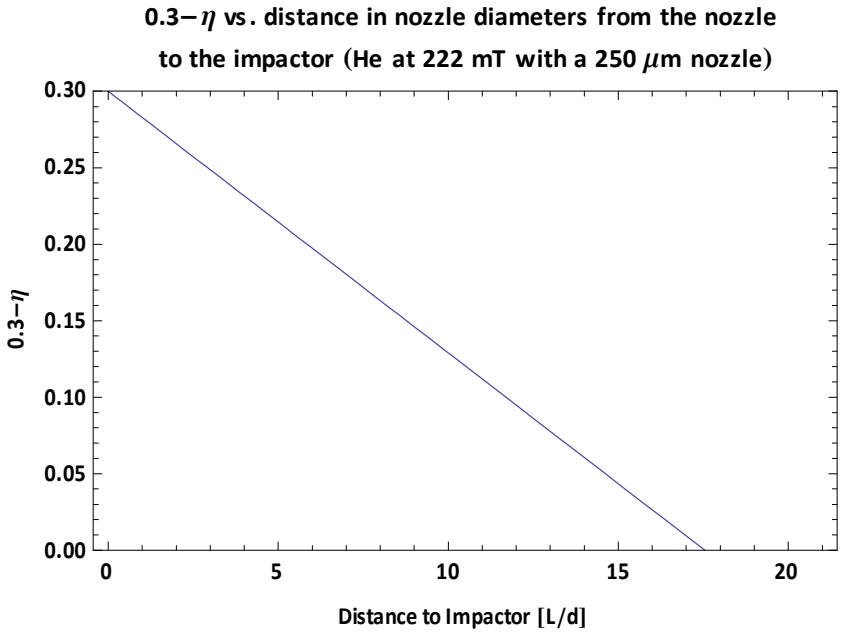

Figure 24. 0.3 - η vs. distance from the nozzle to the impactor in nozzle diameters. For distances beyond the zero crossing the collection efficiency will diminish.

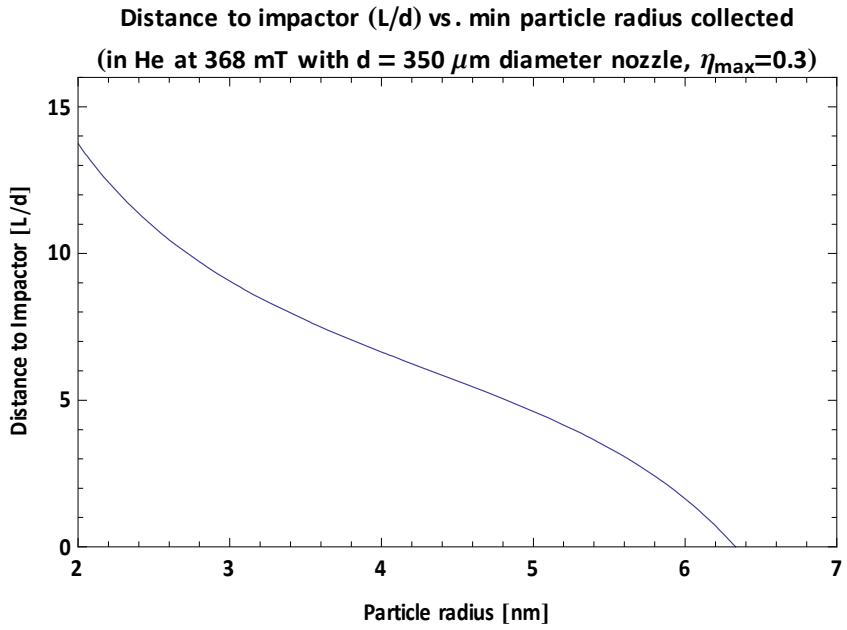

Figure 25. Distance from nozzle to impactor for 50% collection as a function of the critical particle radius. At a fixed distance particles to the right of the curve have greater than a 50% probability of impacting the surface.

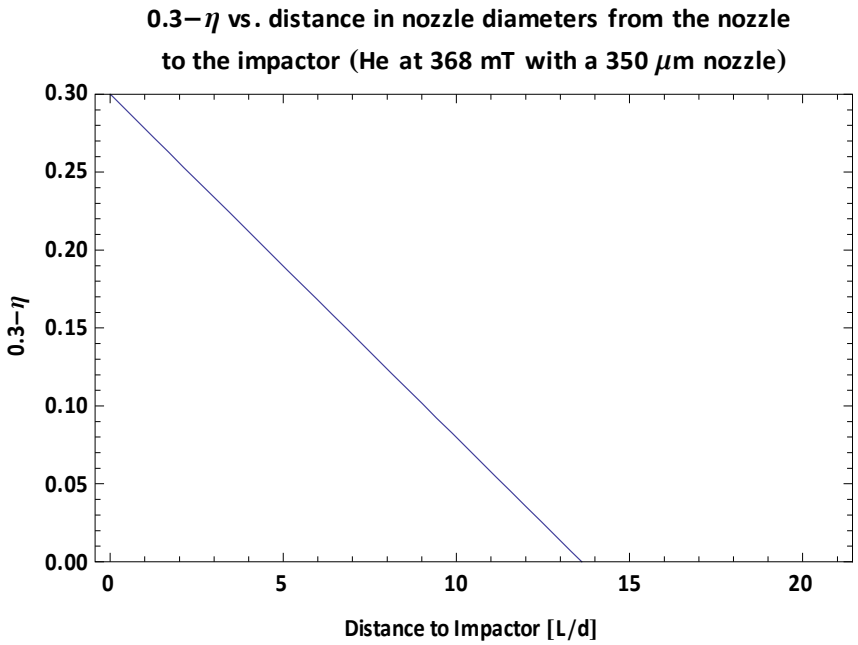

Figure 26 0.3 - η vs. distance from the nozzle to the impactor in nozzle diameters. For distances beyond the zero crossing the collection efficiency will diminish.

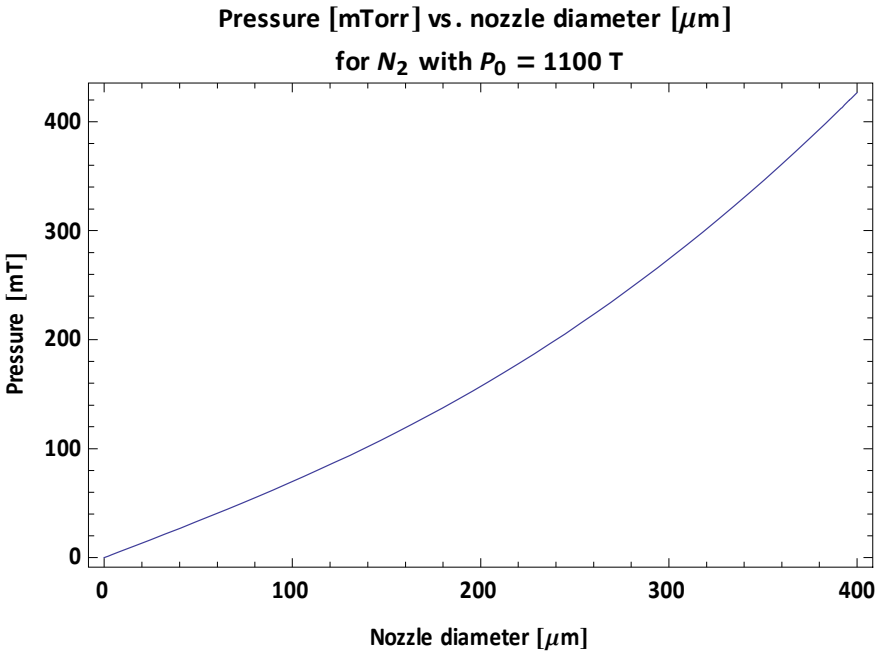

Figure 27. Chamber pressure vs. nozzle diameter for nitrogen at an elevated backing pressure.

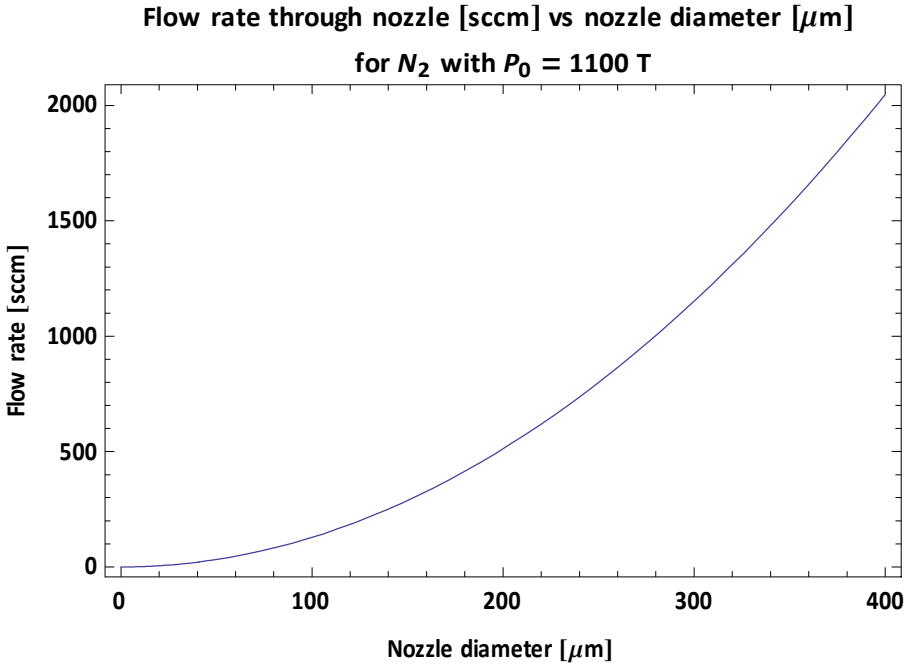

Figure 28. Flow rate through the nozzle as a function of nozzle diameter.

When ablating in nitrogen with P=760 T, and a 250 μm nozzle the pressure is ~120 mT and the flow rate is ~500 sccm. The counter flow operates at 2200 sccm and the center flow at 80 for standard double ablation operation. Thus by constricting the flow to the exhaust, the pressure in the horn cell can be controlled. Since the thermodynamic parameters of the gas in the horn cell control the cooling and expansion rate of ablated micro-particles and hence the size of the droplets that nucleate in the ablation plume, it is possible to operate the horn cell at an arbitrary pressure thereby tuning the size of the nanoparticles produced from the vapor.

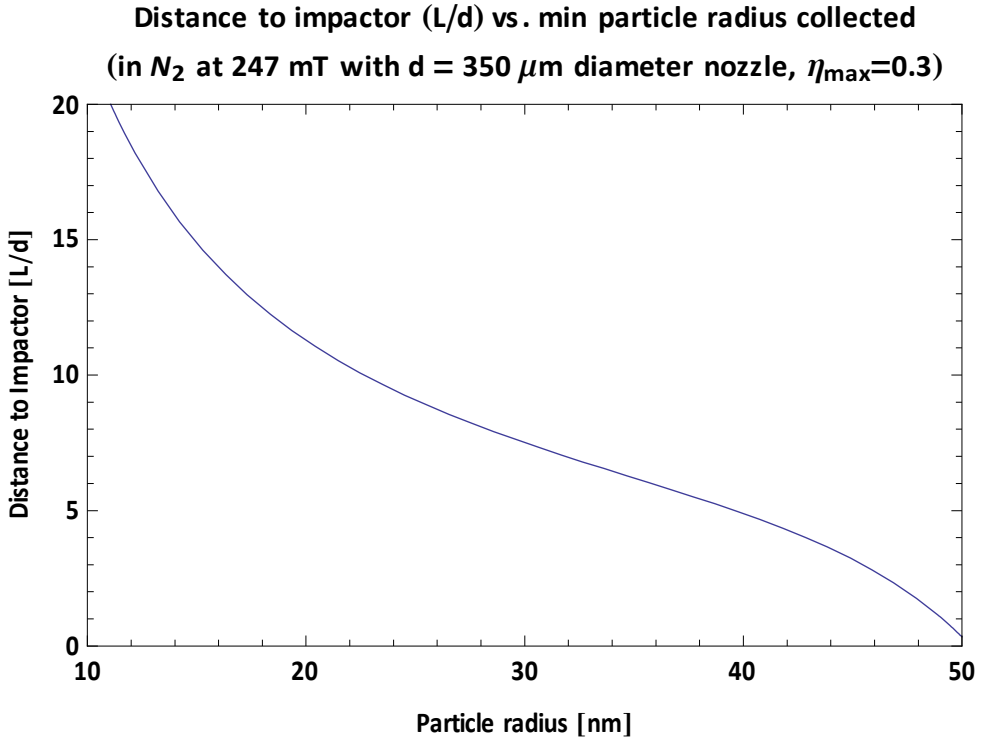

Figure 29. Distance from nozzle to impactor for 50% collection as a function of the critical particle radius. At a fixed distance particles to the right the curve have greater than a 50% probability of impacting the surface.

Figure 27 and Figure 28 show the chamber pressure and flow rates as a function of nozzle diameter for a horn cell pressure of 1100 Torr. Figure 29 shows the impaction

criteria for an elevated horn cell pressure of 1100 Torr. The cut radius increases significantly under these operating conditions and was consistent with TEM work measuring the average particle diameters produced under a variety of operating conditions.

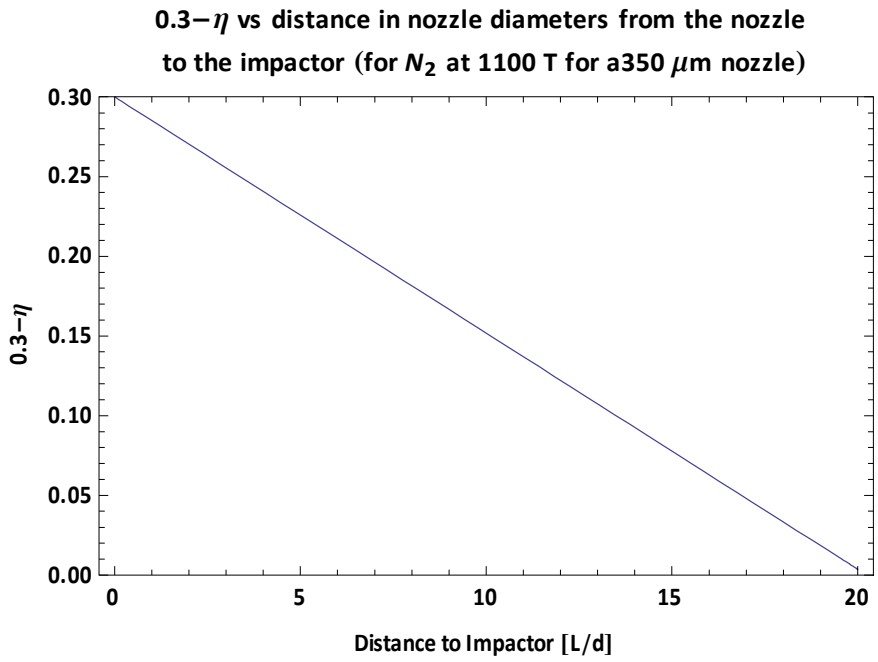

Figure 30 0.3 - η vs. distance from the nozzle to the impactor in nozzle diameters. For distances beyond the zero crossing the collection efficiency will diminish.

The results obtained in the new collection chamber demonstrate the effectiveness of the new impactor design. As shown in the plots above, carefully optimizing the cut of the impactor can significantly affect the collection efficiency at the smallest particle diameters. The increase in collection efficiency combined with enhanced reliability and repeatability dramatically improved both the production rate and quality of samples. The potential for improvement in collection efficiency is apparent when comparing the operation of the old chamber to the new system. The previous system, though designed

for similar operating conditions did not meet its design specifications due to an error in attributing the pressure inside the gas manifold as the internal chamber pressure for collection chambers built on the South Side of the LAM. The length of the bellows and the design of the previous manifold resulted in an underestimation of the chamber's pressure by 15-25%, depending on the collection chamber employed. Using the above equations for the conductance of the system to analyze the previous chamber's performance we can see that it has a significantly larger cut diameter than originally thought due to the increased operating pressure.

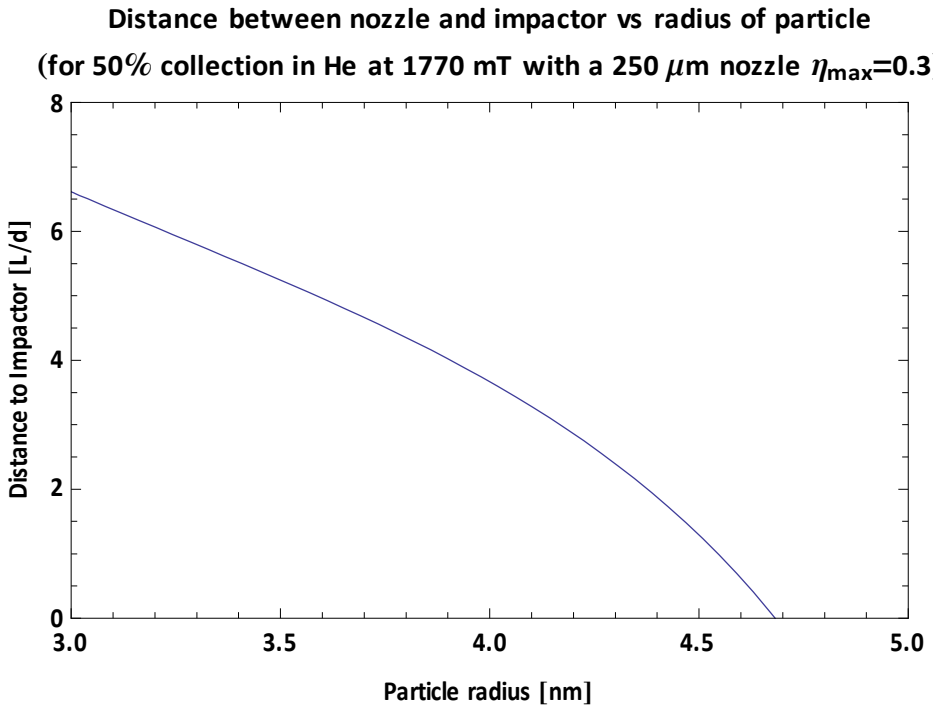

Figure 31. Original chamber: distance from nozzle to impactor for 50% collection as a function of the critical particle radius. At a fixed distance particles to the right of the curve have greater than a 50% probability of impacting the surface.

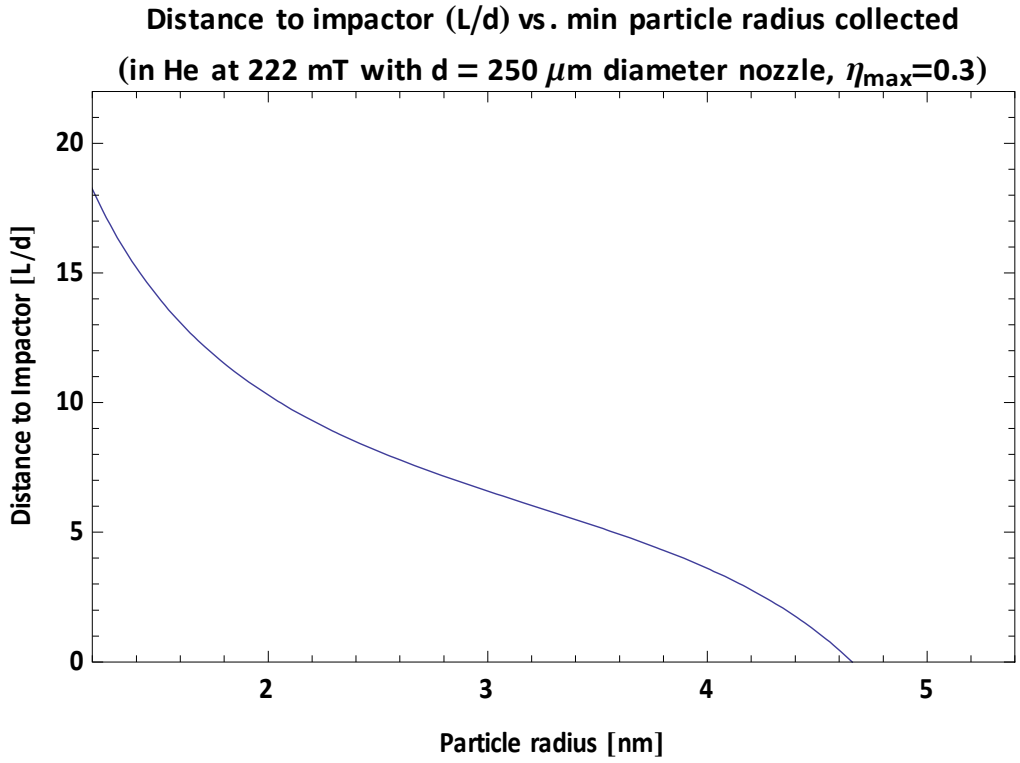

Figure 32. New Chamber: distance from nozzle to impactor for 50% collection as a function of the critical particle radius. At a fixed distance particles to the right of the curve have greater than a 50% probability of impacting the surface.

Comparing the performance of the two chambers reveals a striking difference in performance. Figure 31 and Figure 32 compare the operating conditions of the two chambers for η = 0.3 (the experimental limit found by de la Mora for the operation of a well behaved impactor)[40]. The figures show the size of the cut as well as the distance from the nozzle in the new chamber have both improved by more than a factor of two. Furthermore, since we are collecting in a liquid instead of on a solid surface, greater separation seems to decrease the amount of splattering which is a significant source of lost production during prolonged collection.

The new chamber is 8 inches in diameter and features an inertial impactor positioned in the middle of an inverted bell shaped glass with a wide mouth to aid

conductance to twin NW50 ports connected with 3 inch (ID) x 1.0 m bellows to the 4" manifold. With the Edwards 250 and roots blower (pumping speed 0.11 m^3/s) currently in use, the effect on the chamber pressure of using both NW50 connections is minimal: approximately 10%. However, if a pump with greater pumping speed were utilized the effect on the chamber pressure could reach nearly 30%. The chamber also features a window for viewing the performance of the collection system, a 4 inch blank port designed to provide access for future diagnostics, and a magnetic feed-through to adjust the impactor height.

Challenges in designing the system included providing a movable seal that allowed the chamber to smoothly translate without leaking, as well devising a homemade system of thrust bearings capable of transferring the limited torque generated by the magnetic drive to the relatively large static load of the fluid manifold. The drive system relies on the opposite polarity of several magnets in the handle to attract their counterparts mounted in the screw housing base plate inside the chamber. The torque is converted into linear motion via a 100 threads/inch optical screw and brass nut. The gear ratio of this system is very large and the torque from the magnets is sufficient to move the load. However, because the attractive force of the magnets is relatively large the base plate must be suspended a fraction of an inch above the chamber floor to prevent a large frictional force from causing the mechanism to seize. This creates the need for two thrust bearing surfaces to give the screw something to push or pull against when moving the load. These surfaces are metal-to-Teflon washers which result in a small amount of hysteresis in the translation.

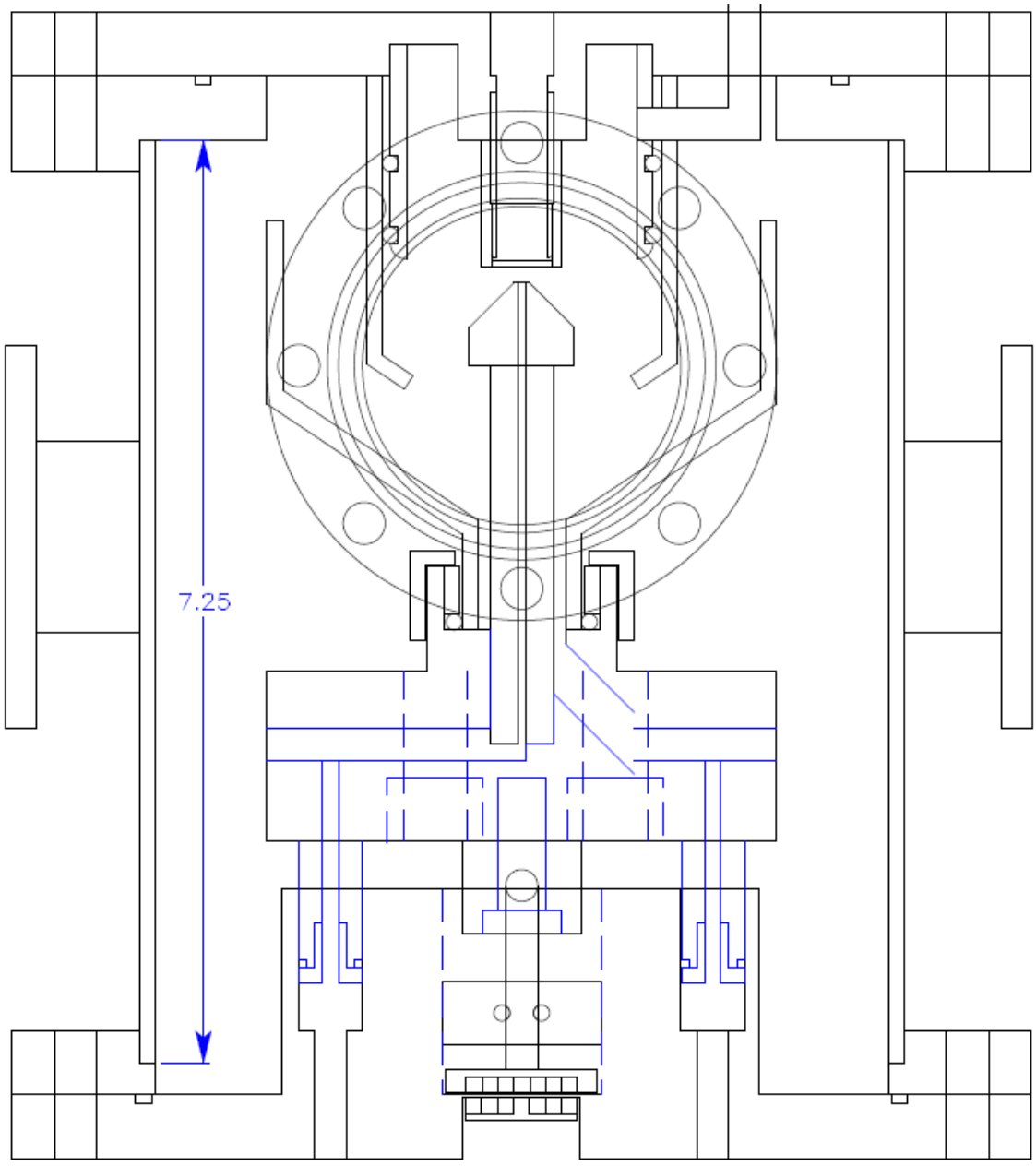

Figure 33. The fluid collection chamber.

Figure 33 shows the chamber as it was originally designed. A few details were altered to facilitate its construction. Welds were eliminated where possible to prevent warping of precision components. All welds were completed before further machining of

precision components. Where components needed to be hermetic but couldn't tolerate welds, the male end of the mating pieces were fabricated slightly over the tolerance and then frozen in liquid nitrogen before being dropped into place. This is how both the guide threads for the supersonic nozzle and the impactor probe post were fitted into their respective assemblies during the final stages of construction.

A selection of supersonic nozzles was made for the chamber with various diameters ranging from 150-300 μm with variable plate thicknesses. These supersonic nozzles were precision turned and polished to mate with the nozzle adaptor to within <10 μm of any starting position. They require a custom made Teflon gasket to provide a seal between the nozzle plate and edge of the adapter. Like many precision components care must be taken when handling the nozzles since dropping or bumping them could force them out of round preventing repositioning and possibly causing a leak.

Several different impactor heads were also created with a range of angles between 0 – 90 degrees with several choices of tip diameter. These also screw onto a stem for easy cleaning and rapid turnaround. The stem ends in a tapered NPT threaded screw that is designed to bottom out with the impactor probes. Liberal quantities of Teflon tape (4-5 layers) are required to achieve a seal and thereby prevent galling of the threads. These design features allow for removal and cleaning of both the nozzle and impactor probe without having to re-zero and redial the impactor height before running.

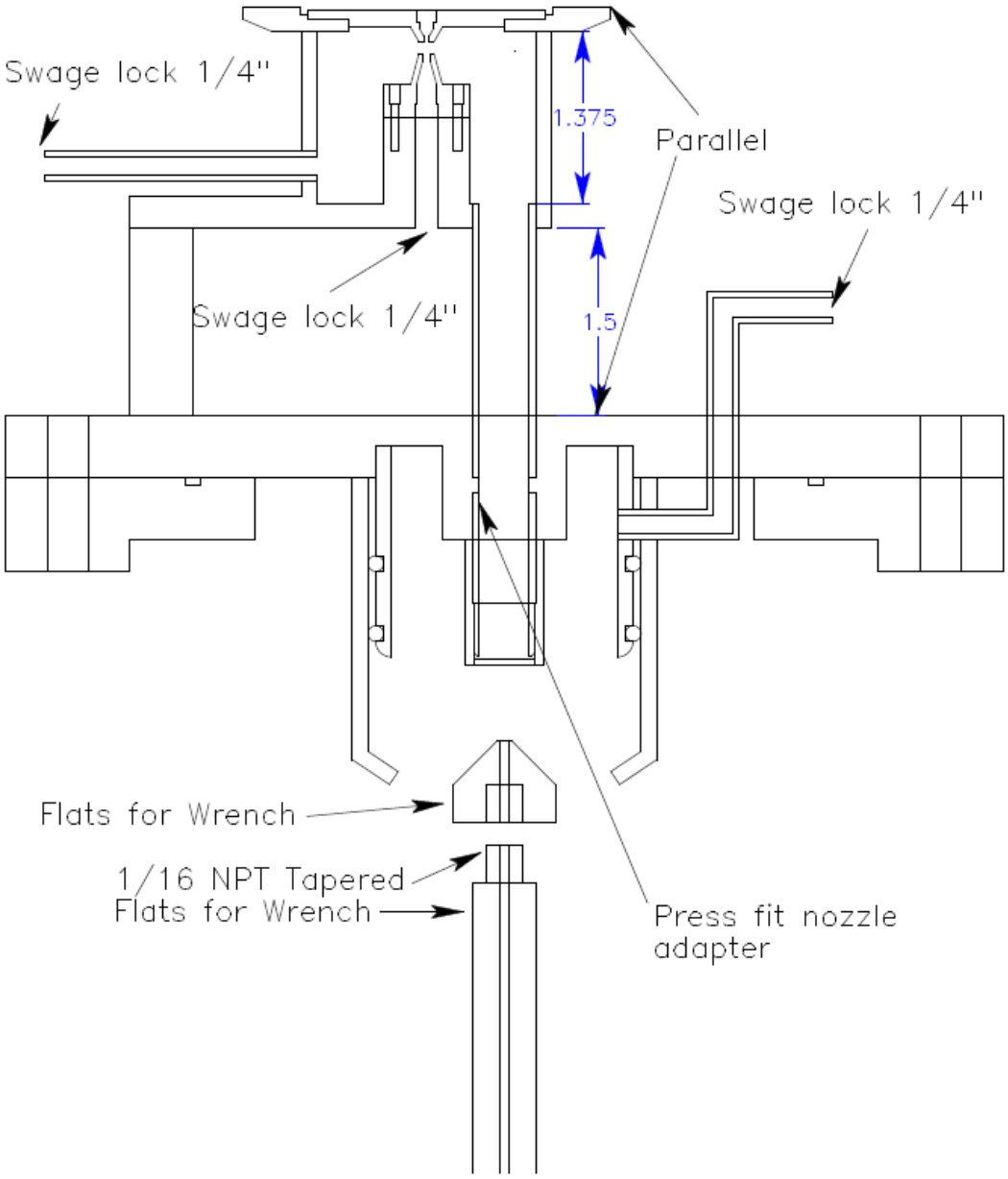

Figure 34. The top flange of the fluid collection chamber and virtual impactor.

The exploded view of the collection manifold (Figure 35) reveals the mechanism for holding the glass splatter guard in place. This consists of a Viton o-ring held in place atop a Teflon disk that prevents glass and metal from needing to come into contact. This was essential due to the potentially large torque that the glassware would experience

when manipulating the heavy bottom flange into place. The posts on the underside of the manifold each hold a Teflon seal which snaps onto the small lip on the end of the post. These seals are held in place by hollow screws seen in the bottom of the exploded view.

In the top view of the manifold (Figure 36) the bushings for the guide rails can be seen. The manifold translates on a screw drive that is magnetically coupled to the external chamber. The whole apparatus glides up and down on four delron clad steel posts that precisely fit into the bushings Figure 37. The seals provide the majority of the resistance to the motion.

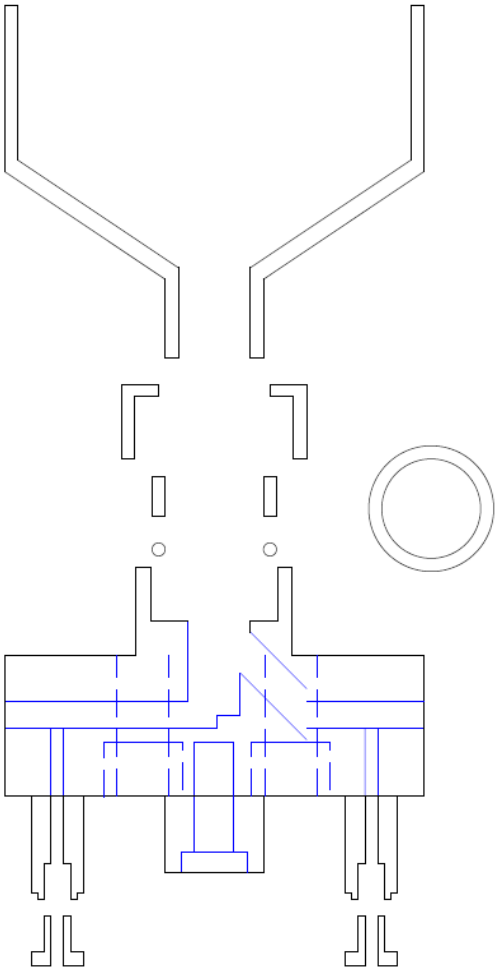

Figure 35. Cross sectional exploded view of the fluid collection funnel and translation manifold with the impactor probe removed.

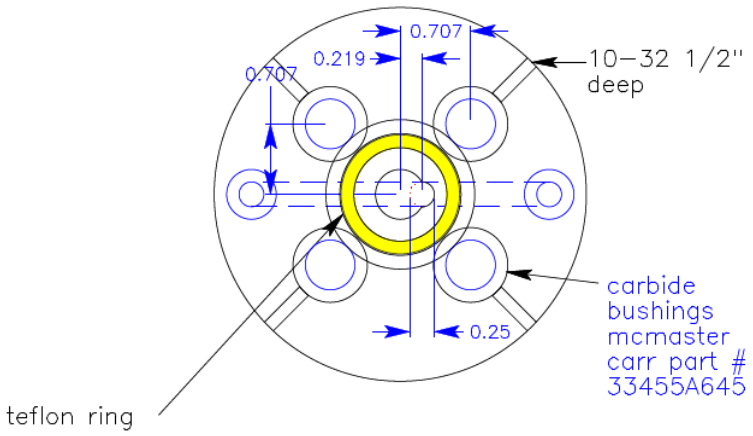

Figure 36. Top view of the translation manifold.

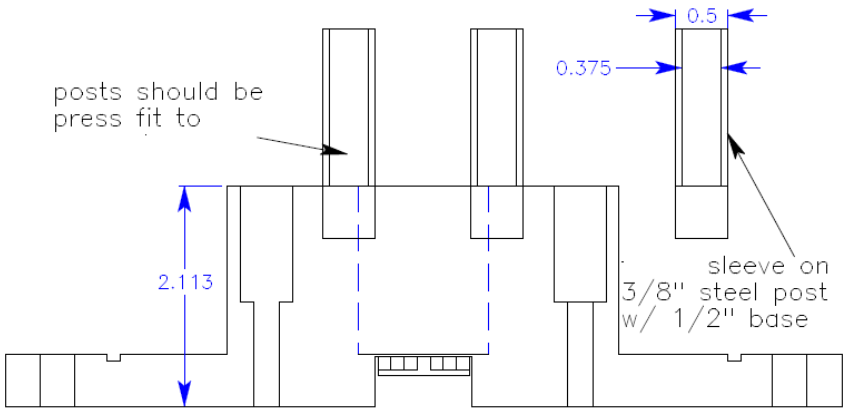

Figure 37. Bottom flange of the fluid collection chamber with the translation guide posts.

The entire flange and drive assembly is almost normal to the plane of the supersonic nozzle plate. The deviation in horizontal position of the impactor probe over its entire ~1" translation range was measured to be less than 10 μm. Once the entire assembly was constructed, the bottom flange was centered along the axis of the nozzle using both the machine table with a precision indicator to verify its position and an optical imaging system to co-locate the center of the nozzle with the center of the probe using a nozzle as a pinhole camera. Once a proper alignment was achieved the flange was pinned in place with three steel dowel pins pressed into the bottom flange in an

asymmetric pattern to guarantee the chamber always aligned to the same position when disassembled and re-assembled. Setscrews were incorporated into the top and bottom flanges to aid in disassembling the apparatus since the pins form a press-fit when the chamber bolts are tightened. For the duration of its use as a precision impaction collector, it is imperative that no mechanical modifications be made to any parts of the chamber assembly since the stresses involved in machining or welding could cause significant displacement of the impactor along its axis of translation.

Chapter 6: *The Design of the Primary Spectroscopic Diagnostics*

Throughout the early stages of this experiment the issue of detection plagued the production process. Most samples that were prepared had no detectable fluorescence or absorption spectra. The reasons for this were unclear. The lack of any detectable particles in solution could have been due to a number of reasons including, but not limited to, poor aerosol performance, insufficient laser fluence, problems with the collection apparatus, agglomeration and settling of small nanoparticle flocks, and chemical reactions with, or dissolution of the nanoparticles in the surfactant. Therefore, engineering a solution to the problem of low nanoparticle production rates was challenging, and obtaining a rough estimate of particle concentration became a priority.

Rough estimates of particle concentration were obtained from TEM studies and used to predict the maximum possible fluorescence from a reasonable volume of fluid. The LG-760 glass used in these experiments contained 2% Nd^{+3} by weight, had a density of 2.6 g/cc, and a fluorescence lifetime of ~360 μs. From studies of TEM grids dipped in colloidal nanoparticles, the concentration was estimated to range from $4x10^{-5}$- $4x10^{-6}$ percent. According to the rate equations, a 1 cm cuvette with the latter concentration of LG-760 pumped by a 300 mW, 0.25 mm diameter beam tuned to the peak absorption wavelength would contain at most $1x10^{-11}$ excited ions. Assuming the solid angle available for collection is about 0.1, the power on the detector can be calculated.

$$Power\,on\,detector = 1\times10^{-11}(ions)\frac{1}{2\tau_{rad}}\Omega\frac{r^3}{3}\frac{hc}{\lambda} \approx 5\times10^{-10}W$$

This calculation demonstrates that an instrument capable of reliably measuring signals in the pW-nW range would be required to detect the fluorescence from the nanoparticles. Given the specifications of available detectors, designing an apparatus

capable of making accurate measurement on samples at these concentrations is challenging. A solution to the problem of low sample concentration needed to be found before any conclusions as to the nature of the failure of the attempted lifetime and fluorescence spectroscopy measurements on the THOR[45] laser could be made.

Therefore, to boost the available signal, the sample was heated using a Rotovap machine to evaporate excess nonanoic acid. The final volume of the sample was reduced from 20 mL to 1.5 mL. Fluorescence from the sample was then detectable in a standard Cary fluorometer with a liquid nitrogen cooled PMT. This probably means the sample possessed a concentration of particles closer to the upper limit estimated by the TEM measurement. Absorption measurements were also performed on the concentrated sample. In parallel with the efforts to increase the concentration of nanoparticles in suspension, a new type of Nd^{+3} glass was acquired from Kigre with 20% Nd^{+3} by weight instead of 2% Nd^{+3}. This glass is based on Q-88, a high performance phosphate glass used to build an edge pumped thin disk multi-kW laser[21, 22]. It was hoped that by utilizing this glass to manufacture the nanoparticles a factor of 3-10 in fluorescence signal could be gained. The disparity between the increase in concentration and expected signal gain is due to the phenomenon of concentration quenching which at 20% Nd^{+3} by weight decreases the fluorescence lifetime from ~360 μs at 2% to ~100 μs at 20% doping.

Given the assumptions described above, it was possible to design diagnostics capable of detecting the particles using worst case estimates of production rates with sufficient dynamic range to conveniently measure particles at more optimistic concentrations. This was accomplished primarily by increasing the optical path-length of the sample by a factor of 100. A 1 m long liquid waveguide capillary flow cell was procured and then reengineered to perform fluorescence spectroscopy, lifetime and concentration measurements[46]. The liquid waveguide consisted of a glass capillary tube

with a fluoropolymer coating. The index of refraction of the fluoropolymer is less than that of both the capillary glass and fluid. The condition of total internal refraction is modified by the annular interface between the fluid and fluoropolymer, decreasing the effective NA of the capillary[47]. In total, the factor of 100 gained by increasing the length was augmented by purchasing a fiber-coupled 4 W laser diode, increasing the available power of the pump laser by 13 times, and offset by a decrease in the numerical aperture of the system by approximately half. Thus, combining the various improvements to the system, it was possible to calculate the expected increase in signal of the new diagnostic apparatus for the lower bound nanoparticle concentration.

$$Power\,on\,detector = 1\times10^{-11}(ions)\frac{1}{2\tau_{rad}}\Omega\frac{r^3}{3}\frac{hc}{\lambda}\eta_{glass}\eta_{capillary}\eta_{NA}\eta_{pump} \approx 1\times10^{-6}W$$

Additional factors of 2-3 were achieved by procuring a custom built Ocean Optics USB4000 spectrometer with optics better suited to near IR operation.

The diode laser selected is a 4 W 100 μm fiber pigtailed JDSU 2495-L-4 with a 15°-35° C operating temperature range, an output centered at 804 nm at 25° C and a tuning rate of approximately 0.3 nm/°C. This diode was selected due to its relatively high power and large tuning range. The diode is powered with a Newport 500B current driver. This driver is capable of supplying up to 6000 mA at 3 V and can be modulated by external signals at 50 Ω. In low power operation (<3000 mA) its bandwidth is 100 kHz and in high power operation (>6000 mA), its bandwidth 10 kHz. The diode was cooled by a TEC cooler capable of dissipating ten times the heat load generated by the diode operating at full power. The TEC was attached to a commercially available heat sink capable of dissipating 10 times the heat load from the TEC. A custom built thermal plate was machined from aluminum and polished until reflective using 500 nm abrasive fluids on a velvet cloth to assure optimum thermal contact. The reason for utilizing such

a robust thermal solution arose from the need to have a laser capable of rapid tuning and equilibration with almost no required warm up time. A 55 W Newport 350B series TEC controller was used to drive the Peltier cooler. Both the Peltier module and the heat sink were originally intended for use in CPU cooling and capable of working with heat loads above 100 W. This excess capacity in the cooling circuit, combined with the excessive but unfortunately necessary thickness of the aluminum cooling plate, required the feedback parameters in the TEC driver circuit be modified using a firmware update program that can be obtained from Newport along with instructions on how to find the correct parameters. The reason a thick and hence slower cooling plate was utilized stemmed from a desire to avoid designing and polishing a more sophisticated, less mechanically robust cold plate and heat sink assembly, and to obtain as uniform a thermal footprint on the diode as possible since gradients in temperature cause stresses that lead to failure, especially during the type of rapid cycle operation typical of these experiments.

As originally designed, the liquid capillary waveguide flow cell (LCWFC) used a t-shaped precision machined plastic compression fitting to hold a 0.4 mm capillary tube a fixed distance from the end of a 0.3 mm optical fiber also held in place with a precision swage type ferruel. The other end of the fiber connected to a standard SMA optical jack. The third branch of the fitting supplied fluid to the channel connecting the fiber to the capillary tube (Figure 38). The gap between the fiber and the capillary tube should be small enough that the expanding cone of light from the fiber does not overfill the glass tube. Unfortunately, the mismatch between the numerical aperture of the fiber and the annular capillary tube results in a degree of insertion loss[48]. This loss if not properly controlled can deposit a significant amount of energy into the fitting resulting in dramatic failure.

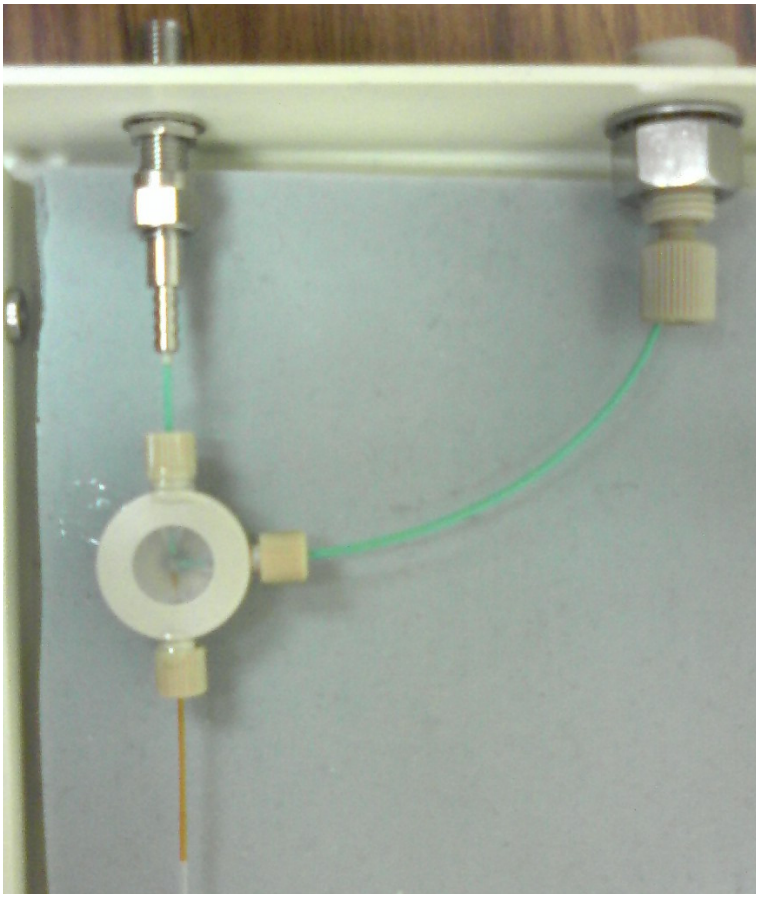

Figure 38. Liquid waveguide capillary flow cell input fitting. The capillary tube (brown) is oriented vertically facing the input to an optical fiber. Fluid is injected from the right into the tee.

Therefore it became necessary to redesign the LWCFC using a stainless steel fitting instead of plastic (Figure 39). It was also necessary to replace the fiber connection with a window and optics for mode matching the beam into the capillary tube (Figure 40). The fitting is a commercially available swage-type fitting for capillary tubes (Idex U-428), modified to hold a window. Figure 39 shows a cross sectional view of the fitting in Figure 40.

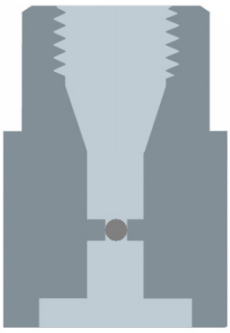

Figure 39. Top view of a stainless steel LWCFC fitting modified to hold a window.

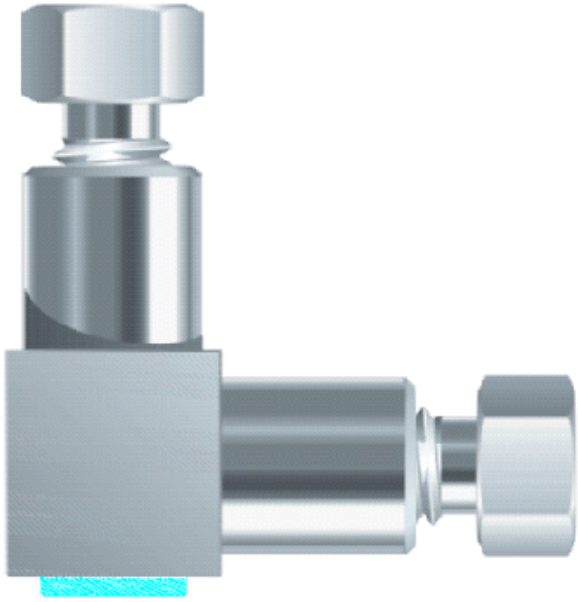

Figure 40. Side view of a stainless steel LWCFC fitting modified to hold a window.

Operating at high power would still deposit significant energy into the fitting resulting in minor damage to the optics and capillary tube that degraded performance over time. This type of damage would have been very difficult to detect and diagnose in an all fiber system, thus the presence of a window enhanced the overall utility of the device at the expense of alignment time. For example, bubbles present in the system provide both the oxygen and scattering interface necessary to start a small fire. This type

of fire burns quickly and can leave behind a thin layer of soot on optical components. Minor contamination of optical surfaces can alter results catastrophically or subtly and is luckily visible to the naked eye. Once a sufficient quantity of this grey film would coat the surface and begin to absorb significant pump light, the optical surface would rapidly damage. The failure of the windows tended not to correlate with the operating conditions of the LWCFC other than the flow conditions at the time of failure. Suboptimal flow rates occur often during extended routine operation since there are many failure points in the system. The peristaltic pump squeezes an elastomer tube that loses its elasticity over time. Also, the tubing upstream from the pump becomes less rigid and starts breathing with the pump, further decreasing the flow by limiting the pressure in the system to some fraction of the pump's displacement and the tube's elasticity. Finally, the filters necessary to ensure that only nanometer-scale particles can enter the capillary tube eventually become clogged and severely choke the flow. Minor air bubbles can be introduced into the system which may not choke the flow but instead serve as dielectric interfaces with high curvature in the path of an intense roughly collimated laser beam. Thus a bubble will act like a lens, reflecting and focusing significant portions of the beam into the fluid and the walls of the capillary tube. During low power static flow operation, regions of the tube that contain bubbles grow warm to the touch. During high power operation (>1 kW/cm^2) bubbles can catch fire, destroying or melting components. Significant time was therefore saved by treating the windows and capillary tube as consumables and replacing them if their performance was ever in doubt.

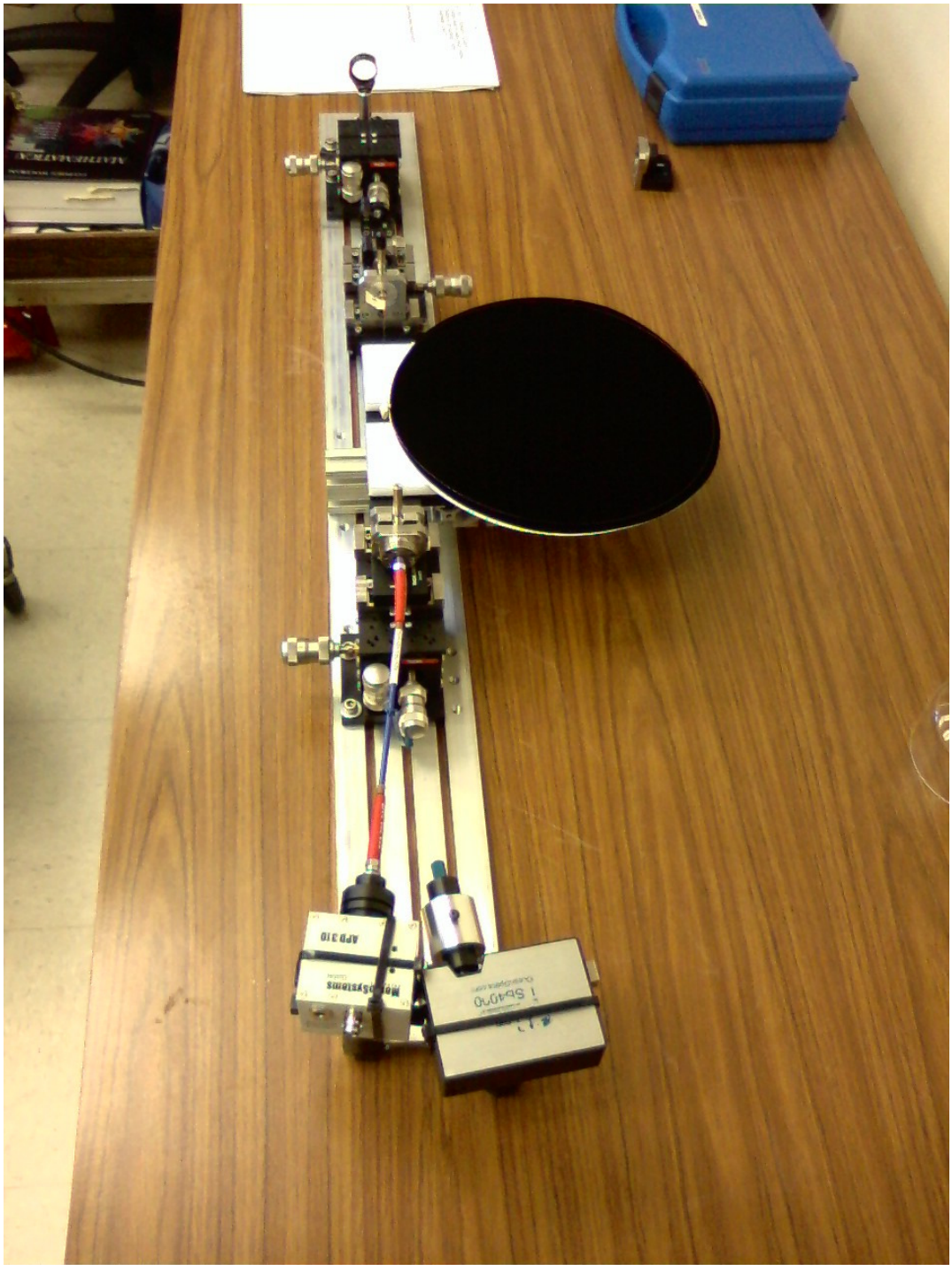

Figure 41. Top view of the home built LWCFC spectroscopy rig.

Figure 42. The input optics coupling pump light into the capillary tube.

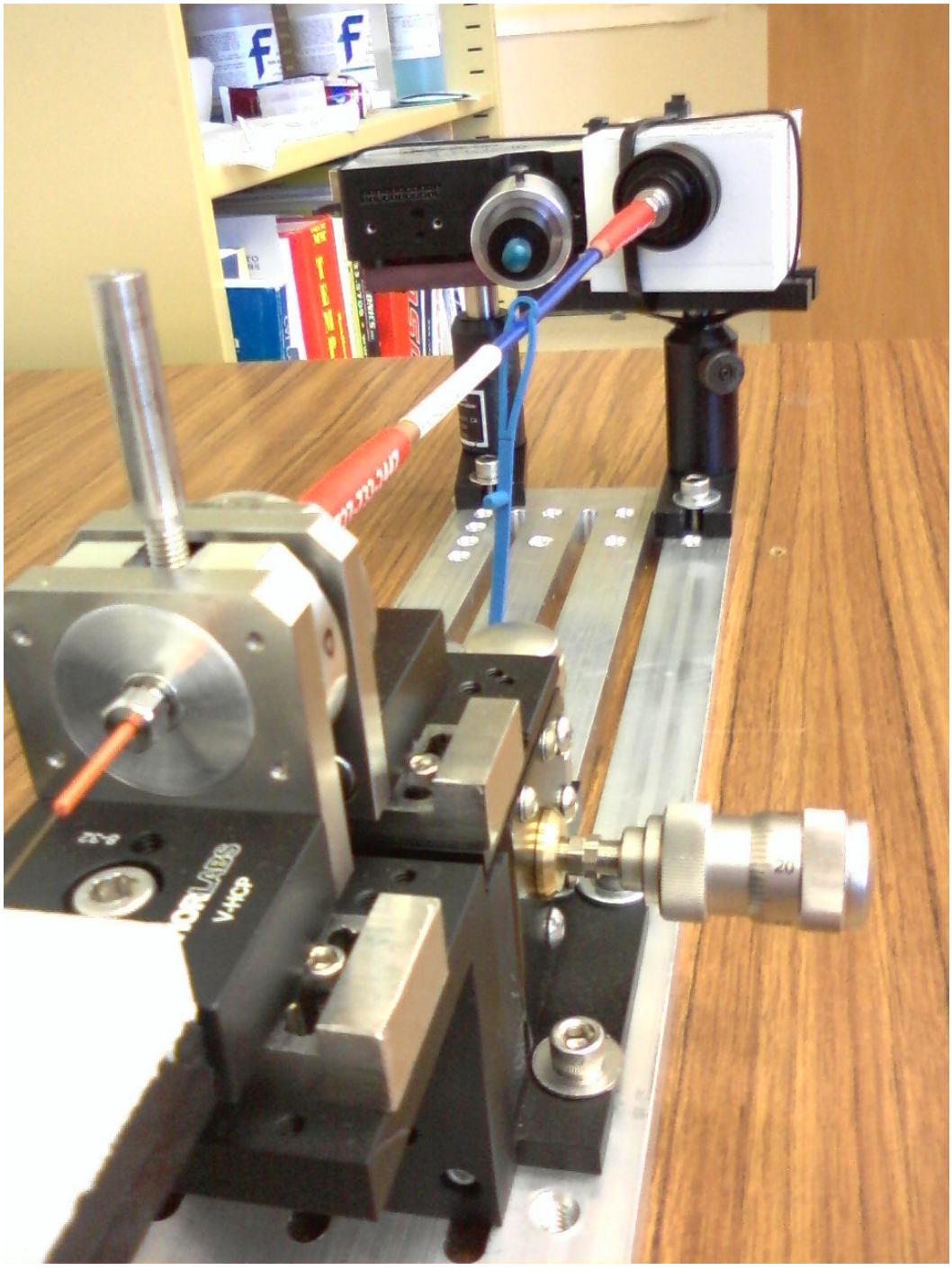

Figure 43. The exit port for the capillary tube into the diagnostics.

Figure 44. Side view of the 300 μm diameter capillary tube and LWCFC custom mount.

Thus, with these problems in mind, the design for a more rugged LWCFC evolved featuring easy to manufacture, disposable, hot-swappable components. The final product is shown in Figure 41 through Figure 44. The light from a fiber coupled diode laser is roughly collimated with an aspheric lens mounted in a fiber port. Like most commercially available collimation systems, the asphere is designed for single mode or small diameter multimode fibers. The diameter of the fiber is 200 μm and therefore has significant multimode content. The output of the fiber more closely resembles semi-coherent emission from an extended object than a beam. Thus, it is not possible to actually collimate the beam, only to relay image it. Fortunately, the diameter of the fiber is greater than the diameter of the capillary tube and the numerical aperture of the capillary is greater than that of the fiber. Therefore coupling the pump light into the

capillary tube is a relatively straightforward problem in geometric optics. Unfortunately, given the relative size of the extended source of the object and the focal length and radii of curvature of the optics, spherical aberration and coma seem to significantly affect the performance of the design[49]. Originally the design consisted of a relay lens to focus the collimated beam to a smaller spot size followed by a negative lens on a translation stage to re-collimate the beam with a diameter smaller than that produced by the asphere, and then a short focal length lens to focus the beam to its diffraction limited spot. This spot was intended to be larger than the original fiber diameter with a lower angle of divergence. A ray trace calculation was run for a conventional laser and those values used to select the lenses and their positions in the diagnostic system. The oscillator beam from THOR was then collimated to a spot size that matched the waist of the collimated fiber laser and then sent through the lens system. The oscillator beam reproduced the desired spot size with a ~250 μm diameter and a numerical aperture of 0.2 in the expected focal plane. The beam from the fiber laser produced a minimum spot size of ~1 mm with a focal plane that deviated by several millimeters from the design. A solution to this problem was found experimentally by removing the negative lens and repositioning the remaining optics. The negative lens possessed a significantly larger radius of curvature than the last lens in the system. This was a hedge originally incorporated into the design to make the final spot size and numerical aperture adjustable parameters. However, manipulation of the position of this optic proved insufficient to remedy the coupling issue. An ~260 μm spot was eventually obtained with NA<0.3 which coupled significant power into a capillary tube without using the negative lens. It should be emphasized that even in this configuration, the relative position of the lenses, the image size, the spot size and its position disagreed with the behavior predicted by OSLO (commercial ray tracer) and the behavior of the oscillator beam through the same optical system. It was at this

point that significant time was invested in developing a program capable of performing ray tracing calculations on this type of beam. Each mode supported by the fiber has its own rate of divergence and hence slightly different focal length. The presence of high order modes in the fiber is reasonable considering the diode emits from an extended source with a relatively small aperture resulting in a significant amount of diffraction and hence high frequency spatial content. The result of this is a beam that even when collimated by the aspheric lens to a diameter in excess of 2 mm diverges significantly over relatively short distances, more than doubling its size in approximately 2 meters. Ultimately, the instrument was designed to measure the absorption and fluorescence of nanoparticles and did not require an in depth understanding of the behavior of the diode laser to proceed with the measurements. Insertion losses of order 10-15% were predicted by the custom built ray tracer when using singlet lenses. Though it was ultimately possible to couple significant energy into a different capillary tube (>70%), at some point in considering the design of a capillary based nanoparticle laser this problem of efficiently coupling the pump light will need to be well understood.

With the issue of the pump laser spot size and divergence relatively in hand, the capillary tube presented its own challenges. With the optics in place an attempt was made to run the system with pure nonanoic acid. The results were negative. It was not possible to detect more than a few mW on the output side of the system. Moreover, the peak of this signal coincided with the fiber glowing brightly when examined with the IR viewer. Given the trouble associated with the behavior of the pump laser, it was assumed the failure to detect efficient transmission was due to poor mode matching. Therefore, considerable time was invested in attempting to find a solution by modifying the optical design. During the course of this work a glow was seen to emanate from the capillary tube. This result seemed at odds with the notion that the capillary tube was not well

mode matched. To resolve this issue, the oscillator beam was once again used as the pump source since both its diameter and numerical aperture could be well controlled. The beam was prepared with a diameter of 250 μm and a divergence compatible with a numerical aperture of ~0.22. Using the power meter, the transmission through the capillary was maximized and again appeared to glow when examined through the IR viewer. After several lengthy attempts to diagnose the system the capillary tube was removed and found to have been crushed at some point and its remaining structural integrity only a result of its polymer cladding.

To remedy this problem a fluoropolymer (Teflon-AF n = 1.29) capillary tube was obtained from Biogeneral Inc. for ~$200/m. The tube possessed an internal diameter of 250 μm and when used with nonanoic acid would have a numerical aperture of ~0.4. This tubing performed well but also tended to glow brightly when operating. This is thought to be caused by either fine particulate contamination on the tube's surface or the result of surface irregularities produced during the extrusion process. The high coupling efficiency (>70%) was only obtained by using a short ~10 cm section of tubing as longer lengths tended to suffer more pronounced losses. It should also be emphasized that this tubing is only suitable for single use since, even after cleaning, it tends to retain traces of nanoparticles. No attempt was made to reclaim the tubing by circulating a solution with pH < 1. This would likely dissolve any particulates present in the tube and could be used to verify whether the cause of the glow and subsequent loss was intrinsic to the fiber or the result of contamination. Figure 45 shows the diagnostic integrated with the collection chamber to make real time absorption measurements. Operating this system was significantly more challenging than the original LWCFC. The alignment of the diode into the capillary was sensitive since transmission needed to be at its absolute maximum in order to compare a series of measurements. Fortunately, the system was

stable enough that it was possible to confirm the reproducibility of the transmission measurements for a control sample of nonanoic acid over a period of several days.

After a significant concentration of nanoparticles was measured and a strong fluorescence signal detected, the diagnostic system was returned to the THOR lab in an attempt to measure the lifetime. The lifetime measurement attempted to excite the nanoparticles with a short pulse from THOR and then detect the resultant decay from an amplified detector. An AC coupled avalanche photodiode (Thorlabs APD 310) was chosen for its sensitivity and integrated amplifier circuit. The first step in performing the measurement was simply an attempt to detect any fluorescence using THOR as the pump source. As a control the fluorescence was measured from a piece of bulk glass pumped by THOR. Since the detector was AC coupled it should have produced a pulse with the bandwidth of the detector and proportional to the fluorescence. This signal was independent of the pulse from THOR as verified by placing a piece of paper in the beam path in front of the collection optics. Filters were used to establish that the response of the detector was proportional to the intensity of the fluorescence.

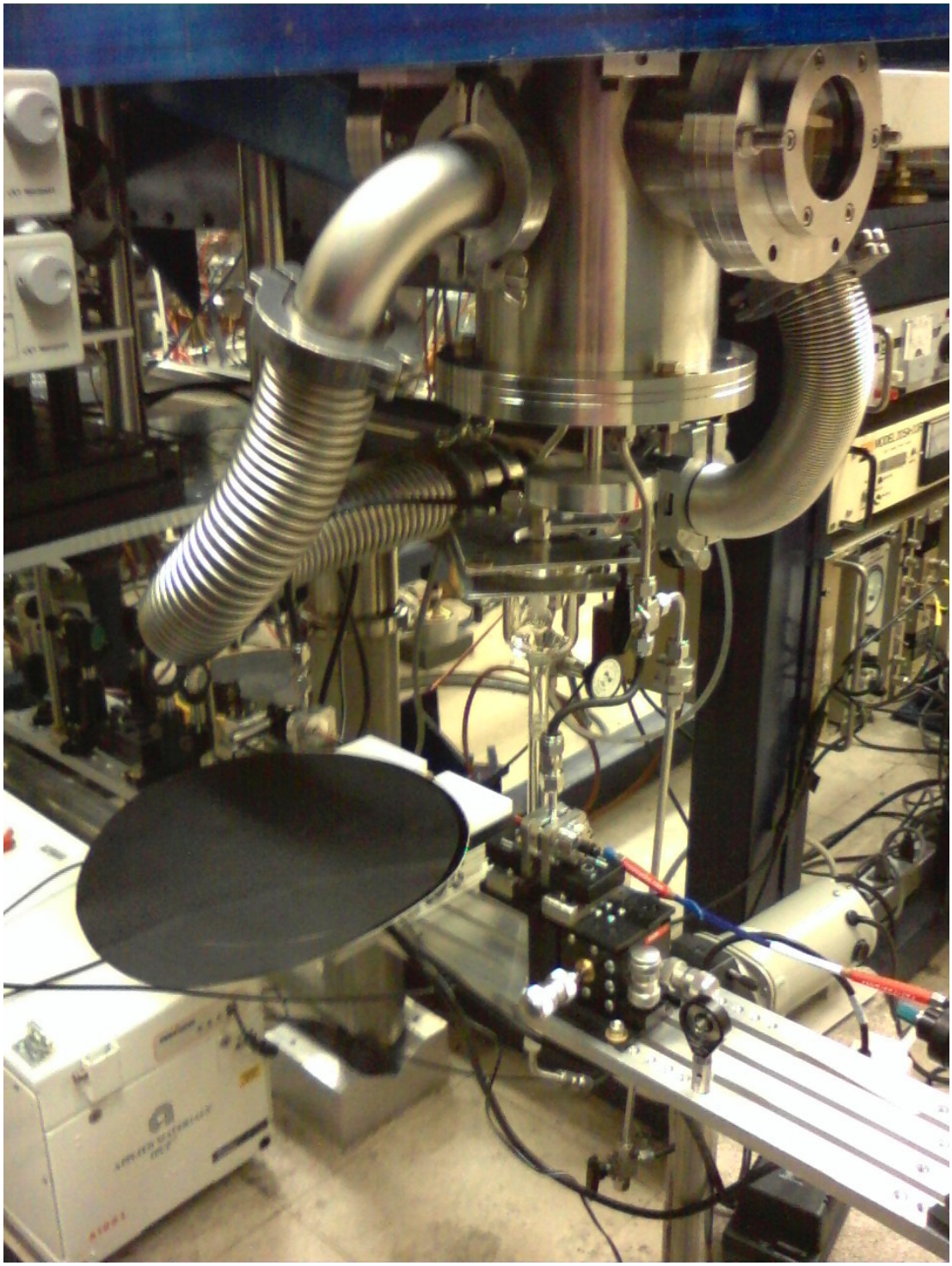

Figure 45. The LWCFC fully integrated into the collection chamber for real time concentration measurements.

Substituting the capillary for the bulk material produced no signal. Because the duration of the stretched pulse is ~1 ns the maximum energy that could be safely utilized in the lifetime experiment was approximately 50 μJ. A simple back of the envelope calculation reveals that the expected intensity of the fluorescence signal incident upon the detector is near the reported detection limit of the APD 310. The typical concentration measurements from samples capable of producing high quality fluorescence spectra reveal approximately 25-75% transmission through the capillary. Since the damage threshold of the optics for this pulse length is less than the saturation fluence and the number of ions present in solution is large compared to the number of photons in the pulse, the total expected fluorescence from the sample capable of coupling into the fiber can be calculated using the integrated steady state population inversion as a starting point[50]. The power incident on the detector can then be estimated by accounting for the various measured loss mechanisms (insertion loss of capillary tube ~50%, solid angle of fluorescence with correct numerical aperture ~1%, the effect of Nd^{+3} concentration quenching on radiative vs. fluorescence lifetime 1/3, the branching ratio ~50%, transmission filters at 1050 nm capable of eliminating a 50 μJ pulse at 800 nm 30%, and the pump laser spectral overlap with cross section ~15%). The expected incident power obtained by accounting for the various loss mechanisms is ~0.6 μW which is just below the 0.7 μW noise floor of the detector. In terms of the average population inversion over the duration of the experiment (set by the unquenched radiative decay rate ~300 μs), the 50 μJ pulse from THOR is at best equivalent to a 20 mW CW beam centered at the peak absorption wavelength of the transition. Considering that the diode laser can operate at 4 W a strategy that relied upon a CW method was pursued when the pulsed radiation proved undetectable.

To measure the lifetime of the nanoparticles with a CW pump source requires a less direct approach. The diode laser was modulated with a sinusoidal current and the difference between the phase of the diode light was compared to the phase of the response from the fluorescence signal as reported by a lock-in amplifier. The diode's current source (Newport 500B) was modulated using an external function generator over a range of frequencies from 100-5000 Hz, but since the current driver has a 10 kHz bandwidth at frequencies above a few kHz, the diode's output would appear significantly distorted. The diode laser was monitored using a Thorlabs DET 210 while the fluorescence was measured by a Thorlabs PDA10CS. The noise floor on the PDA10CS is slightly better than the APD310 but the PDA10CS produces significantly smaller A/W response than the APD310 and benefits from external amplification. It is interesting to report here that the signal intensities recorded by the lock-in amplifier during the lifetime measurements corresponded to a range of intensities at the detector surface between one and several hundred times the minimum signal needed for an APD310 to operate above threshold. Thus, the extra factor of 100 in signal gained by CW pumping proved essential, implying that the above description of the total losses is reasonably accurate and complete. Moreover, the integrated output from the Ocean Optics spectrometer for a nanoparticle sample was taken utilizing the same set of filters required to completely block the diode emission and used to calculate the total power incident on the spectrometer's detector (Toshiba TCD1304ap). Dividing this total power by the spectrometer's transfer function at 1050 gives the expected power available to the PDA10CS. Thus the expected signal to noise ratio from the PDA10CS was at best in the neighborhood of 1.2:1. It should be stated that this measurement was performed on a sample of low concentration and the signal intensity from the PDA10CS was consistent with operation in the 0.5-1 μW range and was only detectable using a lock-in amplifier in

a high sensitivity mode. Thus, it is clear that a direct measurement of the lifetime at these intensities, while theoretically possible with proper instrumentation, would not be practical as a routine diagnostic.

A robust method capable of operating at low power and low signal to noise ratios was required. When it is possible to modulate the carrier signal of a desired source of information, the orthogonality of periodic functions can be exploited, significantly depressing the signal from uncorrelated sources. This condition is readily apparent when looking at the Fourier transform of a signal that contains a certain quantity of random uncorrelated noise.

$$I(t) = I_0 \sum_{\omega} c_{\omega} e^{i\omega t} + N_0 \sum_{\omega} n_{\omega} e^{i\omega t} \tag{36}$$

Thus, if it is possible to restrict the signal to a specific frequency, the power spectrum will only have support from that component.

$$I(t) = I_0 e^{i\omega t} + N_0 \sum_{\omega} n_{\omega} e^{i\omega t} \tag{37}$$

Therefore, even if the signal to noise ratio is 1:1 the power spectrum of uncorrelated noise will typically scale like 1/f + thermal + shot, which in general is a relatively monotonic function. The integrated power from noise around some frequency component can be then written as:

$$P_{noise} = N_0 n_{\omega} \Delta\omega \tag{38}$$

where the width of $\Delta\omega$ is determined by the bandwidth of the measurement apparatus or response of the system producing the signal to the modulation. Thus if the signal is detected and then multiplied in instrumentation by a periodic function the measurement becomes:

$$Mixed\ Signal = \int_0^{\frac{2\pi}{\omega}} \left[I_0 e^{i\omega t} + N_0 \sum_{\omega} n_\omega e^{i\omega t} \right] \cos(\omega t) d\omega$$

$$Mixed\ Signal = \frac{\pi}{\omega}\left[I_0 + N_0 n_\omega \right] \quad \textbf{(39)}$$

If $I_0 \approx N_0$ and the system possesses a smooth noise spectrum and a sharp frequency response (sufficient bandwidth), the signal to noise ratio inside the instrumentation will be significantly greater than at the detector since $N_0 >> n_\omega$ and therefore $I_0 >> N_0\, n_\omega$.

This is known as homodyne detection and is the principle underpinning the operation of a lock-in amplifier. The amplifier is capable of reporting information of the intensity and phase of the signal relative to the reference. Though both modes of operation could be used to measure the lifetime of the fluorescence transition, difficulties with the stability of the system necessitated relying only on the measurement of the phase for reasons that become clear when examining the response of a fluorescence signal to a sinusoidal pump source.

Since the fluorescence signal generated by a short pump pulse should decay with an exponential envelope, the fluorescence response to an arbitrary pump waveform is given by the convolution of the instantaneous response function with the driving waveform.

$$F_R(t) = \int_0^t I_D(t') e^{\frac{t-t'}{\tau}} dt \quad \textbf{(40)}$$

This integral can be evaluated analytically to produce the response function:[51].

$$F_R(t) = \int_0^t I_0[1+\cos(t')]e^{\frac{t-t'}{\tau}}dt = I_0\tau + \frac{I_0\tau}{1+(\omega\tau)^2}\left(-e^{-\frac{t}{\tau}} + \cos(\omega t) + \omega\tau\sin(\omega t)\right)$$

$$= I_0\tau + \frac{I_0\tau(\cos(\omega t) + \omega\tau\sin(\omega t))}{1+(\omega\tau)^2}, \quad t >> \tau \qquad \textbf{(41)}$$

$$= I_0\tau + \frac{I_0\tau\cos(\omega t + \tan^{-1}(\omega\tau))}{\sqrt{1+(\omega\tau)^2}}$$

Notice that the phase and amplitude vary with frequency but that the response frequency is unchanged. Thus, the phase-shift between the driving function and the fluorescence response is written in terms of the driving frequency and decay rate.

$$\Phi = \tan^{-1}(\omega\tau) \qquad \textbf{(42)}$$

For the purposes of the measurements conducted on the nanoparticle colloids, only the phase was measured since the response of the diode laser to a sinusoidal driving function also varied with frequency. Both the DC offset as well as the peak to peak power would change as the frequency was adjusted, making it difficult to accurately determine the relative magnitude of the pump pulse and the fluorescence response.

Chapter 7: *Experimental Overview and Nanoparticle Characterization*

7.1 EXPERIMENT ONE (08/2004)

The first experiment, conducted in late 2004, attempted to collect Nd^{+3} doped LG-760 (phosphate glass) nanoparticles in several fluids with the goal of measuring the fluorescence spectrum of the colloid. Particles were produced from ball milled powder using a collection system that was constructed from previously existing components with a few modifications to make it compatible with increased production goals. These improvements included a silver soldered supersonic nozzle that was clamped via the housing of the virtual impactor to the table, a deeper collection cup with a transparent splash guard, and a gas handling manifold with gauges to control the hydrostatic pressure driving the fluid column through the needle valve to the impactor. This latter adaptation was designed to prevent splattering in the chamber where fluid containing a high partial pressure of dissolved gas would otherwise encounter a vacuum and effervesce. The chamber consisted of a cross with four NW50 connectors. One horizontal port was used for a vacuum connection and the other as a window. The vertical connections were used as feed-throughs for the supersonic nozzle and fluid collection system. The distance between the fluid collection impactor and the nozzle could be set by adjusting the chamber height. A seal was made around the ¼ inch supersonic nozzle with an ultra-torr compression fitting.

The pressure was monitored at the vacuum system manifold where the cross of the chambers was connected via a two meter by two inch diameter plastic hose. The pressure during this experiment was measured to be approximately 200-250 mT. However, a port was subsequently attached to the cross in a later experiment, allowing direct measurement of the pressure near the impactor surface and it was found that the

200-250 mT pressure in the manifold corresponded to 500-600 mT pressure in the cross. Several samples were collected with the laser energy approximately 280 mJ and the center flow rate approximately 40 sscm. This corresponds to what is termed the "single ablation feed rate" given the area of the center flow nozzle used. Single ablation operation means the linear velocity of the powder through the interaction region of the LAM apparatus divided by the vertical extent of the excimer's beam on target equals the repetition rate of the laser. Thus, the volume of powder dispensed into the LAM apparatus during the off time of the laser's duty cycle is guaranteed to completely overlap with the beam during the next shot.

Ablation was moderate to weak and tended to be intermittent. Each collection would take 10-15 minutes to deplete the fluid reservoir. Samples fed too slowly tended to freeze while those fed too quickly tended to splatter. Several samples, particularly those collected in fluids with a high dielectric mismatch, appeared cloudy, indicating the presence of small particles. These samples, specifically those collected in mineral oil and fomblin, remained semi-foggy for many days after their creation indicating that the particles present in the colloid were submicron in size.

It was not possible to determine why these colloids settled out or the size of the particles or agglomerates present in the suspensions. The particles did not fluoresce, meaning that they were either not present in sufficient quantity to be detected or they experienced a high degree of quenching or contained significant levels of impurities. Samples collected in benzene and benzene plus siloxane revealed fluorescence at the expected wavelength, as well as TEM images of individual nanoparticles.

7.2 EXPERIMENT TWO (03/2005)

Another attempt to collect particles in benzene was made and TEM images taken from grids dipped in the colloid revealed the presence of nanoparticles. Problems feeding the powder prematurely ended this attempt. However, XDS spectra revealed the nanoparticles to have the expected composition.

7.3 EXPERIMENT THREE (11/2005 – 04/2006)

To attempt a quantitative study of the production process, the next run focused solely on dry collection. Films of nanoparticles were collected on several solid substrates and directly impacted onto TEM grids. The experimental conditions were essentially the same as in experiment two, helium at a flow rate of 40 sccm with a chamber pressure of 500-600 mT and the laser operating at 250-280 mJ. Decent ablation produced thin films of significant density (10-20 μm thick and 1-2 mm in diameter) after about 20 to 30 seconds of collection.

Diagnostics from this collection, consisting of spectroscopy and TEM measurements, dominated the work during the following months. Unfortunately, none of these efforts produced any quantifiable information relevant to improving the production process. However, these efforts yielded useful data about the optical properties of these materials. Since studying these materials was highly dependent upon creating a sample with sufficient nanoparticle concentration to detect via optical measurements, during this early work three intractable problems consistently confounded all efforts to produce useful quantities of nanoparticles: selection of a surfactant compatible with particle surface chemistry , low aerosol density, and poor reproducibility or reliability of the collection apparatus.

7.4 EXPERIMENTS FOUR AND FIVE (05/2006 – 08/2006)

Getting a foothold with the first of these three problems eventually facilitated the incremental progress necessary to tackle the other two. Identifying potential surfactants was challenging since little relevant information about the surface chemistry of phosphate nanoparticles was available at the time. However, investigation of the chemistry of these glasses revealed that they react with acids and bases[18]. Reaction in acidic and basic solutions leaches out many of the dissolved additives present in the phosphate glass. This chemistry leads to weathering at the surface of phosphate glass exposed to humid air for long periods of time[17].

To minimize the damage to these surfaces it was believed that siloxane molecules could be applied and incorporated into the glass matrix at the surface providing a buffer coating that would prevent the formation of a hydration layer and decrease the rate of weathering of a glass plate. Surprisingly, this proved to be incorrect. In her dissertation Amy Barnes studied the weathering in phosphate glass using Raman spectroscopy to test this hypothesis[17]. The candidate molecule she chose was an amino siloxane. Instead of the siloxane head reacting with the glass, she found that the amine preferentially bonded to the surface leaving the highly reactive siloxane group exposed to the environment. This result confounded the development of this type of weather resistant coating technology.

However, her results allow the chemistry of potential surfactants to be specified. A viable surfactant for phosphate glass nanoparticles should probably have an amine R group but no siloxane[52]. It turns out that this area of chemistry is nontrivial and identifying candidate molecules challenging. Nevertheless, the acid-base reactivity of potassium oxide-based phosphate glass suggests that it may be temporarily compatible with weakly acidic R groups in non-aqueous environments[18]. Therefore, since nonanoic

acid was found to be a useful surfactant for silver nanoparticles and was also compatible with the collection apparatus, we chose to study its potential as a surfactant[53].

In experiment four, thin LG-760 films comparable to those made in experiment three were produced with 40 sscm He at 500 mT and 220 mJ. These films were characterized and found to possess optical spectra similar to those in the previous experiment. Nonanoic acid was then added to the films and allowed to evaporate on a hot plate at 40° - 50° C. The films were then studied with Raman spectroscopy and results compared to several controls. Raman spectra taken from these thin films of nanoparticles coated in nonanoic acid suggested the presence of a chemical bond between the nanoparticles and nonanoic acid[54]. Determining a likely surfactant allowed for the design of experiments capable of producing colloids of sufficient density to study in a systematic manner.

During this time the issue of supplying a dense aerosolized powder to the LAM Reactor was pursued in parallel. Several samples of nanoparticles were prepared using SiO_2 spheres to test the hypothesis that a powder of irregular particles of high surface potential was responsible for the aerosol density problem and hence low nanoparticle density in all samples prepared to date.

In experiment five Duke Scientific spheres of various diameters were ablated. Some TEM and glass film samples were collected, but the main purpose was to determine the feeding rate of the spheres which was found to be 0.5 to 1 gram in 5 to 15 minutes. The conditions of the LAM process were nearly identical to the previous experiment with 40 sscm helium, 500 mT, 220 mJ. During this experiment the powder was depleted so rapidly and stopped so abruptly that it seemed the material had clogged the machine. In a surprising turn of events, disassembling the apparatus revealed a completely empty powder feeder in contrast to the results using crushed LG-760 powder

produced in house. The work performed in experiments four and five led to the successful production of a quantifiable colloidal sample in experiment six.

7.5 EXPERIMENTS SIX AND SEVEN (11/2006 – 08/2007)

Experiment six consisted of preparing five samples of LG-760 in nonanoic acid. These samples were approximately 20 ml and took 10 minutes to collect. They were then reloaded into the fluid reservoir to be recirculated into the chamber. The average loss of fluid due to splatter was in the 2 to 4 ml range. Due to this fact after about six reloads, assuming a uniform production rate, the loss of nanoparticles due to splatter approximately equaled the additional nanoparticles gained by running the LAM for another 10 minutes. The result was that over the course of three weeks after preparing five samples, each requiring six breakdowns of the collection chamber, only one sample with detectable quantities of nanoparticles was produced. However, that sample provided a wealth of information in the form of spectroscopy and TEM images, facilitating the design of a new chamber and practical diagnostic experiments capable of producing and studying the particles in near real time. Most importantly the new chamber ultimately increased production rates and experimental throughput by a factor of at least one hundred.

In order to be able to detect the presence of nanoparticles produced in the previous experiment with optical techniques, it was necessary to concentrate the material by evaporating excess nonanoic acid in a Rotovap. This procedure reduced the 20 ml sample to approximately 1.5 ml, increasing the concentration about ten fold.

7.6 EXPERIMENTS EIGHT AND NINE (04/2008 – 09/2008)

With the suitability of nonanoic acid as a surfactant confirmed, and measurable concentrations of nanoparticles produced, it was possible to design an improved

collection chamber capable of enhancing sample production rates by factors of 100. In the old chamber 10 minutes collection would require approximately 30 minutes turn around. An increase in production rate of 4 fold was achieved by re-circulating the fluid. Because of alignment issues between nozzle and impactor, as well as the problems with minor leaks, only one of five samples produced contained detectable quantities of nanoparticles. Thus, by making a chamber that always snaps together within less than 10 μm of variation from run to run, we achieved a 5 fold increase in total sample throughput. Finally, the in-chamber pressure was reduced by a factor of about 2 - 4, which for relatively small nanoparticles places them above threshold for collection at η less than 0.4. Given the relatively sharp cutoff of collection curves reported in the literature it is possible that a 10 fold gain in collection efficiency for the smallest particles was achieved while probably managing at least two times increase for the larger. Thus we predicted and obtained roughly a 100-fold increase in sample throughput. Moreover, it became possible to collect samples for 6 to 8 hours versus 60 to 80 minutes, yielding a net increase in starting suspension density of at least ten times.

Once the chamber was constructed and characterized, an experiment was conducted to evaluate whether it was suitable for collecting nanoparticles. In this experiment several samples of nanoparticles were collected on TEM grids. The chamber performed as designed. A significant increase in the density of nanoparticles was obtained at the predicted optimal collection point of 12-16 nozzle diameters between the nozzle and TEM grid compared to the previous chamber, even with lackluster aerosol density.

The next step was to collect the particles in fluid and use diagnostics that were designed to have the capability of detecting samples with concentrations 10 times smaller than measured in experiments five and six. The primary diagnostic tool used was a one

meter long liquid waveguide capillary flow cell (LWCFC). This system consisted of a glass capillary tube coated in a fluoropolymer with a lower index of refraction to produce an annular waveguide with a numerical aperture of 0.22. With the nonanoic acid filling the core the NA would be reduced to ~0.09 resulting in high insertion loss from the 0.22 NA diode laser. Inside the LWCFC the capillary tube is located within a few thousandths of an inch of an optical fiber inside a Peek plastic 3 channel T style micro-fluidic compression fitting. The other end of the fiber is connected to a standard SMA jack. One end of the capillary tube was then connected to a diode laser, the other to a custom built fiber coupled Ocean Optics spectrometer. Operating at low power < ~100 mW, this system could reliably monitor very small changes in nanoparticle concentration over long periods of time. Alternatively, at high power (2-4 W) the system was capable of providing high quality low noise fluorescence spectra.

Unfortunately, this system contained several plastic components which proved incompatible with nonanoic acid as well as the high temperatures present when studying the fluorescence. The challenge with this instrument, which was not designed to operate at very low pressure, was to maintain uninterrupted flow through the capillary tube during characterization.

This difficulty was not just a problem from the perspective of leaks but also rarefaction of the peristaltic pump, which tended to nucleate bubbles or voids in the flow as the elastomer tube changed its performance characteristics over the course of a run. The introduction of a bubble in the capillary tube combined with the decreased pumping rate of a fatigued tube can lead to the failure and rapid melting of the LWCFC in the diode laser input fitting. It should be noted that this instrument is not designed to support more than 50 mW of input power with low flow rates. However, before melting and

burning, the LWCFC provided a font of information about the range of production rates for the new chamber.

7.7 Experiments Ten to Fourteen (01/2009 – 07/2009)

Several different approaches to overcome the LWCFC melting and flammability problem were attempted including salvaging the LWCFC and reverse engineering some of its components. A few techniques were developed as workarounds but current designs still fail catastrophically, damaging either the optics or capillary tube. With the new collection system built, verifiable production rates measured and the LWCFC flammability problem partially resolved, it was possible to begin studying the properties of this type of colloid in earnest. A series of samples were produced with varying particle diameters. Fluorescence spectra and lifetime measurements were collected.

This effort demonstrated that the nanoparticles possess similar properties to bulk laser materials but with a few notable differences that can be explained by their size. It was even possible to conduct a gain measurement using a modified LWCFC-like apparatus. This series of experiments made a strong case for the suitability of using colloidal nanoparticles as a gain medium in lasers. Issues that remain unexplored, including the identification of compatible surfactant chemistries, may yet prove intractable but the process of discovering whether this is the case should be straightforward with a systematic study of the chemistry. In the following section some of the more relevant experimental details will be discussed and the data that represents the bulk of this work presented.

7.8 Results from Experiments One through Three

In the first collection, samples were prepared in several fluids and their presence verified via TEM and fluorescence spectroscopy. The results of this first fabrication run

were poor but attributed to the inhomogeneous and agglomerated feedstock supplied to the LAM. This is where the powder processing work began to take shape. A search was undertaken for a commercial source or process capable of producing uniform powder that was easily aerosolized. Simultaneously with this search a method to produce useable powders in house was developed with qualified success. The powder used in this first experiment was produced by ball milling partially ground 2% Nd^{+3} (wt) LG-760 phosphate glass with alumina spheres for twenty four hours. The powder tended to agglomerate into a brittle cake or hard brick when left undisturbed for several days. A "coffee grinder" style powder feeder was utilized to deliver the aerosol to the LAM. Due to the low flow rates and clearance between the fan blade and the enclosing can of the grinder, any powder in the system would rapidly accumulate at the bottom of the device or on the walls of the container. On average the grinder would work for a few seconds to a few minutes and then stop feeding unless a significant jolt was applied to the system, dislodging powder coating the walls. The ablation occurred in a "horn-cell" that was retained for use with a few modifications throughout these experiments. During this experiment the laser energy per pulse was sufficient to break down the entire volume of the aerosol or "center flow". This flow operated at about 40 sccm guaranteeing that each segment of powder was ablated by the beam at least once. Samples were collected in fluid in the first generation cross chamber described above. Setting the nozzle to impactor distance as well as vertical alignment proved difficult in this design. Moreover, achieving reproducible fluid flow rates and minimizing splattering due to air bubbles or instabilities in the flow was not possible.

Figure 46. The original impactor collection cup and splash guard.

Samples of 20 mL surfactant were prepared using an air pressure differential between the fluid reservoir and collection chamber to drive the fluid against the supersonic flow from the nozzle. This flow was controlled by a needle valve and needed to be carefully monitored since the fluid tended to freeze and then occlude the impactor head. The freezing of the fluid on the impactor surface likely occurred because of evaporative cooling from the solvent/surfactant, aided by the rapid expansion of the supersonic jet into the vacuum chamber. The breakdown of the exact gas dynamics in the presence of so many potential supersonic effects is difficult to understand without better measurements of the parameters in the system. Thus a less general description of the frozen surfactant effect was not possible. However, it was noted that the surfactant would freeze if the flow was too gradual and violently and rapidly erupt if the flow was too great. The line between these two extremes was unfortunately narrow. This propensity for the impactor nozzle to violently disgorge its contents into the vacuum

chamber proved hazardous when working with dangerous surfactants like aminopropyltrimethyloxysilane (APTMOS), or solvents like toluene and benzene.

For the purposes of the first experiments several surfactants were chosen including mineral oil, benzene, toluene, chloroform, and TOPO. These chemicals were selected due to their lack of hydroxide ions, low toxicity and low vapor pressures. In all cases except for benzene and APTMOS dissolved in benzene, no nanoparticles were detected in the fluorescence experiments. The TEM measurements only detected the presence of nanoparticles for the benzene-dipped grids. The grids that were dipped in the benzene APTMOS solution contained an APTMOS residue that would not evaporate under any conditions and eventually hardened into a stiff coating. Subsequent research into APTMOS revealed that it was likely that the amine head reacts with the phosphate glass surface allowing the silane tail to cross-polymerize with other silanes in an irreversible reaction that eventually lead to a glassy substance settling to the bottom of the sample after a few months. The work with this reagent was abandoned due to both the difficulty of safely operating the chamber with such a hazardous material combined with its limited success as a stable capping agent. Further experimentation revealed that APTMOS in solution would rapidly polymerize as the temperature increased above 30° C. This rendered APTMOS all but useless as a surfactant in optical experiments that were designed to operate at high fluence and hence remain stable under moderate heating. However, the work done by Dr. Barnes indicates that, if the issues of toxicity and cross-polymerization can be solved, that alkyl chains with amine heads and properly passivated tails could function as capping agents for many species of phosphate glass nanoparticles[17].

Given the difficulties with this setup, approximately 4 out of 5 samples were insufficiently loaded with nanoparticles, rendering them undetectable to even the most

sensitive methods. Two measurements of the sample produced in the 8-04 run were undertaken: fluorescence spectroscopy, and TEM studies.

Using the Thor oscillator in a CW mode tuned to an unstable wavelength of operation between ~800-805 nm operating at ~400 mW, the samples were excited and the fluorescence measured for all samples collected during the first run. Only the APTMOS sample produced any detectable emission in the 1050 nm region. The apparatus used to measure the spectrum in Figure 47 was simple to assemble and work with, consisting of a fiber coupled Ocean Optics spectrometer borrowed from Ghost lab, a cuvette, a filter to block any stray 800 nm light and a lens to collimate the fluorescence. The laser was focused to a 0.5 mm waist inside a four-sided optical quality quartz cuvette which contained the sample, and fluorescence was collected at 90 degrees using a lens with a focal length of 0.5 inches. In transferring the sample between its storage vial and the cuvette, care was taken to ensure that the sample was not significantly perturbed when opening the vial and that sufficient time was given to allow any micro-particles or agglomerates to settle before a pipette tip was introduced into the fluid and gentle suction applied without significantly disrupting any micro-particles at the bottom.

With the fiber and collection optics locked in place after a rough alignment, a piece of the bulk laser glass with a polished surface was used to optimize the position of all beams and optics prior to inserting the cuvette. This normally would not have been an effective alignment procedure, but benzene was chosen since its index of refraction closely resembles that of LG-760. Physical stops on the collection side of the cuvette allowed the distance and orientation to be preserved between both the cell and the rod. The fluorescence intensity of the nanoparticles turned out to be quite sensitive to the wavelength of the pump laser and aligning the laser to operate above 400 mW in the 800-805 nm region proved difficult as the laser had a propensity to mode hop in the middle of

acquiring data. Thus to produce the spectra (blue curve) in Figure 47, first a control measurement needed to be made and then the oscillator wavelength tuned to optimize the signal (pink curve). Finally, the position of the beam relative to the lens needed to be optimized. However, this process could not be undertaken in real time since it required a significant period of integration to observe a signal. Nearing the end of the allotted laser time a weak fluorescence spectra was produced but shortly thereafter, the laser mode hopped (most likely due to temperature drift in the lab) and I was unable regain stable operation at sufficient power to produce a spectrum of high quality.

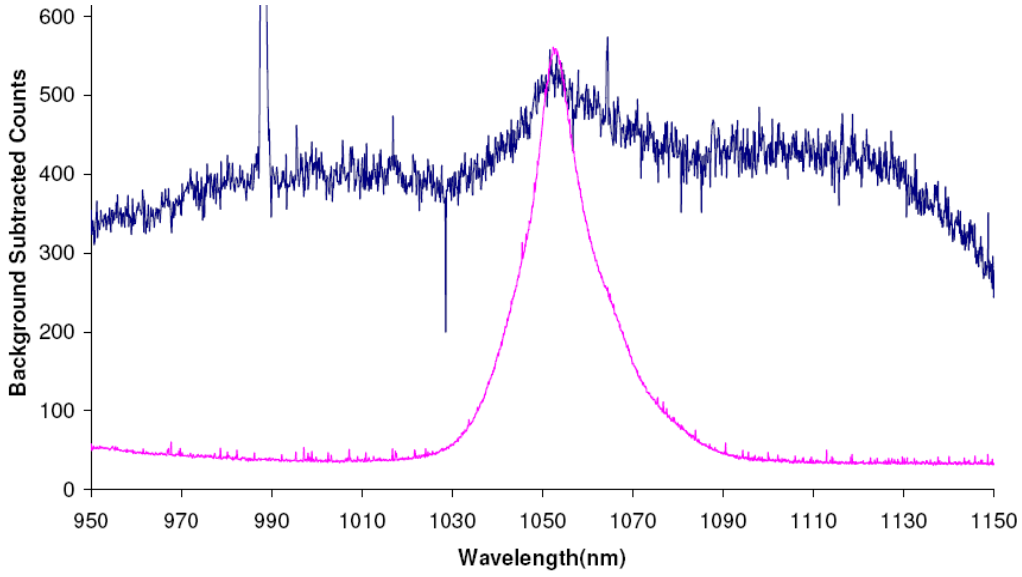

Figure 47. Fluorescence from Nd^{+3} doped LG-760 nanoparticles in benzene stabilized by aminopropyl trimethoxysilane (blue curve) compared with fluorescence from the bulk material (pink).

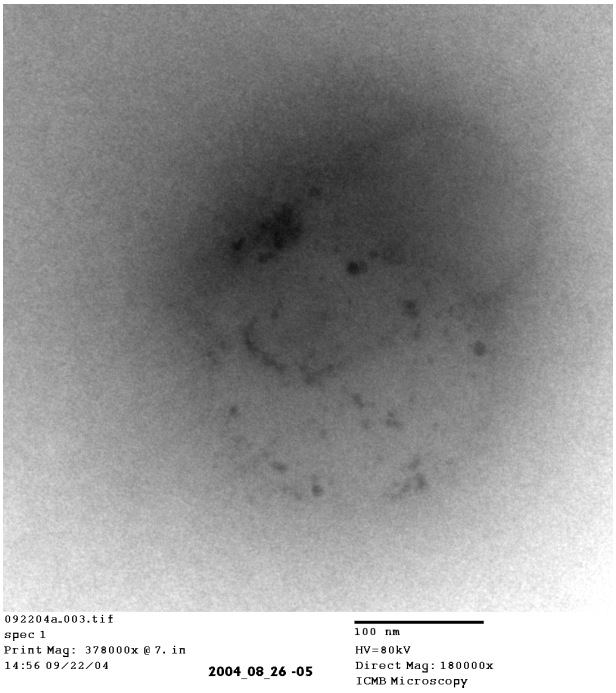

Figure 48. TEM image of Nd^{+3} doped LG-760 nanoparticles collected in benzene.

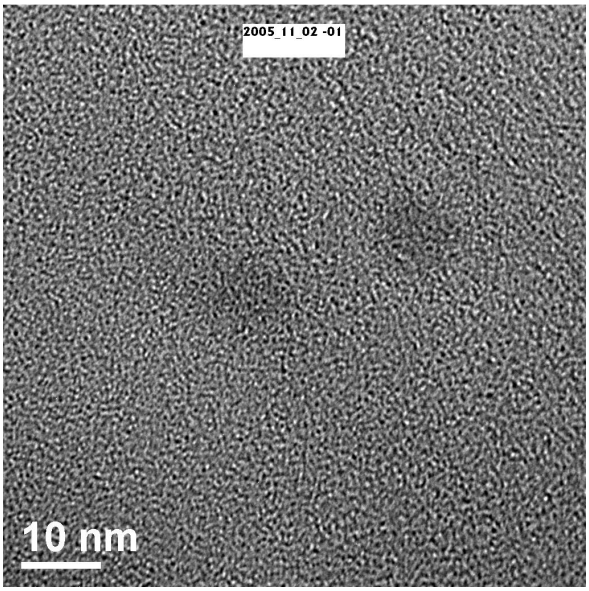

Figure 49. High resolution TEM image of Nd^{+3} doped LG-760 nanoparticles collected in benzene.

Overall, it took approximately five days of dedicated laser time from both Thor and Ghost labs, due to the unusual configuration of optics and electronics required to work at both 800 and 1054 nm, making this experiment resource intensive, highlighting the need for a different approach. From this point forward, the design of all the diagnostics emphasized two key features, significant engineering margin for sensitivity and stable turn key operation.

Figure 48 is a TEM image obtained from a grid dipped into a colloid of nanoparticles collected in benzene in the sample fabricated just prior to the APTMOS sample that produced the fluorescence curve in Figure 47. This image shows that the nanoparticles collected were in the 5-10 nm range. A year was invested in trying to repeat and improve upon the results of the first experiment. The only significant results obtained were high resolution TEM images verifying the size of the particles collected in a benzene sample with production conditions closely resembling those of the first experiment. Figure 49 clearly shows two particles with a diameter of approximately 10 nm in diameter. Though not a high resolution image, Figure 48 also contains particles in the 10 nm range.

Ultimately, all attempts to repeat or improve the fluorescence measurements of the first experiment proved unsuccessful. Though TEM grids dipped in samples verified the presence of nanoparticles, a commercial fluorometer with a liquid nitrogen cooled PMT detected no fluorescence. The THOR laser, taken after the 4 pass amplifier, (~10 mJ 1 ns beam centered at ~800 nm) was used as a pump source with the GHOST spectrometer as the detector. This also produced no results. A final attempt was made to pump the sample at 532 nm using a DCR and look for fluorescence spanning the visible to the near IR, though none was observed. It is important to note that the solvents being used were highly flammable, so care was taken especially during pulsed operation to

avoid focusing or breakdown due to focusing of stray beams in or around the solvents. Nevertheless, it was possible to approach the saturation fluence of bulk glass with the pulsed beams without mishap. Future experiments would reveal that the problem with measuring the fluorescence was simply due to low sample density combined with the poor efficiency of detectors available in the 1000 nm region.

7.9 Results of Experiments Three through Five

The perennial lack of signal during these early experiments lead to the idea of adapting a highly sensitive microscope based Raman spectrometer to the job of fluorescence spectroscopy. However, due to the limited depth of field of the microscope and the low density of particles in the colloidal samples, the aim of this work would be to study the fluorescence of nanoparticle films collected on solid substrates, attempting to detect any variation between nanoparticles and the bulk glass. Toward this end, two series of nanoparticle samples were produced and studied alongside a sample of crushed bulk glass re-melted into a thin film in an Argon atmosphere on a microscope cover slip. The ambient pressure in the chamber in this case probably closely resembled the conditions near the impactor (500-600 mT), since the collection splatter guard was not present on the impactor surface. Thus the impactor likely operated at a higher efficiency in this mode of collection compared with the previous experiments.

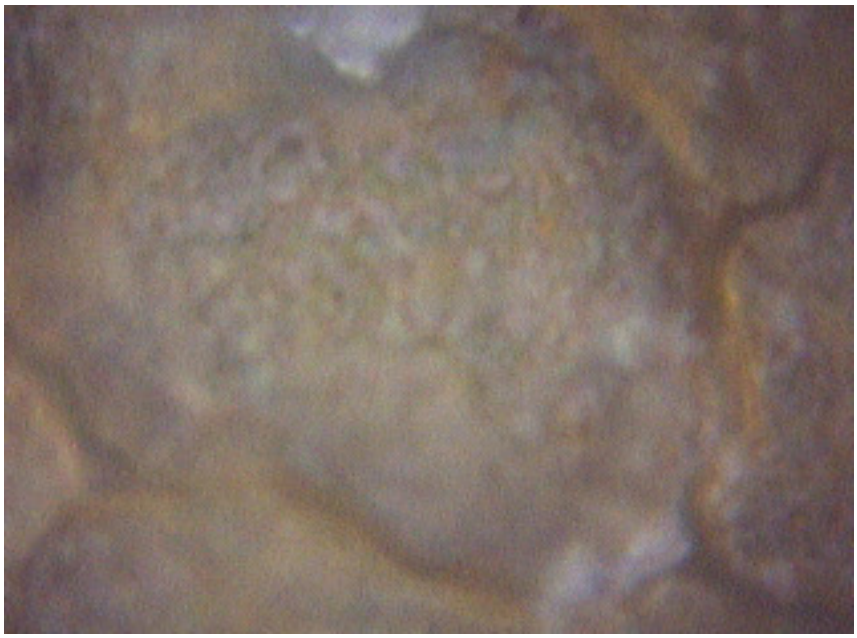

Figure 50. Image of a nanoparticle film (deposited onto a microscope coverslip via supersonic impaction) using a 100 x objective.

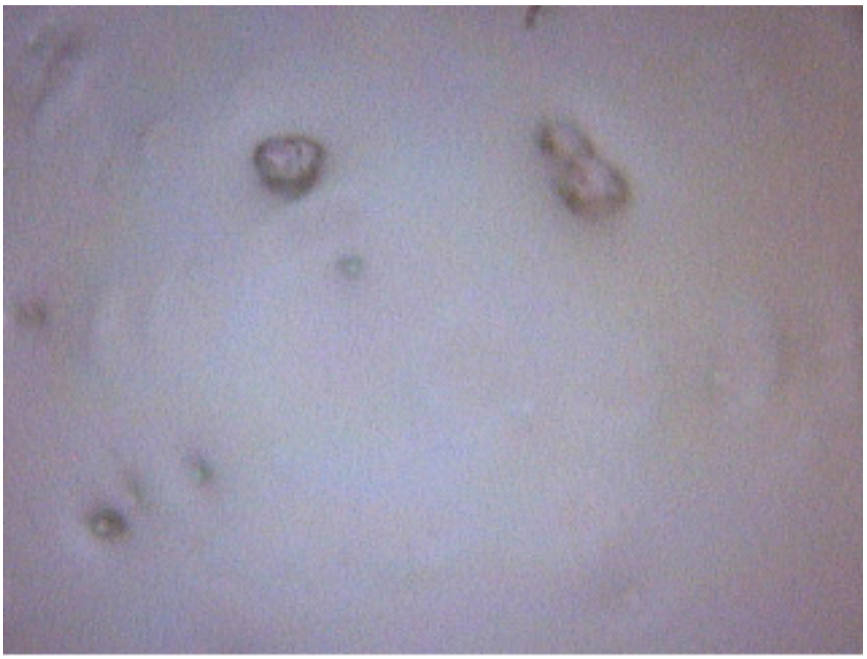

Figure 51. Image of a micro-particle film (sintered at 450° K on a microscope coverslip) using a 100 x objective.

It should be noted that the nanoparticle samples had a rough opaque appearance while the bulk film was smooth, glassy and transparent since this distinction becomes critical later. The difference in the surface quality of the nanoparticles (Figure 50) and the re-melted micro-particles (Figure 51) is apparent. Using the Renishaw spectrometer with a 785 nm pump laser and IR grating, a high quality fluorescence spectrum of the nanoparticles was finally collected (Figure 52). This spectrum displays the expected behavior of bulk LG-760. At first no differences were apparent between the bulk glass and the nanoparticles.

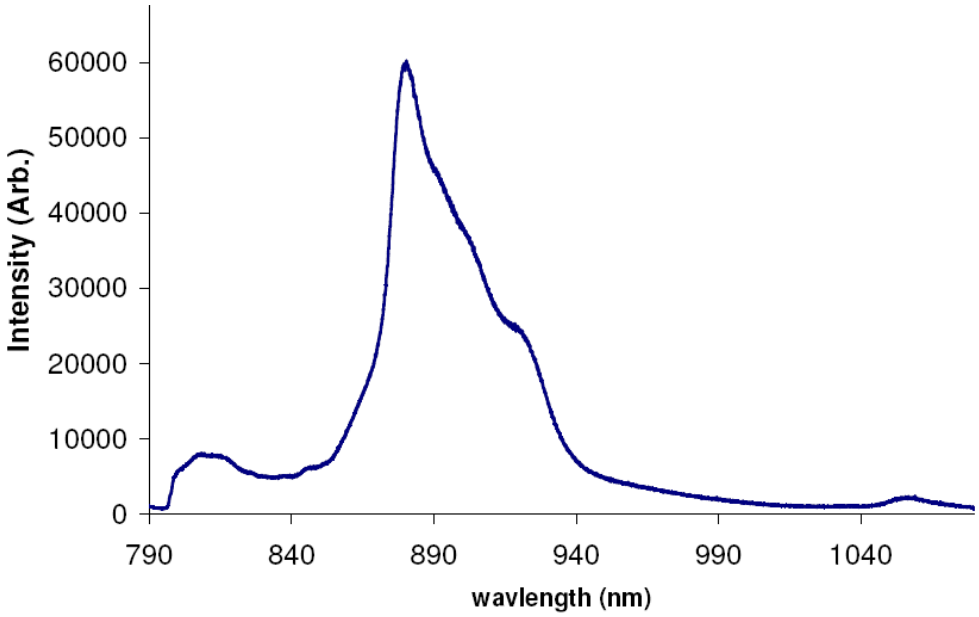

Figure 52. Fluorescence spectra from a nanoparticle film excited at 785 nm.

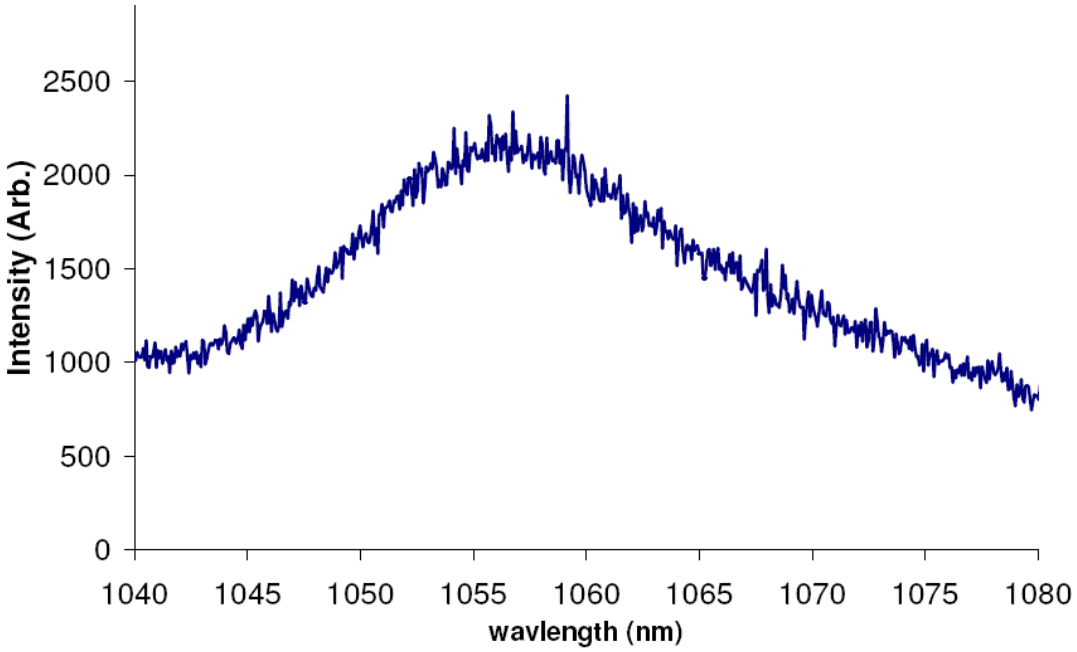

Figure 53. Fluorescence from a nanoparticle film excited at 785 nm.

The 785 nm pump likely excites the $4S_{3/2}$ transition or the tail of the $4F_{5/2}$. The 880 line characteristic of the transition between the thermally populated $4F_{3/2\text{-a}}$ and $4I_{9/2}$ ground state is dominant. However, several other transitions between the sublevels of the $4F_{3/2}$ and the ground state are also resolved in the 900 nm region[55]. Compared with the relatively bright transitions between the metastable state and the ground state, the primary laser line between the $4F_{3/2}$-a to $4I_{11/2}$ transition appears noticeably subdued. Comparing spectra from the Renishaw spectrometer to other measurements of the bulk glass, reveals that the scaling of the fluorescence between the 800 nm and 1050 nm peaks is an artifact of the instrument.

Thus the data from this measurement is of limited use. Discussions with the manufacturer indicated that the instrument and configuration were calibrated to provide an absolute measurement of the intensity independent of wavelength. However, since it

was necessary to run the instrument significantly beyond its specifications to detect light in the 1050 nm range, the validity of the software auto-correction is questionable. Nevertheless, the major lines relevant to the operation of a phosphate glass laser are present in the data.

In the visible range of the spectrum the nanoparticle films produced unexpected results (Figure 54). The large bulge spanning the visible, varied in shape and intensity with its location and from sample to sample. This lack of repeatability suggested that there was some strange variation in the nanoparticles. Ultimately, it was discovered that the odd character of the spectrum was due entirely to the quality of the surface. Diffuse scatter from any rough surface, independent of composition, produced similar spectra in the visible region. Surfaces were scratched using a diamond scribe and tested under the same conditions as the nanoparticles, producing the broad bell shaped peak in the 600-700 nm range.

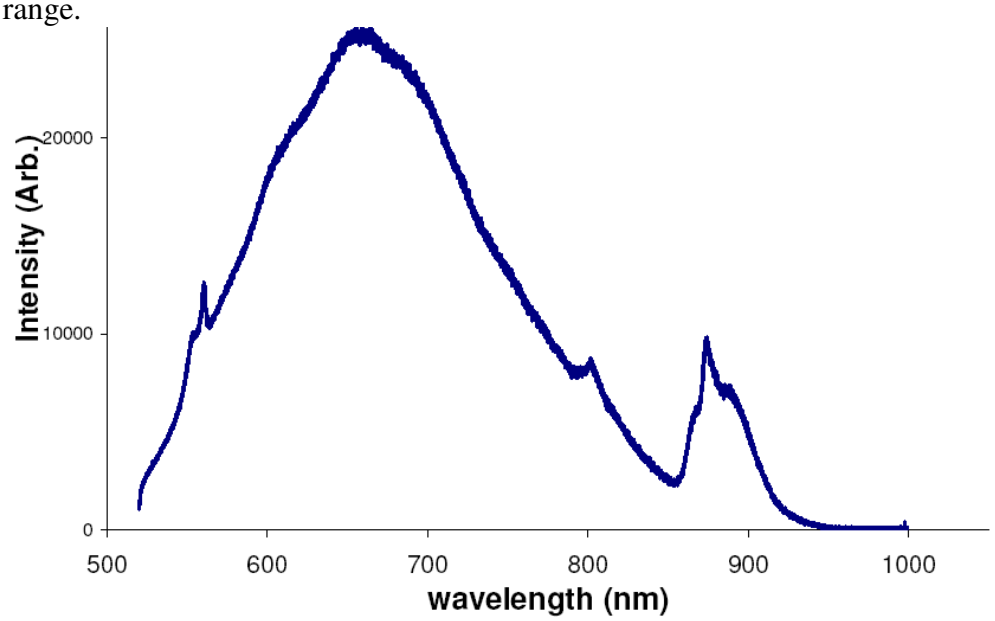

Figure 54. Fluorescence from a nanoparticle film excited at 514 nm using a Renishaw Raman spectrometer with a visible grating.

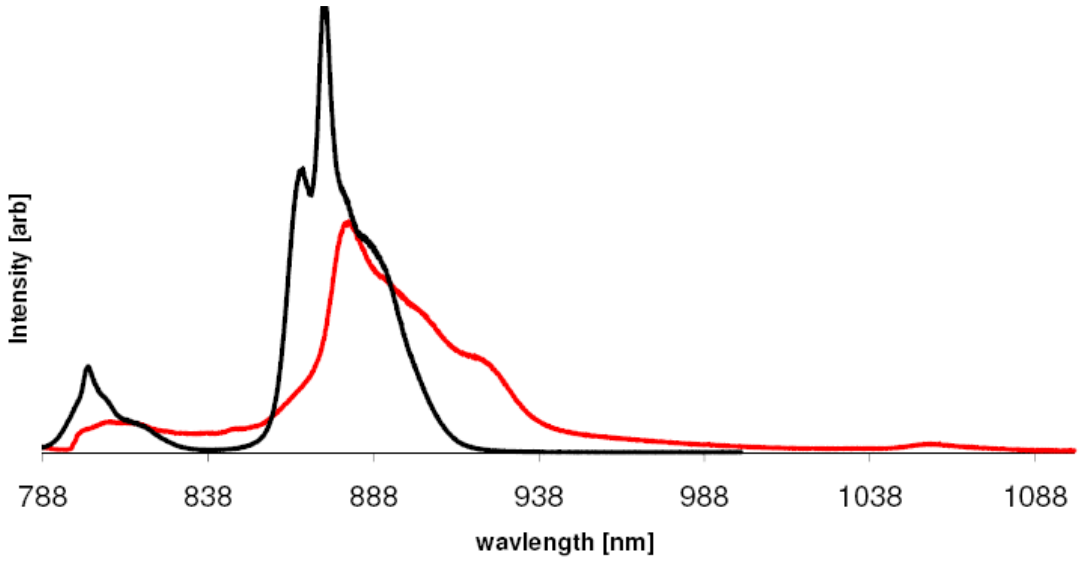

Figure 55. Fluorescence from a nanoparticle film excited at 785 nm (red) and 514 nm (black).

Materials tested included various plastics, microscope cover slips, aluminum, and optical substrates (i.e. a damaged 532 high reflector dielectric mirror). However, the absence of any discernable peaks at ~550 nm, 800 nm and 880-900 nm indicated that these portions of the spectrum were due to the composition of the nanoparticles. Another interesting feature of Nd^{+3} glass is presented in Figure 55 comparing the IR fluorescence of the nanoparticles excited with 785 nm light to the fluorescence from glass excited at 514 nm. This spectral shift was observed for both bulk glass and nanoparticle samples and though interesting it is not relevant to the current discussion and only mentioned to prevent confusion when comparing the IR spectra to the visible spectra.

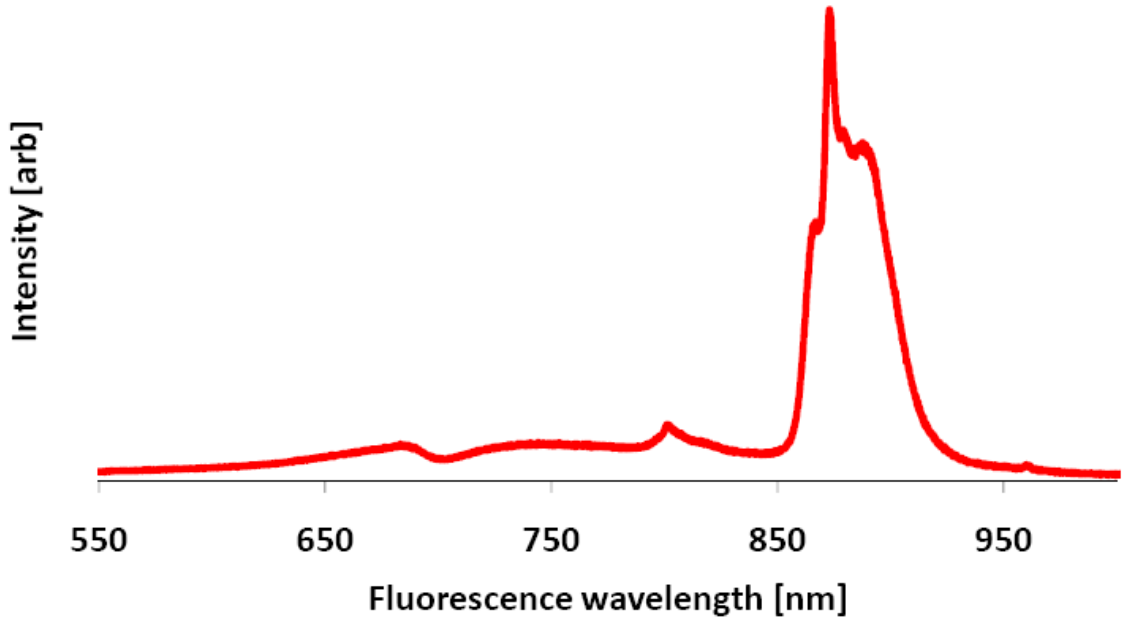

Figure 56. Fluorescence from a nanoparticle film excited at 514 nm using a Renishaw Raman spectrometer with an IR grating.

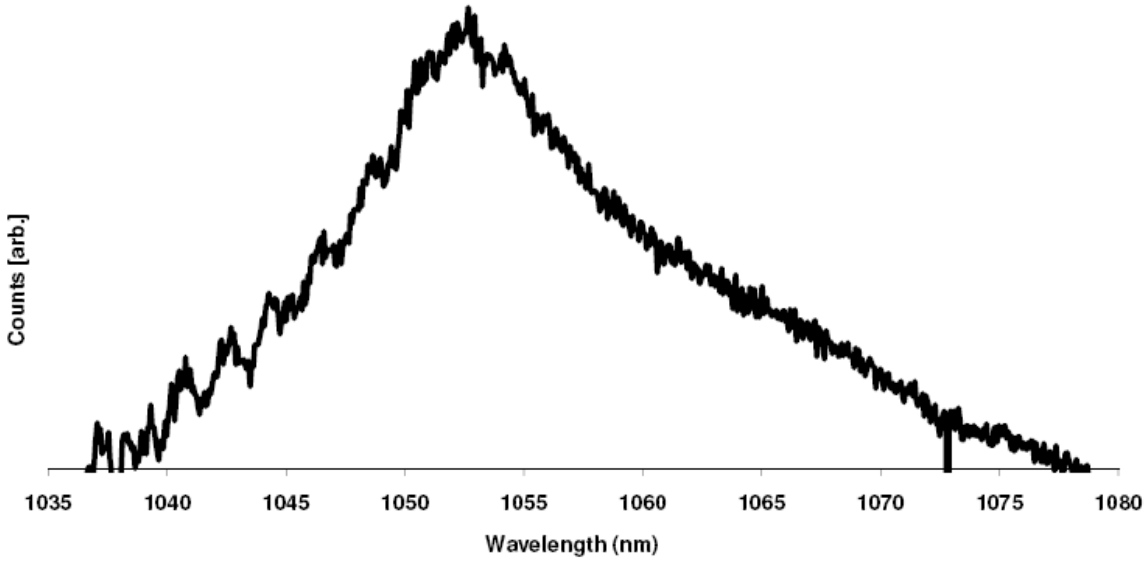

Figure 57. Fluorescence from a nanoparticle film excited at 514 nm using a Renishaw Raman spectrometer with an IR grating.

Since the anomalies in the spectra were due to the operation of the instrument, the spectrometer was reconfigured to run using an unorthodox combination of an IR grating and visible optics to generate the spectra in Figure 56 and Figure 57. In this configuration the broad central peak is significantly diminished. The totality of this picture combined with other experiments allows us to present the following quantitative data about how nanoparticles actually alter the spectra of the Nd^{+3} ions.

In Figure 58 it can be seen that the location of the peak has shifted about 2 nm to the red for the nanoparticle sample. We also note that the nanoparticles have a 5 nm diameter which places them toward the region where size can start to play a role in shaping the quantum mechanics of the host environment.

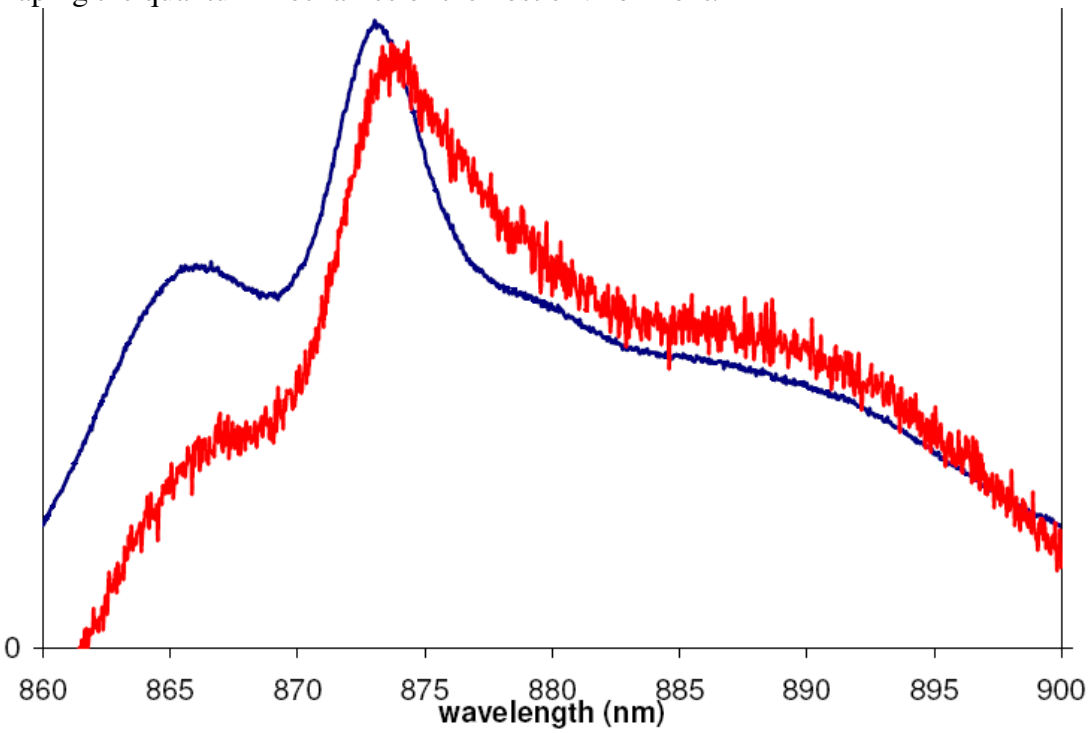

Figure 58. Fluorescence from a nanoparticle film excited at 514 nm (red curve). Fluorescence from a sintered micro-particle film excited at 514 nm (blue curve).

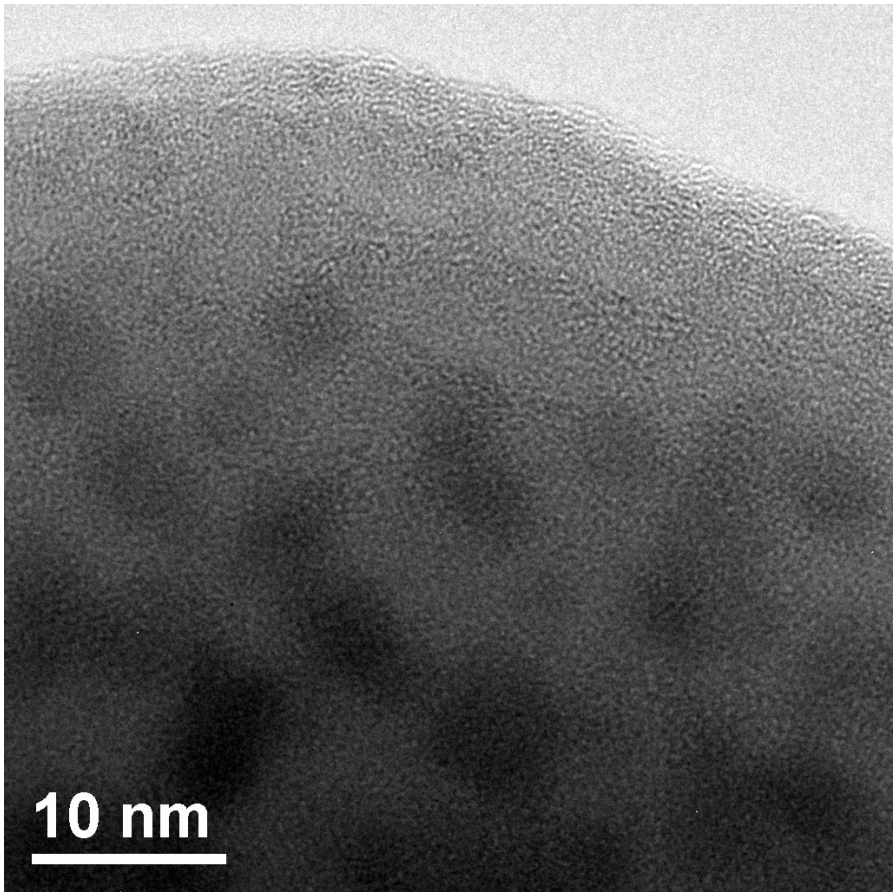

Figure 59. A high resolution TEM image of Nd^{+3} doped LG-760 nanoparticles collected by direct impaction onto a TEM grid.

Inhomogeneous materials shift the absorption and emission spectra of their optically active dopant species on a site-by-site basis according to subtle variations in the local environment. Effectively, every ion sees a different potential and therefore, a continuum of energy levels clustered around the collective average broadens the spectrum. Thus, by changing the wavelength of the pump laser, different subpopulations of ions can be targeted[56]. Unfortunately, in bulk materials the excited atoms can communicate via a process called migration where an exciton can hop from ion to ion by essentially borrowing or expending thermal energy, making it difficult to isolate sub-

populations for study just by tuning the pump wavelength[57]. In nanoparticles the range of exciton mobility is limited to an individual particle, decreasing the amount of cross-relaxation toward the mean ion population distribution when exciting a minority population, hence the shift in Figure 58. It should be stated that as particles grow larger the magnitude of this effect decreases hence the significance of the relatively small size of the particles found in the TEM work.

This TEM session was uniquely challenging since nearly all grids had been severely damaged by the pressure of the supersonic nozzle. Moreover, the small size of the particles collected on dry surfaces when combined with future TEM work from liquid samples, serves as evidence that the impactor was operating near its cutoff when collecting smaller particles, especially when using the splash guard.

Once the validity of the results produced by the Raman spectrometer came into question, a few attempts were made to use the instrument in its intended application. Several Raman studies were undertaken utilizing six different thin film samples, four separate controls and four different configurations of the instrument. All six thin film samples were characterized in the two standard modes of operation using both the 514 and 785 nm instrument configurations. Care was taken to verify reproducibility of these baseline spectra. Figure 60 shows a representative sample of the data obtained. Some spectra depending on the sample had different slopes, but all had the same feature of a sharp knee around 225 corresponding to the tail of the filters used to block the pump light, followed by a smooth line into the 500 cm^{-1} region.

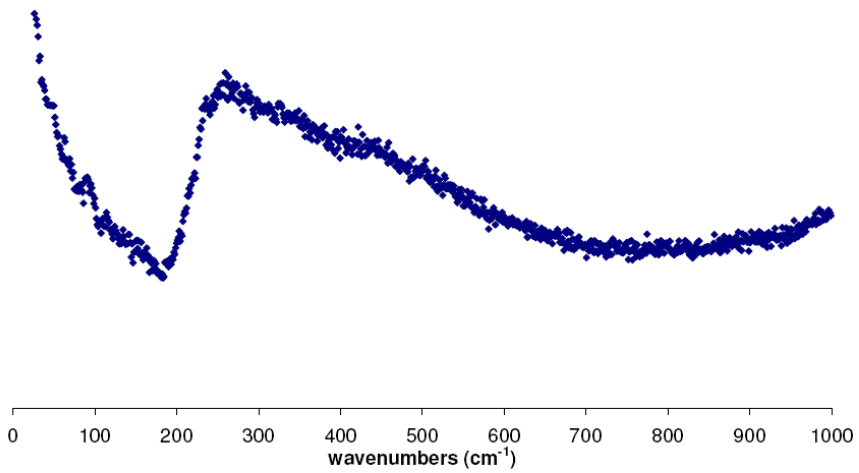

Figure 60. The Raman spectra from a Nd^{+3} nanoparticle film.

Once the samples had been well characterized, nonanoic acid was applied to the films and allowed to evaporate at 30°-40° C. Raman spectra were then taken and compared to the existing baseline scans. Next, the same procedure was conducted on the cover slips used as collection substrates for the nanoparticles. The cover slips were then coated with nonanoic acid and heated at 30°-40° C until the liquid evaporated. The Raman spectra from these surfaces were then compared to the spectra from the nonanoic acid treated nanoparticles in Figure 61. The difference between the spectra is stark. There is clearly a shift in the nonanoic acid-coated surface in the spectral region associated with P-O-C torsion[54]. Though not precisely in the proper position for the direct assignment of the peaks to the published lines, the exotic nature of the surface could perturb the resonance through a number of reasonable mechanisms, such as impurities or strained bonds. There are several lines in trimethyl phosphate and trimethyl phosphite corresponding to both symmetric and antisymmetric bending modes (including an antisymetric bending mode at 239 for phosphate and 225 and 280 in phosphite and a symmetric mode at 367 in phosphate and 370 in phosphite). The figure shows peaks at 250, 290 and 309.

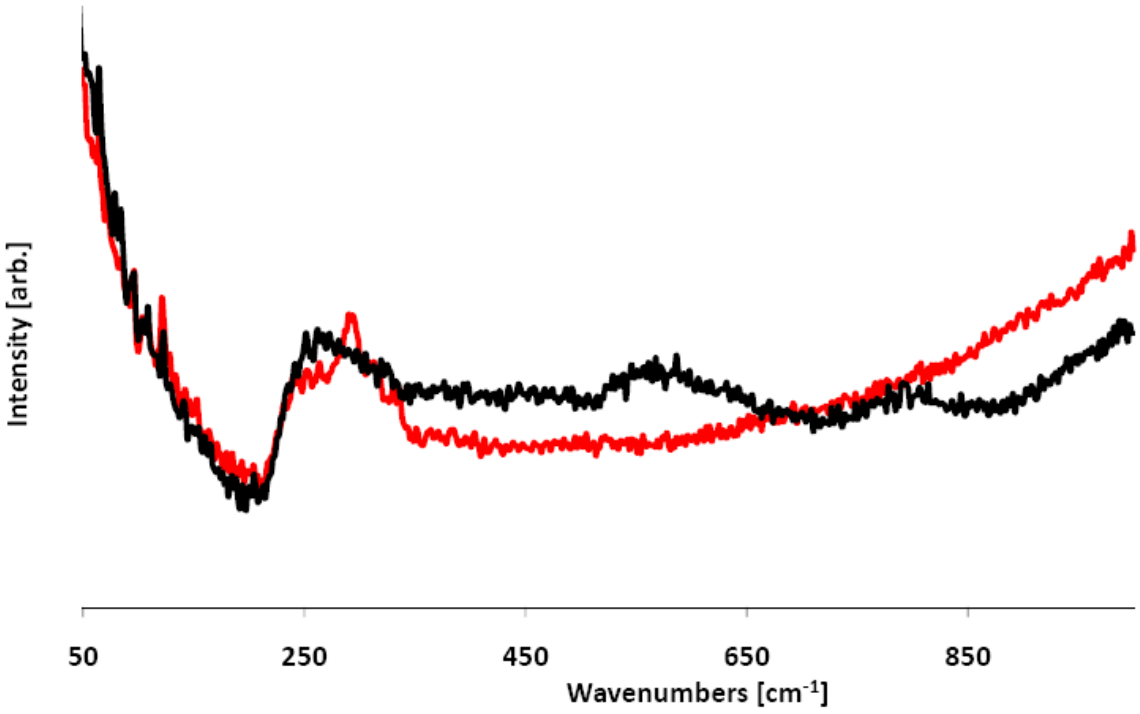

Figure 61. The Raman spectrum from a Nd^{+3} doped LG-760 nanoparticle film coated with nonanoic acid (blue). The Raman spectrum from a blank fused silica coverslip coated in nonanoic acid (pink).

Though the correct assignment of the peaks is questionable, their presence in only the nonanoic acid treated nanoparticles suggests some reaction has taken place. The kinetics of an acid base reaction have been investigated for several different phosphate glass compositions by Bunker et al[18]. Using a back of the envelope calculation to estimate the reaction rates for nonanoic acid and the nanoparticles, it appears that sufficient energy is present at room temperature to allow the carboxylic head to react with a non-bridging oxygen at the surface of the bulk glass and presumably the nanoparticles as well.

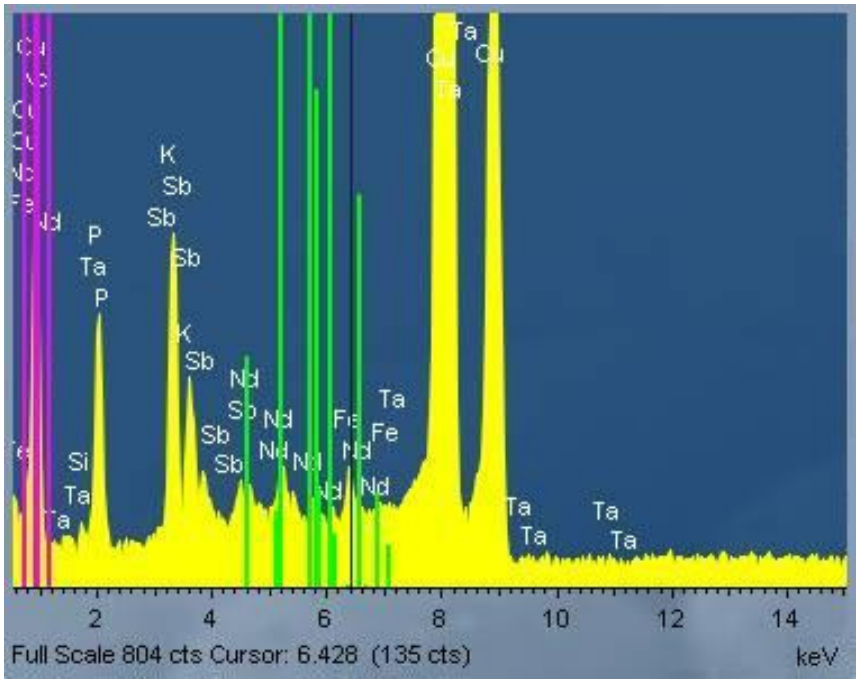

Figure 62. The X-ray spectrum of Nd^{+3} doped LG-760 nanoparticles collected via direct impaction onto a TEM grid.

In the presence of water the reaction should be reversible, but in non-aqueous environments it should probably last long enough to allow the nonanoic acid to successfully coat the surface of the particle, providing a steric barrier around the nanoparticle preventing agglomeration. Over time a small quantity of water will be produced as a reaction byproduct. This water combined with the acidic nature of the nonanoic acid could begin to leach out the stabilizing impurity salts from the glass matrix disrupting the structure of the material. Bunker et al. report that potassium phosphate glass is susceptible to this type of reaction[18]. X-ray fluorescence spectroscopy taken during the TEM session that produced Figure 62 confirms that the nanoparticles contain a significant percentage of potassium.

There are two reaction mechanisms presented in Bunker that could account for the Raman spectra presented above, and the fact that over long periods of time the brightness of the nanoparticles diminishes. These are the hydrolysis reaction model and the hydration model. Bunker et al. state[18]:

> Using the simple hydration model, it is possible to explain why glass dissolution is accelerated in an acidic solution. In acids, phosphate chains are protonated, which disrupts ionic cross links between chains. Water can then penetrate the glass faster leading to rapid chain hydration and uniform dissolution.

This mechanism explains the result of several titration experiments where the average ratio of protons consumed to phosphates detected in solution is approximately one in twenty[18]. Furthermore, the reaction rate for the hydrolysis model is about 10 times too slow to account for the measured dissolution rate.

However, in the case of nonanoic acid, its hydrophobic alkyl chain significantly limits the quantity of water present in solution, making hydration an unlikely process in this environment. Depriving the system of significant quantities of water could allow the slower hydrolysis mechanism to dominate the kinetics. For example, it has been demonstrated that hydrogen terminated phosphate polymers possess more chemical stability than unprotonated oxygen terminated chains[17]. The hypothesized reason for this is inter-chain hydrogen bonding, which "…would result in longer effective chain lengths…"[18]. Unsurprisingly, protonation of the surface increases in acidic environments. But in the presence of water the protonated end chain is exactly the condition leading to the slower hydrolysis reaction and an increased susceptibility to the hydration process.

Assuming the nanoparticle already has a hydrogenated end chain surface site due to the presence of ambient hydrogen or water in the chamber during fabrication, it is possible to propose an alternative to the hydrolysis reaction by replacing the water as the

reagent with nonanoic acid. Instead of introducing a water molecule to break the inter-chain bond in the glass network, a carboxylic group could donate its hydrogen to the phosphate glass, allowing it to release a molecule of water and then substitute its single bonded oxygen into the matrix forming a C-O-P chain leaving the double bonded oxygen to associate with any nearby protons on neighboring sites. This process would free a water molecule to hydrate the glass beginning another cycle of hydrolysis or reverse the reaction depending on the equilibrium constant. Such a mechanism enhanced by the nanoparticle's surface potential could eventually lead to quenched fluorescence by effectively hydrating the particle's interior over time. This could explain the slow degradation of the fluorescence signal from the colloids despite still being able to detect the presence of particles via absorption and in TEM studies.

7.10 Results From Experiments Six and Seven

Once the plausibility of the formation of C-O-P bonds was established, a series of experiments collecting nanoparticles in nonanoic acid was performed in parallel with attempts to increase the performance of the aerosol feed (which was discussed in Chapter Four). The nonanoic acid collection trials failed to produce detectable quantities of nanoparticles using the THOR laser system as the excitation source. However, TEM work on the samples produced the first quantifiable results for nanoparticles from this material. Samples were prepared by dipping grids into a settled solution, placing them on a microscope cover slip and then evaporating the excess on a hotplate before storing them in vacuum.

The sample preparation procedure required many attempts to produce a few useful grids, since the surface tension of the nonanoic acid tended to produce large droplets which would spread onto the glass substrate making it difficult to quantify the

meniscus height, and therefore estimate the final volume and hence density of nanoparticles from an image. The meniscus height on the successfully dipped grids could only be estimated by examining them from the edge and comparing them to available objects. It was found that the meniscus thickness was on the order of the width of a human hair in the range of 40-100 μm. Expanding this out to 10-150 μm sets absolute upper and lower bounds on the volume of fluid sampled in any TEM image of that grid.

To facilitate automated counting and size measurement, efforts were made to achieve high contrast images, if at slightly lower resolution. As a result, the particles imaged at lower magnification tended to appear on average 10-20% larger than those imaged at high magnification. However, any error this introduces into a concentration measurement is small compared to the order of magnitude window set by the rough estimate of the meniscus. A computer program was written to count the particles and report their diameters based upon the assumption that they were perfect spheres. In Figure 63 a TEM image shows a high density field of nanoparticles with few contaminants. Other areas of the grid had similar particle densities but counting was impaired by the presence of other detritus. An image of the same field at higher magnification reveals the size difference in the particles due to the tradeoff between contrast and resolution (Figure 64). In the high magnification image the particles don't fully saturate the CCD producing a better measure of their size, whereas in the low magnification image most particles fully saturate the detector. Finally, a third image is added to demonstrate the nature of the detritus marring the field of view in certain areas of the grid (Figure 65). Though contaminated, this characteristic image still demonstrates a relatively high density of particles.

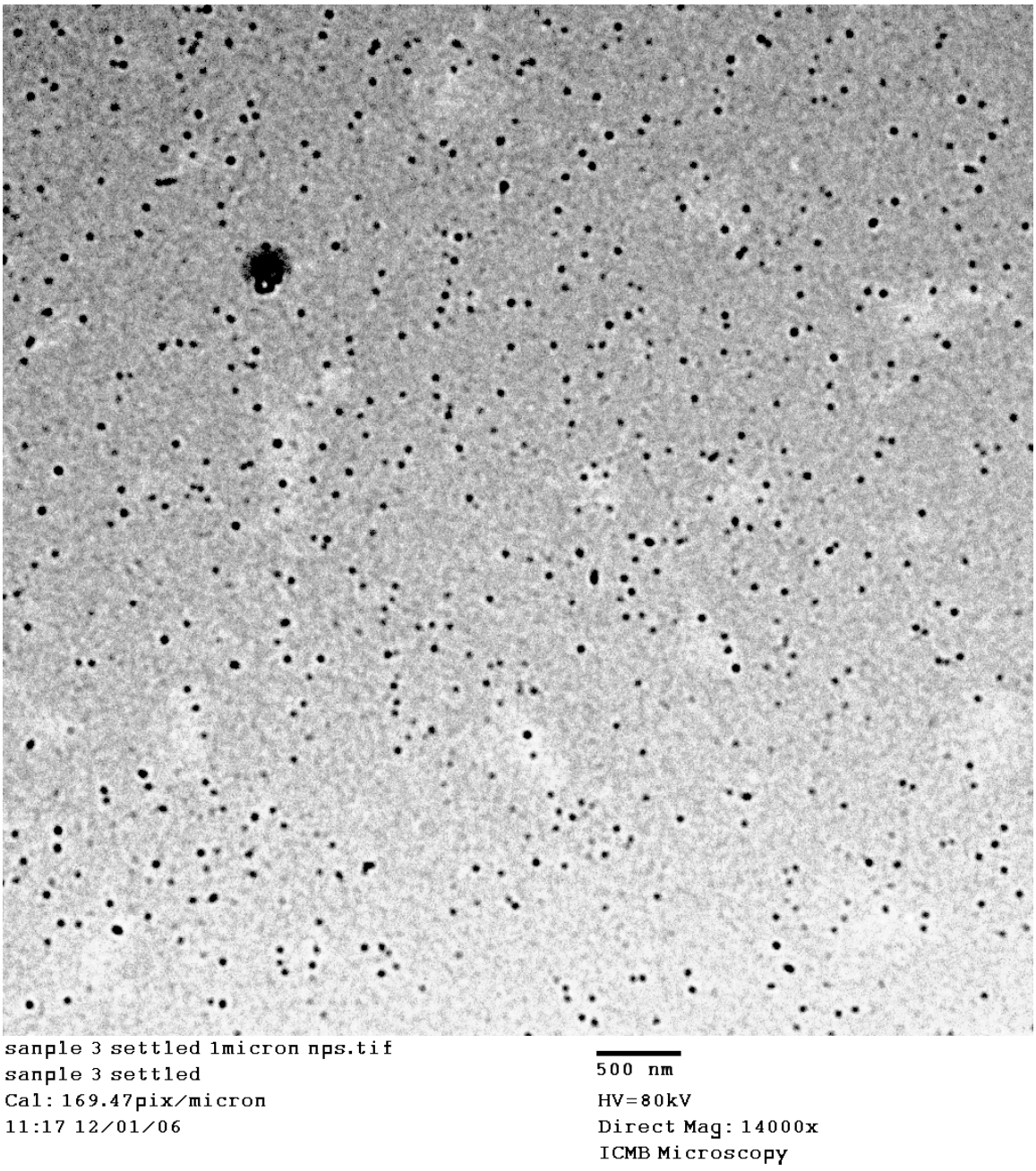

Figure 63. A TEM image of Nd^{+3} doped LG-760 nanoparticles collected and stabilized in nonanoic acid.

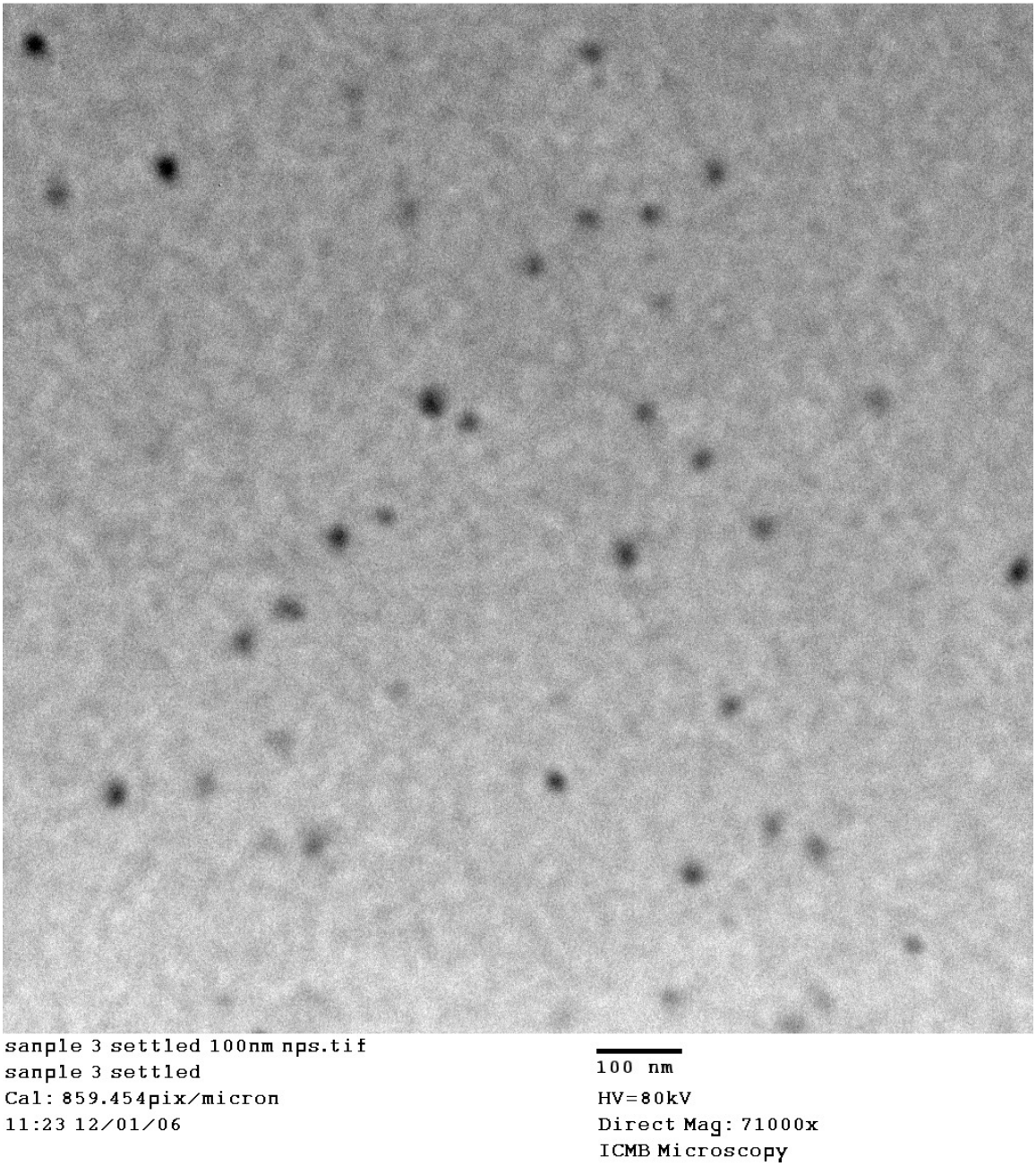

Figure 64. A view of the particles from the previous figure at higher magnification.

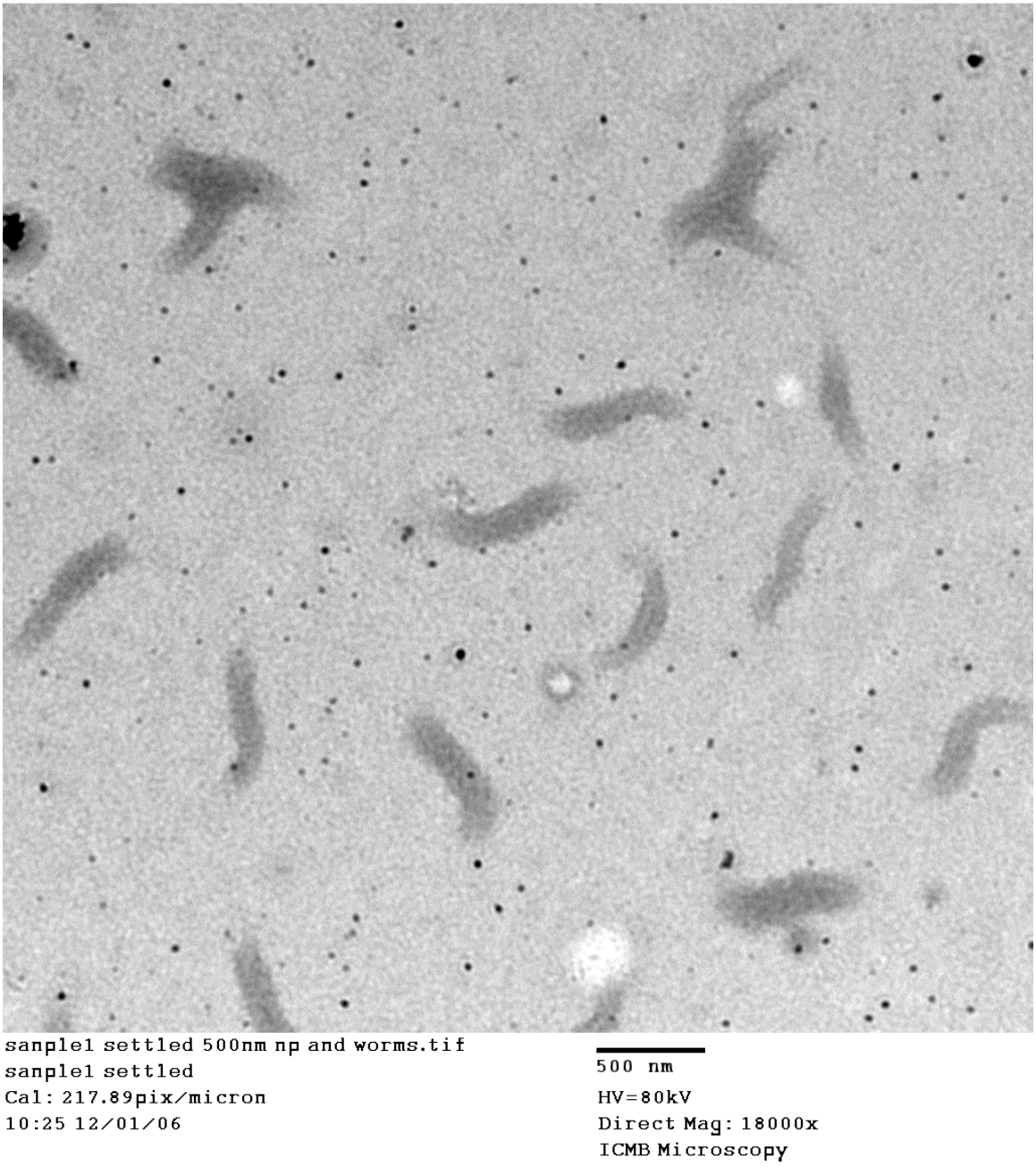

Figure 65. A TEM image of Nd^{+3} doped LG-760 nanoparticles and various contaminants collected and stabilized in nonanoic acid.

Comparing these images to those from the solid collection experiments (for example Figure 59) reveals a significant increase in particle size. This is likely due to both the impactor conditions and health of the laser at the time these samples were made. During the majority of this collection the laser operated in the 190-210 mJ range which could result in less energetic particle explosion and formation. Also using the splash guard and therefore increasing the pressure of the impactor by a factor of two would increase the minimum radius of the particles collected. This could in principle account for the particle radius of 5 nm in figure 59 growing to 18 nm in figure 64.

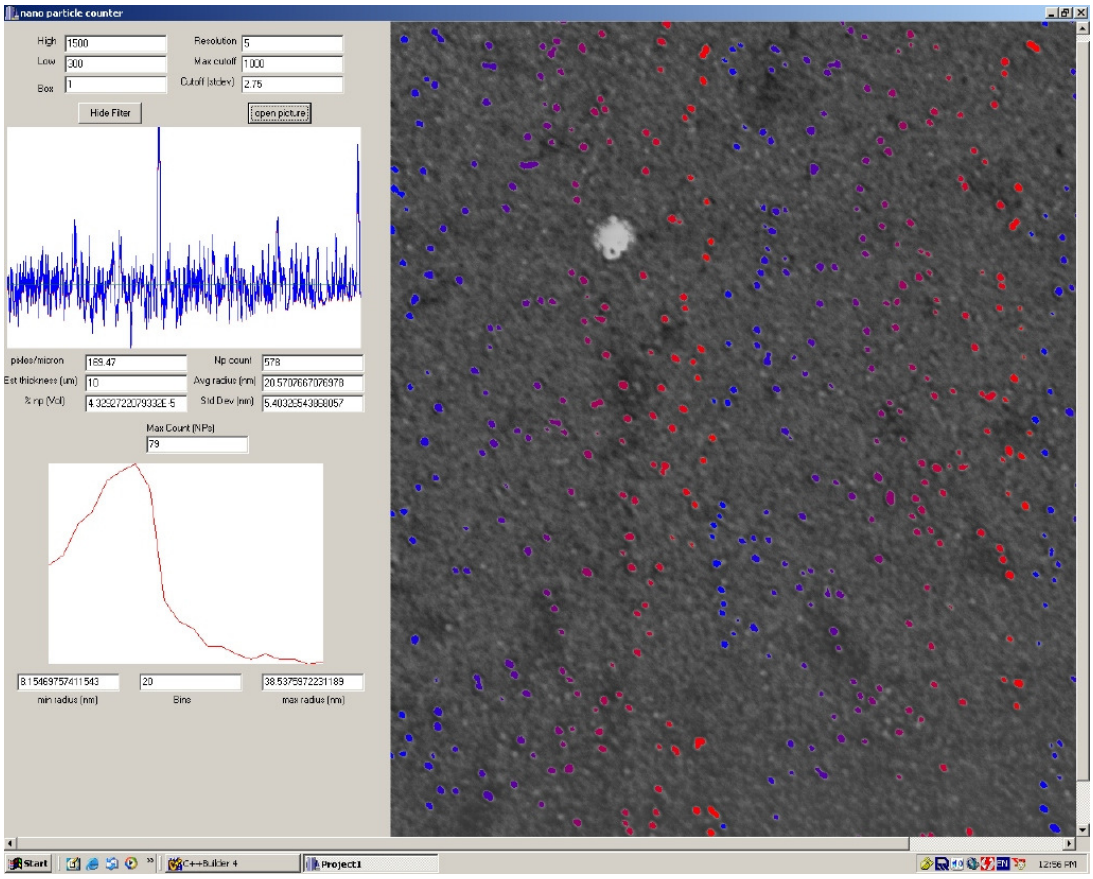

Figure 66. A screenshot of the computer program written to count the nanoparticles shown in the images above.

A screen shot from the program written to count the particles is reproduced in Figure 66. It should be noted that the average radius reported by the program does not correspond to the position of the peak in the histogram below. This program also does not distinguish between single particles and agglomerates. It counts the agglomerates as single particles which upon careful inspection of the program and image accounts for the peaks in the tail of the distribution at ~50 nm, ~65 nm, and 70 nm in Figure 67. This was possible to determine since the program, when running in debug mode allows the user to reference the particles in a specific area of the distribution graph to the particles highlighted in the image. This feature could have been integrated into the GUI with additional work but was not pursued further since its purpose had already been served.

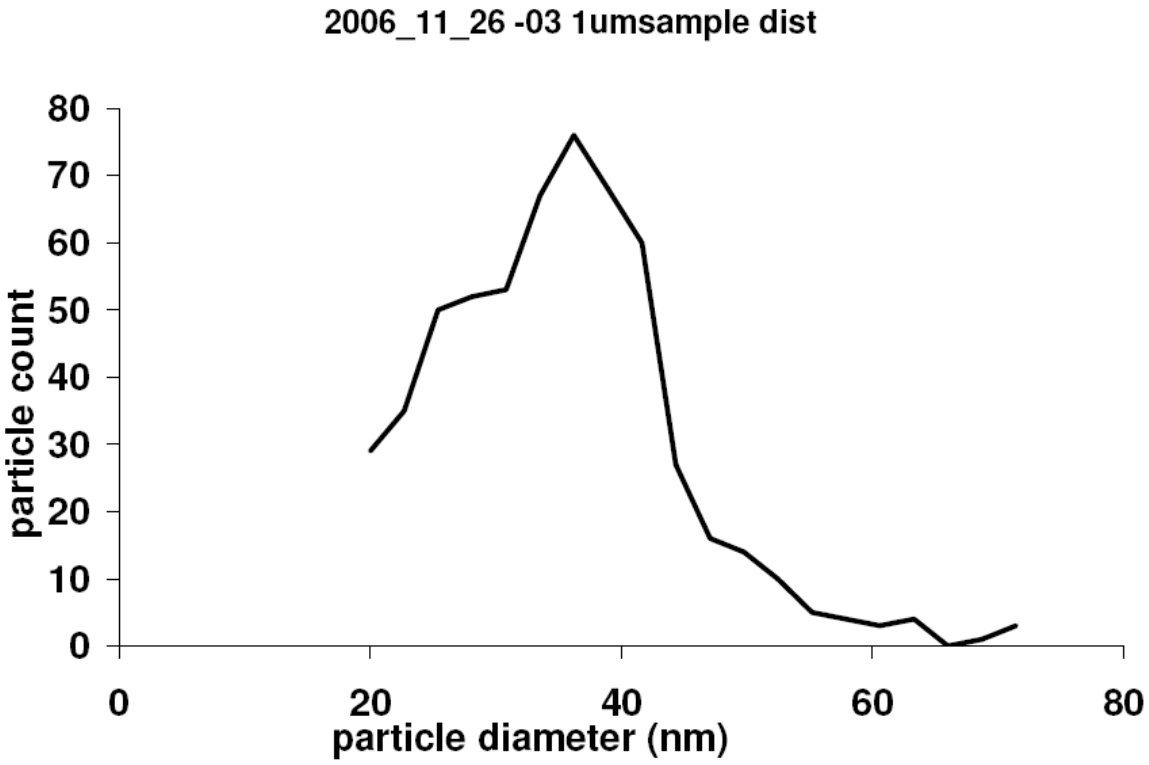

Figure 67. A histogram generated by the computer program written to count the nanoparticles in the TEM images shown above.

From these images it is possible to estimate the nanoparticle concentration in the sample. The concentration reported by the program of ~$4x10^{-5}$ % nanoparticles by volume corresponds to a combined nanoparticle production and collection rate of between ~.002 mg/hr and ~.02 mg/hr. Multiplying this rate by the expected increase in production of 100 due to the new chamber design, yields between 0.2mg/hr and 2 mg/hr. Ultimately when the new system was characterized, production rates were found to vary between 0.2 mg/hr and 1.2 mg/hr.

Spectroscopic measurements of these early samples were also conducted. The absorption data demonstrates a significant difference between the colloidal nanoparticles and micro-particles in the UV-Vis region. To collect these spectra, first a baseline absorption spectrum was collected for the nanoparticles revealing a flat response. The nanoparticle colloid was then placed in a Rotovap and heated to nearly 100 °C at ~200 mT. Over the period of an hour the sample's volume was reduced from 20 ml to 1.5 ml and the absorption measurement repeated. This measurement was then compared to a series of micro-particle controls. Micro-particles used in the ablation process were placed into a spectroscopic cuvette with nonanoic acid and agitated. The absorption spectrum of this sample was flat. After a few minutes had elapsed the spectra was again taken revealing a flat response. Next the micro-particle emulsion was placed in the Rotovap for approximately an hour and the volume reduced from 20 ml to 1.5 ml before repeating the absorption measurement.

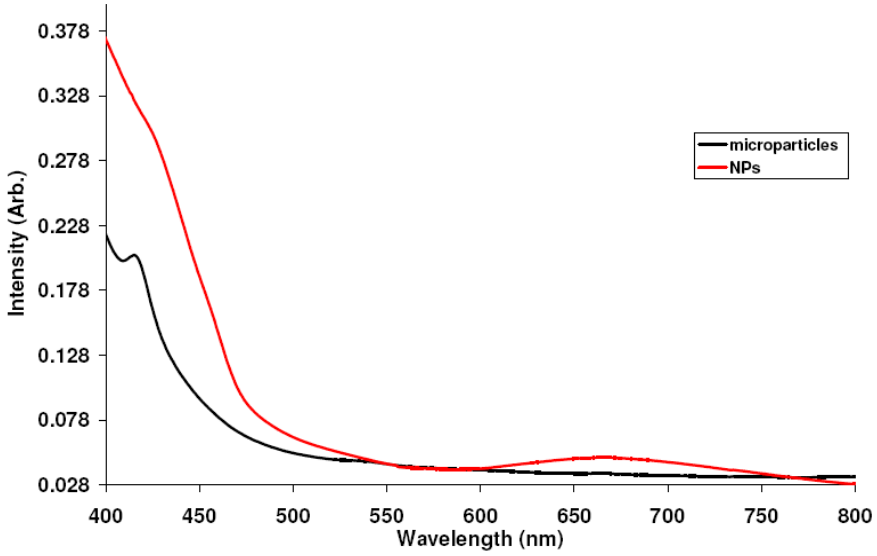

Figure 68. The absorption spectrum of Nd^{+3} doped LG-760 nanoparticles suspended in nonanoic acid (red). The absorption spectrum of Nd^{+3} doped LG-760 micro-particles suspended in nonanoic acid (black).

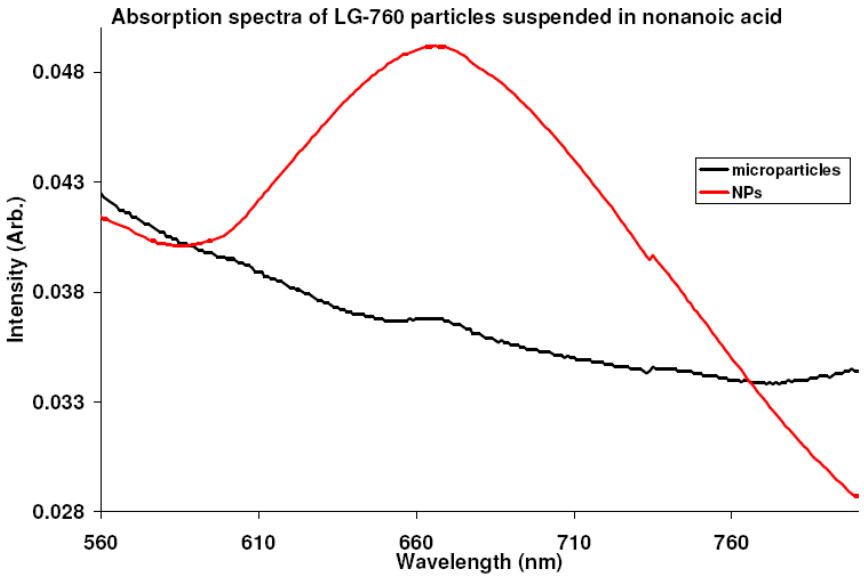

Figure 69. The absorption spectrum of Nd^{+3} doped LG-760 nanoparticles suspended in nonanoic acid (red). The absorption spectrum of Nd^{+3} doped LG-760 micro-particles suspended in nonanoic acid (black).

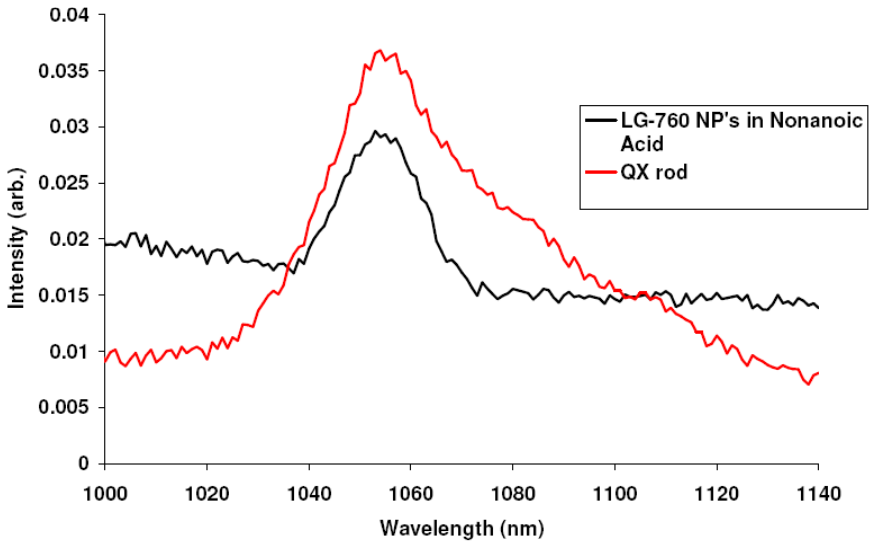

Figure 70. Fluorescence from Nd^{+3} doped nanoparticles in suspended in nonanoic acid excited at 660 nm (black). Fluorescence from Kigre LG-760 bulk glass.

As the plots in Figures 68 and 69 demonstrate, a change in the solution's absorption was produced by heating the micro-particles. This could be due to the fact that some of the smallest particles present in the emulsion were stabilized by the process and allowed to remain in suspension. It could also mean that the Nd^{+3} ions had somehow leached into solution. Nevertheless, there still existed a distinct difference between the micro-particle spectra and the nanoparticle spectra, which can't be accounted for by the leaching explanation. The peak at 430 nm in the micro-particle sample is significantly narrower than the peak in the nanoparticle sample. This peak is an expected feature of the bulk glass well documented in the literature, so perhaps the spectra is a combination of leached ions and bulk glass powder in emulsion. Thus if a leaching hypothesis were the correct interpretation, the nanoparticle and micro-particle spectra should resemble each other with the micro-particle spectra still retaining characteristics of the bulk glass.

However, though the two spectra are well matched in terms of approximate absorption in the blue region, in the 600 nm region they sharply diverge, contradicting the notion that the micro-particle spectra should be the spectra to possess features not present in the nanoparticles. The persistence of nanoparticles in suspension for weeks to months, as verified by TEM measurements using the grid dip and evaporation method, also does not support the leaching hypothesis. However, the significant degradation of fluorescence signal over a similar period of time supports the conclusion that, after being stabilized by the nonanoic acid, they continue to react in some manner. Finally, examining the fluorescence spectra from the nanoparticle emulsion sample reveals good qualitative agreement with the expected fluorescence from bulk glass. The conclusion that can be drawn by comparing these spectra is that something is fundamentally different about the behavior of the nanoparticle emulsion as compared to a micro-particle emulsion in the visible but not in the near IR (Figure 70).

A second sample was prepared using the same method and a more extensive fluorescence study conducted, including an attempted lifetime measurement using THOR in pulsed operation. The idea was to excite the sample using the beam after the regen amplifier and measure the fluorescence decay. Though detectable in the fluorometer given sufficient integration time, the signal was not detectable using THOR as a pump source. Fluorescence studies on the sample conducted both before and after the attempted lifetime measurement revealed the expected spectra. The inability of the THOR pulsed lifetime measurement to detect any fluorescence signal was not surprising given the low concentrations of particles produced and the sensitivity of the detectors available.

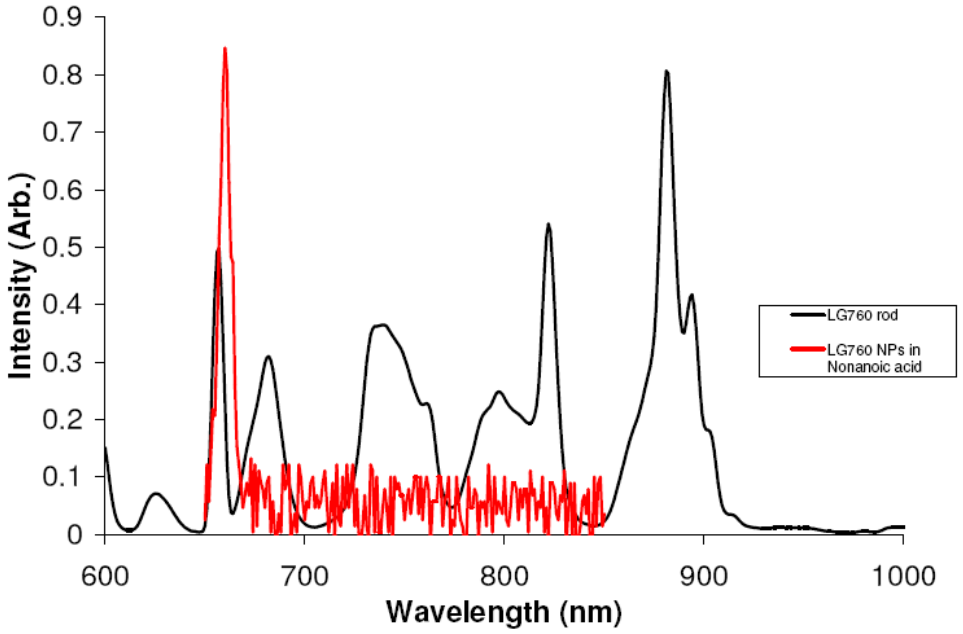

Figure 71. Excitation spectra of 1054 nm line for Nd^{+3} doped LG-760 bulk laser glass (black) LG-760 nanoparticles (red).

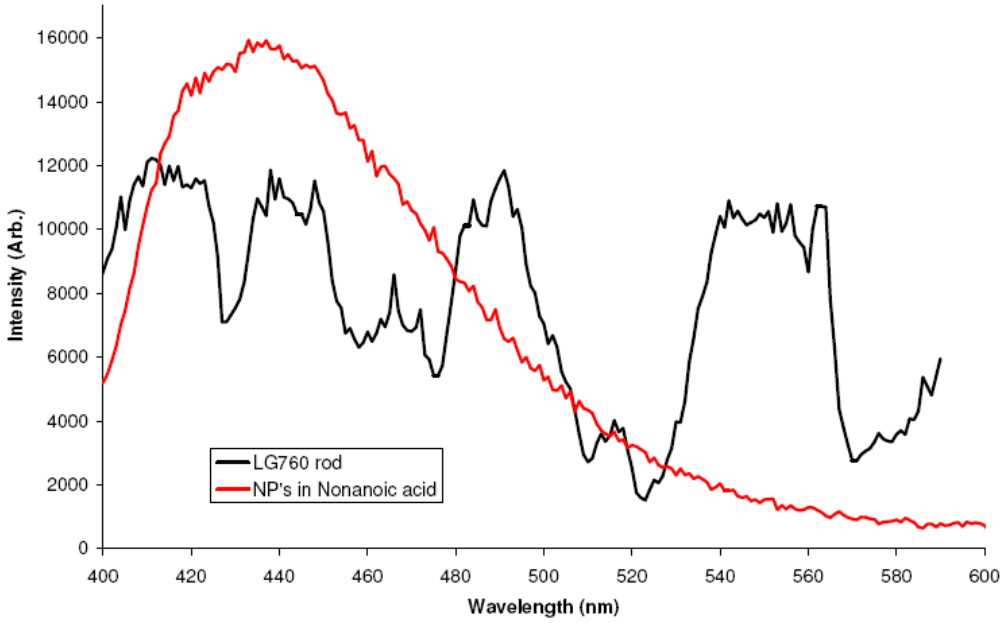

Figure 72. Excitation spectra of 800 nm line for Nd^{+3} doped LG-760 bulk laser glass (black) LG-760 nanoparticles (red).

Figure 71 shows a strong signal in the blue region of the spectra. The excitation spectra in Figure 72 show a departure from the expected response in the visible regions for both the 1050 nm transition and the 800 nm transition. The 800 nm transition was chosen instead of the 880 since fluorescence of the 880 nm transition was difficult to resolve. It is also interesting that the 1050 transition was only detected when exciting in the nanoparticle sample at approximately 380 nm, 670 nm and 800 nm.

TEM work on this second sample reveals similar images to those in Figure 63 verifying the reproducibility of the dipping technique. The sample's estimated density fell within the estimate obtained during the previous TEM study. Though efforts were made to produce a grid with a decently controlled meniscus it should be noted that excess nonanoic acid residue was found around the periphery of the grid after the evaporation process was complete, lowering the estimated density of the particles. The yield of useful grids from this sample was also depressed due to oxidation of the copper in the grids. This oxidation could probably be attributed to elevated ambient humidity and was observed during subsequent TEM sample preparation. Another interesting result of this run was the relatively small size of the nanoparticles collected (Figure 73). The decreased particle size indicates the impactor was probably running a bit farther away during collection, and highlights the difficulty of controlling the impactor distance in the original chamber.

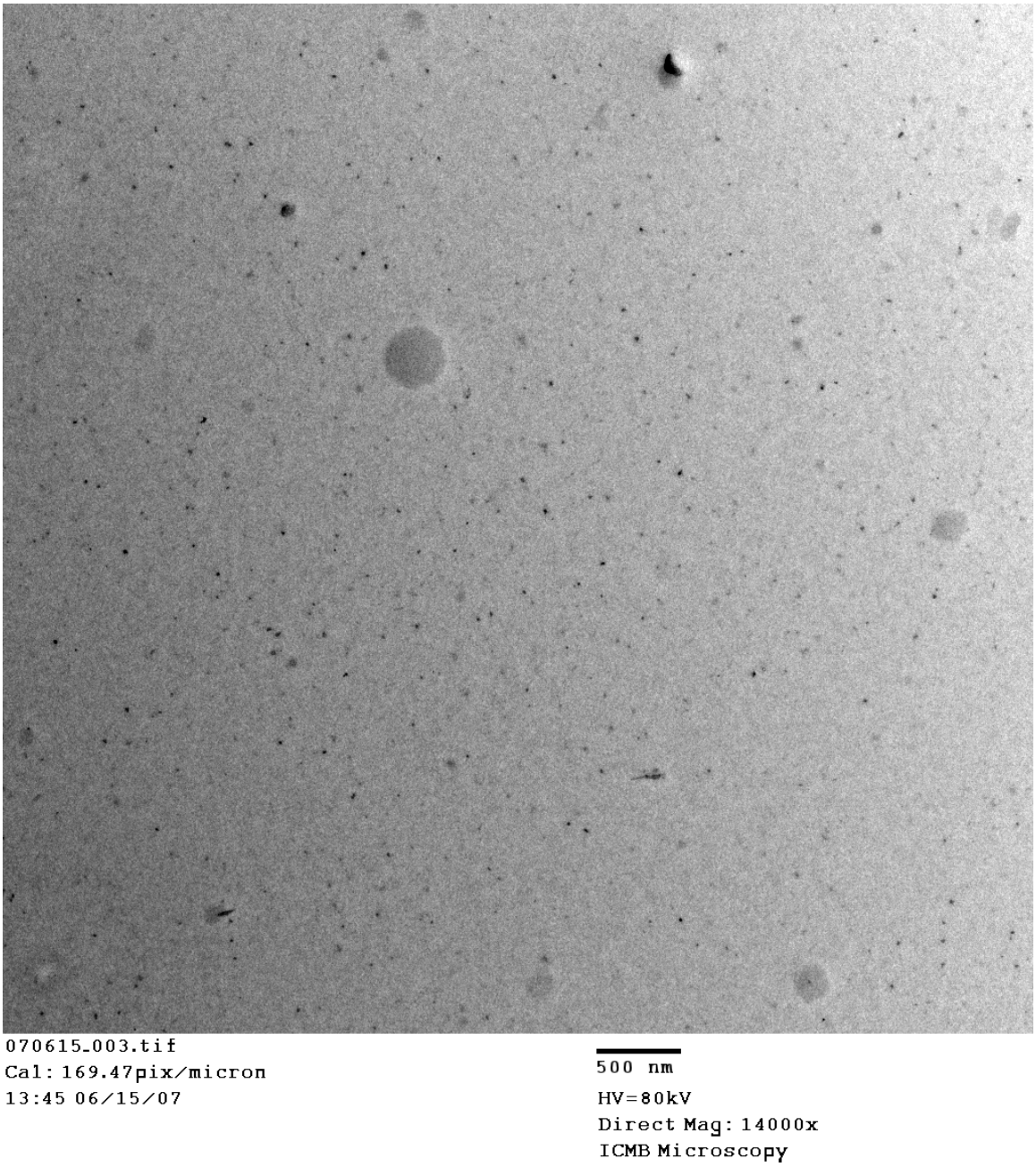

Figure 73. Nd^{+3} doped LG-760 nanoparticles suspended in nonanoic acid.

7.11 RESULTS FROM EXPERIMENTS EIGHT AND NINE

Once the new chamber was online its performance was characterized and compared to its design. Good agreement was found between the measured pressure in the impactor region with a (KJL300801) Kurt J. Lesker convectron gauge. Using the 250 μm nozzle, and a gas flow rate of 2200 sccm, the measured pressure when the chamber was first installed was 127 mT when operating with nitrogen. The predicted pressure was approximately 120 mT. Operating with helium under the same conditions, the measured pressure was 256 mT, while the predicted value was 248 mT.

Operating under the conditions described above, a series of TEM samples were collected via direct impaction. These samples showed dramatic improvements in density and size over previous attempts at dry impaction. As previously mentioned, fused silica micro-spheres in the original chamber attained excellent feeding rates with a bright ablation plume, but a relatively limited number of particles were actually observed on the grids. The relatively high chamber pressure and small nozzle diameter made it likely that a small misalignment of the nozzle (approximately 1 mm) could move the chamber from efficient operation to the region of deceleration near the mach disk. The combination of large nozzle diameters, higher conductance and mechanically robust positioning conspire to make the new chamber considerably more forgiving during routine operation.

Figure 74 shows images acquired by collecting nanoparticles in the original chamber made from fused silica spheres under a variety of ablation conditions. Figures 75 through 79 show images produced with the new chamber. Side by side comparison of the images reveals a stark difference in performance. It should be noted that spheres double ablated at 100 mJ and spheres double and single ablated at 215 mJ yielded even more sparsely populated TEM images.

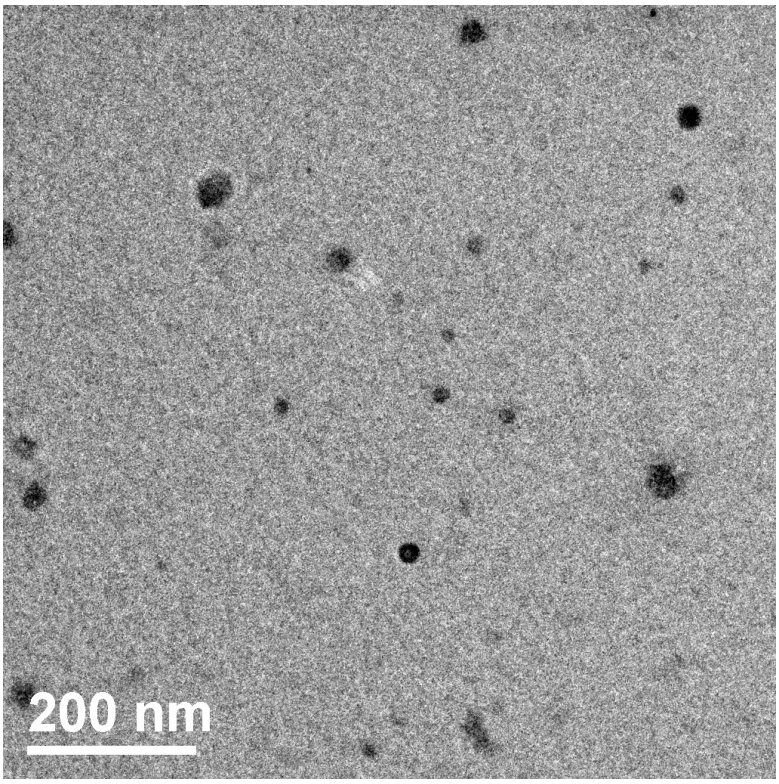

Figure 74. Nanoparticles made from fused silica spheres and collected via direct impaction on a TEM grid in the original chamber.

While it is probable that all runs of the experiment represented in Figure 74 produced inconsistent random results attributable to difficulties relocating the position of the impactor to the sweet spot $0.13 = \eta = 0.3$, it is also likely that the majority of the particles produced at higher energy and under double ablation conditions were too small to make the cut off and therefore impact given the conditions in the chamber. This would not pose as significant a problem for previous experiments on silver since the particles are almost five times as dense and therefore the critical distance to the nozzle is considerably more tolerant. This experiment, however, did produce one very useful result. Spheres appear to ablate at much lower energies than their amorphous counterparts. Thus, given a spherical powder and a laser capable of operating at spec

(400 mJ @ 200Hz) for long durations, the area of ablation could be increased by a factor of two to four. Increasing the flow rate proportionally could also enhance the aerosol density resulting in a nonlinear increase in aerosol density and production rates.

By contrast, the nanoparticles in Figure 75 through Figure 79, show uniform size distribution in the 5-10 nm region vs. 20-50 nm for those collected in the original chamber, which is also consistent with the relatively large average particle size collected in the fluid samples presented above. The incredibly dense collection and the development of a range of new optical diagnostics facilitated the success of the first experiments designed to measure the nanoparticle production rates in near real time.

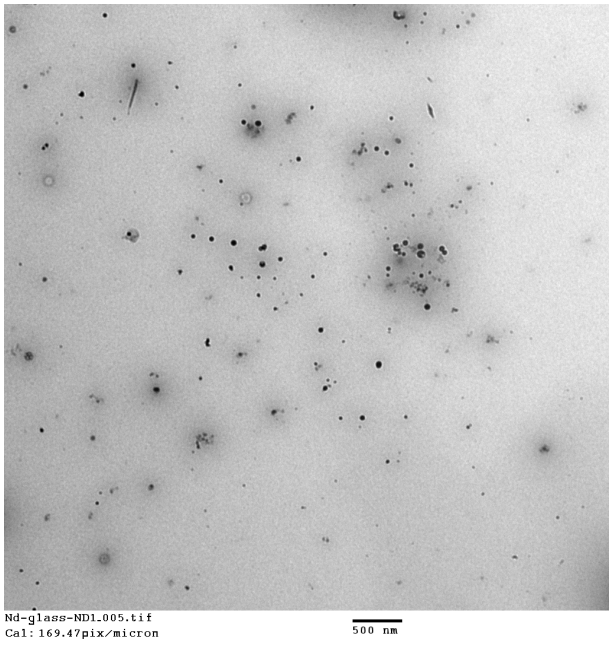

Figure 75. Nanoparticles made from Nd^{+3} doped Q-X glass and collected via direct impaction on a TEM grid in the new chamber.

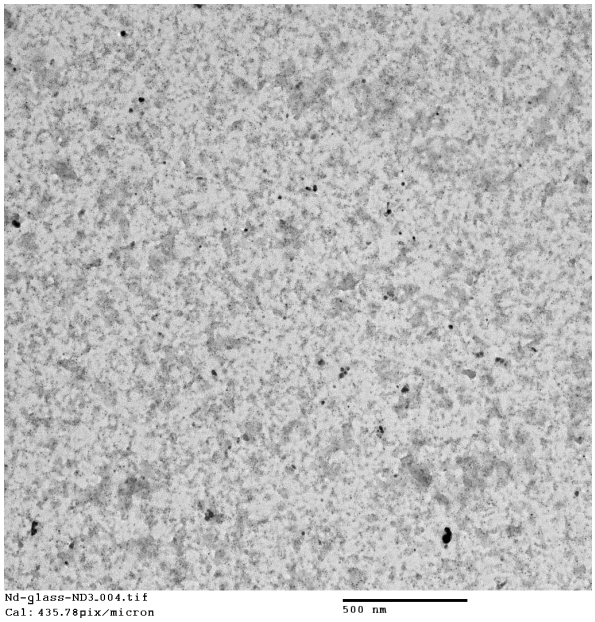

Figure 76. Nanoparticles made from Nd^{+3} doped Q-X glass and collected via direct impaction on a TEM grid in the new chamber.

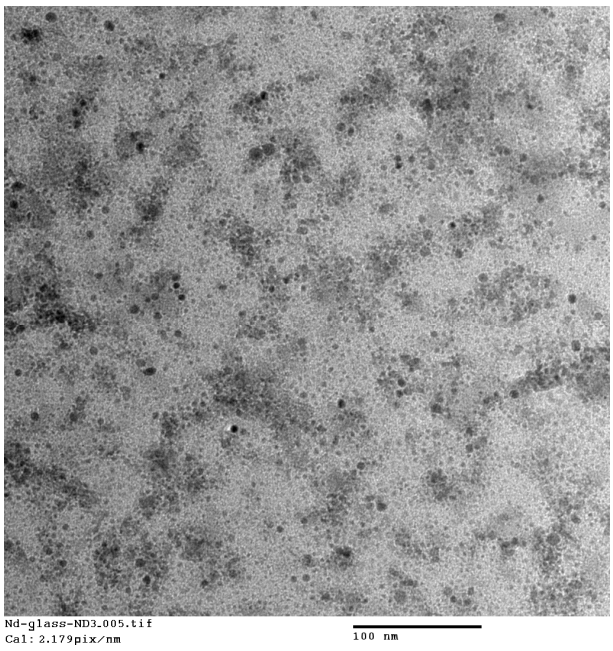

Figure 77. Nanoparticles made from Nd^{+3} doped Q-X glass and collected via direct impaction on a TEM grid in the new chamber.

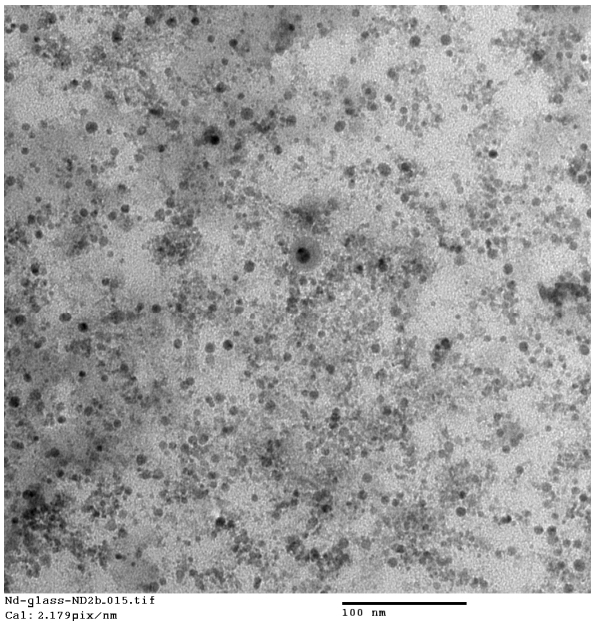

Figure 78. Nanoparticles made from Nd^{+3} doped Q-X glass and collected via direct impaction on a TEM grid in the new chamber.

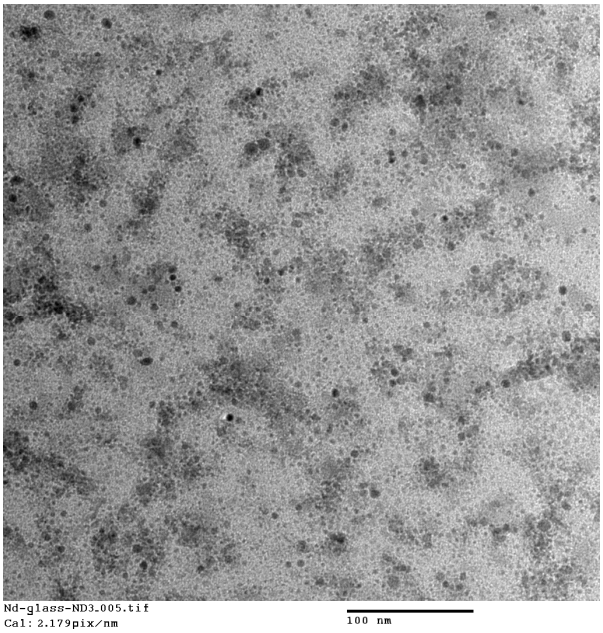

Figure 79. Nanoparticles made from Nd^{+3} doped Q-X glass and collected via direct impaction on a TEM grid in the new chamber.

7.12 RESULTS FROM EXPERIMENTS TEN THROUGH FOURTEEN

A series of three experiments measuring nanoparticle concentration vs. collection time were conducted using 20% Kigre Q-X glass. These measurements used the new collection system with the d = 300 μm nozzle and an impactor height of L/d = 15. Under these conditions the impactor should collect particles larger than approximately 3 nm in diameter. The primary diagnostic used was a transmission measurement through the LWCFC discussed in Chapter 5.

The baseline transmission was measured over several days before collecting particles to establish the characteristics of the fluid handling system and discern any problems with reproducibility. The baseline transmission spectra from the diode laser had some noise in the 2-5% range when the peristaltic pump supplying the fluid flow through the LWCFC was operating. Also during this time the compatibility of various tubing with nonanoic acid was established. The only tubing found to survive sustained operation in the peristaltic pump was Viton (Norprene loses its elasticity and can crack after only a few hours of operation).

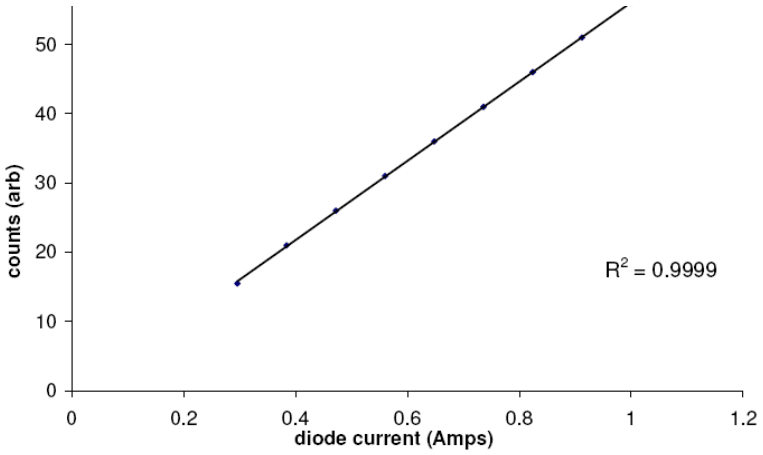

Figure 80. The response of the Ocean Optics spectrometer is linear.

From these efforts it was discovered that the transmission baseline was sensitive to strain in the collection fiber, but relatively insensitive to the diode laser's connection. Therefore, the spectrometer and LWCFC were clamped to the table for the duration of the transmission experiments. The diode laser was also stable from day to day producing repeatable power and spectra as a function of current and diode temperature (Figure 80). The linearity of both the spectrometer and diode laser was verified as a function of current. The rate of wavelength tuning vs. diode laser temperature conformed to the manufacturer's stated specification. Therefore in the event that the diagnostic system was significantly disrupted the most recent baseline measurement could be used as a reference to return the system to the same operating conditions.

Because of the rigidity of the diagnostic and its attachment to the fluid system, only two adjustments proved necessary: making sure the collection fiber cladding had not twisted and that its bend radius minimized the strain. Normally the strain on the fiber would only affect the total magnitude of the signal but if significant torque were applied

to the filter pack the angle of light entering the spectrometer could be affected and distort the spectrum (see Figure 81 hour 0 and hour 5).

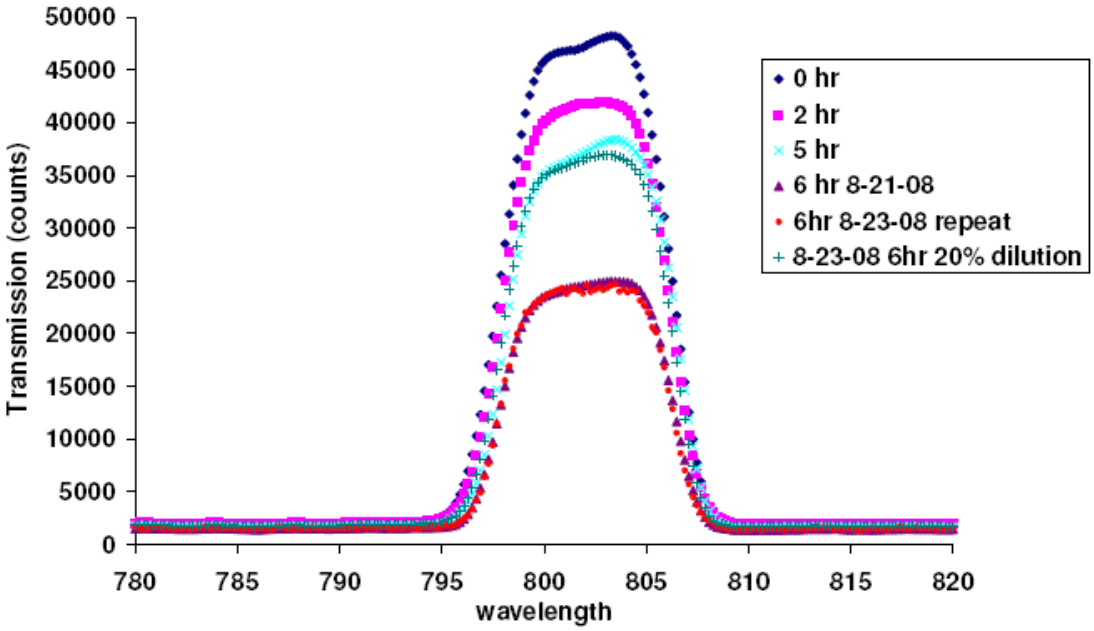

Figure 81. The transmission through a 1 m LWCFC at several times during the production and collection of Nd^{+3} doped Q-X nanoparticles.

Failure to account for these alignment issues had minor effects on the overall measurement. During the process of deploying this experiment the entire system was built and torn down repeatedly without major changes in the performance of the diagnostic. Later, homemade versions of the LWCFC designed to tolerate significantly higher intensities were not as forgiving and required careful handling to maintain alignment.

The typical concentration study provided raw data similar to that displayed in Figure 81. The variable asymmetry in the spectra and the presence of a peak in the 5 hour spectrum is an anomalous result attributable to either the action of the peristaltic

pump or fiber strain. This type of transient feature could be minimized and eliminated with careful attention to the flow in the system and was imperative in later measurements of the fluorescence spectra. The basic procedure for eliminating those features is to adjust the pumping rate and pumping pressure and wait for the system to settle down. If this failed the next step would have been to check for and minimize any strain present in the fiber or torque on the filter assembly. This is a time consuming process and did not affect the results significantly for this measurement and was therefore not performed. After hour 6 this procedure was performed and a spectrum taken. The filters were then changed to permit a fluorescence measurement (Figure 82).

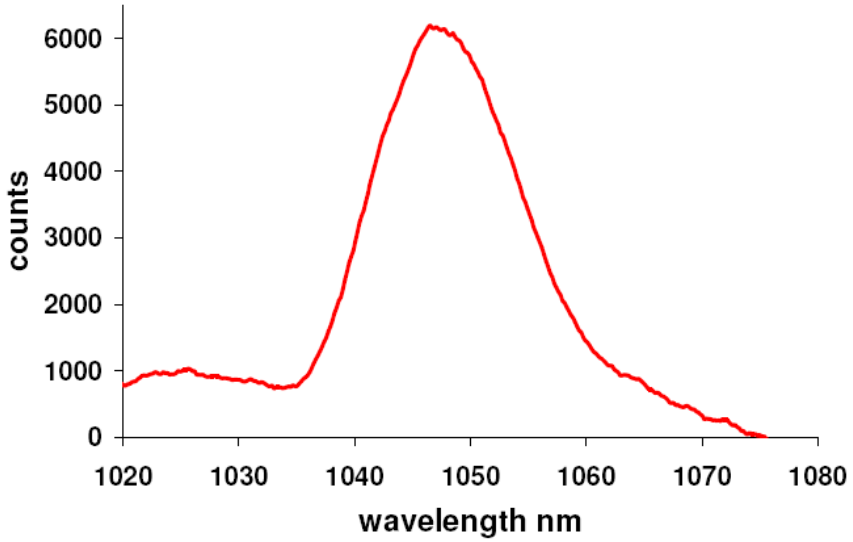

Figure 82. The fluorescence of Nd^{+3} doped Q-X nanoparticles excited by an 800 nm diode laser in a 1 m LWCFC.

The following day the filters were changed allowing the transmission measurement to be repeated. Care was taken to minimize strain and torque and select optimal pumping conditions. The measurement agreed well with the previous day's results. Using the same filters the fluorescence of the bulk material was also measured.

The position of the peak in the case of the nanoparticles is noticeably shifted toward the blue. The 900 nm peak present in the bulk spectra was not well resolved due to the superradiance spectrum of the diode (Figure 83).

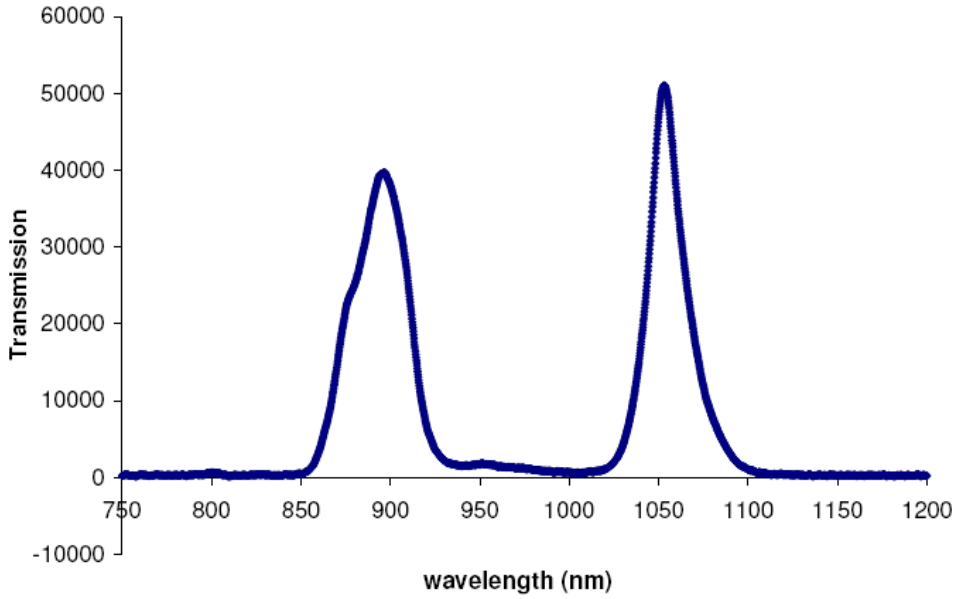

Figure 83. The fluorescence of Nd^{+3} doped Q-X bulk glass excited by an 800 nm diode laser.

With the same filters used to measure the fluorescence, the diode's spectrum was measured (Figure 84). The lines in the 900-1000 nm range are attributed to diode laser superradiance. The superradiance from the diode is akin to ASE present in other lasers. This superradiance occurs at approximately the same intensity as the fluorescence from the nanoparticles. Thus resolving the 900 nm transition in the nanoparticles was not possible. However, a shift of the 910 nm diode superradiance spectrum towards 900 nm was seen in the nanoparticle samples as well as the bulk glass.

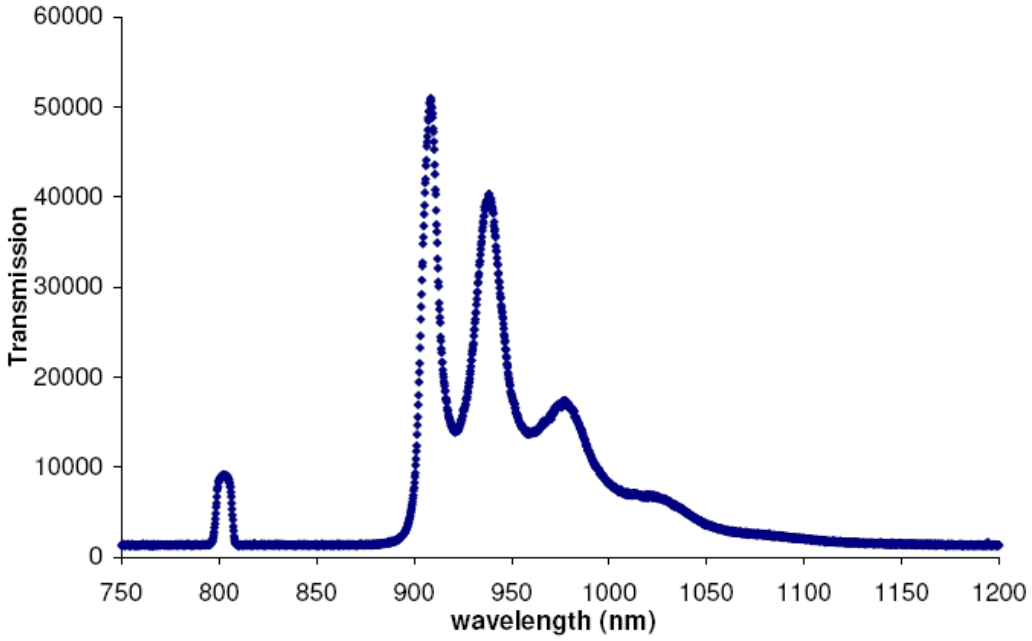

Figure 84. The diode laser spectrum observed through the same filters used to measure the fluorescence spectra.

The experiment measuring the concentration of nanoparticle samples was repeated a few months later and produced similar results. The only major difference was that the excimer laser had been serviced and was now operating at 350-450 mJ. The pressure and other LAM variables remained the same. With the laser functioning properly, gains in the maximum production rate were seen. However, the problems with powder feeding still resulted in significant hour to hour variation in the production. The variation in production rate can be seen in Figure 85 and Figure 86. In the first two hours of production on 2_24_09, no nanoparticles were detected in solution. Using the instrument's 2-5% noise limit as a reference, in the following two hours at least five times as much production was achieved. Similar difficulties were noticed between hours 4.5 and 5.5 in Figure 86.

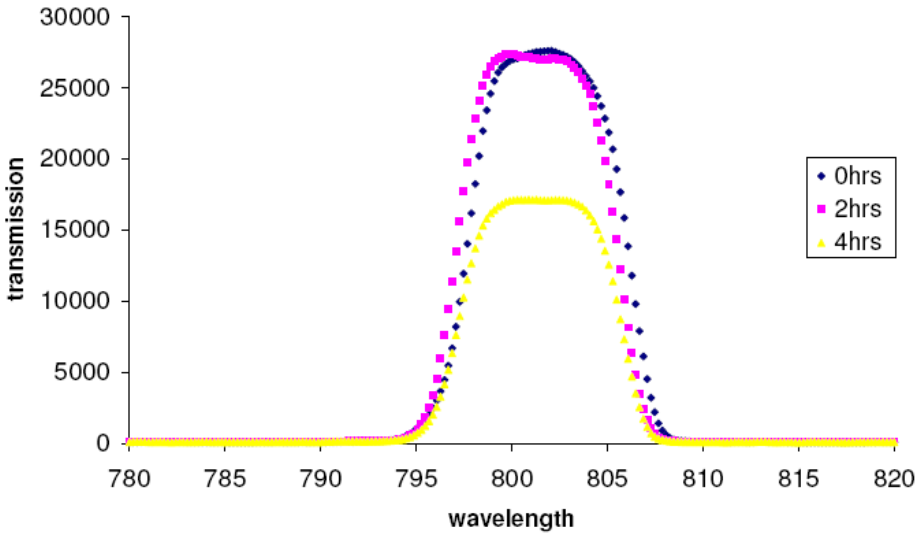

Figure 85. The transmission through a 1 m LWCFC at several times during the production and collection of Nd^{+3} doped Q-X nanoparticles.

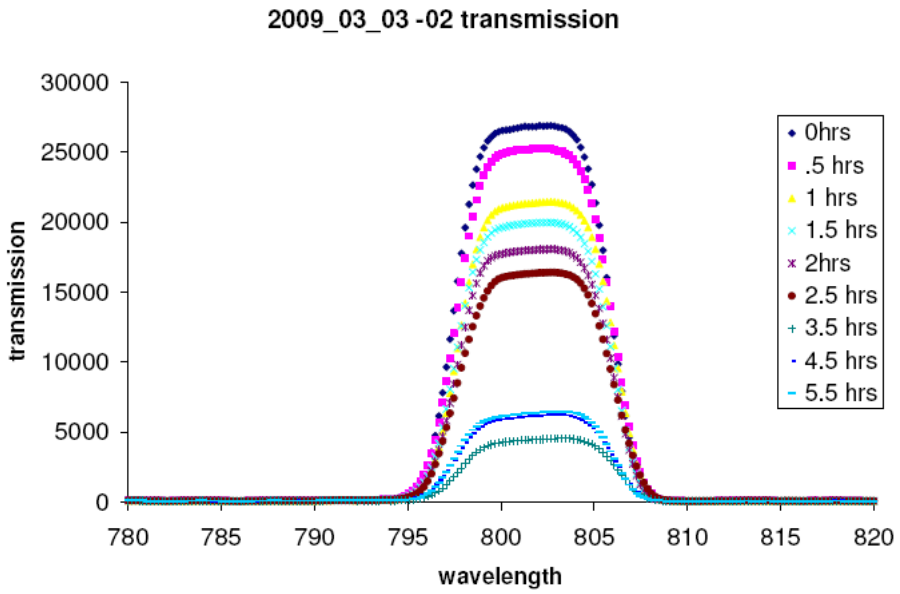

Figure 86. The transmission through a 1 m LWCFC at several times during the production and collection of Nd^{+3} doped Q-X nanoparticles.

The haphazard production rate is exacerbated by splattering. During the first four hours approximately 5 ml was lost due to splatter. The splattering is most likely to occur when the peristaltic pump or vacuum pump is cycled on and off to fix various problems that arise with the LAM reactor. This can include refilling the powder feeder or needing to change the location on the elastomer tube that the peristaltic pump clamps onto. Other difficulties that can arise include small air leaks which can cause significant sample loss and clogged nozzles. Leaks are a common problem since there are several transitions between different materials including glass, steel, plastic, Teflon, and elastomer. The least robust connections are those between the elastomer tube and glass. Leaks at this point can suddenly occur due to the mechanical stress and vibration caused by the constant pulsation of the elastomer tube as the peristaltic pump turns. Usually these problems can be addressed with minor intervention but several times during the course of a run the entire system must be shut down in order to address a problem. When this occurs gas has an opportunity to dissolve into the nonanoic acid and bubbles can enter the fluid lines. This poses a risk of splatter and sample loss. During the course of a 5-8 hour run it is often necessary to add some additional surfactant to the reservoir to continue collection. When this occurs, this dilution can require hours to recover the previous concentration. This occurred during the 03-03-2009 run requiring a 5 ml dilution of a 25 ml starting sample and after another hour of poor LAM performance the loss was not recouped and collection terminated after hour 6 following another system malfunction.

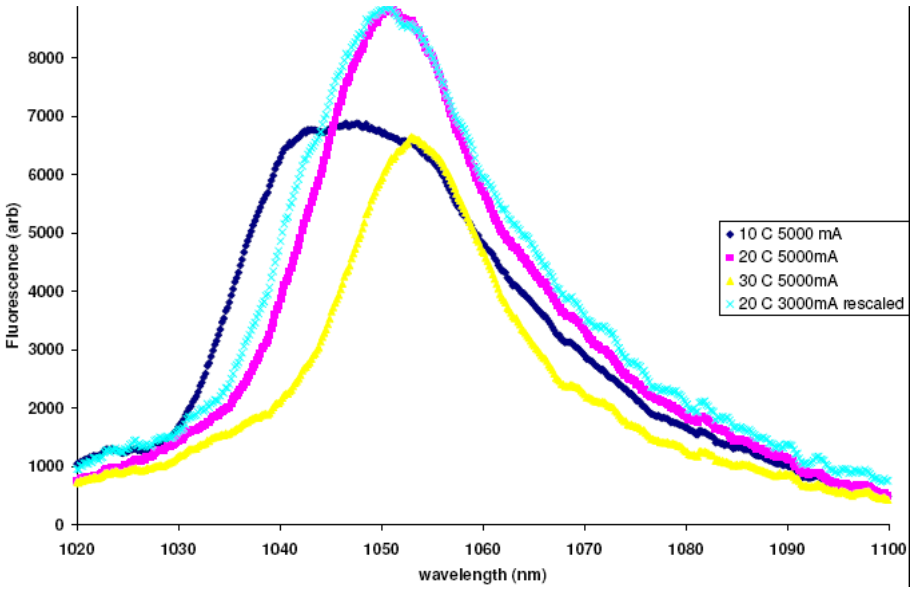

Figure 87. The fluorescence of Nd^{+3} doped Q-X nanoparticles excited by a diode laser at several wavelengths in the range of 795-810 nm in a 1 m LWCFC.

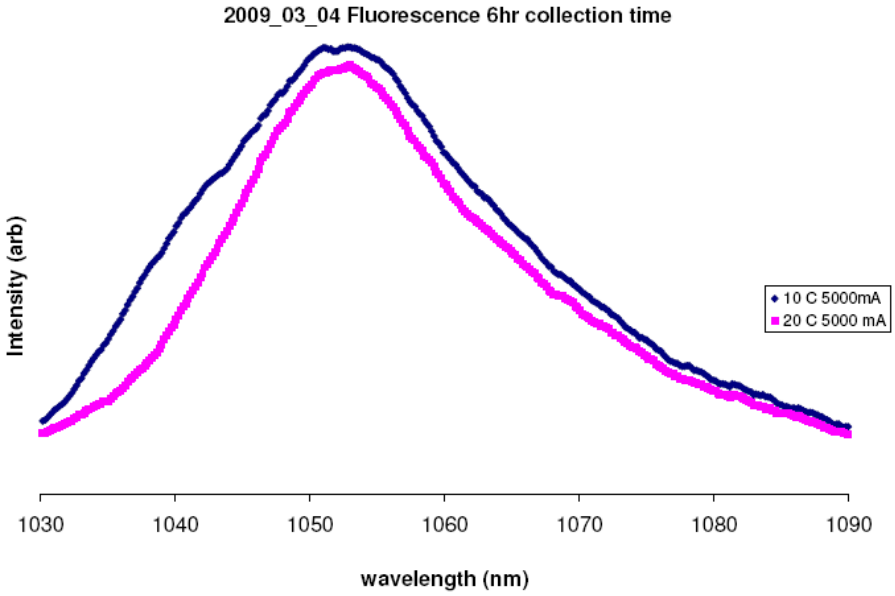

Figure 88. The fluorescence of Nd^{+3} doped Q-X nanoparticles excited at 795 nm (blue curve) and 804 nm (pink curve) in a 1 m LWCFC.

Though the experiments discussed above focused primarily on preparing and measuring the concentration of the samples, originally the samples themselves were produced to measure the fluorescence lifetime. The fluorescence signal of the sample was measured within the LWCFC and an accidental discovery occurred when setting the diode temperature to the wrong value (Figure 87 and Figure 88). As the diode equilibrated back to 20° C from an incorrect setting, the fluorescence spectrum also drifted, leading to a series of spectra measuring the fluorescence as a function of diode wavelength. The diode could be tuned over a range from approximately 795-810 nm.

Clearly there is a peak in the absorption and a change in line shape as the pump wavelength varies. At the time, this was a curiosity and wasn't given much consideration since the goal was performing a lifetime measurement using THOR. It was hoped that the increase in sample density would enable a fluorescence signal to be detected using a ~5 mJ 1 ns pulse from THOR to excite a nanoparticle sample in a spectroscopic cuvette. The beam was focused to a spot size of 0.5 mm yielding a fluence of ~1 J/cm^2 to avoid significant risk of breakdown and fire. The fluorescence signal was measured at 90° to the pump beam and was not detectable on a DET210 biased photodiode or an APD310 avalanche photodiode. The system was aligned by optimizing the signal from a small bulk glass sample to locate the correct position for the detector relative to the beam. When properly filtered, the bulk glass produced a significant response. However, the signal from the sample remained indistinguishable from noise.

The inability to directly measure the fluorescence signal in a 1 cm path length with THOR serving as the pump source resulted in a switch to the Lock-in-Chopper technique discussed in Chapter 5, where the current to the diode laser was directly modulated instead of using a chopper. This technique was employed in a series of five experiments that measured the fluorescence lifetime, the average size of nanoparticles in

a sample and the fluorescence spectra as a function of excitation wavelength for particles manufactured under a number of conditions.

Of six experiments conducted, five provided lifetime, fluorescence, and TEM information and are listed in Table 1. The experiment that had to be abruptly curtailed only provided lifetime data due to the home made LWCFC breaking during the lifetime measurement. As a result of the incomplete fluorescence data, efforts were focused primarily on the other five experiments.

Experiment	**Nozzle Diameter (μm)**	**Gas**	**Pressure measured (mTorr)**	**Pressure predicted (mTorr)**	**Particle radius (nm)**	**Impactor Cut (nm)**
05/08/08 – 08/04/08	270	N_2	125	130	NA	1.75
08/04/08	270	He	256	248	3 – 5	0.45
02/04/09	310	He	293	305	NA	0.5
05/11/09	358	N_2	215	192	10 - 12	2.5
05/18/09	358	He	382	382	1.5 – 2.2	0.75
05/31/09	358	70% He 30% N_2	~250	~260	4 – 5	1.5
6/11/09	358	40% He 60% N_2	~210	~220	7 – 8	2
6/13/09	358	N_2 @ 1100 T	~255	252	14-17	5.5

Table 1

In the first experiment conducted on 05/11/09 (see Table 1) nitrogen was used in the LAM with the goal of producing larger particles. The particles produced in this manner were significantly larger than those produced in helium and possessed altered spectra. Absorption data was not collected from these experiments due to the limitations of the new LWCFC. The second experiment utilized a helium environment producing results similar to those reported previously. The third experiment used a mixture of 70-

80% helium and 20-30% nitrogen gas in the LAM reactor. The operation of the LAM with this configuration was similar to the operation using pure nitrogen or helium, the only difference being that the flow rate controlled by the MKS mass flow controller needed to be corrected to account for a mixed gas. The procedure for doing this is straightforward and found in the controller's manual. The main potential difficulty came from estimating the fraction of each gas since the flow meters used were crude and matching the pressures using two regulators is challenging. However, the characterization of the chamber and nozzle proved useful to these purposes since the pressure in the chamber is a function of the gas density and effective polytropic exponent. Thus, the calculation used to design the chamber was easily adapted to determine the ratio of gas species from the ambient pressure in the chamber. Minor tweaks to the pressure regulators along the way were necessary to keep the pressure constant in the chamber. This had the added benefit of shifting the collection cut diameter up from ~1-2 nm to ~ 3-4 nm, guaranteeing that larger particles would be collected. The chamber pressure varied between 248 mT and 267 mT as the collection proceeded. During the third run the desired gas ratio was 60% nitrogen and 40% helium which translated into a chamber pressure between 200 mT and 220 mT and a collection cutoff of approximately 4-5 nm. The final sample was prepared in nitrogen at an elevated pressure in the horn cell. This was accomplished by placing a needle valve between the baffles box and the fume hood. The operating pressure chosen was approximately 1100 T as this produced decent powder feeding. If the pressure was increased beyond this point, the powder feeding rate decreased. Nevertheless, a useful sample with larger diameter particles was successfully produced. The cut diameter for the chamber operating under these conditions should be approximately 10 nm. Significant difficulties were encountered preparing the last two samples with adequate particle density. The powder flow was

intermittent at best and during the course of both runs several leaks developed requiring the replacement of fittings. The fourth run was terminated early due to the inability of both the primary and backup Teflon fittings to maintain a seal.

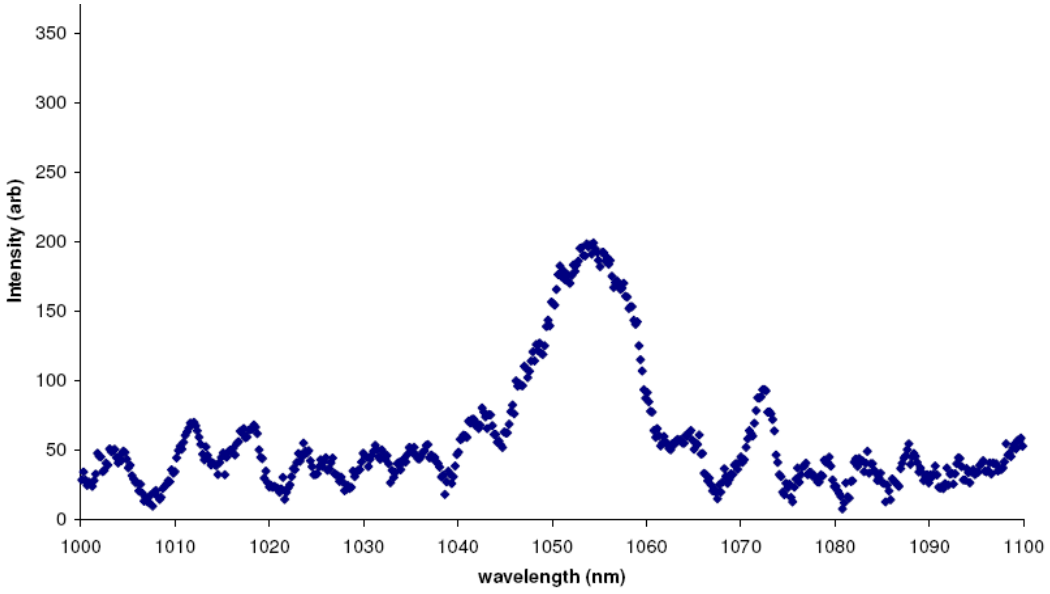

Figure 89. Fluorescence spectra from Nd^{+3} doped Q-X nanoparticles in a 1m LWCFC with sufficient filters to eliminate all stray light from the laser diode.

Due to the low nanoparticle concentrations, the lifetime measurements proved challenging, since at higher frequencies the number of photons available for detection approached the noise floor of the diode (Figure 89). This fact was verified using the Ocean Optics spectrometer with the same set of filters used to completely eliminate all light from the laser diode (both laser light and superradiance). The number of counts from the spectrometer was measured for a 100 ms integration window and translates roughly into a maximum of 200 photons per lifetime with an integrated signal-to-noise ratio of ~1.2. Normally the presence of noise wouldn't prove problematic for this measurement technique except for the possibility that some of the noise could be

correlated to the drive signal in the form of pump light leaking through the filters. The ability of the lock-in amplifier to report a stable value was correlated to the laser diode's power and frequency indicating that correlated noise might be the culprit. At low pumping power the phase would drift randomly. As the power was increased the phase would stabilize and hover around a value and then drift off again as the power crossed some threshold. The severity of this problem would change with the frequency of the current applied to the diode laser. Finally, the diode's DC offset needed to be monitored carefully since the impedance of the current driver is not perfectly flat in the kHz range and the fidelity of the sine wave could be distorted if the wrong choice of parameters was selected causing the reference frequency to drift. The reference frequency was provided to the lock-in amplifier by monitoring scattered light with a DET210 photodiode pointed towards a transport optic.

For the sample that was discarded due to failure of the home made LWCFC an attempt was made to find a set of filters and operating conditions that would permit simultaneous fluorescence and absorption measurements. The sample was produced in helium under normal operating conditions (double ablation, excimer pulse energy 450-350 mJ, 260 mT chamber pressure). However, after only about two hours of collection the instrument broke in the middle of the first measurements. The absorption measurement functioned as expected with the drawback being that the fluorescence signal was significantly attenuated. Due to this fact and persistent reliability problems with the home made LWCFC, the real time concentration diagnostics were abandoned for the remaining experiments in favor of rapid sample production and turnaround.

TEM work was also conducted on the samples. The goal of these measurement was to obtain a size estimate of the particles in solution, and though the distributions are noisy and the images not as clear as those obtained earlier (Figure 63 and Figure 64), the

data proved sufficient. When possible the size estimates were verified both on multiple grids and different sections of the same grid.

These images though more challenging to analyze were eventually interpreted. The extra effort in the analysis phase was more than offset by time saved preparing the grids. Figure 90 shows a TEM image from the sample produced in pure nitrogen with a horn cell pressure of 760 Torr and a chamber pressure of 215 mT. Higher resolution images reveal that the solvent damaged the grid in areas and in flocs like these it is possible to discern a few layers of spheres deposited on top of each other. Despite low quality, careful counting of the particles in this image produces both histograms in Figure 91. The two histograms generally agree with each other despite different filters and binning choices.

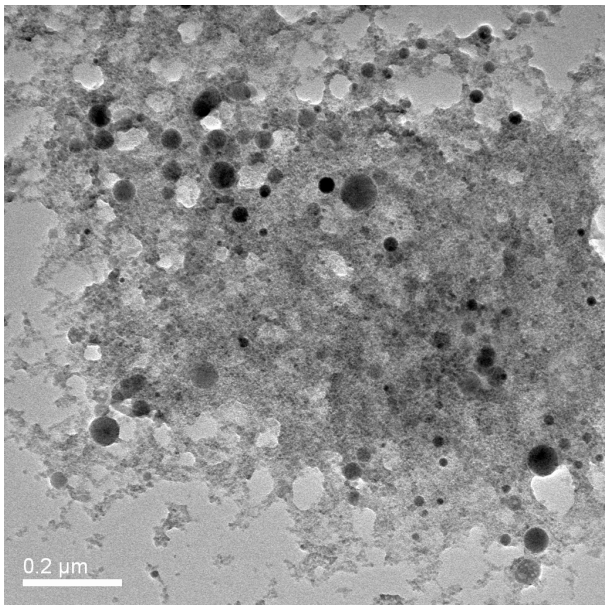

Figure 90. TEM image from a grid dipped in a suspension of Nd^{+3} doped Q-X nanoparticles collected in nonanoic acid

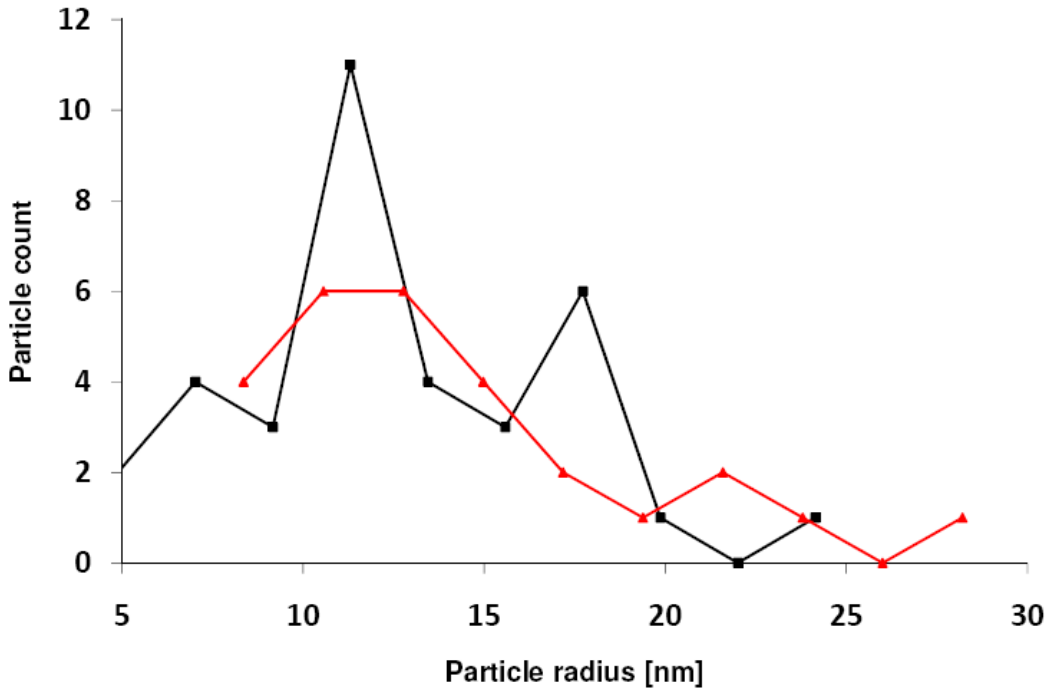

Figure 91. Histograms of particles ablated in N_2 at 760 Torr count vs. radius obtained from TEM images.

The uncertainty in the average particle radius that will later influence the analysis of the fluorescence and lifetime data, arises from the difficulty in accurately determining the size and particle count from images like these. Though noisy the general trend is usually very clear. In this example the image appears to have an average particle size between 9-12 nm. Similarly, the images from the smallest particles also show significant variation in the measured particle radius. The error in these size estimates can be attributed to uncertainty in the selection of the appropriate digital filters which define the boundaries of the particles in noisy images with imperfect resolution. Figures 92 through 95 demonstrate how the average size estimates are produced for particles produced in pure helium. The upper limit on the radius for these particles is apparent from the image but the lower bound is clipped due to TEM resolution and the physics of the impactor. It

is unphysical to have a significant number of particles well below the critical radius, which for this experiment was ~0.75 nm.

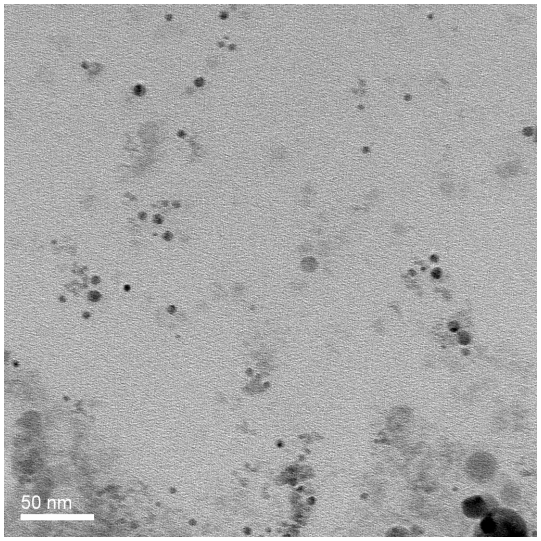

Figure 92. TEM image from a grid dipped in a suspension of Nd^{+3} doped Q-X nanoparticles collected in nonanoic acid

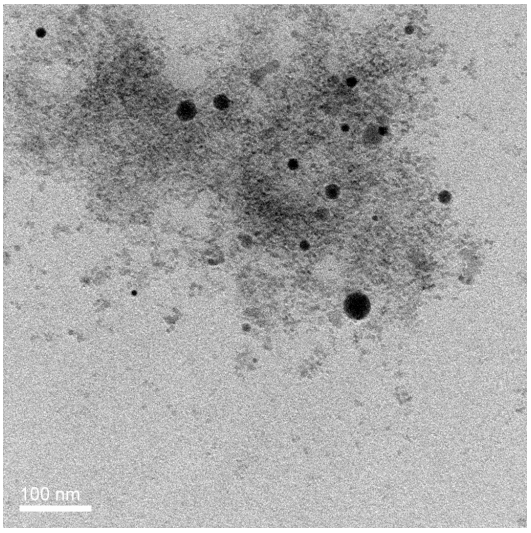

Figure 93. TEM image from a grid dipped in a suspension of Nd^{+3} doped Q-X nanoparticles collected in nonanoic acid

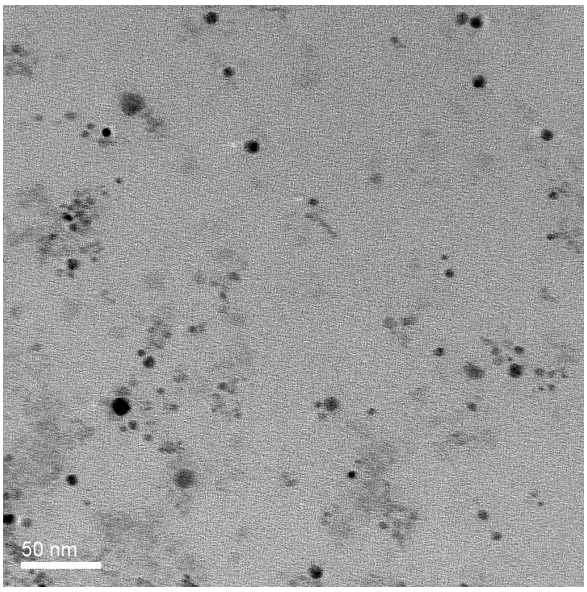

Figure 94. A TEM image obtained from a grid dipped in a suspension of Nd^{+3} doped Q-X nanoparticles collected in nonanoic acid.

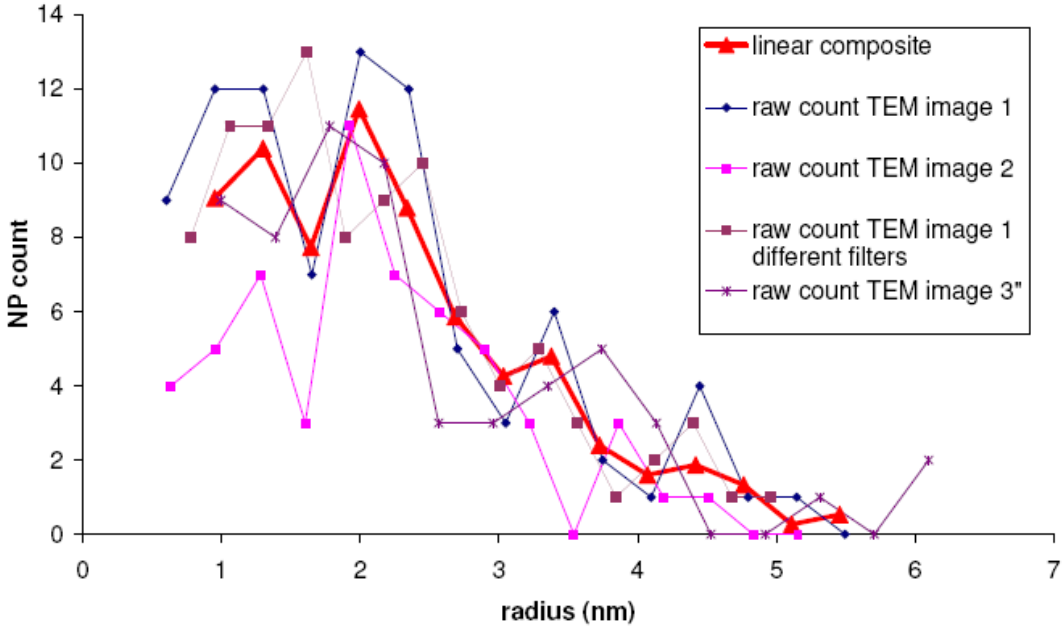

Figure 95. Histograms of particles ablated in helium at 760 Torr count vs. radius obtained from TEM images.

Occasionally some of the images were so noisy that hand counting was the only option. Nevertheless, it is still possible to extract useful information by directly counting the pixels in each particle. Figure 96 gives an example for a sample produced in 70% helium 30% nitrogen of both the necessity of this approach as well as the challenge it poses. The contrast during this TEM session was decreased by the fact that the TEM was operating at 200 kV instead of 110 kV in the previous images. This was not by design but rather by the requirements of accessing the instrument on that particular day. The particles as counted have been turned black (Figure 97). It should be emphasized that since some particles can be seen to overlap, the black colored nanoparticles do not represent all the particles in this image. An effort was made to identify and count all individually discernable particles in these images. Figure 98 shows an EDS spectrum that was taken to verify that the composition of the nanoparticles was similar to the bulk. The composition of the nanoparticles conforms to the parameter space of known phosphate laser glass and presents approximately the appropriate concentration by weight of Nd^{+3}. The expected concentration by weight was supposed to be 20% but for the particles surveyed it appears to be 25%.

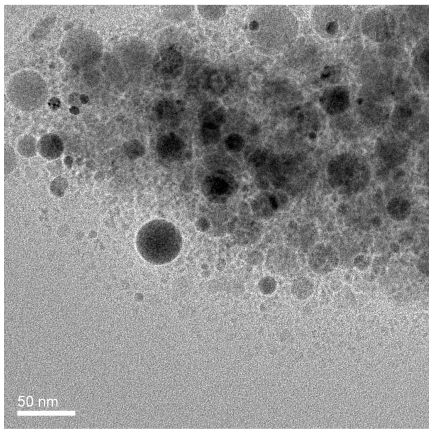

Figure 96. TEM image from a grid dipped in a suspension of Nd^{+3} doped Q-X nanoparticles collected in nonanoic acid

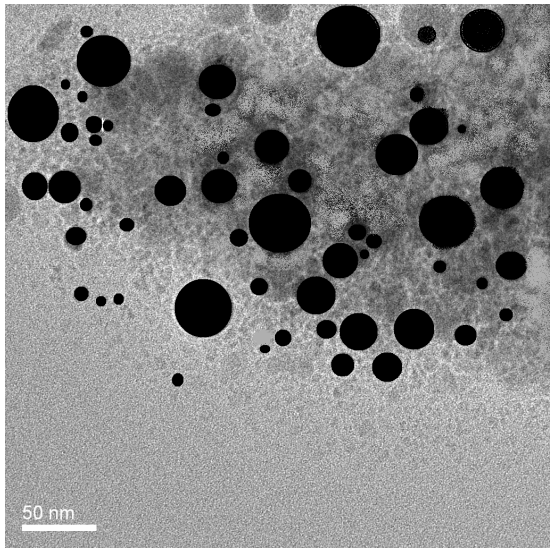

Figure 97. TEM image from a grid dipped in a suspension of Nd^{+3} doped Q-X nanoparticles collected in nonanoic acid with some of the identifiable particles highlighted in black

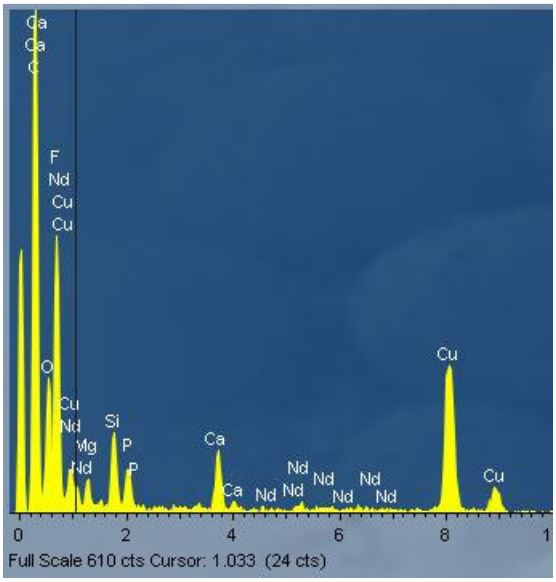

Figure 98. An EDS spectrum from a grid dipped in a suspension of Nd^{+3} doped Q-X nanoparticles collected in nonanoic acid

A screen shot of the counting program is presented in Figure 99 along with TEM images from the 60% nitrogen 40% helium sample described above. The top screen shot is for an un-doctored raw image. With a little help from an airbrush to get the more obvious particles to stand out better, a more accurate census is possible. Notice that these efforts have little effect on the approximate result. Both histograms peak in the 6 nm to 7 nm range and depending on the filters and binning can reach 5 nm or 8 nm. Though somewhat subjective, it is reasonable to correct the image when it is obviously misidentifying something as over threshold or not able to find an obvious boundary due to significant but uncorrelated noise in the vicinity. The raw image is posted next to the program's screen shot to demonstrate the validity of this procedure. The program was not written to be anything more than a quick aid to the measurement process and doesn't boast any robust detection or learning algorithms. Nevertheless, it has proven very useful. It should be stated that the picture exceeds the size of the frame so the particles will appear slightly larger as the bottom right corner of the image is clipped in the screenshot.

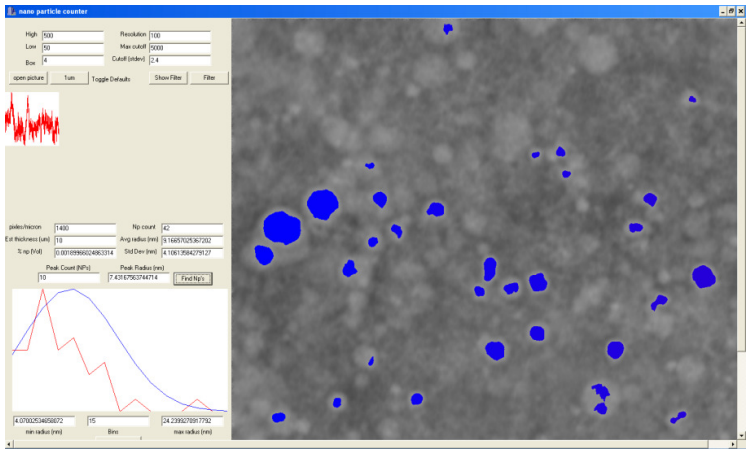

Figure 99. A screen shot of a computer program written to count particles in a TEM image obtained from a grid dipped in a suspension of Nd^{+3} doped Q-X nanoparticles collected in nonanoic acid.

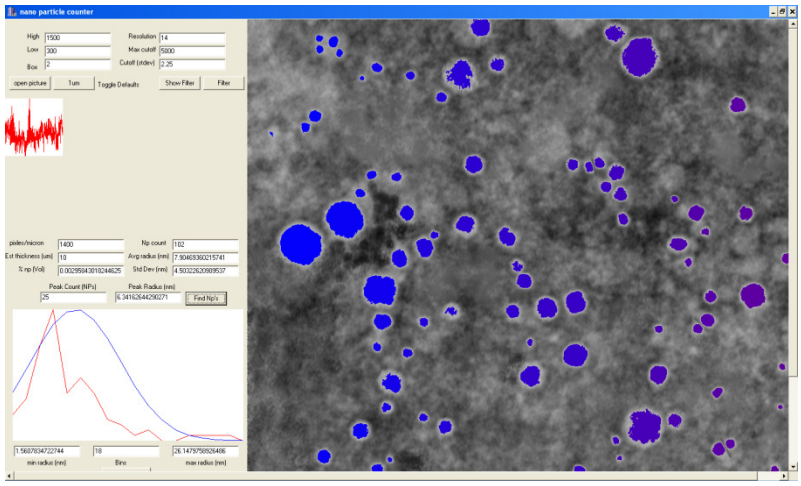

Figure 100. A screen shot of a computer program written to count particles in a TEM image obtained from a grid dipped in a suspension of Nd^{+3} doped Q-X nanoparticles collected in nonanoic acid.

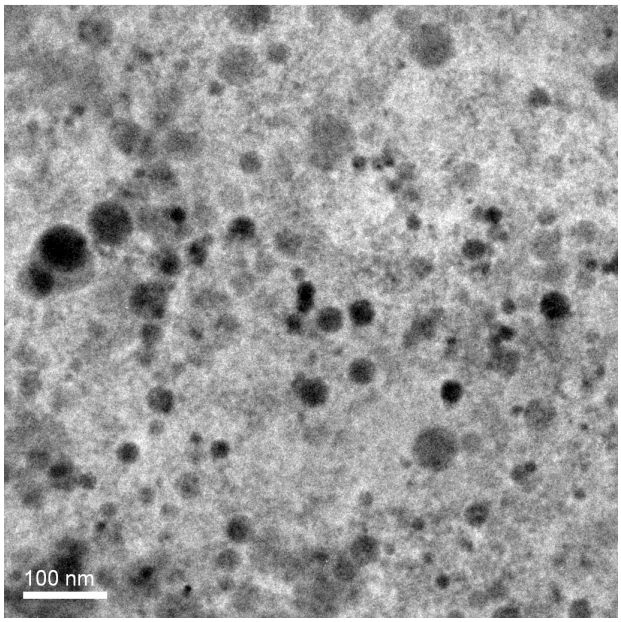

Figure 101. A TEM image obtained from a grid dipped in a suspension of Nd^{+3} doped Q-X nanoparticles collected in nonanoic acid. It needs to be explicitly stated that X-ray diffraction scattering conducted in the grainy areas of this image reveled no trace of Nd^{+3} it is likely that these areas of the grid were damaged by the acid.

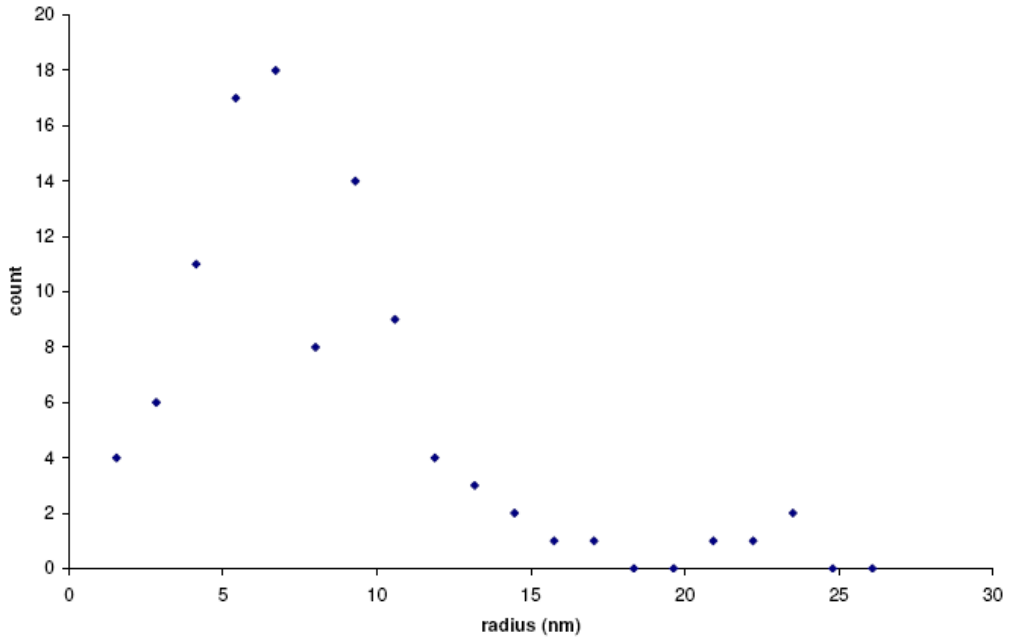

Figure 102. A histogram of particles ablated in a mixture of 60% N_2 and 40% He obtained from TEM images.

Close inspection of the image in Figure 101 reveals that some of the smaller particles are quite well resolved but due to the grainy nature of this image, the program struggled to define the particle's boundary. This led to an under representation of the smallest particles in the final count, resulting in the histogram shifting from ~8 nm to ~7 nm, which given the quality of the image is an acceptable level of uncertainty (Figure 102). Nevertheless, the trend is clear and consistent across a range of counting methodologies, and conforms to the expected range of performance from the impactor for this sample.

Having shown some of the worst cases encountered for TEM size measurements Figure 103 shows a relatively trouble free example. This sample was prepared in pure nitrogen at 1100 Torr in the horn cell. The reported radius varies from 14-17 nm depending upon the filters and binning options used.

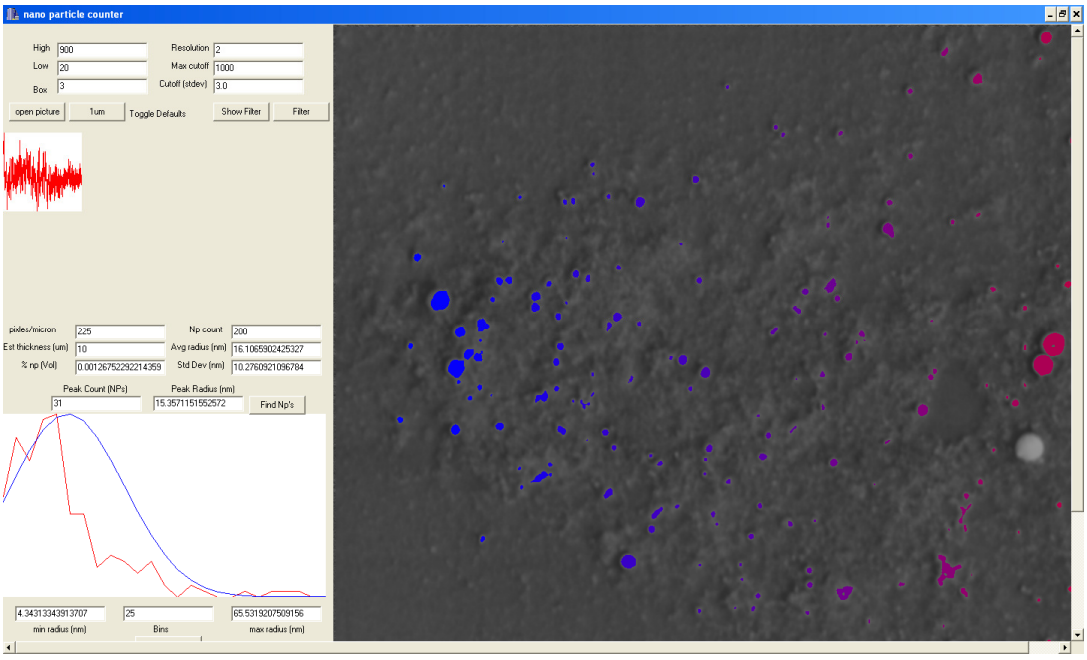

Figure 103. A screen shot of a computer program written to count particles in a TEM image obtained from a grid dipped in a suspension of Nd^{+3} doped Q-X nanoparticles collected in nonanoic acid.

Lifetime and fluorescence data collected on these samples was routine and followed the general procedure laid out in the previous chapter with the few exceptions noted above. Data from all of the fluorescence measurements will be discussed in the following chapter highlighting important features and limitations of these experiments.

Chapter 8: *Discussion of Spectroscopic Results*

The last chapter focused on a presentation of results relevant to the evolution of production and measurement techniques that culminated in the successful characterization of the spectroscopic properties of the nanoparticles. This chapter will discuss the spectroscopic data obtained over the course of these experiments highlighting the characteristics of the spectra that distinguishes the nanoparticles from the bulk material. The most significant experiments in this work were conducted on Kigre Q-X nanoparticles, collecting fluorescence spectra at 1050 nm and 910 nm as well as lifetime and size information. Table 2 lists the most important results obtained from these particles.

Gas composition	Radius (nm)	Lifetime (μs)	Excitation wavelength (nm)
Nitrogen @ 760 T	10	61.2	Partial 803-806 (3 measurements w/ full spectra)
100% Helium @ 760 T	0.85	20.7	802-807 (9 fluorescence spectra, 11 gain measurements w/ full spectra)
70% Helium 30% Nitrogen @ 760 T	4.5	37.9	802-807 (9 fluorescence spectra)
65% Nitrogen 35% Helium @ 760 T	7.5	53.2	802-807 (9 fluorescence spectra, 9 fully filtered signal)
Nitrogen @ 1100 T	15	72.9	802-807 (9 fluorescence spectra)

Table 2

8.1 FLUORESCENCE DATA

The fluorescence spectra of the nanoparticles and the bulk differed slightly from one another. In bulk glass the spectra of Nd^{+3} doped laser glass is a result of inhomogeneous broadening and exciton migration[2, 23,56]. Studies of laser glasses and

crystals at cryogenic temperatures reveal a dependence of fluorescence spectra on the excitation wavelength[56,57].

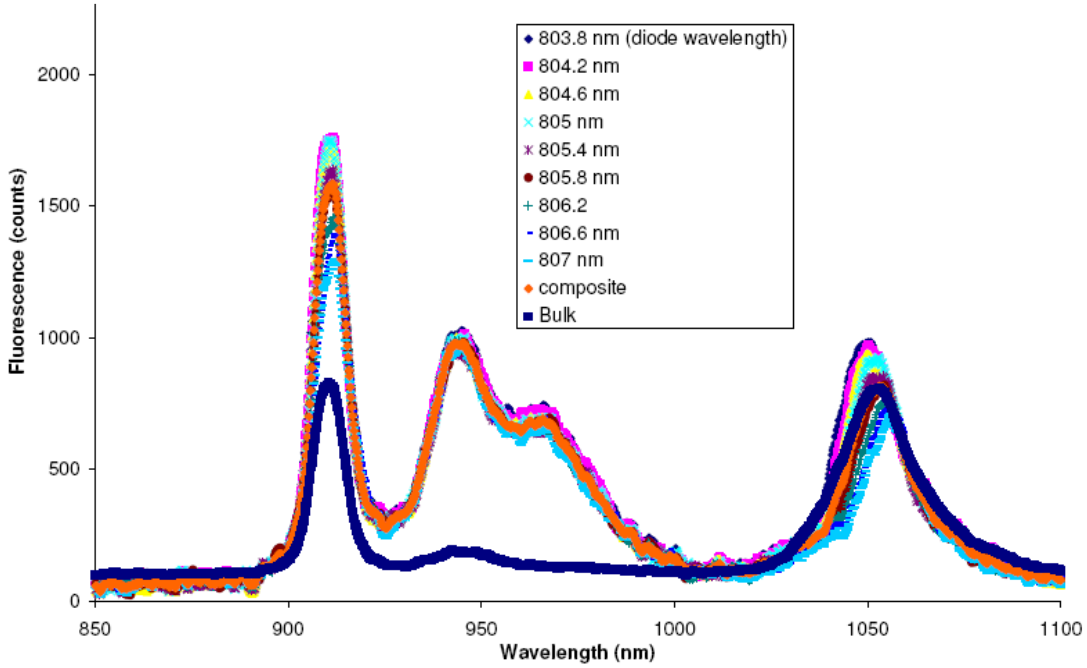

Figure 104. Fluorescence spectra of ~5 nm Nd^{+3} doped Q-X nanoparticles excited at several wavelengths.

The fluorescence data for colloidal nanoparticles in the IR produced qualitatively similar results to those presented by Brecher et al. in a study of fluorescence line narrowing in Nd^{+3} doped glass. Their experiment attempted to resolve the spectroscopic properties of sub-populations of ions in several different host materials. The glass samples were cooled to liquid helium temperatures and then excited by a narrow pulse from a tunable dye laser into the $P_{1/2}$ state, since at low temperatures it is not affected by Stark splitting. They studied the fluorescence for a fraction of the lifetime to minimize the effects of cross relaxation. For several samples they reported being able to resolve individual lines in the sub-manifold. Tuning the dye laser caused the position of the

peaks to shift revealing the effect of both the coordination species and their relative position on the spectra. By comparison, fluorescence spectra obtained from the nanoparticles were significantly narrower than the bulk spectra and also shifted as the pump was tuned. Moreover, it was also possible to resolve individual lines present in the spectra. The strength of this effect seemed to correlate with particle size.

Figure 104 shows the complete fluorescence spectra obtained from a population of ~4 nm particles. The spectrum in Figure 104 consists of three main features common to all fluorescence data collected using the LWCFC apparatus discussed in Chapter 6. First, the peak at 910 is a combination of diode superradiance and fluorescence from the nanoparticles between the $4F_{3/2}$ and $4I_{9/2}$ levels. Second, the signal in the 930 nm – 1000 nm range is just diode superradiance convoluted with the filters designed to cut the 800 nm light. The filter combination was generally an 800 nm 0° dielectric mirror, a notch filter at 800 nm and an RG 850 absorption filter. Thus, the absolute magnitude of the fluorescence peaks is not measured in these plots. The important feature to take from these spectra is that the magnitude and position of the peaks at 910 and 1050 change significantly with pump wavelength while the 950 light remains roughly constant.

The third feature is revealed when zooming in on the 1050 nm region of the spectra which demonstrates a significant variation in the character of the spectra as a function of pump wavelength (Figure 105). To obtain the data shown in figure 105 the laser was operated at 10° C which was 5° below its minimum rating. Because operation at this temperature placed the diode at a significant risk of failure, the measurement was not repeated. The reason for taking this risk was to ascertain whether the curve would roll-over below 16° C.

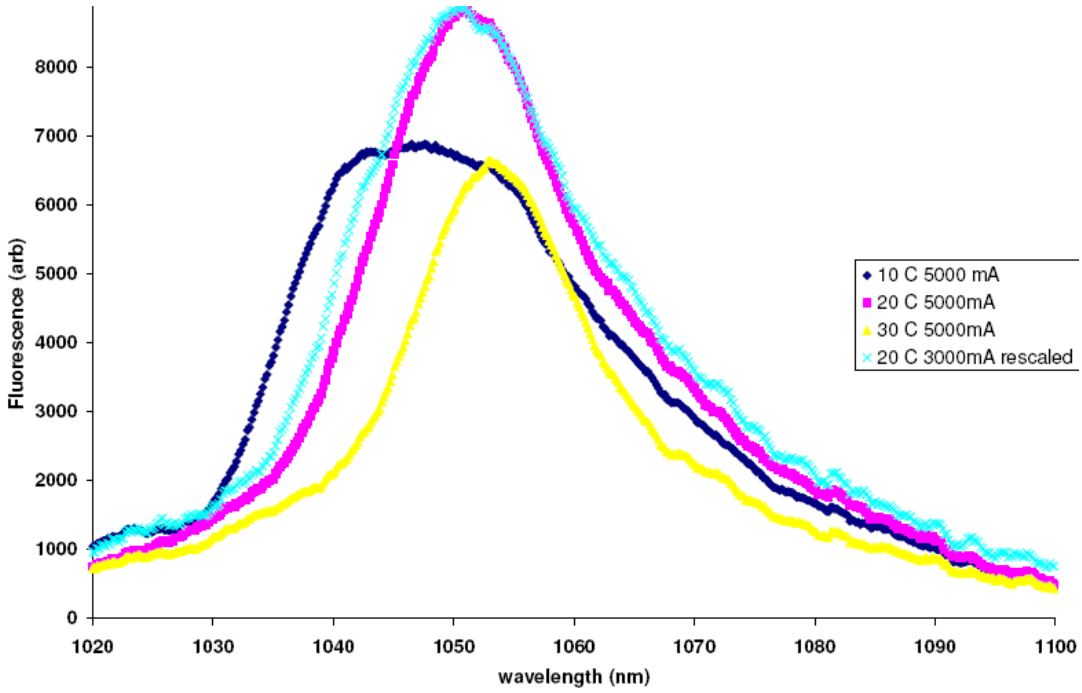

Figure 105. Fluorescence of Nd^{+3} doped Q-X nanoparticles excited at several wavelengths showing a significant sensitivity to excitation wavelength.

The curve indeed rolled over showing decreased fluorescence intensity as well as an enhanced contribution from a line between 1035nm and 1040 nm. As figures 106 through 108 show, the fluorescence peak shifts as the excitation wavelength is tuned. Moreover, as seen in Figure 107 and Figure 108 several individual lines are resolved. The peaks seem to occur near 1042, 1050, 1054, 1064, and 1072 with varying offset for different particle sizes.

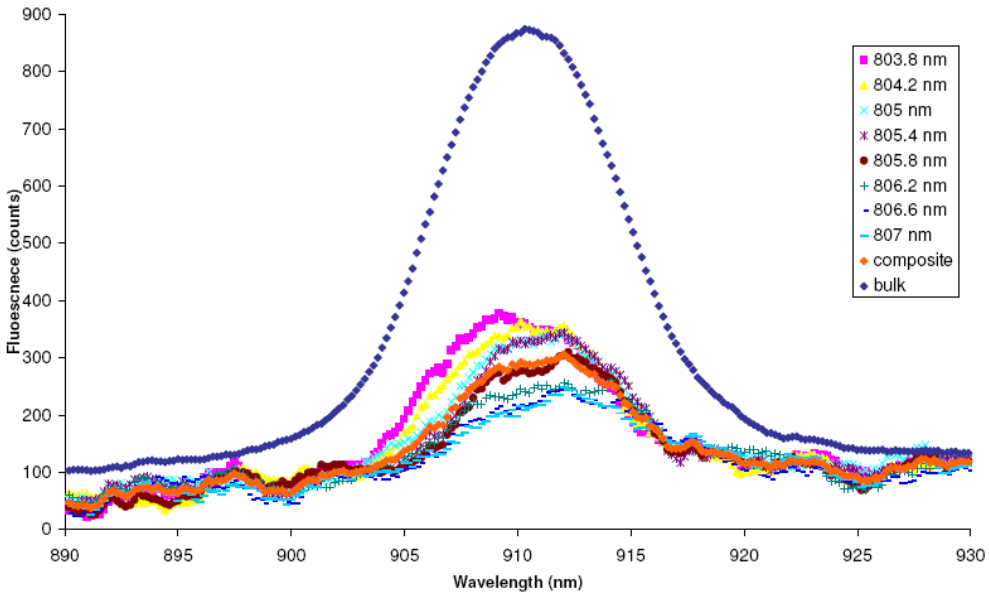

Figure 106. . Fluorescence of Nd^{+3} doped Q-X nanoparticles excited at several wavelengths showing a significant sensitivity to excitation wavelength.

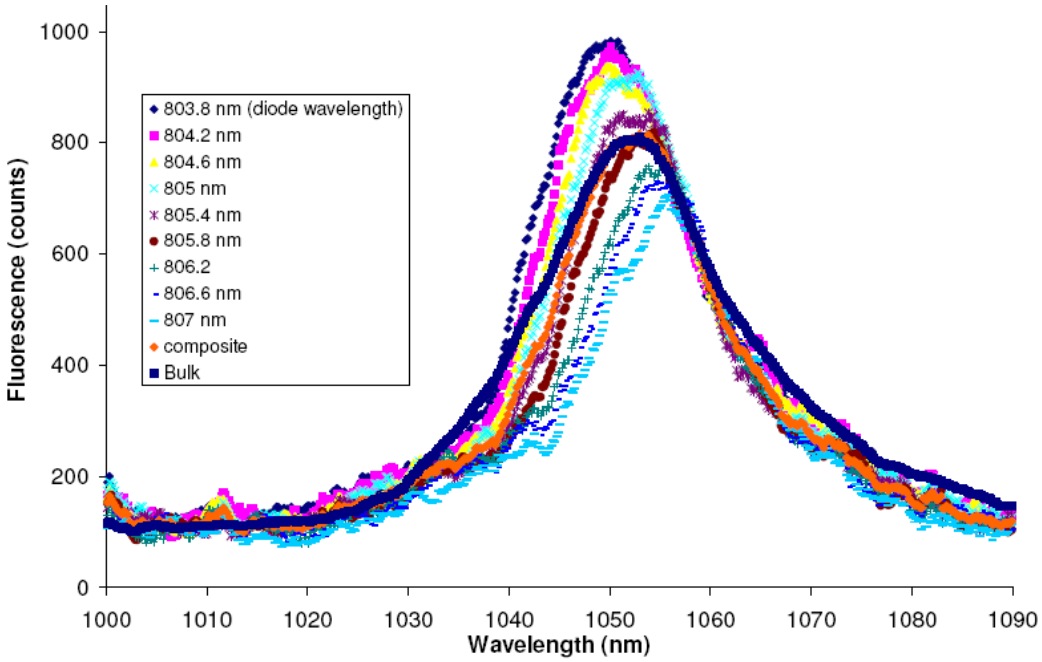

Figure 107. Fluorescence of Nd^{+3} doped Q-X nanoparticles excited at several wavelengths with a few observable lines.

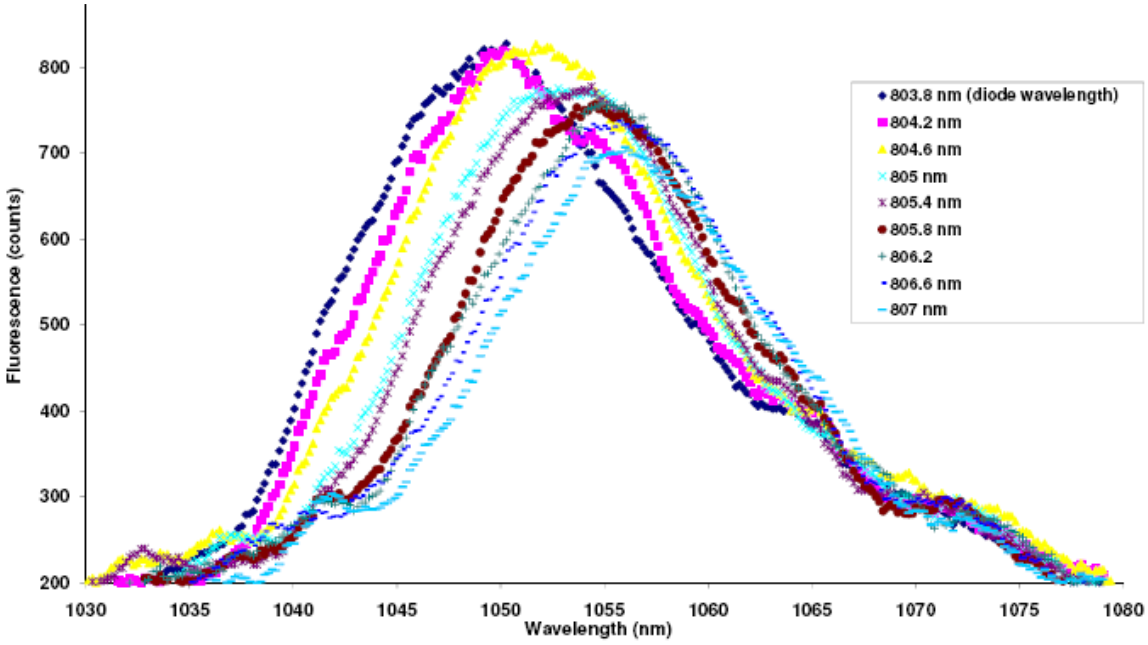

Figure 108. Fluorescence of Nd^{+3} doped Q-X nanoparticles excited at several wavelengths with a few observable lines.

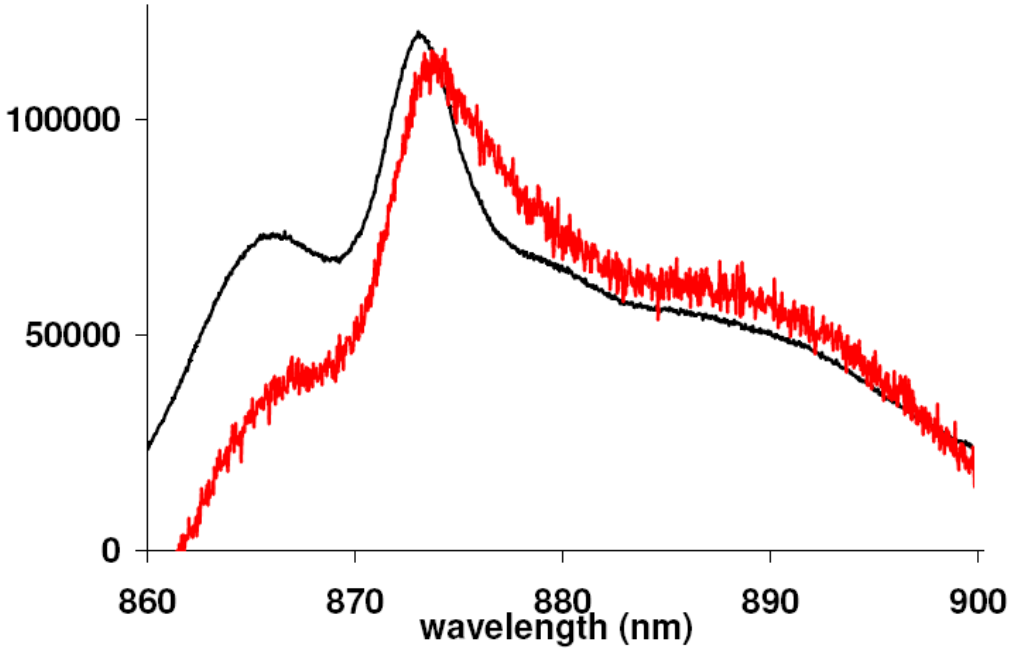

Figure 109. Fluorescence from a thin film of LG-760 nanoparticles (red) reveals shifted spectra from bulk (black).

The above results appear to agree with spectral shifts observed in the IR fluorescence of solid nanoparticle films mentioned in the previous chapter (Figure 109).

Though the primary thrust of the experiments conducted here was aimed at measuring the properties in the near IR, because of interest in the potential of this material for use in a laser application, some data in the visible range was collected. Unlike the IR spectra, the behavior of the nanoparticles in the UV-VIS region show pronounced departure from the bulk (Figure 110 through Figure 118). The differences between the bulk and nanoparticle spectra become most pronounced around 400 nm (Figure 111). The absorption spectra of colloidal micro-particles and nanoparticles also differ as shown in figure 112 and 113. The key feature is a broad peak not present at 660 nm in the micro-particles but present in the nanoparticles. This peak corresponds to a shifted peak in the excitation spectra shown in Figure 114. It is interesting that both the excitation and absorption spectra (Figure 113) should have such a strong response at 660 since this transition is no stronger than many others measured in the bulk. Another feature of the nanoparticles' 1050 excitation spectrum that is noteworthy is the fact that the peak appears on the tail end of a line in the bulk material. This feature could either represent a shift in the branching ratio of a sub-manifold or the shift in the position of the peak itself. Contrasting the narrow excitation peak with the broad absorption peak centered in the same region suggests that the shape of the excitation spectrum is in fact related to branching processes.

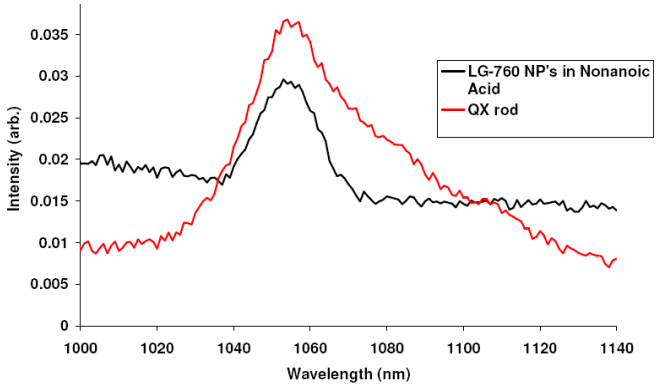

Figure 110. Fluorescence spectra from bulk LG-760 (red) and nanoparticles in nonanoic acid (black).

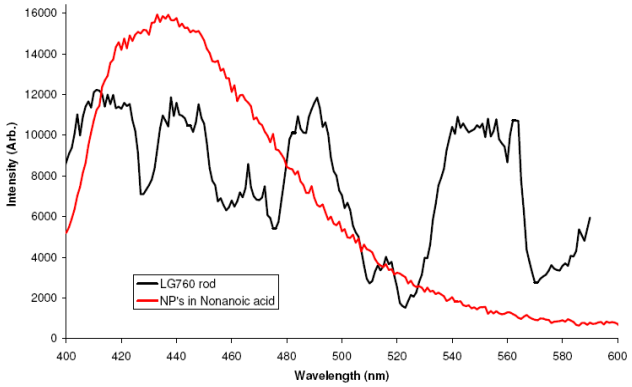

Figure 111. Excitation spectra of the 800 nm line in bulk LG-760 (black) and nanoparticles in nonanoic acid (red).

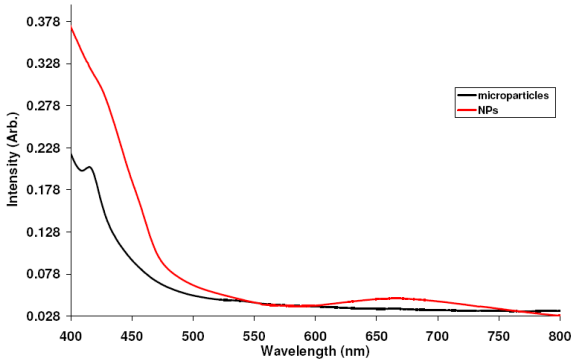

Figure 112. Absorption spectra from LG-760 micro-particles (black) and nanoparticles in nonanoic acid (red).

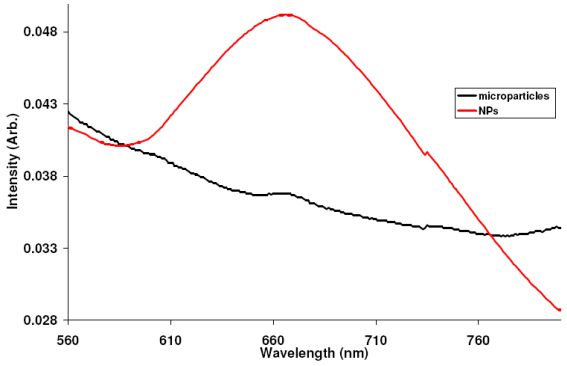

Figure 113. Absorption spectra from LG-760 micro-particles (black) and nanoparticles in nonanoic acid (red).

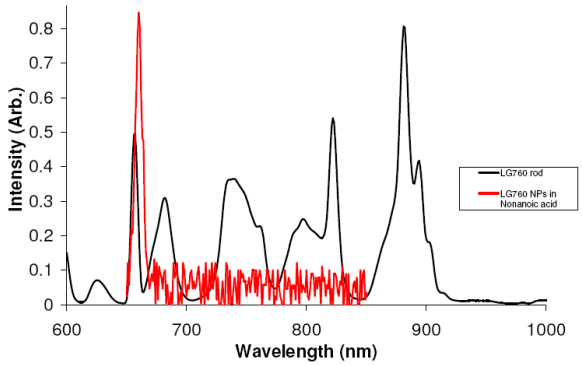

Figure 114. Excitation spectra of the 1054 nm line in bulk LG-760 (black) and nanoparticles in nonanoic acid (red).

The nanoparticle fluorescence excitation curve in Figure 111 shows a single peak compared to the multiple peaks observed in the bulk. This manifold also shows significant fluorescence in the visible region with a similar line-shape as seen in Figure 115 through Figure 117. The 440 nm peak fluorescence signal in this region was seen in Figure 115 when exciting at 400 nm. This occurs very near the 440 nm excitation peak for 800 nm. It should also be noted here that the 380 nm excitation peak of the 1050 nm line also possessed a similar shape to the 440 nm peak. The bulk excitation spectra reported here are consistent with data available from the manufacturer (Shott Inc.).

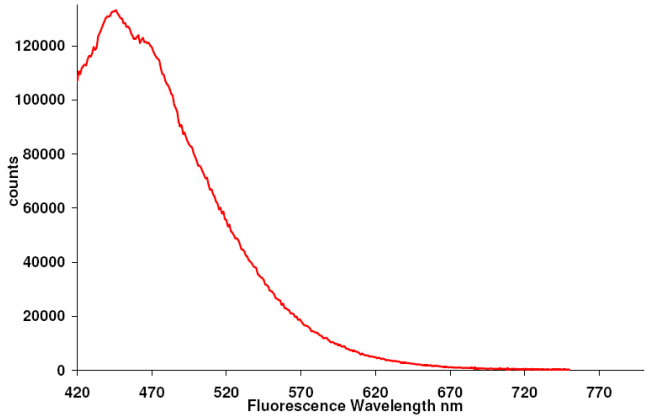

Figure 115. Fluorescence spectra of nanoparticles in nonanoic acid excited at 400 nm.

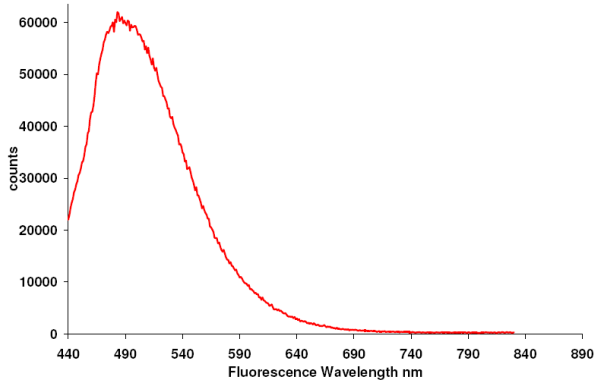

Figure 116. Fluorescence spectra of nanoparticles in nonanoic acid excited at 420 nm.

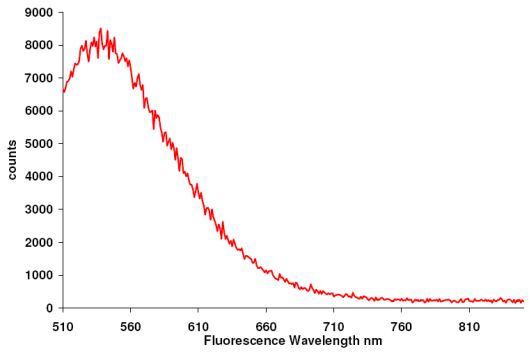

Figure 117. Fluorescence spectra of nanoparticles in nonanoic acid excited at 500 nm.

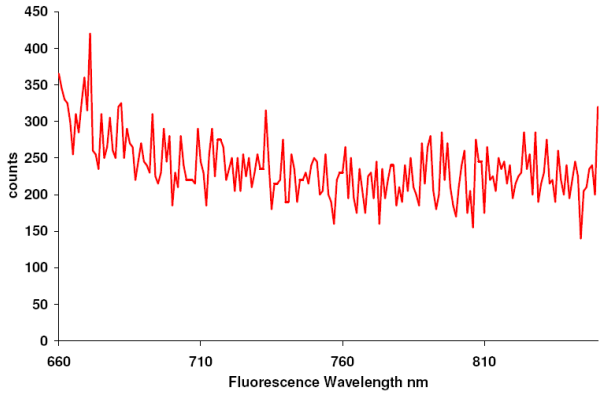

Figure 118. Fluorescence spectra from nanoparticles in nonanoic acid excited at 660 nm.

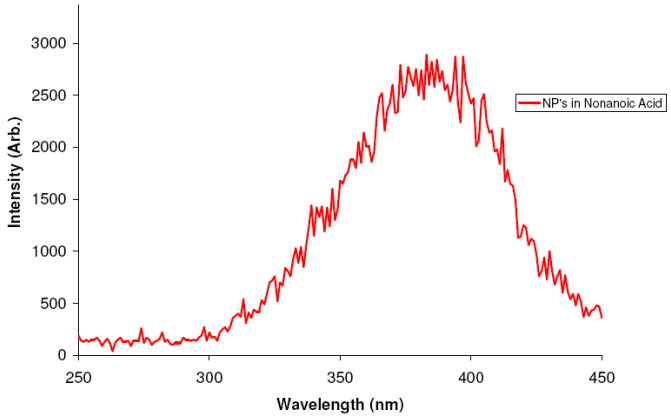

Figure 119. Excitation spectra of the 1054 transition for nanoparticles in nonanoic acid.

From the shape and breadth of both the visible fluorescence and excitation spectra discussed above it seems as though the nanoparticles contribute a continuum of perturbations to the manifolds below 660 nm, which suppress the transitions between 500 nm and 650 nm as well as 670-800 nm. Finally, it is curious that while strong fluorescence was detected at 800 nm when exciting near 440 nm, 1050 was not detected when exciting at 800 nm. It seems like the relative strength of the 660 nm line was enhanced by the nanoparticles while the branching ratio of this transition heavily favors the $4F_{3/2}$ over the $4F_{5/2}$ state. Without better data in the visible including lifetime information it is difficult to draw any quantitative conclusions about the effects of the

nanoparticle host on the visible spectra. Nevertheless, a simple explanation may exist for why the near IR and visible spectra could reveal such radically different pictures about the effect of a nanoparticle host on the excitation spectra of the Nd^{+3} ion. This behavior is consistent with the fact that excitations with average radii similar to the ground state would be shielded by the 5s and 5p electrons while wavefunctions with larger radii will interact more with the host. It is possible that mixing with 5d wavefunctions could also contribute significantly to the manifold structure in the excited states below 500 nm[57]. Moreover, if the excited states in the UV-visible region were strongly coupled to a continuum of perturbations (such as those present at a fluid interface) it might act to broaden any fluorescence transitions into bands. It is possible to imagine such a scheme accounting for the differences between the excitation spectra for the bulk and the nanoparticle in the visible region but tapering off in the near IR where other electrons still shield the $4F_{3/2}$ metastable states.

In the LG-760 and Q-X bulk excitation spectra in Figure 114, the absorption spans the visible in a nearly continuous band. This contrasts with the case of the nanoparticles for which the excitation spectra only peaks in the 650 region. An explanation consistent with the above hypothesis might attribute the significant decrease in width of the excitation spectra to a decrease in the inhomogeneity in nanoparticles of the same size, while an increase in the density of states of available perturbations at the surface of the nanoparticle due to its contact with the fluid broadens the higher energy transitions around 440 nm.

Supporting this idea is the fact that the number of active sites in the nanoparticle depends on the particle's size. Assuming the spherical nanoparticles measured in the TEM work presented in the previous chapter possess densities comparable to the bulk material, the number of optically active ions in a particle can be plotted as a function of

particle diameter. In the 2% LG-760 glass, particles with a diameter of 2 nm will contain only 1 active ion while particles with diameters of 10 nm will have approximately 100.

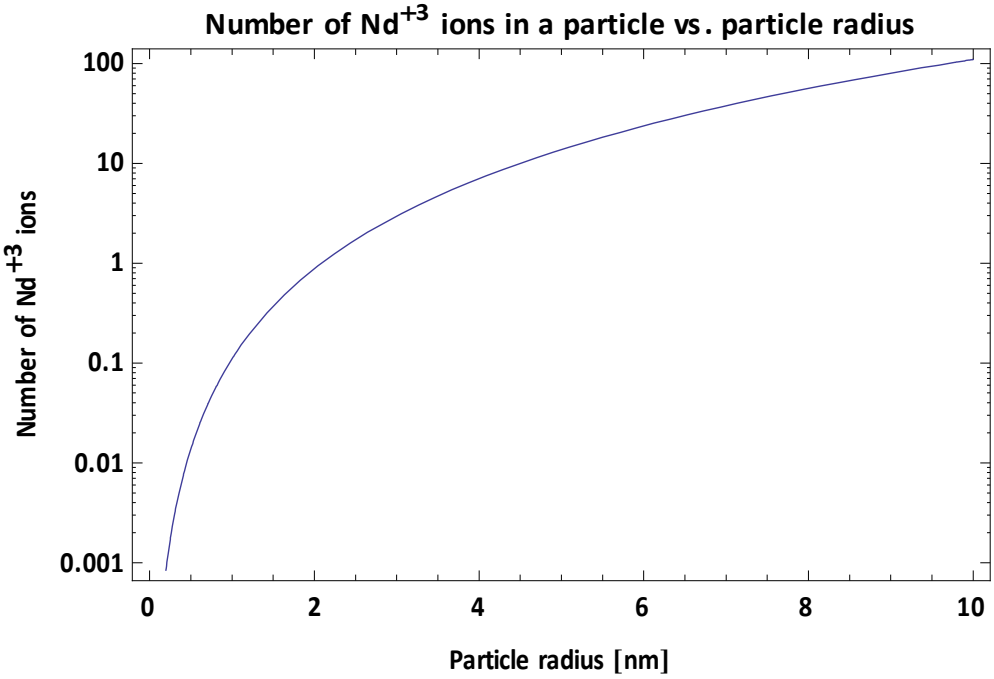

Figure 120. Number of neodymium ions in a nanoparticle as a function of its radius.

Thus on average, a 4-6 nm diameter particle will contain only a few ions and between a few hundred and a few thousand host atoms. Moreover, ~70% of these ions will be within 1nm of the particle's surface. In this manner, the particles may represent a more homogeneous environment than bulk while allowing the ions to weakly couple with the extra degrees of freedom present in the fluid.

8.2 LIFETIME DATA

Lifetime data was collected on all samples described above using the method discussed in Chapter 6 and plotted in figures 121 through 125. The quality of the data depended upon the quality of the samples prepared. For example, the density of the 15.5

nm particles was significantly less than earlier samples. Figure 126 shows the total signal available to the detector when sufficient filters are present to remove all stray light from the diode laser. When this signal is integrated it corresponds to ~10^{-7} W which is the noise floor of the detector. Though it was possible to measure the lifetime, above 500 Hz the amplifier would drift randomly around zero. As noted in Chapter 6 the laser's DC offset, waveform, and peak to peak intensity would all vary as a function of the driving signal, thus it is possible that the signal from the laser would swamp the fluorescence at certain frequencies. This interpretation of the result is consistent with the fact that turning up the power from the diode also would cause the lock-in to drift randomly about zero.

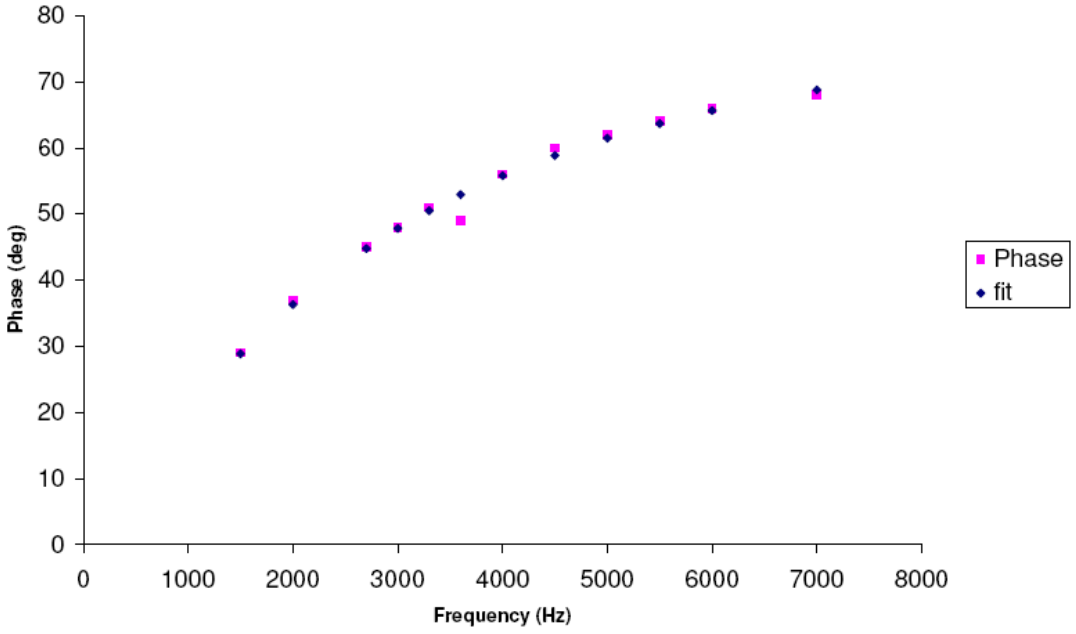

Figure 121. The phase shift between the laser diode and fluorescence signal as a function of frequency for Nd^{+3} doped Q-X nanoparticles ablated in N_2 at 760 Torr and excited by a diode laser driven with a sinusoidal current. Particle fluorescence lifetime = 58.5 μs.

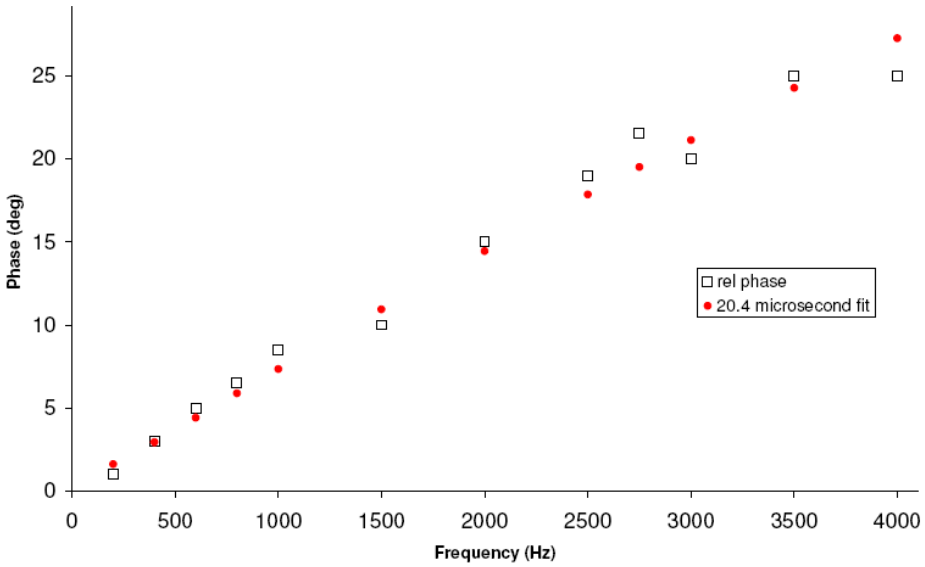

Figure 122. The phase shift between the laser diode and fluorescence signal as a function of frequency for Nd^{+3} doped Q-X nanoparticles ablated in He at 760 Torr and excited by a diode laser driven with a sinusoidal current. Particle fluorescence lifetime = 20.4 μs.

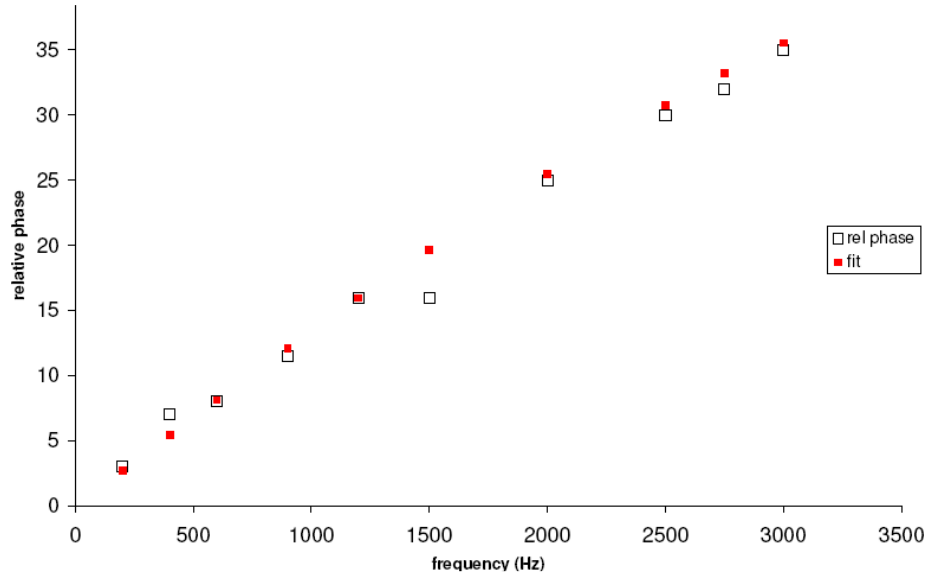

Figure 123. The phase shift between the laser diode and fluorescence signal as a function of frequency for Nd^{+3} doped Q-X nanoparticles ablated in a mixture of 70% He and 40% N_2 at 760 Torr and excited by a diode laser driven with a sinusoidal current. Particle fluorescence lifetime = 38 μs.

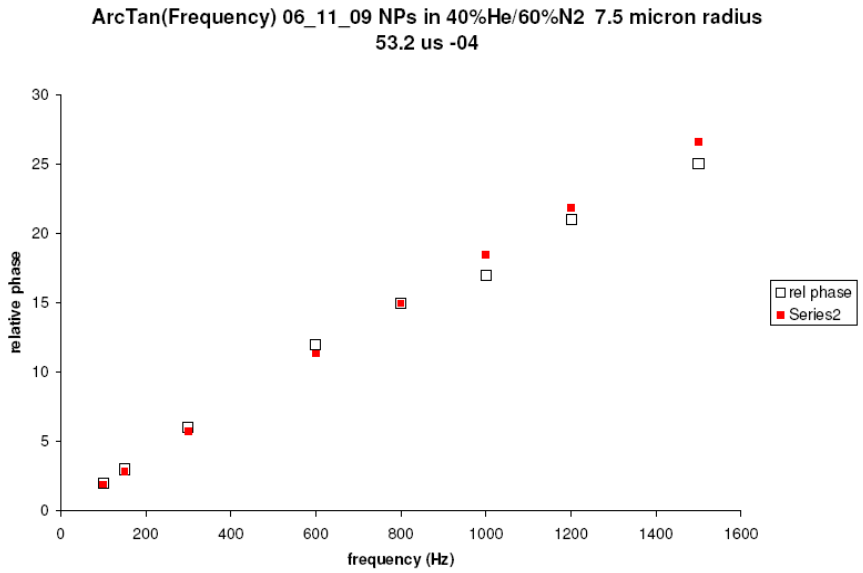

Figure 124. The phase shift between the laser diode and fluorescence signal as a function of frequency for Nd^{+3} doped Q-X nanoparticles ablated in 40% He and 60%N_2 at 760 Torr and excited by a diode laser driven with a sinusoidal current. Particle fluorescence lifetime = 62 μs.

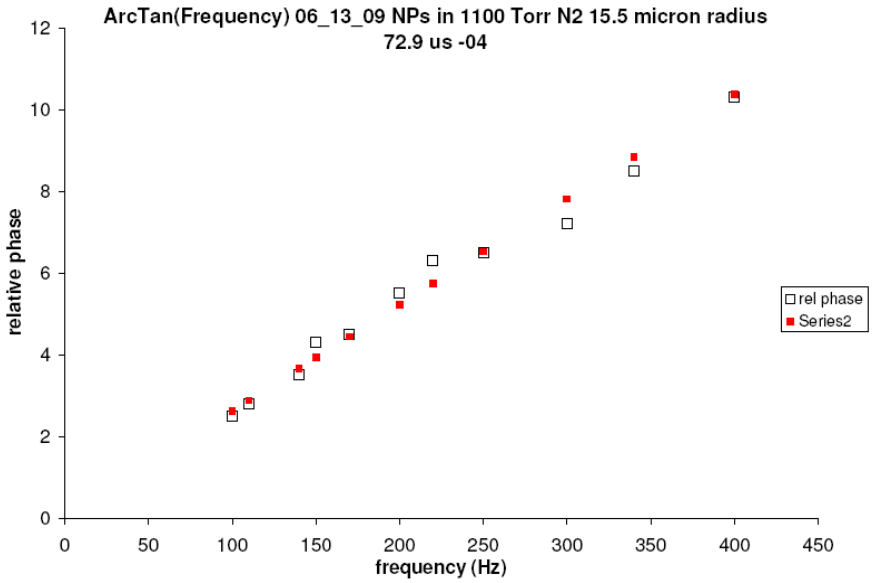

Figure 125. The phase shift between the laser diode and fluorescence signal as a function of frequency for Nd^{+3} doped Q-X nanoparticles ablated in N_2 at 1100 Torr and excited by a diode laser driven with a sinusoidal current. Particle fluorescence lifetime = 73 μs.

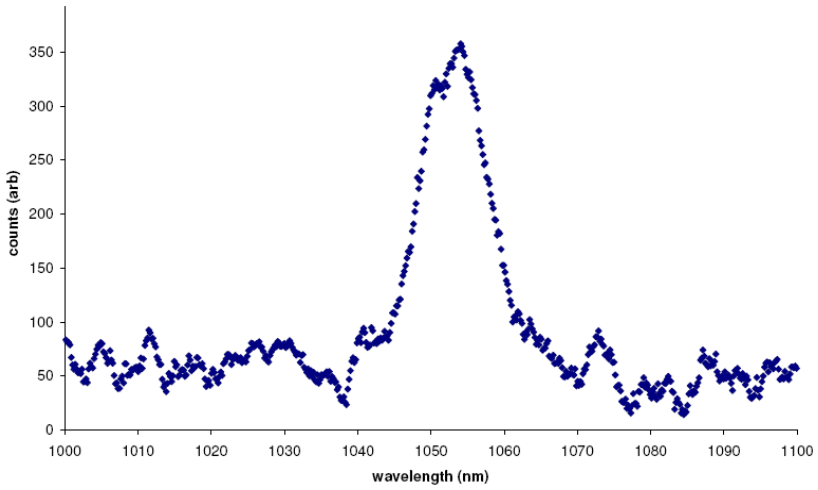

Figure 126. This fully filtered fluorescence spectrum from the nanoparticles taken at the same time as the phase measurement in the previous figure shows that the signal is near the detection threshold.

8.3 Gain Measurement and Cross Section Data

The final measurement that should be discussed was an attempt to measure gain at 1054 nm. The preparation of the sample in pure helium proceeded smoothly. The diagnostics yielded a bright fluorescence signal, visible using an IR viewer, that easily produced high quality fluorescence and lifetime data. Thus, with time to spare, a gain measurement was attempted (Figure 127). The LWCFC apparatus was configured as previously described with only minor modifications. A dichroic mirror was inserted before the lens that focused light into the capillary tube. The mirror transmitted the 800 nm pump light but reflected the 1054 at 45 degrees. On the other end of the capillary tube a broad band high reflector was placed after a collimation lens and aligned to couple light back into the tube. The spectrometer was situated on the return path pointed toward the dichroic mirror. The collection fiber was optimized on the small fraction of 800 nm pump light reflected from the dichroic mirror. Filters were then inserted to block the pump light.

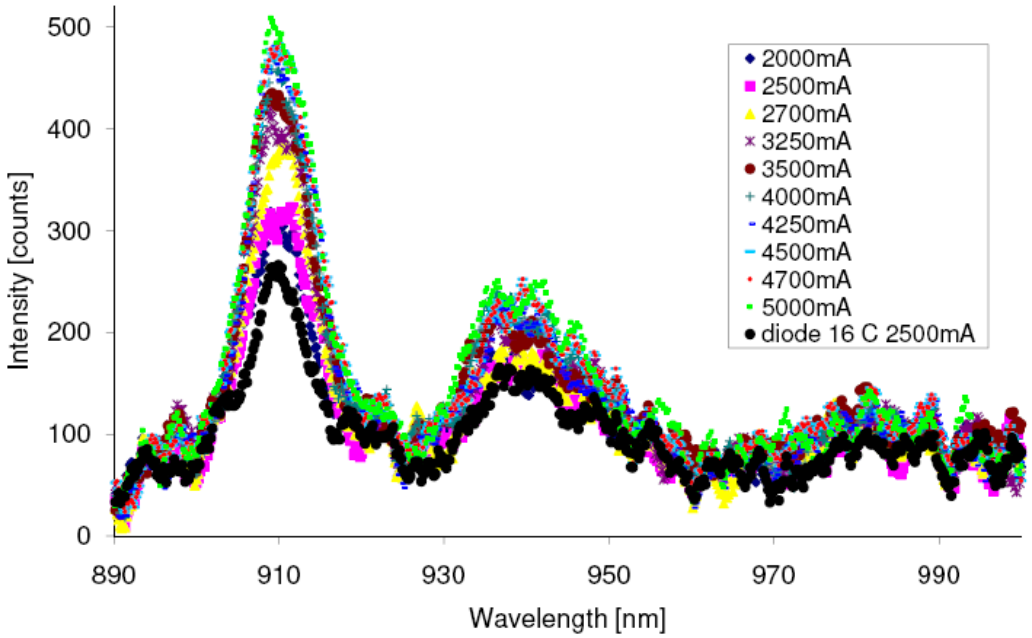

Figure 127. Raw fluorescence data shows gain at the 910 nm diode superradiance line that overlaps with the fluorescence transition in the nanoparticles. The ratio of the unamplified 910 nm peak to the 940nm diode peak at 2500 mA and at 4500 mA was ~1.6 ± 5%.

Once completely aligned with adequate filters in place to mask the laser transition and suppress the superradiance lines from the diode, an effort to resolve the fluorescence from the 1054 line was made. No fluorescence transition was observed. The 1054 line had completely disappeared on the return trip and one of the RG850 filters suppressing the superradiance was removed in an attempt to boost the signal. Still, almost no light was seen at 1050 nm. However, the 910 nm line was unusually strong and the fluorescence vs. pumping power was measured (Figure 127).

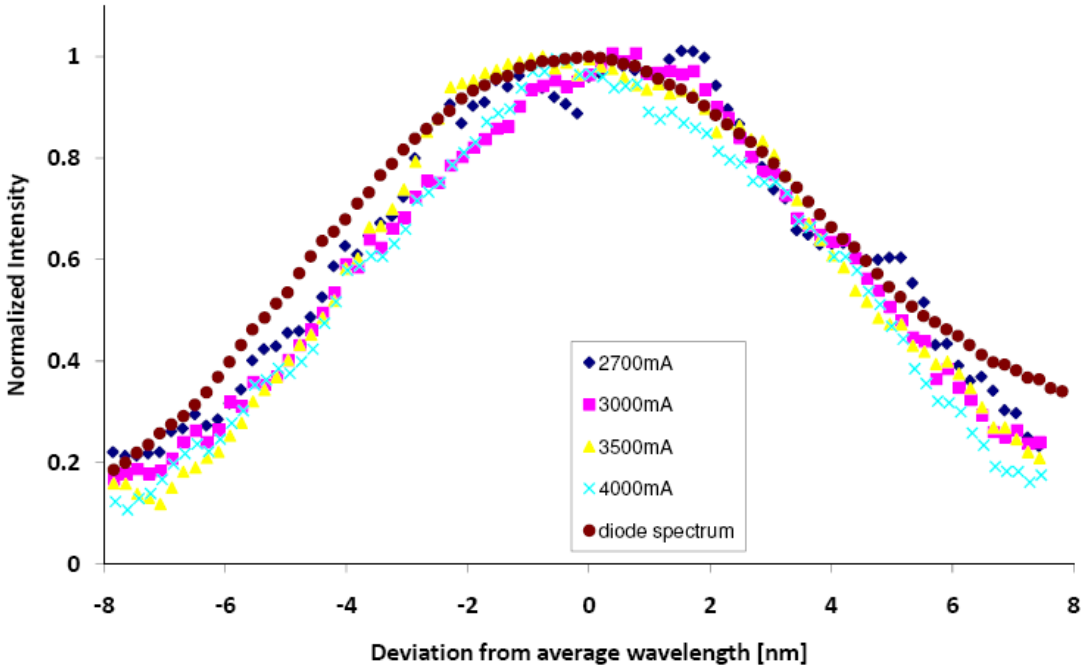

Figure 128. Evidence of gain narrowing was seen in the normalized amplified spectra as the diode current was increased.

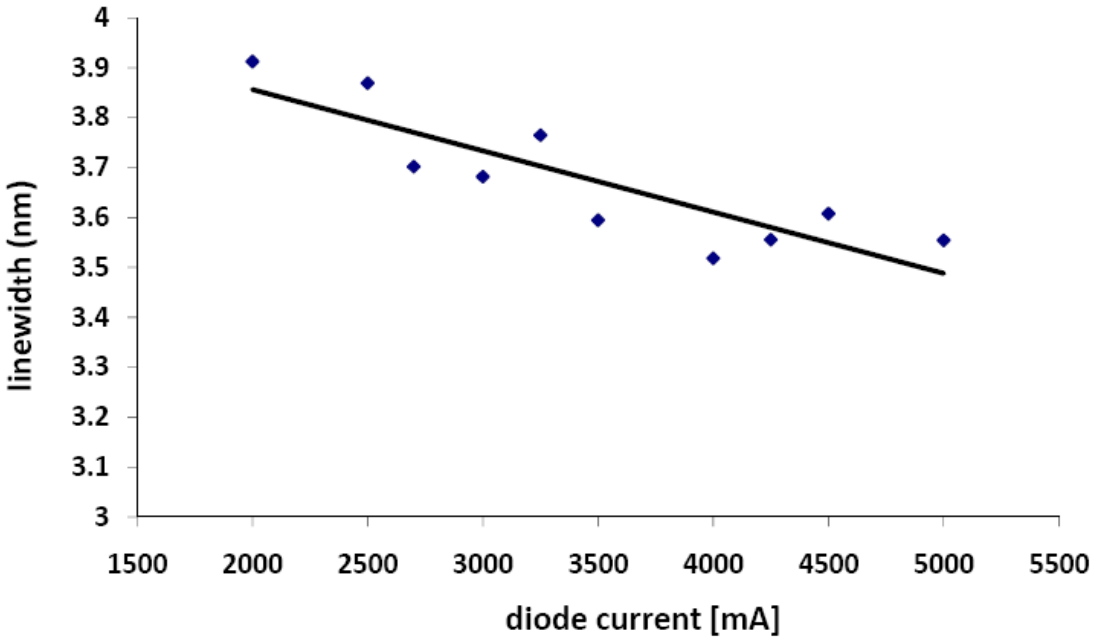

Figure 129. Gain narrowing as a function of diode current.

Gain narrowing of the 910 nm transition was observed (Figure 128 and Figure 129). At the time of the measurement there was no way to tell if the gain was due to some artifact of the diode laser or the result of the nanoparticles fluorescing. Comparison of the 910 nm line with the 930 and 950 superradiance lines facilitated the missing piece of the measurement since the optical path at 930 is similar to that at 910 except for lacking gain. During the 1 m round trip in the LWCFC, the signals diverged by approximately 20 percent.

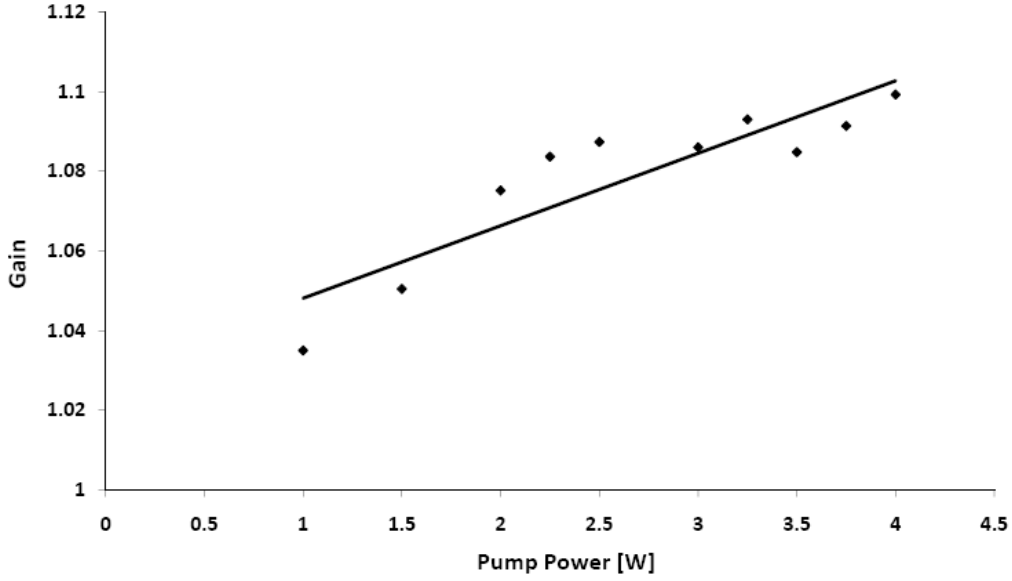

Figure 130. Gain over a 1m path for colloidal Nd^{+3} doped nanoparticles pumped at 4 W in a LWCFC.

The single pass gain at 910 nm over 1 m was measured to be ~10%, when pumping with 4 W in a 0.260 mm diameter spot or ~7.5 kW/cm^2 (Figure 130). Since the lifetime was measured at 20 μs for this sample, the saturation fluence was 365 kW/ cm^2, therefore the pump was not saturating the transition and the exponential approximations to the equations for the pumping rate and small signal gain hold, assuming the density of this sample was comparable to past samples and the cross section was within a factor of 2

of the bulk. According to a fit to the equations for single pass gain presented in Chapter 2 (corrected for the fact that the terminal level of the 910 nm transition is thermally coupled to the ground state), the predicted single pass gain lies between 5% and 10%. However, this does not account for the fact that the wavelength of the pump drifts with both power and temperature. The diode was running at 16° C and therefore it was not possible to further detune it without causing potential damage. The effect of the pump wavelength on the gain should be measured in future experiments. As mentioned in the previous chapter, the values obtained for the nanoparticle concentration using both the TEM and absorption measurements are consistent with the values measured for the gain thus verifying that the absorption cross section does not deviate substantially from the bulk cross section reported by Kigre of $\sigma_p \approx 4 \times 10^{-20}$ cm^2. Moreover, since the path length through the sample was sufficient to significantly deplete the pump (i.e. absorbing >50% of the pump light), the gain measurement pins down the cross section for stimulated emission at 910 nm to within a factor of two of bulk $\sigma_l \approx 7 \times 10^{-20} \pm 2 \times 10^{-20}$ cm^2, despite not having an accurate measurement of the nanoparticle concentration for this sample. With concentration, fluorescence spectra, lifetime, and gain measurements available, it was possible to perform the types of scaling calculations discussed in Chapter 2. Though broad, the range of the laser parameters reported in this chapter do not significantly alter the conclusion of the scaling arguments made in Chapter 2 that colloidal nanoparticles are a suitable gain medium for high average power lasers.

Chapter 9: *Data Analysis*

To interpret the results of the experiments presented in the last chapter the brief review of QM presented in Appendix A will be helpful. The goal of this analysis is to understand how changing the host material from bulk to a nanoparticle affects the behavior of the transitions relevant to laser operation. The spectroscopic properties of the samples presented in the previous chapter were generally found to be consistent with those of bulk Nd^{+3} doped materials and suitable for laser development. The fluorescence peak of the $4F_{3/2}$ ->$4I_{11/2}$ transition (1064 nm in YAG and 1047 nm in YLF) varied between ~1047 nm and ~1057 nm and on average was shifted from the 1054 nm line observed in bulk glass. The lifetime of the $4F_{3/2}$ metastable state was measured to between 20 μs and 70 μs depending upon the average particle radius compared to 98 μs in bulk.

The starting material was produced from a puck of Kigre Q-X 20% Nd^{+3} doped phosphate laser glass ground into a fine powder with a mortar and pestle. During production we measured the concentration of the nanoparticles with a 1 m optical path length absorption flow cell and used Beer's Law to infer the concentration of Nd^{+3} ions. To obtain the concentration estimate, the cross section for absorption of the nanoparticles near 800 nm was assumed to be similar to that of the bulk material. With this assumption, the estimated nanoparticle concentration of a typical sample was ~0.01% ± 0.0025% (by volume) in ~35 mL of fluid (Figure 131). This corresponds to a nanoparticle production rate of approximately 1 mg/hr. Using a lock-in amplifier and a diode laser driven by a sinusoidal current, the fluorescence lifetime was measured to vary monotonically with particle radius between 17 μs and 73 μs. The fluorescence peak was

measured between 1047 nm and 1057 nm and found to depend on the wavelength of the diode laser as well as the average particle diameter. As mentioned in Chapter 5, a 0.5 μm mesh filter ensured that any micro-particulates present in the fluid could not enter the flow cell and affect the measurement. As demonstrated in Figure 131, the production rate changes significantly over the course of a run. In hour 5-6 the solution gained nearly as many particles as it did in hours 1-5. The variation in production rate is attributed to the difficulties encountered preparing and feeding an aerosol of uniform density to the LAM reactor.

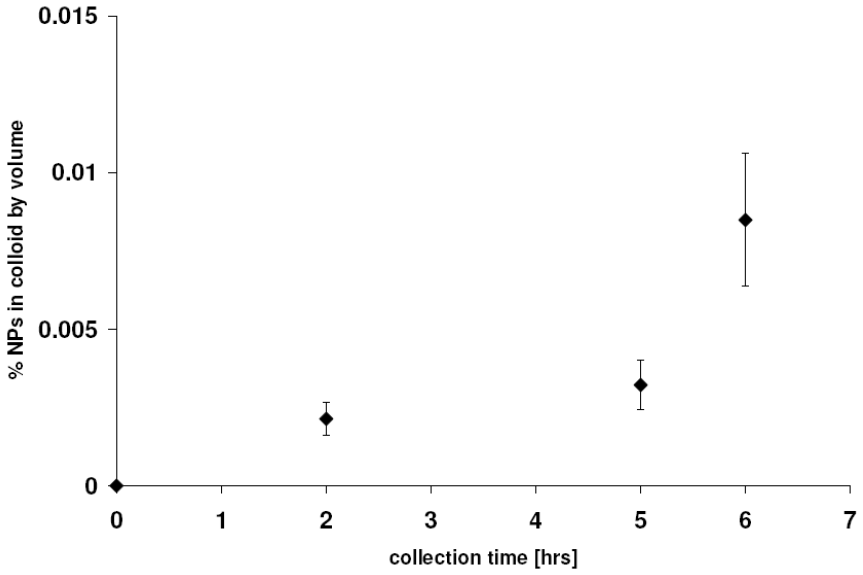

Figure 131. nanoparticle density [% vol] vs. time [hr].

Earlier estimates of particle density obtained by dipping TEM grids in the fluid and evaporating the excess solvent and then counting the particle density with a computer (Figure 132) agree with the optical technique as mentioned in Chapter 6. The error bar on the counting method is set by an estimate of the height of the meniscus that formed on the grid due to the surface tension of the colloid. This method, while crude, provided an

important consistency check on the validity of the absorption measurement by providing an absolute upper bound of 0.005% nanoparticles by volume (for an ~50 μm meniscus) and a 0.0005% nanoparticles by volume lower bound (for an ~500 μm meniscus) for the solution's concentration, as well as indirectly verifying that the absorption cross section, crucial to laser design, was not drastically changed by the LAM process (i.e. σ nanoparticle /σ_{bulk} ~ O(1)).

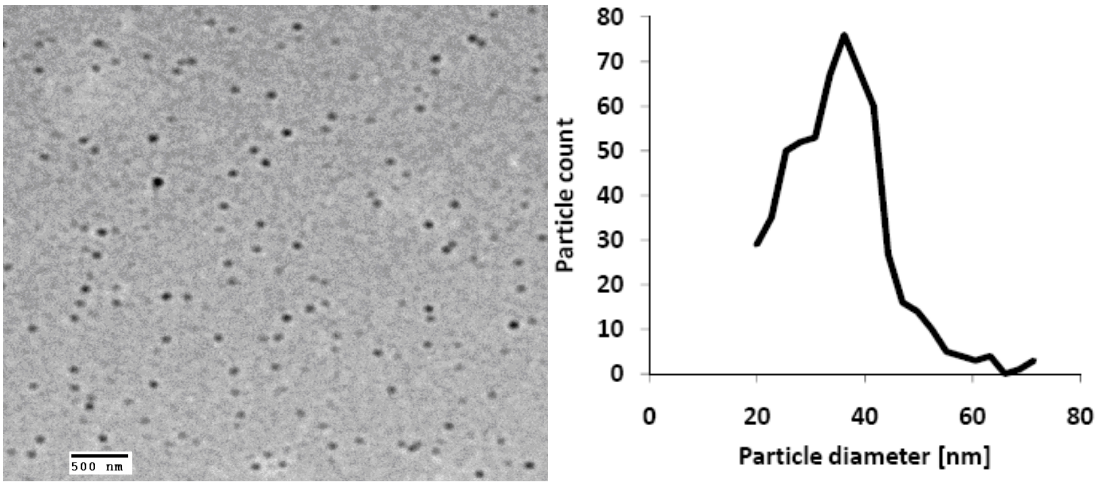

Figure 132. TEM image of Nd^{+3} doped nanoparticles collected in nonanoic acid and the size distribution [count] vs. particle diameter [nm] with a peak at 38 nm and an 8 nm standard deviation obtained by counting the particles in the image.

Given the fact that the nanoparticles condense from a vapor and rapidly cool it is reasonable to expect the particles to be spherical and possess a structure similar but possibly more open than the bulk[58]. The stoichiometry should also resemble that of the original material. To verify these assumptions samples of nanoparticles were collected both by direct supersonic impaction onto and by dipping TEM grids in the colloid and evaporating the excess solvent. TEM images and the X-ray dispersion spectra (EDS) of the particles show spherical particles as well as the expected composition of the glass for both sample preparation methods[2]. As expected, FFT of the particles revealed no

crystalline phase. Moreover, as discussed in the previous chapter the spectra of solid and liquid nanoparticles show shifts away from their bulk counterparts.

Given the size distribution, potential inhomogeneities in phase, unknown surface chemistry and interactions with stabilizing surfactant, the behavior of this system, like many on this scale of nature is complex. Because of its robust quantum mechanical properties, the Nd^{+3} ion was chosen as the active ion in our first experiments to minimize the risk that the nanoparticle system's complexity would interfere with the ability to engineer robust optical properties into the colloid.

The Nd^{+3} ion has a xenon-like 5s25p6 configuration. The remaining valence electrons occupy the 4f sublevels that orbit well inside the 5s25p6 shells which provide an electrostatic screen from the external environment in accordance with Gauss' Law. Moreover, the active laser lines occur at forbidden dipole-dipole transitions to a ground state that is typically split into 4 sublevels with spacing large compared to kT. This is why the Nd^{+3} ion is utilized in such a wide variety of host materials with only minor changes in its behavior in laser systems. The robustness of its quantum mechanical properties makes the Nd^{+3} ion a good system to examine first when exploring the effect of system size. Other host particles and ions that interact more strongly with their external environment should be examined later for more intriguing behavior, now that the limits of the expected effects are established (for example Ti^{+3} doped sapphire).

Figure 133 shows fluorescence spectra for ~4 nm Nd^{+3} doped nanoparticles excited at different pump wavelengths. It is important to recall when studying the spectroscopy of these materials that rare earth doped laser glass is inhomogeneously broadened and the spectra is due to the collective local perturbative environment at each ion site and hence have very broad fluorescence peaks without suffering a decrease in

fluorescence lifetime. However, excitons in these materials are known to possess high mobility and can migrate over macroscopic distances during their lifetime.

This accounts for the insensitivity of the fluorescence spectrum to pump wavelength as well as the long red tail in the bulk spectra since it is more thermodynamically favorable for an exciton to move from a higher to a lower energy site. By contrast, the fluorescence spectra of Nd^{+3} in crystalline hosts that are broadened by dynamic or thermal effects have similar lifetimes but relatively narrow peaks typically in the range of 0.5 nm[23].

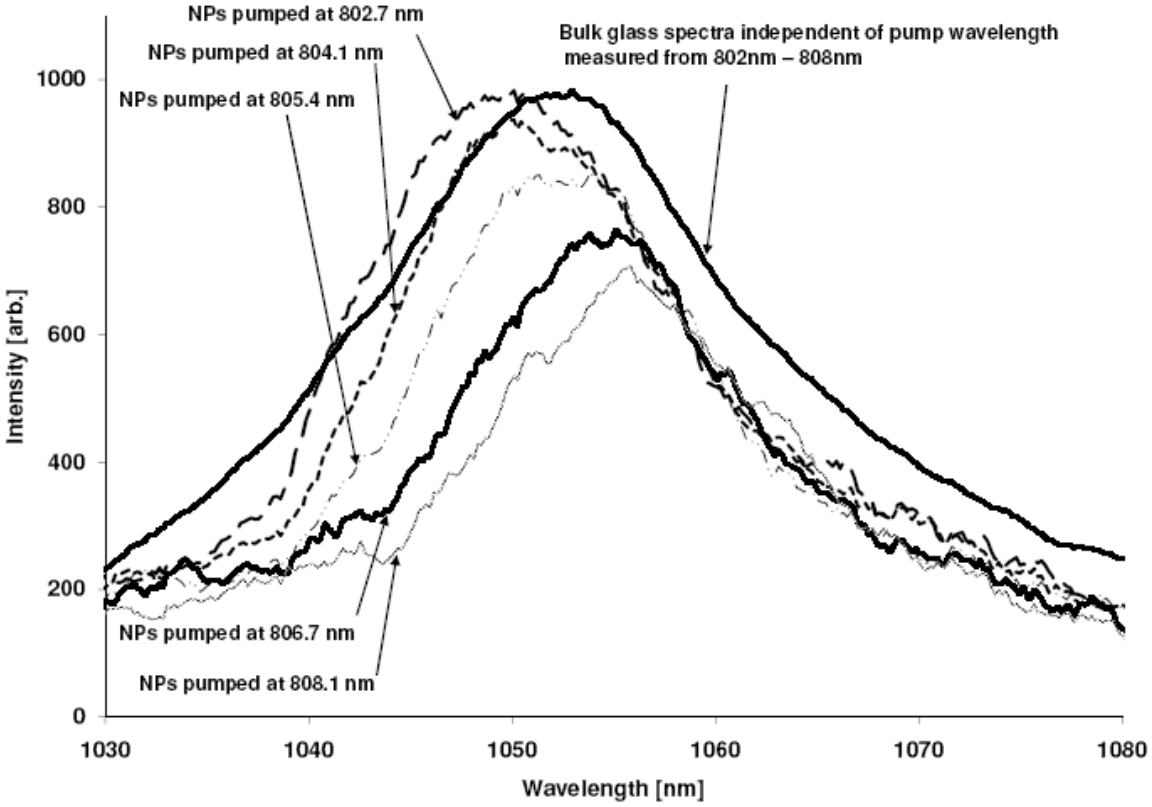

Figure 133. Fluorescence intensity [arb] vs. wavelength [nm] of 4 nm particles pumped at a range of wavelengths from 802 nm - 808 nm with the bulk glass spectrum as a reference.

The properties of the emission spectra can be explained by variations in the size of the nanoparticles[16]. The ions in the nanoparticles experience compressive forces due to the strain induced by the curvature at the surface during droplet formation as well as structural defects in the particle. The distribution of sizes of nanoparticles and small number of ions per particle prevent the excitons from experiencing significant migration. Therefore given the narrow size distributions accessible to the LAM technique it was possible to target specific local ion environments in a sample by simply varying the wavelength of pump light[56].

As mentioned in Appendix A, the quantitative recipe for calculating these emission spectra follows the standard variational and perturbative prescription for solving the Hartree-Fock equations for the Hamiltonian:[59]

$$
\begin{aligned}
&H = H_0 + H_{S.O.} + H_{CF},\\
&H_0 = -\frac{\hbar}{2m}\sum_i \nabla_i^2 - e^2\sum_i \frac{Z_i}{r_i} + e^2\sum_{i>j}\frac{1}{r_{ij}},\\
&H_{S.O.} = \sum_i \xi(r_i) l_i \cdot s_i,\\
&H_{CF} = \sum_{j,m} A^*_{jm}\sum_i r_i^l C_{jm}(\hat{\mathbf{r}}_i),\\
&C_{lm}(\hat{\mathbf{r}}) = \left(\frac{4\pi}{2l+1}\right)^2 Y_{lm}(\theta,\phi),\\
&A_{lm} = \sum_i \frac{Z_i C_{lm}\left(\hat{\mathbf{R}}_i\right)}{R_i^{l+1}}
\end{aligned}
\qquad \textbf{(43)}
$$

where R_k is the position of the k^{th} ligand relative to the Nd^{+3} ion center, Z_k is the charge of the ligand, C_{lm} is the spherical tensor corresponding to angular momentum l with projection m and r_i is the position of the i^{th} electron.

Using the data available for the tensor elements of the $4I_{11/2}$ and $4F_{3/2}$ wave-functions in YAG as a starting point, it is possible to expand the crystal field energies in

terms of the inter-atomic separation[60]. It is clear from Figure 133 that the bulk and an ensemble of nanoparticles possess approximately the same spectra. However, to accurately describe the spectra of Nd^{+3} ions in specific hosts, Judd-Olfelt theory requires that parameters, (usually labeled Ω_k) related to the oscillator strength, be fit to known spectra. These J-O parameters act to mix states and describe the approximate coupling between the multiplets and the host field. Unfortunately, due to limitations present in the collection and measurement apparatus available at this time we were unable to obtain useful absorption spectra that span the visible range. Thus to estimate the cross section of the ions in our nanoparticle we must carefully examine J-O theory and the data.

A consequence of Judd-Olfelt theory states that[23]:

$$\Omega_\lambda \propto \frac{1}{R^{(2\{\lambda \pm 1\}+2)}} \qquad \textbf{(44)}$$

Thus the terms of rank 2 (i.e. λ=2) in the crystal field will be most sensitive to inter-atomic separation, the 4th rank term less so, and the 6th rank terms will be relatively insensitive to perturbations in the radius. The 4th and 6th rank terms primarily affect the inter-multiplet branching ratios and contribute little to the splitting of energy levels.

By superimposing the fluorescence spectra for different particles excited over the range 802-808 nm a spectrum nearly identical to the bulk is produced (Figure 134). Therefore, on average the nanoparticles in our ensemble deviate by a small amount from the bulk and hence the changes to the individual particle spectra should be accessible with perturbation theory, which supports the hypothesis, discussed in the previous chapter that nanoparticles narrow the line widths of their emission by restricting the mobility of excitons to the small number of ions present in the particle.

Returning to the discussion of J-O theory while keeping in mind these qualitative observations will facilitate a quantitative interpretation of the dynamics underpinning

these spectra. The deviation in the 4^{th} and 6^{th} rank constants would manifest primarily as changes in the inter-spin-orbit multiplet branching ratios which we were unable to observe[59,60]. The inter-multiplet branching ratio is related to the spectroscopic quality parameter [59]:

$$Quality\ \ Parameter = \frac{\Omega_4}{\Omega_6} \tag{45}$$

For large values of this parameter the $4I_{11/2}$ transition is favored, while small values favor the $4I_{9/2}$ transition. Thus, if neither Ω_4 nor Ω_6 change from the bulk to a nanoparticle ensemble, then the branching ratio among the multiplets remains constant for the laser transition as will its contribution to the slope efficiency of a laser operating on either of these transitions. Hence, carefully inspecting the scaling of the J-O parameters will eventually allow us to extract estimates of the laser parameters for our material.

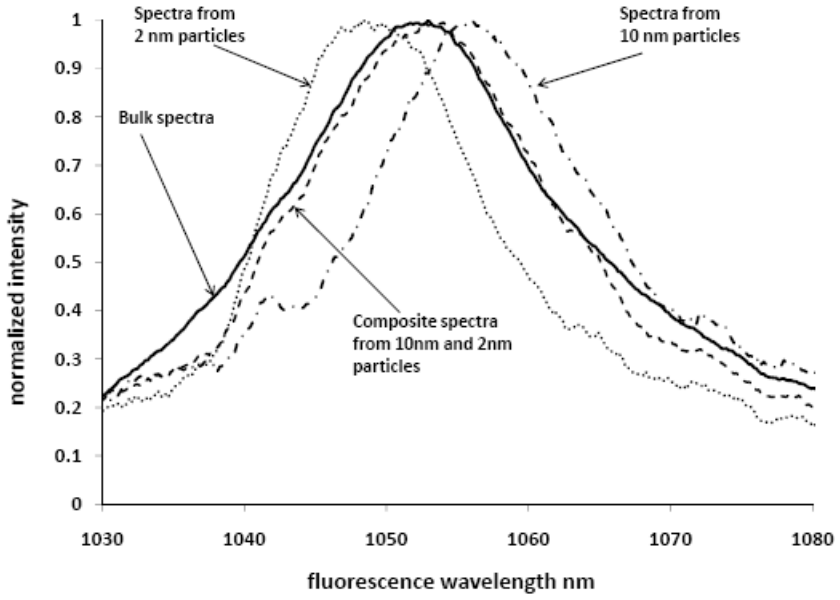

Figure 134. Fluorescence intensity [arb] vs. wavelength [nm] for a composite spectra of 2 nm particles pumped at both 802 nm and 808 nm added to the spectra from 10 nm particles also pumped at 802 nm and 808 nm to form a composite spectra that closely resembles the bulk.

The expression for the J-O parameters is related to the expression for the coefficients for spontaneous emission and hence the radiative lifetime by:[23]

$$A_{ab} = \frac{(8\pi^2 e)^2 \chi}{3h\lambda^3} \sum_{\lambda=2,4,6} \Omega_\lambda \frac{\left| \left\langle 4f^n \alpha_a J_a \right\| U^{(\lambda)} \left\| 4f^n \alpha_b J_b \right\rangle \right|^2}{2J+1} \quad \textbf{(46)}$$

$$\frac{1}{\tau_a^r} = \sum_b A_{ab} \quad \textbf{(47)}$$

Since the $\langle a||U^{(\lambda)}||b\rangle$ terms depend weakly on the host environment we can write for both the nanoparticles and bulk[59]:

$$A_{ab} = \frac{(8\pi^2 e)^2 \chi}{3h\lambda^3} \frac{c_2^{ab}\Omega_2 + c_4^{ab}\Omega_4 + c_6^{ab}\Omega_6}{2J+1}, \quad \textbf{(48)}$$
$$A_{ab} = c_0\left(c_2^{ab}\Omega_2 + c_4^{ab}\Omega_4 + c_6^{ab}\Omega_6\right)$$

The branching ratio for both the $4I_{13/2}$ and $4I_{15/2}$ levels are small compared to the $4I_{11/2}$ and $4I_{9/2}$, hence we neglect their contribution to the radiative lifetime. Moreover, the second rank matrix terms are 0 for the $4I_{11/2}$ and $4I_{9/2}$ transitions allowing us to rewrite equation(48).

$$\frac{1}{\tau_{4F^{3/2}}^r} \approx c_0\left(c_4^{4I_{9/2}}\Omega_4 + c_6^{4I_{9/2}}\Omega_6 + c_4^{4I_{11/2}}\Omega_4 + c_6^{4I_{11/2}}\Omega_6\right) \quad \textbf{(49)}$$

Considering the fact that the sum of the c_4 constants (c_4 = 0.45) approximately equals the sum of the c_6 constants (c_6 = 0.35) and the structure of the glass should be similar to that of the bulk except for a small uniform compression, the changes in ligand distance will primarily affect the 4th rank J-O parameter due to the scaling of equation (45). Therefore by collecting terms in equation (49) we can write an expression for how a change in the lifetime would affect the 4th rank J-O parameter to first order:

$$\Omega_4^{NP} - \Omega_4^{bulk} \approx c_t \Delta\tau_{4F^{3/2}}^{r_{NP}} \left(b\Omega_4^{NP} + 1\right)\left(b\Omega_4^{bulk} + 1\right)$$

$$\Delta\Omega_4 \approx \frac{c_t \Delta\tau_{4F^{3/2}}^{r_{NP}} \left(b\Omega_4^{bulk} + 1\right)^2}{1 - c_t \Delta\tau_{4F^{3/2}}^{r_{NP}} b\left(b\Omega_4^{bulk} + 1\right)} \quad \textbf{(50)}$$

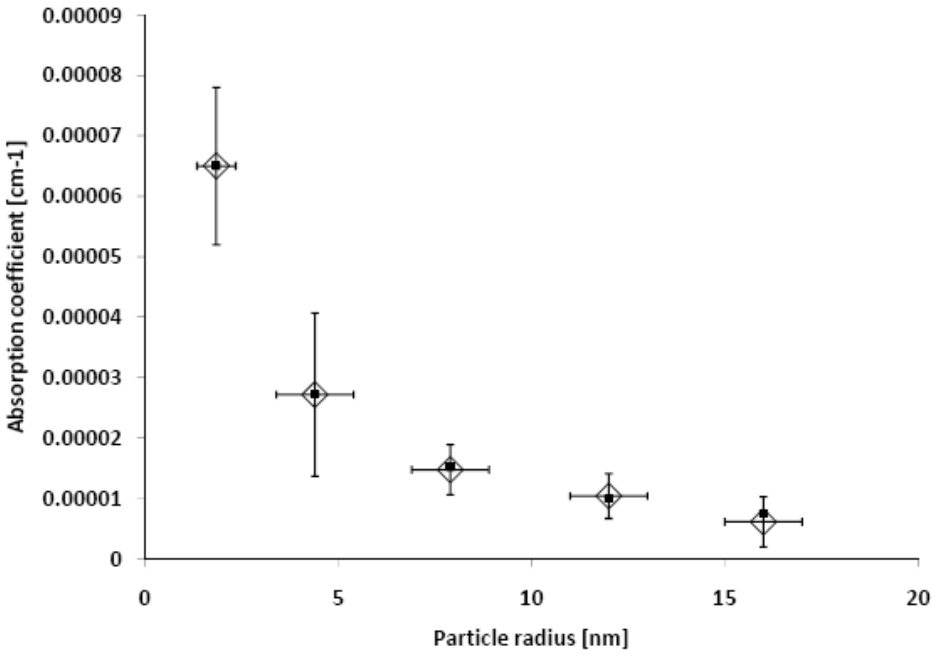

Figure 135. Absorption coefficient α_{OH} [cm^{-1}] at 3000 cm^{-1} vs. particle radius [nm]. Clear diamonds correspond to the measured value and squares correspond to a fit to the model: constant/r.

Figure 135 plots the absorption coefficient at 3000 cm^{-1} due to OH^- concentration as a function of particle size. From Campbell et al. we know the additive nonradiative decay rate due to OH^- can be written as[2]:

$$k_{OH} = \frac{1}{\tau_{quenched}} - \frac{1}{\tau_{rad}} \quad \textbf{(51))}$$

$$k_{OH} = Q_{OH}\alpha_{OH}$$

Q_{OH} is the quenching rate ~600 Hz/cm, extrapolated from measurements cited by Campbell et al. for 20% Nd^{+3}, and α_{OH} is the absorption coefficient (in cm) which should

therefore correspond to the average density of OH^- ions[61,62,63,64,65,66]. In our nanoparticles, the density of OH^- proximate to the average Nd^{+3} ion should scale like the surface area to volume ratio or 3/r. The curve in Figure 135 follows a 1/r power law with a single fit parameter which agrees well with the predicted scaling for a 20% Nd^{+3} nanoparticle surrounded by OH^- ions. In this manner we have shown that OH^- quenching accounts for the measured change in fluorescence lifetimes for all particle sizes. Thus using equation (50) we can conclude that within the accuracy of our measurements the radiative lifetime and therefore Ω_4 remain unchanged.

Finally, since neither the spectra from the entire nanoparticle ensemble nor the radiative lifetime of the particles significantly differ from that of the bulk, we can conclude that the branching ratio must also remain approximately constant and hence the cross section for stimulated emission must not have significantly changed from the bulk. Thus we can see that within the resolution of our measurement, the spectroscopic properties of the $4F_{3/2}$ to $4I_{11/2}$ laser transition in the nanoparticle agree with bulk values.

While direct measurement of the spectroscopic parameters of our system would be preferable to indirect arguments, we were unable to obtain absorption spectra in the visible region, due to the challenging nature of the experiment. The absorption data tended to be noisy and broad band, possessing only a few resolvable peaks. The data was therefore unsuitable for Judd-Olfelt analysis.

For the $4I_{11/2}$ transition, the fluorescence spectra of the nanoparticles are both shifted and narrower than that of bulk glass (Figure 133, 133 and 134). As discussed above we can attribute this feature to a compression stress due to the surface configuration of the particle as well as a decrease in the number of available potential migration sites. Strain and hence compressive force increases as particle size decreases.

Similar effects were obtained from x-ray diffraction data for Ce doped YAG nanoparticles and modeled using similar arguments by Li et al[16].

Each size of nanoparticle produces a slightly different range of local crystal field environments for the Nd^{+3} ions. Moreover, the decrease in full-width half-max of the spectra with nanoparticle size points to a decrease in excitation migration effects that effectively redistribute site specific excitations among the larger population present in the bulk (Figure 136). The signature of this effect is the wavelength dependence on excitation spectra and the long red tale seen in the larger particles which is not present in the smallest particle sizes[67].

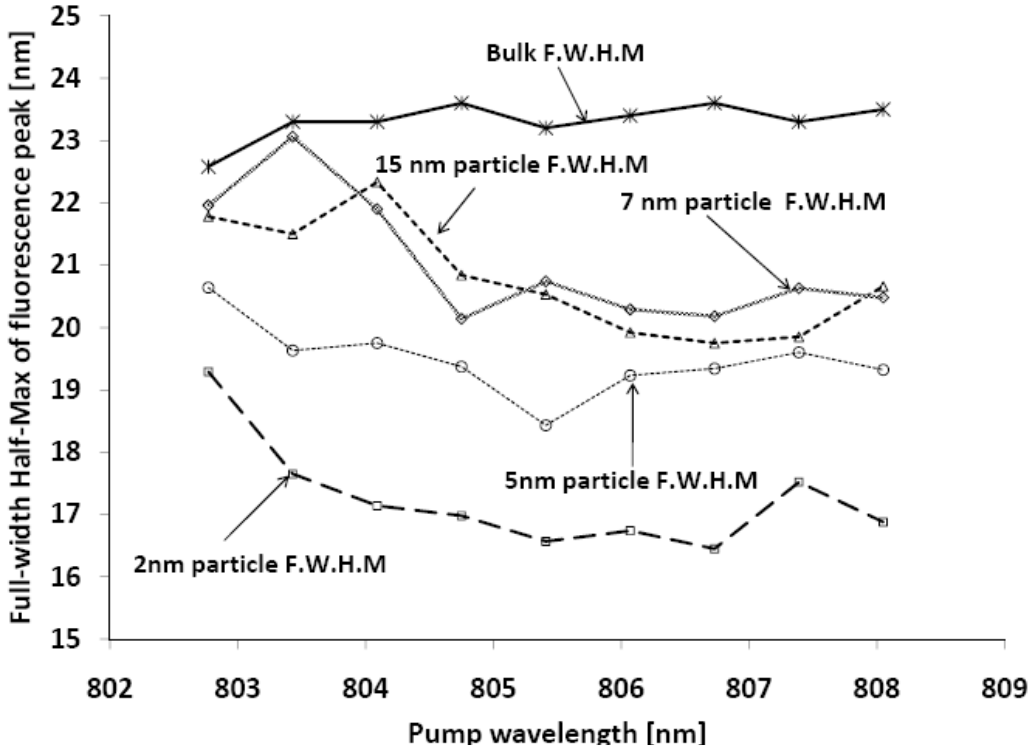

Figure 136. Full width half max of fluorescence peak [nm] vs. pump wavelength [nm] for a range of particle sizes

In preparing a mono-disperse population of nanoparticles we effectively selected a more homogeneous population of ions and moreover, can tune the ions we excite by varying the frequency of the pump laser. Powell et al reached similar conclusions in their studies of YAG where defects in the YAG structure that altered the average ligand distance gave rise to shifted emission spectra[57]. To estimate the change in interatomic separation for the phosphate glass sample without a complete description of the crystal field potential, one can make the somewhat unlikely assumption that the tensor elements of the multipole expansion of the ligand field for the $4F_{3/2}$ to $4I_{11/2}$ transition is approximately the same for both YAG and our sample.

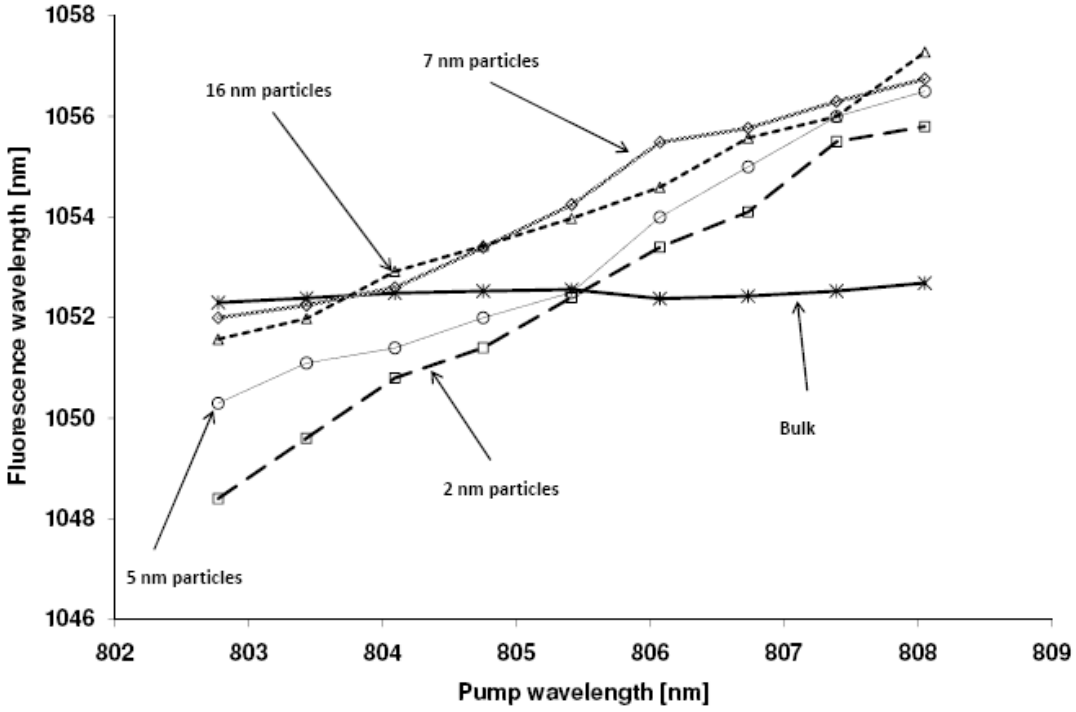

Figure 137. Peak fluorescence wavelength [nm] vs. Pump wavelength [nm] for a range of particle sizes.

Given the fact that the emission spectra from our particles contains a strong 1064 nm component one might conclude from the orthogonality principle that at least to

first order some of the local sites in the nanoparticle have similar tensor components. Therefore the data in Figure 137, allows us to indirectly measure the approximate change in distance between the ligands and active ions due to the surface conditions of the nanoparticle, using our understanding of the Nd^{+3} ion's behavior in YAG as a toy model. Though crude, this assumption allows us to describe the perturbations a host field could produce in the wave functions without wading into the complexities that make rigorous ab initio crystal field calculations for rare earth ions challenging. Moreover, the results agree to within a factor of two with results obtained for YAG nanoparticles measured by XRD by Li et al[16]. They report a 3.8% change in the lattice parameter in YAG nanoparticles while we calculate at most a 1.2% shift in lattice spacing based on the data presented in Figure 137.

Thus utilizing the model for YAG, the crystal field parameters that affect the laser transition are written[59]:

$$V_{cf} = A_{20}\left\langle r^2 \right\rangle + A_{40}\left\langle r^4 \right\rangle \tag{52}$$

Orthogonality dictates:

$$\begin{aligned} \left\langle 4I_{11/2} \middle| r^4 \middle| 4I_{11/2} \right\rangle &= 0, \\ \left\langle 4F_{3/2} \middle| r^2 \middle| 4F_{3/2} \right\rangle &= 0 \end{aligned} \tag{53}$$

Treating Vcf perturbatively we can calculate an expansion in terms of a small radial displacement. We then compute dr from the change in the energy between the bulk and the nanoparticles in equation (54), from which the required shift in average radial distance of the ions is obtained.

$$\Delta V_{cf} = \left\langle 4F_{3/2} \middle| \delta H \middle| 4F_{3/2} \right\rangle - \left\langle 4I_{11/2} \middle| \delta H \middle| 4I_{11/2} \right\rangle \approx$$
$$\left\langle 4F_{3/2} \middle| A_{40} r^4 \middle| 4F_{3/2} \right\rangle (4\varepsilon) - \left\langle 4I_{11/2} \middle| A_{20} r^2 \middle| 4I_{11/2} \right\rangle (2\varepsilon)$$
$$\varepsilon \approx \frac{\Delta V_{cf}}{4A_{40}\left\langle r^4 \right\rangle - 2A_{20}\left\langle r^2 \right\rangle}, \qquad \textbf{(54)}$$
$$where \quad \varepsilon = \frac{dr}{r}$$

Thus some of the features present in the spectra seem to be related to the compression in the nanoparticle. The inability of excitons to access a large thermal population of Nd^{+3} sites for migration, contributes to the upward sloping trend seen in Figure 137. This is complemented by the fact that smaller nanoparticles have fewer Nd^{+3} ions and hence should have a restricted continuum of sites available for migration, while compression of the particle due to its high surface potential shifts the average energy of the transitions as particle size decreases.

Chapter 10: *Conclusions and Future Directions*

In summary, we have fabricated a new type of laser gain material that we believe could dramatically improve the performance of future laser systems facilitating the development of practical high average power systems. High average power lasers have long been pursued by many sectors of society. Proposed applications include heavy industry, defense and energy. Despite many years of investigation, the goal of creating a laser gain medium capable of supporting high performance high average power laser operation remains elusive.

We believe this can be explained a priori by basic thermodynamic arguments about the gain materials. For example, heat transport in dielectric solids is primarily achieved through acoustic processes determining both the temperature of the solid and the magnitude of internal stresses that can distort optical properties and lead to material failure. Therefore, the maximum achievable power from lasers that depend on dielectric hosts will be limited to some multiple of the rate of heat transport through the surface (set by the heat capacity, geometry and volume of the material) and the quantum mechanical efficiency of the available dopant species' optical transitions. For currently available crystalline, glass, and ceramic materials this number peaks in the multi kW range for sustained operation.

In liquids the amount of QM phase space available to dyes due to collision rates and rotational coupling, results in a large continuum of possible perturbations to wave

functions and hence rapid depopulation of metastable excitations, resulting in poor energy storage.

Lasers based on gas or plasma phases have a more simplistic relationship between performance and one extensive thermodynamic parameter in particular: volume. The physical extent of the gain medium required to store large quantities of energy often exceeds the limitations of practical laser design. The air-born laser (ABL) and THEL laser systems are prime examples of this problem, requiring a one billion dollar modified 747 and a small base respectively for deployment. Moreover the metastable states in these systems tend to have relatively large cross sections for stimulated emission and hence excessive gain which makes it difficult from an engineering perspective to preserve beam coherence at the large beam diameters required to achieve high power operation. In a first step toward circumventing these difficulties we have synthesized and measured the optical properties of a laser material in a different thermodynamic phase, namely a colloidal emulsion of nano-scale solid-state laser material. The absorption and excitation spectra of the new material as well as the fluorescence lifetime were comparable to the original solid state laser material and scale with particle diameter. Therefore, we believe that a colloidal emulsion of nanoparticles could possess the advantages of solid state lasers (compactness, high efficiency) with the benefits of liquid hosts (easy to cool, impossible to damage) with none of the disadvantages of gas, plasma, or chemical lasers (excessive gain and limited magazine depth). While it is currently very challenging to prepare a large sample of the material and issues of surfactant and particle stability have yet to be resolved, the scope of investigation required to address these problems at this

point seems more restricted than the original work of engineering methods for mass producing exotic laser crystals and glasses of high purity and optical quality.

YAG laser rods typically have dopant concentrations of only ~1-2%. The final Nd^{+3} concentration of our emulsion is roughly ~$1/100^{th}$ of that found in a typical YAG laser rod. Thus, a LAM reactor would only have to modestly increase its production rate to create practical quantities of viable solid state-like laser materials. For example by simply replacing the 80 W laboratory LAM laser with a more industrial 1 kW system, the nanoparticle production rate could increase from the current ~0.5 mg/hr to ~10-20 mg/hr. Moreover, if the problems with aerosolizing the powder were resolved it should be possible to increase the production rate by another factor of 5-10. For example as stated in Chapter 7 approximately 1000 mg of spherical fused silica glass was fed through the LAM reactor in less than 0.5 hr compared with normal feeding rates for our powder of less than ~250 mg/hr. Finally, by decreasing our chamber's dead space and hence the required collection volume from ~50 mL to 5-10 mL we could rapidly produce useful quantities of material with Nd^{+3} concentrations similar to those found in other high energy high power gain media. Such improvements would allow for the rapid prototyping of various colloidal chemistries to test and optimize the thermal and optical properties of many species of nanoparticle with a host of different surfactants.

The option of using a non-interacting nanoparticle ensemble as a host for active ions, in principle could free the designer of a laser gain material from needing to worry about many of the issues that plague the development of new solid state laser materials. While some particles will contain defects, lattice dislocations, strong birefringence, color

centers and other quenching mechanisms undesirable in bulk laser materials, their effect on laser performance will be limited to only the small number of ions contained in a single particle. This opens up the exciting possibility of engineering new solid state hosts with highly desirable optical properties that would otherwise make poor bulk hosts due to structural, thermal, dielectric, or nonlinear issues.

In addition to the possibility for developing novel host media which can't be manufactured in bulk form, we have demonstrated that we can use the size of our nanoparticle to engineer a medium with tunable emission spectra which by itself is a useful result with potential applications in gain shaping and ultrafast laser technology (for example by mixing multiple species of nanoparticles in a single colloid). Finally, if one can discover mechanisms to functionalize the surfaces of different hosts with compounds that can be linked into a polymer one could imagine creating solid state admixtures of particle species, size and concentration to produce inexpensive broadly tunable solid state gain media for specific low power applications[68]. In principle the process of imbedding nanoparticles into polymers has already been demonstrated for many well known nanoparticle species and provides an avenue for future materials development.

Though it remains challenging to manufacture this material, the data and sample quality suggest that it might be possible to design a small laser system capable of testing the scalability of this material, its sensitivity to heat, and therefore its suitability for high average power applications. Limitations on the performance of these nanoparticle based systems would most likely be determined by the ability to correct wave front distortions

due to scattering off small density perturbations in the fluid flow. Commercially available adaptive optics technology can effectively correct this type of beam distortion, in principle permitting operation of beams at average powers many orders of magnitude greater than is currently possible. In brief, colloidal nanoparticles represent a new class of laser gain media with the potential to break through decades old barriers restricting the development of high performance laser technology.

Appendix A: *Time Dependent Transitions in an External E-M Potential*

This Appendix is just a quick reference guide to help bring the reader up to speed with some of the notation used by R. Powell in his book, The Physics of Solid State Materials (a very solid background in quantum mechanics is presumed). This book and the discussion below are a good jumping off point for learning the underlying physics that governs the spectra of large atoms and not intended as a substitution for reading the Quantum Theory of Atomic Structure by John Slater, or the papers by Judd and Olfelt. For the sake of brevity Powell at times omits some elementary steps in his presentation of the elementary physics underpinning the interaction of an atom with radiation. To aid the reader in their understanding of his presentation the derivation below focuses on filling in and clarifying some of these gaps.

There are several approaches to understanding the operation of lasers. However, the starting point for all of them is a good description of light. The formalism presented here that utilizes quantum mechanical, thermodynamic and electro-dynamic descriptions of light when convenient draws heavily on the presentation put forward by R. Powell in the Physics of Solid State Laser Materials. His derivation partially reproduced here examines the processes of spontaneous and stimulated emission of radiation from an excited atom. Next, Einstein's formalism is used to deduce the bulk properties of an ensemble of interacting atoms and photons. Finally, using classical electro-dynamics the equations for a laser system can be written, demonstrating how atomic processes influence and constrain laser performance.

Starting with Schrödinger's equation:

$$\frac{i\hbar\partial}{\partial t}\Psi = H\Psi \qquad \textbf{(55)}$$

With the Hamiltonian specified in the usual way:

$$
\begin{aligned}
&H = H_0 + H_{S.O.} + H_{CF},\\
&H_0 = -\frac{\hbar}{2m}\sum_i \nabla_i^2 - e^2\sum_i \frac{Z_i}{r_i} + e^2\sum_{i>j}\frac{1}{r_{ij}},\\
&H_{S.O.} = \sum_i \xi(r_i) l_i \cdot s_i,\\
&H_{CF} = \sum_{j,m} A^*_{jm}\sum_i r_i^l C_{jm}(\hat{\mathbf{r}}_i),\\
&C_{lm}(\hat{\mathbf{r}}) = \left(\frac{4\pi}{2l+1}\right)^2 Y_{lm}(\theta,\phi),\\
&A_{lm} = \sum_i \frac{Z_i C_{lm}(\hat{\mathbf{R}}_i)}{R_i^{l+1}}
\end{aligned}
\qquad \textbf{(56)}
$$

the kinetic terms and Coulomb potential are gathered into the term H_0 and are solved using the Hartree-Fock method. The Spin orbit and finally the crystal field terms are treated as perturbations and written in an expansion of spherical tensors. The perturbations to the wave function and eigenvalues take the usual form:

$$\Psi_a = \Psi_{a0} + \sum_b \frac{\langle \Psi_{a0} | H_{perturb} | \Psi_{b0} \rangle}{E_{a0} - E_{b0}} \Psi_{b0} \qquad \textbf{(57)}$$

and are applied in order of decreasing strength. In the case of Neodymium, spin orbit coupling is considered before the crystal field perturbations.

Assuming the wave-functions are known, it is possible to calculate their projection onto any complete basis.

$$|\Phi\rangle = \sum_a \sum_i |\Phi_i\rangle\langle\Phi_i|\Psi_a\rangle \qquad \textbf{(58)}$$

Therefore it is also possible to discern the solution to the question how does an atom interact with a photon assuming the description of the vector potential of a plane EM wave. Much of this discussion is just a review of time dependent perturbation theory, however, following this argument will allow us to develop a useful and consistent framework connecting the fundamental physics and the spectroscopic notation to the

engineering equations of laser operation. To balance brevity against the need to construct a useful framework for interpreting the results and understanding the basic physics underlying our experiments, we will summarize the key points of chapter 3 in Physics of Solid State Laser Materials and refer the reader to that text for clarification of any omitted steps[59]. The frame of reference Powell elected to work with is the second quantized formalism which simply makes use of a quantized photon field that interacts with the Hamiltonian instead of the more prevalent classical description of an electromagnetic plane wave. Conceptually this makes for a tidy if formal connection between the laser rate equations and the atomic physics underpinning them, since it couples the electromagnetic field's contribution to the Hamiltonian using creation annihilation operators for both photons in the field and excited atomic states.

Starting from Maxwell's equations in the Coulomb gauge ($\nabla \cdot A=0$) the wave equation for the vector potential is just:

$$\nabla^2 \boldsymbol{A}(r,t) - \frac{1}{c^2}\frac{\partial}{\partial t}\boldsymbol{A}(r,t) = 0 \qquad \textbf{(59)}$$

This can be solved via the traveling plane wave Ansatz by separation of variables with periodic boundary conditions in the spatial solution where A(r+L) = A(r). Solutions will therefore have the form (α indicates polarization) [59]:

$$\begin{aligned} &\boldsymbol{A}(\vec{r},t) = q(t)\boldsymbol{A}(\vec{r}) + q^*(t)\boldsymbol{A}^*(\vec{r}) \\ &\boldsymbol{A}_\alpha(\vec{r}) = \hat{\varepsilon}_\alpha\left(\frac{4\pi c^2}{L^3}\right)e^{i\vec{k}\cdot\vec{r}}, \quad k_{\alpha i} = \frac{2\pi n_{\alpha i}}{L_i}, \qquad (n_{\alpha i} = 0,\ 1,\ 2,\ ...) \\ &q_\alpha(t) = q_{\alpha 0}e^{-i\omega_\alpha t} \end{aligned} \qquad \textbf{(60)}$$

As usual $\lambda_\alpha = k_\alpha/2\pi$. So the full solution becomes:

$$\boldsymbol{A}(\vec{r},t) = \sum_\alpha \sum_{\lambda_\alpha} q_\alpha^\lambda(t)\boldsymbol{A}_\alpha^\lambda(\vec{r}) + q_\alpha^{\lambda^*}(t)\boldsymbol{A}_\alpha^{\lambda^*}(\vec{r}) \qquad \textbf{(61)}$$

Thus in this choice of gauge the electric field is simply:

$$\boldsymbol{E}(\vec{r},t-)=-\frac{1}{c}\frac{\partial}{\partial t}\boldsymbol{A}(\vec{r},t)=\sum_{\alpha}\sum_{\lambda_\alpha}\frac{i2\pi}{\lambda_\alpha}\left(q_\alpha^{\lambda}(t)\boldsymbol{A}_\alpha^{\lambda}(\vec{r})-q_\alpha^{\lambda^*}(t)\boldsymbol{A}_\alpha^{\lambda^*}(\vec{r})\right) \tag{62}$$

In this form, computing the energy in the field is straightforward. Note that since an atom is significantly smaller than the wavelength of light, the curvature of the E-M field is insignificant and the plane wave approximation is very robust locally, though not generally valid for a propagating beam.

$$\begin{aligned}\boldsymbol{H}_{EM}&=\frac{1}{8\pi}\int\left(E^2+B^2\right)dV=\frac{1}{4\pi}\int\left(E^2\right)dV\\&=\frac{1}{4\pi}\int\left[\left(\sum_{\alpha}\sum_{\lambda_\alpha}\frac{i2\pi}{\lambda_\alpha}\left(q_\alpha^{\lambda}(t)\boldsymbol{A}_\alpha^{\lambda}(\vec{r})-q_\alpha^{\lambda^*}(t)\boldsymbol{A}_\alpha^{\lambda^*}(\vec{r})\right)\right)\left(\sum_{\alpha'}\sum_{\lambda'_{\alpha'}}\frac{i2\pi}{\lambda'_{\alpha'}}\left(q_{\alpha'}^{\lambda'}(t)\boldsymbol{A}_{\alpha'}^{\lambda'}(\vec{r})-q_{\alpha'}^{\lambda'^*}(t)\boldsymbol{A}_{\alpha'}^{\lambda'^*}(\vec{r})\right)\right)\right]dV\end{aligned} \tag{63}$$

Expanding the vector potential using Euler's theorem demonstrates that the homogeneous terms integrate to zero (the cross terms become $\sin^2(ikr) + \cos^2(ikr)=1$). Therefore, by expanding the sum in the Hamiltonian the contribution from a single term becomes:

$$\boldsymbol{H}_{EM}=\cdots+\frac{1}{4\pi}\int\frac{i2\pi}{\lambda_\alpha}\frac{i2\pi}{\lambda'_{\alpha'}}\left(-q_\alpha^{\lambda}(t)\boldsymbol{A}_\alpha^{\lambda}(\vec{r})q_{\alpha'}^{\lambda'^*}(t)\boldsymbol{A}_{\alpha'}^{\lambda'^*}(\vec{r})-q_\alpha^{\lambda^*}(t)\boldsymbol{A}_\alpha^{\lambda^*}(\vec{r})q_{\alpha'}^{\lambda'}(t)\boldsymbol{A}_{\alpha'}^{\lambda'}(\vec{r})\right)dV+\cdots \tag{64}$$

However, orthogonality dictates:

$$\begin{aligned}&\frac{1}{4\pi}\int\frac{i2\pi}{\lambda_\alpha}\frac{i2\pi}{\lambda'_{\alpha'}}\left(-q_\alpha^{\lambda}(t)\boldsymbol{A}_\alpha^{\lambda}(\vec{r})q_{\alpha'}^{\lambda'^*}(t)\boldsymbol{A}_{\alpha'}^{\lambda'^*}(\vec{r})-q_\alpha^{\lambda^*}(t)\boldsymbol{A}_\alpha^{\lambda^*}(\vec{r})q_{\alpha'}^{\lambda'}(t)\boldsymbol{A}_{\alpha'}^{\lambda'}(\vec{r})\right)dV\\&=\frac{1}{4\pi}\frac{i2\pi}{\lambda_\alpha}\frac{i2\pi}{\lambda'_{\alpha'}}\int\left(-q_\alpha^{\lambda}(t)\boldsymbol{A}_\alpha^{\lambda}(\vec{r})q_{\alpha'}^{\lambda'^*}(t)\boldsymbol{A}_{\alpha'}^{\lambda'^*}(\vec{r})-q_\alpha^{\lambda^*}(t)\boldsymbol{A}_\alpha^{\lambda^*}(\vec{r})q_{\alpha'}^{\lambda'}(t)\boldsymbol{A}_{\alpha'}^{\lambda'}(\vec{r})\right)\delta_{\lambda,\lambda'}\delta_{\alpha,\alpha'}dV\end{aligned} \tag{65}$$

Dropping the primes and directly integrating the vector potential produces the following expression:

$$\begin{aligned}&=\frac{1}{4\pi}\frac{\omega_\alpha^2}{c^2}\left[q_\alpha^{\lambda}(t)q_\alpha^{\lambda^*}\int(t)\boldsymbol{A}_\alpha^{\lambda}(\vec{r})\boldsymbol{A}_\alpha^{\lambda^*}(\vec{r})dV+q_\alpha^{\lambda^*}(t)q_\alpha^{\lambda}(t)\int\boldsymbol{A}_\alpha^{\lambda^*}(\vec{r})\boldsymbol{A}_\alpha^{\lambda}(\vec{r})dV\right]\\&=\frac{1}{4\pi}\frac{\omega_\alpha^2}{c^2}\left[q_\alpha^{\lambda}(t)q_\alpha^{\lambda^*}(t)+q_\alpha^{\lambda^*}(t)q_\alpha^{\lambda}(t)\right]\left(4\pi c^2\right)\end{aligned} \tag{66}$$

Thus bringing back the sum yields the interaction Hamiltonian between the field and the atom[59].

$$\boldsymbol{H_{EM}} = 2\sum_{\alpha}\sum_{\lambda}\omega_{\alpha}^{2} q_{\alpha}^{\lambda}(t) q_{\alpha}^{\lambda^{*}}(t) \tag{67}$$

Transforming this expression into canonical coordinates allows the potential to be written in terms of ladder operators[59].

$$\begin{aligned} &Q_{\alpha}^{\lambda} = q_{\alpha}^{\lambda} + q_{\alpha}^{\lambda^{*}}, \quad P_{\alpha}^{\lambda} = \frac{\partial}{\partial t} Q_{\alpha}^{\lambda} = -i\omega_{\alpha}(q_{\alpha}^{\lambda} - q_{\alpha}^{\lambda^{*}}) \\ &q_{\alpha}^{\lambda} = Q_{\alpha}^{\lambda} - \frac{1}{i\omega_{\alpha}^{\lambda}} P_{\alpha}^{\lambda}, \quad q_{\alpha}^{\lambda^{*}} = Q_{\alpha}^{\lambda} + \frac{1}{i\omega_{\alpha}^{\lambda}} P_{\alpha}^{\lambda} \end{aligned} \tag{68}$$

Continuing this classic treatment of the simple harmonic oscillator the commutation relations and then the Hamiltonian are written in terms of the ladder operators[59]:

$$\begin{aligned} &\left[Q_{\alpha}^{\lambda}, P_{\alpha'}^{\lambda'}\right] = i\hbar\delta_{\alpha,\alpha'}\delta_{\lambda,\lambda'} \\ &\left[q_{\alpha}^{\lambda} + q_{\alpha'}^{\lambda'+}\right] = \frac{\hbar}{2\omega_{\alpha}} \\ &a_{\alpha}^{\lambda} = \sqrt{\frac{2\omega_{\alpha}}{\hbar}} q_{\alpha}^{\lambda}, \qquad a_{\alpha}^{\lambda+} = \sqrt{\frac{2\omega_{\alpha}}{\hbar}} q_{\alpha}^{\lambda+} \\ &\boldsymbol{H_{EM}} = 2\sum_{\alpha}\sum_{\lambda}\hbar\omega_{\alpha}^{2}\left(a_{\alpha}^{\lambda+} a_{\alpha}^{\lambda} + \frac{1}{2}\right) \\ &\boldsymbol{N_{\alpha}^{\lambda}} = a_{\alpha}^{\lambda+} a_{\alpha}^{\lambda} \end{aligned} \tag{69}$$

The number operator N will prove useful when considering the coupling between the laser field and the gain medium, while the second quantization formalism of the EM field permits a very clear formulation of transitions between different states in the operator and tensor notation that will ultimately be used to interpret the experiments.

Next, the interaction Hamiltonian for our atom with the now quantized field can be written as the potential energy of a charge moving in a radiation field in the Coulomb gauge.

$$H = \frac{1}{2m}\left(\mathbf{p} + \frac{e}{c}\mathbf{A}\right)^2 - e\phi = \frac{p^2}{2m} + \frac{e^2A^2}{2mc^2} + \frac{e}{2mc}\left(\vec{\mathbf{p}}\cdot\boldsymbol{A} + \boldsymbol{A}\cdot\vec{\mathbf{p}}\right) - e\phi \tag{70}$$

The vector potential can be expressed in terms of ladder operators

$$\boldsymbol{A} = \sum_{\alpha}\sum_{\lambda_\alpha}\hat{\varepsilon}_\alpha^\lambda\sqrt{\frac{2\pi\hbar c^2}{\omega_\alpha V}}\left(a_\alpha^\lambda e^{i\vec{k}_\alpha\cdot\vec{r}} + a_\alpha^{\lambda+}e^{-i\vec{k}_\alpha\cdot\vec{r}}\right) \tag{71}$$

The contribution to the scalar potential is negligible to the interaction contributing a small correction to the atomic Hamiltonian. When necessary it is treated as a separate perturbation. The nonlinear term contributes to second order effects like two photon absorption and will be neglected. Finally, by having previously adopted the Coulomb gauge where $\nabla\cdot A = 0$, the interaction Hamiltonian reduces to only one term.

$$H_{\text{int}} = \frac{e}{mc}\boldsymbol{A}\cdot\vec{\mathbf{p}} \tag{72}$$

With this term the probabilities of transitions due to absorption, stimulated emission and spontaneous emission can be calculated. The first step is to solve the field free problem and then apply the interaction Hamiltonian as a time dependent perturbation coupled to the photon field. The wave function of the photon field for the purposes of this calculation is simply the product space of occupation numbers for the field at different frequencies and polarizations, though eventually it makes sense to adopt a formalism based upon an approximation to a continuum of states. Therefore, the matrix element of a transition is just[5920]:

$$\begin{aligned}
H_{fi}(\lambda_\alpha) &= \left\langle \Psi_f; n_{\lambda_\alpha}+1\middle|H_{\text{int}}\middle|\Psi_i; n_{\lambda_\alpha}\right\rangle \\
&= \left\langle \Psi_f; n_{\lambda_\alpha}+1\middle|\frac{e}{m}\left(\hat{\varepsilon}_\alpha^\lambda\cdot\vec{\mathbf{p}}\right)\sqrt{\frac{2\pi\hbar}{\omega_\alpha V}}\left(a_\alpha^\lambda e^{i\vec{k}_\alpha\cdot\vec{r}} + a_\alpha^{\lambda+}e^{-i\vec{k}_\alpha\cdot\vec{r}}\right)\middle|\Psi_i; n_{\lambda_\alpha}\right\rangle \\
&= \left\langle \Psi_f; n_{\lambda_\alpha}+1\middle|\frac{e}{m}\left(\hat{\varepsilon}_\alpha^\lambda\cdot\vec{\mathbf{p}}\right)\sqrt{\frac{2\pi\hbar}{\omega_\alpha V}}a_\alpha^\lambda e^{i\vec{k}_\alpha\cdot\vec{r}}\middle|\Psi_i; n_{\lambda_\alpha}\right\rangle + \left\langle \Psi_f; n_{\lambda_\alpha}+1\middle|\frac{e}{m}\left(\hat{\varepsilon}_\alpha^\lambda\cdot\vec{\mathbf{p}}\right)\sqrt{\frac{2\pi\hbar}{\omega_\alpha V}}a_\alpha^{\lambda+}e^{-i\vec{k}_\alpha\cdot\vec{r}}\middle|\Psi_i; n_{\lambda_\alpha}\right\rangle
\end{aligned} \tag{73}$$

$$H_{fi_{emit}}(\lambda_\alpha) = \sqrt{n_{\lambda_\alpha}+1}\left\langle \Psi_f \left| \frac{e}{m}\left(\hat{\varepsilon}_\alpha^\lambda \cdot \vec{\mathbf{p}}\right)\sqrt{\frac{2\pi\hbar}{\omega_\alpha V}} e^{i\vec{k}_\alpha\cdot\vec{r}} \right| \Psi_i \right\rangle \tag{74}$$

$$H_{fi_{abs}}(\lambda_\alpha) = \left\langle \Psi_f ; n_{\lambda_\alpha}+1 \left| \frac{e}{m}\left(\hat{\varepsilon}_\alpha^\lambda \cdot \vec{\mathbf{p}}\right)\sqrt{\frac{2\pi\hbar}{\omega_\alpha V}} a_\alpha^{\lambda^+} e^{-i\vec{k}_\alpha\cdot\vec{r}} \right| \Psi_i ; n_{\lambda_\alpha} \right\rangle = \sqrt{n_{\lambda_\alpha}}\left\langle \Psi_f \left| \frac{e}{m}\left(\hat{\varepsilon}_\alpha^\lambda \cdot \vec{\mathbf{p}}\right)\sqrt{\frac{2\pi\hbar}{\omega_\alpha V}} e^{-i\vec{k}_\alpha\cdot\vec{r}} \right| \Psi_i \right\rangle \tag{75}$$

Notice that the coordinates can be chosen such that the axes align with the polarization.

$$H_{fi_{abs}}(\lambda_\alpha) = \sqrt{n_{\lambda_\alpha}}\left\langle \Psi_f \left| \frac{e}{m}\left(p_\alpha\right)\sqrt{\frac{2\pi\hbar}{\omega_\alpha V}} e^{-i\vec{k}_\alpha\cdot\vec{r}} \right| \Psi_i \right\rangle \tag{76}$$

Recall that the Hamiltonian is the generator of time evolution and therefore its commutation relation acts to differentiate with respect to time any operator that it does not commute with.

$$\begin{aligned} &[H, r] = -i\hbar\frac{\partial}{\partial t} r = -i\hbar\frac{p}{m} \\ &p = \frac{im}{\hbar}\left(Hr - rH\right) \\ &\left\langle \Psi_f \left| p \right| \Psi_i \right\rangle = \frac{im}{\hbar}\left(\left\langle \Psi_f \left| Hr \right| \Psi_i \right\rangle - \left\langle \Psi_f \left| rH \right| \Psi_i \right\rangle\right) = \frac{im}{\hbar}\left(E_f - E_i\right)\left\langle \Psi_f \left| r \right| \Psi_i \right\rangle \end{aligned} \tag{77}$$

The transition probability can then be written as an electric dipole operator times an exponential operator.

$$\begin{aligned} H_{fi_{abs}}(\lambda_\alpha) &= \sqrt{n_{\lambda_\alpha}}\left\langle \Psi_f \left| \frac{e}{m}\left(\frac{im\vec{r}\cdot\hat{\varepsilon}_\lambda^\alpha\left(E_f - E_i\right)}{\hbar}\right)\sqrt{\frac{2\pi\hbar}{\omega_\alpha V}} e^{-i\vec{k}_\alpha\cdot\vec{r}} \right| \Psi_i \right\rangle \\ &= \sqrt{n_{\lambda_\alpha}}\left\langle \Psi_f \left| ie\vec{r}\cdot\hat{\varepsilon}_\lambda^\alpha\sqrt{\frac{2\pi\hbar\omega_\alpha}{V}} e^{-i\vec{k}_\alpha\cdot\vec{r}} \right| \Psi_i \right\rangle \end{aligned} \tag{78}$$

Finally the exponential term is expanded to first order in r, since r<<λ. The matrix terms for electric dipole transitions are written:

$$H_{fi_{abs}}^{ed}(\lambda_\alpha) = \sqrt{n_{\lambda_\alpha}}\left\langle \Psi_f \left| ie\vec{r}\cdot\hat{\varepsilon}_\lambda^\alpha\sqrt{\frac{2\pi\hbar\omega_\alpha}{V}} \right| \Psi_i \right\rangle, \quad H_{fi_{emit}}^{ed}(\lambda_\alpha) = \sqrt{n_{\lambda_\alpha}+1}\left\langle \Psi_f \left| ie\vec{r}\cdot\hat{\varepsilon}_\lambda^\alpha\sqrt{\frac{2\pi\hbar\omega_\alpha}{V}} \right| \Psi_i \right\rangle \tag{79}$$

Higher order terms in r such as magnetic dipole and electric quadrapole transitions do not contribute significantly to the transitions in these experiments and will be ignored. To convert this matrix element to a more useful form for calculation of laser transitions it is necessary to calculate the cross sections for the transitions as well as the spontaneous transition rates. The first step is deriving Fermi's golden rule from time dependent perturbation theory in the interaction picture[69]. The formalism developed in Sakuri is convenient for these purposes, utilizing a constant Hamiltonian modified by a time dependent perturbation[69]. Assuming it is possible to choose a basis that includes the full time dependent solution in the Schrödinger picture, a new time dependent basis is constructed by multiplying the eigen kets with the time evolution operator obtained from the constant portion of the Hamiltonian. It is important to recall the purpose of this method is to construct a relationship between a time independent and hence separable solution to a Hamiltonian that can readily be solved and a murky arbitrary time dependent potential.

$$i\hbar\frac{\partial}{\partial t}\left|\Psi_n(t)\right\rangle = \left[H_0 + H'(t)\right]\left|\Psi_n(t)\right\rangle$$
$$\left|\Psi^0(t)\right\rangle = \sum_n e^{i\frac{H_0 t}{\hbar}}\left|\Psi_n(t)\right\rangle \qquad \textbf{(80)}$$

The next step is to evaluate Schrödinger's equation for this new basis

$$i\hbar\frac{\partial}{\partial t}\left|\Psi^0(t)\right\rangle = i\hbar\frac{\partial}{\partial t}e^{i\frac{H_0 t}{\hbar}}\sum_n\left|\Psi_n(t)\right\rangle$$
$$= -H_0 e^{i\frac{H_0 t}{\hbar}}\sum_n\left|\Psi_n(t)\right\rangle + e^{i\frac{H_0 t}{\hbar}}i\hbar\frac{\partial}{\partial t}\sum_n\left|\Psi_n(t)\right\rangle \qquad \textbf{(81)}$$

But axiomatically, the elected basis solves the Schrödinger equation for the total Hamiltonian. Thus by substitution and insertion of the identity, Schrödinger's equation becomes:

$$
\begin{aligned}
i\hbar\frac{\partial}{\partial t}\left|\Psi^0(t)\right\rangle &= -H_0 e^{i\frac{H_0 t}{\hbar}}\sum_n\left|\Psi_n^0(t)\right\rangle + e^{i\frac{H_0 t}{\hbar}}\left(H_0+H'(t)\right)\sum_n\left|\Psi_n^0(t)\right\rangle = e^{i\frac{H_0 t}{\hbar}}H'(t)e^{-i\frac{H_0 t}{\hbar}}e^{i\frac{H_0 t}{\hbar}}\sum_n\left|\Psi_n^0(t)\right\rangle \\
i\hbar\frac{\partial}{\partial t}\left|\Psi^0(t)\right\rangle &= e^{i\frac{H_0 t}{\hbar}}H'(t)e^{-i\frac{H_0 t}{\hbar}}\left|\Psi^0(t)\right\rangle
\end{aligned}
\tag{82}
$$

Therefore, in this choice of basis the Schrödinger equation reduces to a convenient form for determining the transitions among time independent eigenvalues assuming the time independent basis spans (or is extended to span) the time dependent problem[69].

$$
\begin{aligned}
&\left\langle\Psi_n\left|i\hbar\frac{\partial}{\partial t}\right|\Psi^0(t)\right\rangle = \left\langle\Psi_n\left|e^{i\frac{H_0 t}{\hbar}}H'(t)e^{-i\frac{H_0 t}{\hbar}}\right|\Psi^0(t)\right\rangle \\
&= i\hbar\frac{\partial}{\partial t}\left\langle\Psi_n\left|\Psi^0(t)\right\rangle\right. = \left\langle\Psi_n\left|e^{i\frac{H_0 t}{\hbar}}H'(t)e^{-i\frac{H_0 t}{\hbar}}\sum_m\right|\Psi_m\right\rangle\left\langle\Psi_m\left|\Psi^0(t)\right\rangle\right. \\
&= i\hbar\frac{\partial}{\partial t}c_n(t) = \sum_m H'_{nm}(t)e^{i\frac{E_n-E_m}{\hbar}t}\left\langle\Psi_m\left|\Psi^0(t)\right\rangle\right. \\
&i\hbar\frac{\partial}{\partial t}c_n(t) = \sum_m H'_{nm}(t)e^{i\omega_{nm}t}c_m(t)
\end{aligned}
\tag{83}
$$

Providing that the time dependent Hamiltonian is reasonably well behaved (i.e. conforms to the requirements of the existence and uniqueness theorem) this becomes a system of ordinary differential equations and can be explicitly solved for the vector c(t) allowing a solution to the fully time dependent problem to be derived from the time independent eigenvalues. This is a useful result for calculating the transition probability of atoms and ions subjected to the time varying potentials of radiation. To solve this system of equations when the time varying potential is a step function that turns on at time t = 0, it is possible to directly integrate equation (83) and then square it to obtain the probability of a transition.

$$\left|\left\langle \Psi_f \left| H(t) \right| \Psi_i \right\rangle\right|^2 = c_{fi}^2(t) = \frac{4\left|H_{fi}\right|^2 \sin^2\left(\frac{\omega_{fi}t}{2}\right)}{\hbar^2\omega_{fi}^2} \tag{84}$$

If H(t) is the vector potential for the radiation field in equation (79), the result possesses the same form since exponentials add when multiplied.

$$c_{fi}(t) = \frac{-i}{\hbar}\int_0^t \left[\sum_\alpha \sum_{\lambda_\alpha} q_\alpha^\lambda(t)\boldsymbol{A}_\alpha^\lambda(\vec{r}) + q_\alpha^{\lambda^*}(t)\boldsymbol{A}_\alpha^{\lambda^*}(\vec{r})\right] e^{i\omega_{fi}t}\,dt \tag{85}$$

$$= \frac{-i}{\hbar}\int_0^t \left[\sum_\alpha \sum_{\lambda_\alpha} e^{i\omega_{fi}t}\boldsymbol{A}_\alpha^\lambda(\vec{r}) + e^{-i\omega_{fi}t}\boldsymbol{A}_\alpha^{\lambda^*}(\vec{r})\right] e^{i\omega_{fi}t}\,dt = \frac{-i}{\hbar}\sum_\alpha \sum_{\lambda_\alpha} \frac{1-e^{i(\omega_{fi}+\omega)t}}{\omega_{fi}+\omega}\boldsymbol{A}_\alpha^\lambda(\vec{r}) + \frac{1-e^{i(\omega_{fi}-\omega)t}}{\omega_{fi}-\omega}\boldsymbol{A}_\alpha^{\lambda^*}(\vec{r}) \tag{86}$$

When computing the probability of the transition, orthogonality in the spatial and frequency terms permits the sum to be dropped[69].

$$c_{fi}^2(t) = \left(\frac{-i}{\hbar}\frac{1-e^{i(\omega_{fi}+\omega)t}}{\omega_{fi}+\omega}\boldsymbol{A}_\alpha^\lambda(\vec{r})\right)^2 = \frac{4\left|\boldsymbol{A}_\alpha^\lambda(\vec{r})\right|^2}{(\omega_{fi}-\omega)^2}\sin^2\left(\frac{(\omega_{fi}-\omega)}{2}t\right) \tag{87}$$

Integrating over the density of final states assuming a constant distribution in the neighborhood of the transition produces Fermi's golden rule. The functional form is a well known approximation of the Dirac delta function.

$$\begin{aligned}\int c_{fi}^2(t)\rho(\omega)d\omega &= \int \frac{4\left|\boldsymbol{A}_\alpha^\lambda(\vec{r})\right|^2}{(\omega_{fi}-\omega)^2}\sin^2\left(\frac{(\omega_{ti}-\omega)}{2}t\right)\rho(\omega)d\omega \\ P_{fi} &\approx \frac{2\pi}{\hbar}\left|\boldsymbol{A}_\alpha^\lambda(\vec{r})\right|^2 \rho(\omega_{fi})\delta(\omega_{fi})\,t\end{aligned} \tag{88}$$

Thus, the transition probability is proportional to the density of states in the coupled problem (i.e. degeneracy of electronic states as well as density of the E-M field) times the square of the matrix element that mixes the electronic states. If a thermal density of states were assumed, application of the above procedure would result in a derivation of the Lorentzian distribution, commonly associated with diffuse atomic vapors and homogenous laser media. Thus the rate of spontaneous emission increases

with the density of states. For example, if an excited state is non-conformational and degrees of freedom are added to the problem by putting an excited atom into contact with a liquid, the transition rate would drastically increase by some factor of the collision rate integrated over any extra degrees of freedom now present in the medium. With organic molecules their size and complexity permit a host of rotations, vibrations, bending, and stretching modes constantly excited by collisions that could serve as a reservoir of perturbations to mix a metastable state with a transition. This in part explains the short excited state lifetimes of molecules used in dye lasers as well as their broad spectral content.

To derive the Einstein-A coefficient (the total rate of spontaneous emission) all that must be done is to integrate the transition rate over the solid angle of the possible emissions and sum over the polarizations. The density of states in frequency space for the photon field times the degeneracy of the final electronic state can be written as:

$$\rho(\omega)d\omega = \frac{V\omega^2 d\omega d\Omega_k}{8\pi^3 c^3} g_f(\omega) \tag{89}$$

Substituting this expression into Fermi's golden rule, the rates of spontaneous and stimulated transitions for electric dipole radiation can be written[20].

$$\begin{aligned} p^{\alpha}_{k_{spont}} d\Omega_k &= \frac{e^2 \omega_{k,\alpha}{}^3}{2\pi\hbar c^3} g_i \left| \left\langle \Psi_f \left| i\vec{r} \cdot \hat{\varepsilon}^{\alpha}_k \right| \Psi_i \right\rangle \right|^2 d\Omega_k \\ A &= \frac{e^2}{2\pi\hbar c^3} g_i \sum_{k,\alpha} \omega_{k,\alpha}{}^3 \int_0^{\pi} \int_0^{2\pi} \left| \left\langle \Psi_f \left| i\vec{r} \cdot \hat{\varepsilon}^{\alpha}_k \right| \Psi_i \right\rangle \right|^2 d\Omega_k \end{aligned} \tag{90}$$

Selecting a polarization axis parallel to the dipole moment makes this integral trivial.

$$Ag_i = \frac{e^2}{2\pi\hbar c^3} g_i \sum_k \omega_k{}^3 \left|\left\langle \Psi_f \left| ir \right| \Psi_i \right\rangle\right|^2 \int_0^{\pi} \int_0^{2\pi} \sin^3\theta \, d\theta d\phi$$
$$= \frac{2e^2}{3\pi\hbar c^3} g_i \sum_k \omega_k{}^3 \left|\left\langle \Psi_f \left| ir \right| \Psi_i \right\rangle\right|^2 \quad \textbf{(91)}$$

The derivation of the absorption case follows an identical procedure to arrive at an expression for the stimulated absorption/emission transition rate.

$$B_{if} g_i = \frac{e^2}{2\pi\hbar c^3} g_i \sum_k \omega_k{}^3 \left|\left\langle \Psi_f \left| ir \right| \Psi_i \right\rangle\right|^2 \int_0^{\pi} \int_0^{2\pi} \sin^3\theta \, d\theta d\phi$$
$$= \frac{2e^2}{3\pi\hbar c^3} g_i \sum_k n_k \omega_k{}^3 \left|\left\langle \Psi_f \left| ir \right| \Psi_i \right\rangle\right|^2 \quad \textbf{(92)}$$

However, this is a difficult expression to work with since the number of photons present in an arbitrary system at an arbitrary wavelength is generally unknown. To obtain the final form of the Einstein B coefficient it is useful to solve the equilibrium case where the distribution of photons is generally well understood. The classic black body problem where the atom is in thermal equilibrium with its environment requires that the transitions into a state equal the transitions out of a state. This condition is called detailed balance and at high temperatures it takes the familiar form[20]:

$$\left(g_2 A + g_2 B_{21} n(\omega_{21})\right) e^{-\frac{E_2}{k_B T}} = g_1 B_{12} n(\omega_{21}) e^{-\frac{E_1}{k_B T}} \quad \textbf{(93)}$$

Solving for A:

$$g_2 A = n(\omega_{21}) \left(g_1 B_{12} e^{-\frac{E_2 - E_1}{k_B T}} + g_2 B_{21} \right) \quad \textbf{(94)}$$

But in thermal equilibrium, Plank's law predicts the correct distribution for n(ω).

$$Ag_2 = \frac{\hbar\omega^3}{\pi^2 c^2 \left(e^{-\frac{\hbar\omega_{21}}{k_B T}} - 1 \right)} \left(g_1 B_{12} e^{-\frac{E_2 - E_1}{k_B T}} - g_2 B_{21} \right) \quad \textbf{(95)}$$

Thus if Plank's law is to correctly predict the distribution in equilibrium, the following constraints on the values of A and B must apply:

$$\frac{\hbar\omega^3}{\pi^2c^2\left(e^{-\frac{\hbar\omega_{12}}{k_BT}}-1\right)}=\frac{\frac{A}{B_{21}}}{\left(\frac{g_1}{g_2}\frac{B_{12}}{B_{21}}e^{-\frac{E_2-E_1}{k_BT}}-1\right)} \qquad \textbf{(96)}$$

$$\frac{A}{B_{21}}=\frac{\hbar\omega^3}{\pi^3c^3}, \qquad B_{21}=\frac{g_1B_{12}}{g_2}$$

This derivation provides the basic formalism that will be used to describe the interaction of atomic systems with light and heat and hence interpret our experimental results. The utility of this discussion becomes apparent when layers of complexity are added to the description of the processes occurring within the optically active Nd^{+3} ions in a solid. The rate equations can be written directly as number operators of the appropriate fields and atomic states and the transitions evaluated directly from the time independent matrix elements obtained through standard methods.

Continuing the discussion along general lines, to describe the operation of a laser one more constant must be derived from atomic physics: the absorption cross section. The first step in such a derivation is to use the above formula for transition probabilities but to reexamine the assumptions that allowed equation (88) to be integrated. At the time, both thermodynamic and quantum mechanical effects on the distribution of allowed transitions were neglected. For example, quantum mechanics allows strict conservation of energy to be violated during atomic transitions. In the usual manner, this translates into the Fourier relationship between lifetime and line width. The physical relationship underpinning this phenomenon is best expressed in terms of the time energy uncertainty principle. Additional sources of line broadening are thermodynamic in origin, which

allows for both thermal broadening of transitions (homogeneous line broadening) and the presence of wide-spread non uniform distributions in composition of materials that host optically active ions (inhomogeneous line broadening). In gaseous materials homogeneous line broadening typically results in relatively narrow transitions and Lorentzian distributions. In solids and liquids the situation is far more complex and interesting. In materials like Ti:Sapphire the atomic physics becomes strongly coupled to the thermodynamic description of the host environment and resists a simple description. Thus to obtain useful rules of thumb for describing laser behavior at a systemic level it becomes necessary to make a few unphysical assumptions namely that the distribution function of optical transitions is uniform over the window of integration where the integral in the derivation of Fermi's golden rule is non zero. Thus by dimensional analysis the cross section for stimulated emission is written

$$\sigma_{12} = \frac{\hbar\omega\rho(\omega)B_{12}}{c} \tag{97}$$

where $\rho(\omega)$ is the line shape of the transition. While lacking rigor this is the only result possible without knowing the specific line shape of the transition and in practice it is sufficient to know the approximate cross section for a transition when designing a laser system, though when actually building the laser the correct values become quite relevant and are best measured directly for the specific material being used. As stated by Payne et al there are 3 ways to measure the cross section for stimulated emission[70]:

> The three main possibilities include: 1) the reciprocity method, 2) the Fuchtbauer-Ladenburg (F-L) equation, and 3) direct measurements of small signal, or saturated gain.

The reciprocity method combines absorption measurements with prior knowledge of the density of the material while the F-L equation is essentially the formula stated

above where ρ is computed by numerically integrating the lineshape[71]. The final method simply relies on a direct measurement with prior knowledge of the dopant density.

Thus for the purposes of laser design the problem of understanding the interaction of light with an optically active medium is reduced to evaluating the matrix elements of the Hamiltonian and calculating the effect on this spectrum of successively decreasing perturbations. The methods for applying these perturbations are very involved (particularly obtaining the proper spin orbit coupling in Nd^{+3}) and discussed in the books already mentioned by both J. Slater and R. Powell.

Appendix B: *Sample Code from Ray-Tracing Program*

The following is the ray tracing code written in C++ (compiled in Microsoft visual studio) used to calculate the insertion loss of a re-entrant beam from a multimode fiber. File IO and interface routines are omitted. The code below compiles and runs when pasted into the appropriately named project files using Microsoft Visual Studio 2005 Express Edition.

```
// test.cpp : Defines the entry point for the console application.

#include "stdafx.h"
#include "stdlib.h"
#include "time.h"
#include "Trace.h"

/* // this program  finds the focal length of a singlet
int _tmain(int argc, _TCHAR* argv[])
{
//srand( (unsigned)time( NULL ) );
Define_Lens_System Singlet(1);
Initialize_Singlet(&Singlet);


Ray tr;
Ray *temp_ray;
temp_ray = &tr;


int N= 1000;
double focal_len = 0;
double min = .005;
double step=Singlet.Exit_Plane-.01;
for( int i=0;i<N; i++)
{
      temp_ray->phi = 0;
      temp_ray->theta = 0;
      temp_ray->x = 0;
      temp_ray->y=.005;
      temp_ray->z=0;
      temp_ray->xhat=0;
      temp_ray->yhat=0;
      temp_ray->zhat=1;
```

```
	Trace(temp_ray,&Singlet);
	step += .00002;
	if (!propigate(temp_ray,step))
		break;
	if(temp_ray->y < 0)
		int k =0;
	if(temp_ray->y > 0 && temp_ray->y < min)
	{
		min = temp_ray->y;
		focal_len = temp_ray->z-Singlet.Lens[0].front_pos.z;
	}
}


}

*/



/*/ this program finds the focal length of an aplanat

int _tmain(int argc, _TCHAR* argv[])
{
//srand( (unsigned)time( NULL ) );
Define_Lens_System Doub(2);
Initialize_Doub(&Doub);


Ray tr;
Ray *temp_ray;
temp_ray = &tr;


int N= 60000;
double focal_len = 0;
double min = .005;
double step=Doub.Exit_Plane-.01;
for( int i=0;i<N; i++)
{
	temp_ray->phi = 0;
	temp_ray->theta = 0;
	temp_ray->x = 0;
	temp_ray->y=.0005;
	temp_ray->z=0;
	temp_ray->xhat=0;
	temp_ray->yhat=0;
	temp_ray->zhat=1;

	Trace(temp_ray,&Doub);
	step += .00000125;
	if (!propigate(temp_ray,step))
		break;
```

```
	if(temp_ray->y < 0)
		int k =0;
	if(temp_ray->y > 0 && temp_ray->y < min)
	{
		min = temp_ray->y;
		focal_len = temp_ray->z-Doub.Lens[0].front_pos.z;
	}
}


}

*/



/*/ this program finds the optimal seperation between a pair of aplanat

int _tmain(int argc, _TCHAR* argv[])
{
//srand( (unsigned)time( NULL ) );
Define_Lens_System Aplanat(4);
Initialize_Lenses(&Aplanat);


Ray tr;
Ray *temp_ray;
temp_ray = &tr;


int N= 60000;
double focal_len = 0;
double min = .005;
double step=0;
for( int i=0;i<N; i++)
{
	temp_ray->phi = 0;
	temp_ray->theta = 0;
	temp_ray->x = 0;
	temp_ray->y=.0005;
	temp_ray->z=0;
	temp_ray->xhat=0;
	temp_ray->yhat=0;
	temp_ray->zhat=1;

	Aplanat.Lens[2].front_pos.z += .00000125;
	Trace(temp_ray,&Aplanat);
	step += .00000125;
	if (!propigate(temp_ray,Aplanat.Exit_Plane))
		break;
	if(temp_ray->yhat > 0)
		int k =0;
	if(temp_ray->y > 0 && temp_ray->y < min)
```

```
	{
		min = temp_ray->y;
		focal_len = temp_ray->z-Aplanat.Lens[0].front_pos.z;
	}
}


}

*/

/*

 //?????????? dont know what this does
int _tmain(int argc, _TCHAR* argv[])
{
//srand( (unsigned)time( NULL ) );
Define_Lens_System Aplanat(2);
Initialize_Sing_Lenses(&Aplanat);

Ray tr,nr;
Ray *temp_ray;
Ray *new_ray;
temp_ray = &tr;
new_ray = &nr;

int N= 10000;
int Count= 0;
bool success=true;

double D_xyz, D_Ang, Dfail_xyz, Dfail_Ang;
D_xyz= D_Ang= Dfail_xyz= Dfail_Ang =0;
for( int i=0;i<N; i++)
{
Launch(temp_ray);
new_ray->copy(temp_ray);
success = Trace(temp_ray, &Aplanat);
if(success && detect_ray(temp_ray,Aplanat.Exit_Plane))
	{
		Count++;
		D_xyz+= sqrt((temp_ray->x)*(temp_ray->x)+(temp_ray-
>y)*(temp_ray->y));//sqrt((temp_ray->x-new_ray->x)*(temp_ray->x-
new_ray->x)+(temp_ray->y-new_ray->y)*(temp_ray->y-new_ray->y));
	}
else
	{
		Dfail_xyz+= sqrt((temp_ray->x)*(temp_ray->x)+(temp_ray-
>y)*(temp_ray->y));//sqrt((temp_ray->x-new_ray->x)*(temp_ray->x-
new_ray->x)+(temp_ray->y-new_ray->y)*(temp_ray->y-new_ray->y));
	}
}
double Integral = ((double)(Count))/((double)(N));
D_xyz/=Count;
```

```
D_Ang/=N;
	return 0;
}
*/

// this program counts the transmission from one fiber face into
another
int _tmain(int argc, _TCHAR* argv[])
{
//srand( (unsigned)time( NULL ) );

Define_Lens_System Aplanat(4);
Initialize_Lenses(&Aplanat);

Ray tr,nr;
Ray *temp_ray;
Ray *new_ray;
temp_ray = &tr;
new_ray = &nr;

int N= 10000;
int Count= 0;
bool success=true;

double D_xyz, D_Ang, Dfail_xyz, Dfail_Ang;
D_xyz= D_Ang= Dfail_xyz= Dfail_Ang =0;
for( int i=0;i<N; i++)
{
Launch(temp_ray);
new_ray->copy(temp_ray);
success = Trace(temp_ray, &Aplanat);
if(success && detect_ray(temp_ray,Aplanat.Exit_Plane))
	{
		Count++;
		D_xyz+= sqrt((temp_ray->x)*(temp_ray->x)+(temp_ray-
>y)*(temp_ray->y));//sqrt((temp_ray->x-new_ray->x)*(temp_ray->x-
new_ray->x)+(temp_ray->y-new_ray->y)*(temp_ray->y-new_ray->y));
	}
else
	{
		Dfail_xyz+= sqrt((temp_ray->x)*(temp_ray->x)+(temp_ray-
>y)*(temp_ray->y));//sqrt((temp_ray->x-new_ray->x)*(temp_ray->x-
new_ray->x)+(temp_ray->y-new_ray->y)*(temp_ray->y-new_ray->y));
	}
}
double Integral = ((double)(Count))/((double)(N));
D_xyz/=Count;
D_Ang/=N;
	return 0;
}
```

```
//Lens_system.h
#define Lens_System_h

#include "Surface.h"

//***************************************
class Define_Lens_System
{
public:
Define_Lens_System(int n);
      Lens_Surfaces *Lens; //array set by constructor
      int Num_Lens;
      double Exit_Plane;
};

//***************************************
bool Initialize_Lenses(Define_Lens_System * Aplanat);
bool Initialize_Singlet(Define_Lens_System * Singlet);
bool Initialize_Doub(Define_Lens_System *Aplanat);

bool Initialize_Sing_Lenses(Define_Lens_System *Aplanat);
//***************************************
```

```
//Lens_System.cpp
#include "stdafx.h"
#include "Lens_System.h"

Define_Lens_System::Define_Lens_System(int n)
{
	Num_Lens=n;
	Lens = new Lens_Surfaces[n];
}

bool Initialize_Singlet(Define_Lens_System *Singlet)
{
	Singlet->Lens[0].ref_index = 1.776;
	Singlet->Lens[0].front_pos.x = 0;
	Singlet->Lens[0].front_pos.y = 0;
	Singlet->Lens[0].front_pos.z = 0.042139; //all #'s in meters
	Singlet->Lens[0].front_pos.phi = 0;
	Singlet->Lens[0].front_pos.theta = 0;
	Singlet->Lens[0].front_radius = 0.0327;

	Singlet->Lens[0].back_pos.x = 0;
	Singlet->Lens[0].back_pos.y = 0;
	Singlet->Lens[0].back_pos.z = Singlet-
>Lens[0].front_pos.z+0.0015;
	Singlet->Lens[0].back_pos.phi = 0;
	Singlet->Lens[0].back_pos.theta = 0;
	Singlet->Lens[0].back_radius = 10000;

	Singlet->Exit_Plane = Singlet->Lens[0].back_pos.z+Singlet-
>Lens[0].front_pos.z;
	return true;
}
bool Initialize_Lenses(Define_Lens_System *Aplanat)
{/*
	Aplanat->Lens[0].ref_index = 1.776;
	Aplanat->Lens[0].front_pos.x = 0;
	Aplanat->Lens[0].front_pos.y = 0;
	Aplanat->Lens[0].front_pos.z = 0.005 +0.0007; //all #'s in meters
	Aplanat->Lens[0].front_pos.phi = 0;
	Aplanat->Lens[0].front_pos.theta = 0;
	Aplanat->Lens[0].front_radius = 0.0043;

	Aplanat->Lens[0].back_pos.x = 0;
	Aplanat->Lens[0].back_pos.y = 0;
	Aplanat->Lens[0].back_pos.z = Aplanat-
>Lens[0].front_pos.z+0.0015;
	Aplanat->Lens[0].back_pos.phi = 0;
	Aplanat->Lens[0].back_pos.theta = 0;
	Aplanat->Lens[0].back_radius = .00942;

	Aplanat->Lens[1].ref_index = 1.776;
	Aplanat->Lens[1].front_pos.x = 0;
	Aplanat->Lens[1].front_pos.y = 0;
```

```
      Aplanat->Lens[1].front_pos.z = Aplanat->Lens[0].back_pos.z +
0.000088;//0.011719;
      Aplanat->Lens[1].front_pos.phi =0;
      Aplanat->Lens[1].front_pos.theta =0;
      Aplanat->Lens[1].front_radius = -.0055;

      Aplanat->Lens[1].back_pos.x = 0;
      Aplanat->Lens[1].back_pos.y = 0;
      Aplanat->Lens[1].back_pos.z = Aplanat-
>Lens[1].front_pos.z+0.000;//0.012711;
      Aplanat->Lens[1].back_pos.phi = 0;
      Aplanat->Lens[1].back_pos.theta = 0;
      Aplanat->Lens[1].back_radius = 0.00942;

      Aplanat->Lens[2].ref_index = 1.776;
      Aplanat->Lens[2].front_pos.x = 0;
      Aplanat->Lens[2].front_pos.y = 0;
      Aplanat->Lens[2].front_pos.z = Aplanat-
>Lens[1].back_pos.z+.00025;
      Aplanat->Lens[2].front_pos.phi = 0;
      Aplanat->Lens[2].front_pos.theta = 0;
      Aplanat->Lens[2].front_radius = 0.00942;

      Aplanat->Lens[2].back_pos.x = 0;
      Aplanat->Lens[2].back_pos.y = 0;
      Aplanat->Lens[2].back_pos.z = Aplanat->Lens[2].front_pos.z+0.001;
//0.030004;
      Aplanat->Lens[2].back_pos.phi = 0;
      Aplanat->Lens[2].back_pos.theta = 0;
      Aplanat->Lens[2].back_radius = -0.0055;

      Aplanat->Lens[3].ref_index = 1.776;
      Aplanat->Lens[3].front_pos.x = 0;
      Aplanat->Lens[3].front_pos.y = 0;
      Aplanat->Lens[3].front_pos.z = Aplanat-
>Lens[2].back_pos.z+0.000088;//0.030085;
      Aplanat->Lens[3].front_pos.phi =0;
      Aplanat->Lens[3].front_pos.theta =0;
      Aplanat->Lens[3].front_radius = .00942;

      Aplanat->Lens[3].back_pos.x = 0;
      Aplanat->Lens[3].back_pos.y = 0;
      Aplanat->Lens[3].back_pos.z = Aplanat-
>Lens[3].front_pos.z+0.0015;
      Aplanat->Lens[3].back_pos.phi = 0;
      Aplanat->Lens[3].back_pos.theta = 0;
      Aplanat->Lens[3].back_radius = 0.0043;

      Aplanat->Exit_Plane = Aplanat->Lens[3].back_pos.z+Aplanat-
>Lens[0].front_pos.z-.002;
return true;

      */
```

```
      //The following parameters optimize the seperation and placement
of the aplanats fairly well in relation to the fiber for
      //CVI Aplanats and the correct fiber NA and diameter available
from molex
      Aplanat->Lens[0].ref_index = 1.776;
      Aplanat->Lens[0].front_pos.x = 0;
      Aplanat->Lens[0].front_pos.y = 0;
      Aplanat->Lens[0].front_pos.z = 0.01047625 -.00065; //all #'s in
meters
      Aplanat->Lens[0].front_pos.phi = 0;
      Aplanat->Lens[0].front_pos.theta = 0;
      Aplanat->Lens[0].front_radius = 0.007706;

      Aplanat->Lens[0].back_pos.x = 0;
      Aplanat->Lens[0].back_pos.y = 0;
      Aplanat->Lens[0].back_pos.z = Aplanat-
>Lens[0].front_pos.z+0.0015;
      Aplanat->Lens[0].back_pos.phi = 0;
      Aplanat->Lens[0].back_pos.theta = 0;
      Aplanat->Lens[0].back_radius = 0.0214;

      Aplanat->Lens[1].ref_index = 1.776;
      Aplanat->Lens[1].front_pos.x = 0;
      Aplanat->Lens[1].front_pos.y = 0;
      Aplanat->Lens[1].front_pos.z = Aplanat->Lens[0].back_pos.z +
0.000081;//0.011719;
      Aplanat->Lens[1].front_pos.phi =0;
      Aplanat->Lens[1].front_pos.theta =0;
      Aplanat->Lens[1].front_radius = -.01154;

      Aplanat->Lens[1].back_pos.x = 0;
      Aplanat->Lens[1].back_pos.y = 0;
      Aplanat->Lens[1].back_pos.z = Aplanat-
>Lens[1].front_pos.z+0.001;//0.012711;
      Aplanat->Lens[1].back_pos.phi = 0;
      Aplanat->Lens[1].back_pos.theta = 0;
      Aplanat->Lens[1].back_radius = 0.026205;

      Aplanat->Lens[2].ref_index = 1.776;
      Aplanat->Lens[2].front_pos.x = 0;
      Aplanat->Lens[2].front_pos.y = 0;
      Aplanat->Lens[2].front_pos.z = Aplanat-
>Lens[1].back_pos.z+0.0175;//+.0690;
      Aplanat->Lens[2].front_pos.phi = 0;
      Aplanat->Lens[2].front_pos.theta = 0;
      Aplanat->Lens[2].front_radius = 0.026205;

      Aplanat->Lens[2].back_pos.x = 0;
      Aplanat->Lens[2].back_pos.y = 0;
      Aplanat->Lens[2].back_pos.z = Aplanat->Lens[2].front_pos.z+0.001;
//0.030004;
      Aplanat->Lens[2].back_pos.phi = 0;
      Aplanat->Lens[2].back_pos.theta = 0;
```

```
	Aplanat->Lens[2].back_radius = -0.01154;

	Aplanat->Lens[3].ref_index = 1.776;
	Aplanat->Lens[3].front_pos.x = 0;
	Aplanat->Lens[3].front_pos.y = 0;
	Aplanat->Lens[3].front_pos.z = Aplanat-
>Lens[2].back_pos.z+0.000081;//0.030085;
	Aplanat->Lens[3].front_pos.phi =0;
	Aplanat->Lens[3].front_pos.theta =0;
	Aplanat->Lens[3].front_radius = .0214;

	Aplanat->Lens[3].back_pos.x = 0;
	Aplanat->Lens[3].back_pos.y = 0;
	Aplanat->Lens[3].back_pos.z = Aplanat-
>Lens[3].front_pos.z+0.0015;
	Aplanat->Lens[3].back_pos.phi = 0;
	Aplanat->Lens[3].back_pos.theta = 0;
	Aplanat->Lens[3].back_radius = 0.007706;

	Aplanat->Exit_Plane = Aplanat->Lens[3].back_pos.z+Aplanat-
>Lens[0].front_pos.z;
return true;

}



bool Initialize_Doub(Define_Lens_System *Aplanat)
{
	Aplanat->Lens[0].ref_index = 1.776;
	Aplanat->Lens[0].front_pos.x = 0;
	Aplanat->Lens[0].front_pos.y = 0;
	Aplanat->Lens[0].front_pos.z = 0.011211; //all #'s in meters
	Aplanat->Lens[0].front_pos.phi = 0;
	Aplanat->Lens[0].front_pos.theta = 0;
	Aplanat->Lens[0].front_radius = 0.026205;

	Aplanat->Lens[0].back_pos.x = 0;
	Aplanat->Lens[0].back_pos.y = 0;
	Aplanat->Lens[0].back_pos.z = Aplanat-
>Lens[0].front_pos.z+0.000081;
	Aplanat->Lens[0].back_pos.phi = 0;
	Aplanat->Lens[0].back_pos.theta = 0;
	Aplanat->Lens[0].back_radius = -0.01154;

	Aplanat->Lens[1].ref_index = 1.75;
	Aplanat->Lens[1].front_pos.x = 0;
	Aplanat->Lens[1].front_pos.y = 0;
	Aplanat->Lens[1].front_pos.z = Aplanat->Lens[0].back_pos.z +
0.000081;//0.011719;
	Aplanat->Lens[1].front_pos.phi =0;
	Aplanat->Lens[1].front_pos.theta =0;
	Aplanat->Lens[1].front_radius = .0214;
```

```
	Aplanat->Lens[1].back_pos.x = 0;
	Aplanat->Lens[1].back_pos.y = 0;
	Aplanat->Lens[1].back_pos.z = Aplanat-
>Lens[1].front_pos.z+0.0015;//0.012711;
	Aplanat->Lens[1].back_pos.phi = 0;
	Aplanat->Lens[1].back_pos.theta = 0;
	Aplanat->Lens[1].back_radius = 0.007706;


	Aplanat->Exit_Plane = Aplanat->Lens[1].back_pos.z;
	return true;
}

bool Initialize_Sing_Lenses(Define_Lens_System *Aplanat)
{
	Aplanat->Lens[0].ref_index = 1.776;
	Aplanat->Lens[0].front_pos.x = 0;
	Aplanat->Lens[0].front_pos.y = 0;
	Aplanat->Lens[0].front_pos.z = 0.01 -0.0003; //all #'s in meters
	Aplanat->Lens[0].front_pos.phi = 0;
	Aplanat->Lens[0].front_pos.theta = 0;
	Aplanat->Lens[0].front_radius = 0.007706;

	Aplanat->Lens[0].back_pos.x = 0;
	Aplanat->Lens[0].back_pos.y = 0;
	Aplanat->Lens[0].back_pos.z = Aplanat-
>Lens[0].front_pos.z+0.0015;
	Aplanat->Lens[0].back_pos.phi = 0;
	Aplanat->Lens[0].back_pos.theta = 0;
	Aplanat->Lens[0].back_radius = 10000;

	Aplanat->Lens[1].ref_index = 1.776;
	Aplanat->Lens[1].front_pos.x = 0;
	Aplanat->Lens[1].front_pos.y = 0;
	Aplanat->Lens[1].front_pos.z = Aplanat->Lens[0].back_pos.z+
2*Aplanat->Lens[0].front_pos.z-.0005;
	Aplanat->Lens[1].front_pos.phi =0;
	Aplanat->Lens[1].front_pos.theta =0;
	Aplanat->Lens[1].front_radius = 10000;

	Aplanat->Lens[1].back_pos.x = 0;
	Aplanat->Lens[1].back_pos.y = 0;
	Aplanat->Lens[1].back_pos.z = Aplanat-
>Lens[1].front_pos.z+0.0015;//0.012711;
	Aplanat->Lens[1].back_pos.phi = 0;
	Aplanat->Lens[1].back_pos.theta = 0;
	Aplanat->Lens[1].back_radius = 0.007706;

	Aplanat->Exit_Plane = Aplanat->Lens[1].back_pos.z+Aplanat-
>Lens[0].front_pos.z-.0005;
return true;}
```

```
//Surface_h
#define Surface_h

#include "Ray.h"

struct cart_cords
{
	double x,y,z, theta, phi;
};
struct sph_cords
{
	double L,sin_theta,cos_theta,sin_phi,cos_phi;
};

//***********************
class Lens_Surfaces
{
private:

	bool l_f(Ray * temp_ray, sph_cords *k);
	bool sin_theta_f(Ray * temp_ray, sph_cords *k);
	bool cos_theta_f(Ray * temp_ray, sph_cords *k);
	bool sin_phi_f(Ray * temp_ray, sph_cords *k);
	bool cos_phi_f(Ray * temp_ray, sph_cords *k);

	bool l_b(Ray * temp_ray, sph_cords *k);
	bool sin_theta_b(Ray * temp_ray, sph_cords *k);
	bool cos_theta_b(Ray * temp_ray, sph_cords *k);
	bool sin_phi_b(Ray * temp_ray, sph_cords *k);
	bool cos_phi_b(Ray * temp_ray, sph_cords *k);

public:

	int name;
	//doub ref_index (int x, int y, int z) { }//returns the ref index
at a pos
	double ref_index ; //start out with constant ref index
	double  front_radius, back_radius;
	cart_cords front_pos; //absolute position of the lens
	cart_cords back_pos; // relative to the front of the lens i.e.
the thickness
	bool Refract_front(Ray * temp_ray); //try n figure out how to
make this a fn pointer that can be assigned during the surface def
	bool Refract_back(Ray * temp_ray);

};
```

```
//Surface.cpp
#include "stdafx.h"
#include "Surface.h"
#include "math.h"
#include "EucVect.h"

#define PI 3.14159265358979323846264338327795
/*
Lens_Surface::Lens_Surface(int N)
{
      Num_Lens = N;
      x = new double[Num_Lens];
}
Lens_Surface::~Lens_Surface()
{
      delete[] x;
} */

// calculate the point of impact of a ray with the lens surface
bool Lens_Surfaces::l_f(Ray *temp_ray, sph_cords *k)
{
      double B,C,R,S,a,b,e,kx,ky,kz, f_pos_z;
      B=C=R=S=a=b=e=kx=ky=kz=0;

      kx = temp_ray->xhat;
      ky = temp_ray->yhat;
      kz = temp_ray->zhat;

      R = front_radius;
      S = front_pos.z;  //measures position of lens surface closest to
or farthest from ray source z axis for pos and neg curvature objs resp.
      f_pos_z = S+R;

      a = temp_ray->x-front_pos.x;
      b = temp_ray->y-front_pos.y;
      e = temp_ray->z-f_pos_z; //the definition of e sets the sign
convention

      B = kx*a + ky*b + kz*e;
      C = a*a + b*b + e*e -R*R;

      double discriminant = (B*B-C); //verify this formula w/hernan...
      if(discriminant < 0)
            return false;
      discriminant = sqrt( discriminant );

      if( R<0 )   // verify this w/hernan
            k->L = -B + discriminant;
      else
            k->L = -B - discriminant;

      return true;
}
```

```
bool Lens_Surfaces::cos_theta_f(Ray *temp_ray, sph_cords *k)
{
	double R,S,e,kz, f_pos_z;
	R=S=e=kz=f_pos_z=0;

	kz = temp_ray->zhat;
	R = front_radius;
	S = front_pos.z;  //measures position of lens surface closest to
or farthest from ray source z axis for pos and neg curvature objs resp.
	f_pos_z = S+R;
	e = temp_ray->z-f_pos_z;

	if (R<0)
		R=sqrt(R*R);

	k->cos_theta = (k->L * kz + e)/R;  // notice that sin depends on
the cos already being calculated!

	if(k->cos_theta > 1) //due to the way we compute cos_theta there
could be f.p. error
	{                                // which could lead to a cos > 1
for theta << 1.
		if(k->cos_theta > 1+1e-3)
			return false;
		k->cos_theta=1;
	}
	return true;
}
bool Lens_Surfaces::sin_theta_f(Ray *temp_ray, sph_cords *k)
{
	k->sin_theta = sqrt( 1-k->cos_theta*k->cos_theta ); // notice
that sin depends on the cos already being calculated!
	return true;
}
bool Lens_Surfaces::sin_phi_f(Ray *temp_ray, sph_cords *k)
{
	double R,b,ky;
	R=b=ky=0;

	ky = temp_ray->yhat;
	b = temp_ray->y-front_pos.y;
	R = front_radius;
	if (R<0)
		R=sqrt(R*R);

	k->sin_phi = (k->L*ky+b)/(R * k->sin_theta);
	if(k->sin_phi > 1) //due to the way we compute cos_theta there
could be f.p. error
	{                                // which could lead to a cos > 1
for theta << 1.
		if(k->sin_theta > 1e-6)
			return false;
		k->sin_phi=1;
```

```
	}
	return true;
}
bool Lens_Surfaces::cos_phi_f(Ray *temp_ray, sph_cords *k)
{
	double R,a,kx;
	R=a=kx=0;

	kx = temp_ray->xhat;
	a = temp_ray->x-front_pos.x;
	R = front_radius;
	if (R<0)
		R=sqrt(R*R);

	k->cos_phi = (k->L*kx+a)/(R * k->sin_theta);
	if(k->cos_phi > 1) //due to the way we compute cos_theta there
could be f.p. error
	{                                // which could lead to a cos > 1
for theta << 1.
		if(k->sin_theta > 1+1e-6)
			return false;
		k->cos_phi=1;
	}
	return true;
}


	// calculate the point of impact of a ray with the lens surface
bool Lens_Surfaces::l_b(Ray* temp_ray, sph_cords *k)
{
	double B,C,R,S,a,b,e,kx,ky,kz, b_pos_z;
	B=C=R=S=a=b=e=kx=ky=kz=0;

	kx = temp_ray->xhat;
	ky = temp_ray->yhat;
	kz = temp_ray->zhat;

	R = back_radius;
	S = back_pos.z;  //measures position of lens surface closest to
or farthest from ray source z axis for pos and neg curvature objs resp.
	b_pos_z = S-R;

	a = temp_ray->x-back_pos.x;
	b = temp_ray->y-back_pos.y;
	e = temp_ray->z-b_pos_z; //the definition of e sets the sign
convention

	B = kx*a + ky*b + kz*e;
	C = a*a + b*b + e*e -R*R;

	double discriminant = (B*B-C); //verify this formula w/hernan...
	if(discriminant < 0)
		return false;
```

```
	discriminant = sqrt( discriminant );

	if( R>0 )   // verify this w/hernan
		k->L = -B + discriminant;
	else
		k->L = -B - discriminant;

	return true;
}
bool Lens_Surfaces::cos_theta_b(Ray *temp_ray, sph_cords *k)
{
	double R,S,e,kz, b_pos_z;
	R=S=e=kz=b_pos_z=0;

	kz = temp_ray->zhat;
	R = back_radius;
	S = back_pos.z;  //measures position of lens surface closest to
or farthest from ray source z axis for pos and neg curvature objs resp.
	b_pos_z = S-R;
	e = temp_ray->z-b_pos_z;

	if (R<0)
		R=sqrt(R*R);

	k->cos_theta = (k->L * kz + e)/R;  // notice that sin depends on
the cos already being calculated!

	if(k->cos_theta > 1) //due to the way we compute cos_theta there
could be f.p. error
	{                              // which could lead to a cos > 1
for theta << 1.
		if(k->cos_theta > 1+1e-3)
			return false;
		k->cos_theta=1;
	}
	return true;
}
bool Lens_Surfaces::sin_theta_b(Ray *temp_ray, sph_cords *k)
{
	k->sin_theta = sqrt( 1-k->cos_theta*k->cos_theta ); // notice
that sin depends on the cos already being calculated!
	return true;
}
bool Lens_Surfaces::sin_phi_b(Ray *temp_ray, sph_cords *k)
{
	double R,b,ky;
	R=b=ky=0;

	ky = temp_ray->yhat;
	b = temp_ray->y-back_pos.y;
	R = back_radius;
	if (R<0)
		R=sqrt(R*R);
```

```
	k->sin_phi = (k->L*ky+b)/(R * k->sin_theta);
	if(k->sin_phi > 1) //due to the way we compute cos_theta there
could be f.p. error
	{                              // which could lead to a cos > 1
for theta << 1.

		if(k->sin_theta > 1e-6)
			return false;
		k->sin_phi=1;
	}
	return true;
}
bool Lens_Surfaces::cos_phi_b(Ray *temp_ray, sph_cords *k)
{
	double R,a,kx;
	R=a=kx=0;

	kx = temp_ray->xhat;
	a = temp_ray->x-back_pos.x;
	R = back_radius;
	if (R<0)
		R=sqrt(R*R);

	k->cos_phi = (k->L*kx+a)/(R * k->sin_theta);
	if(k->cos_phi > 1) //due to the way we compute cos_theta there
could be f.p. error
	{                              // which could lead to a cos > 1
for theta << 1.
		if(k->sin_theta > 1e-6)
			return false;
		k->cos_phi=1;
	}
	return true;
}


////////////////////////////////////////////////

bool Lens_Surfaces::Refract_front(Ray *temp_ray)
{
	sph_cords k;
	k.L=k.sin_theta=k.cos_theta=k.sin_phi=k.cos_phi=0;
	// calculate the point of impact of a ray with the lens surface
	if(!l_f(temp_ray, &k))
		return false;
	if(!cos_theta_f(temp_ray, &k))
		return false;
	if(!sin_theta_f(temp_ray, &k)) // use this stuff to verify the
radial hat vector then comment out
		return false;
	if(!cos_phi_f(temp_ray, &k))
		return false;
```

```
	if(!sin_phi_f(temp_ray, &k))
		return false;

	Euc_Vect k1_hat(3);
	Euc_Vect Radial_hat(3);
	Euc_Vect w_hat(3);
	Euc_Vect k2_hat(3);

	k1_hat.cor[0] = temp_ray->xhat;
	k1_hat.cor[1] = temp_ray->yhat;
	k1_hat.cor[2] = temp_ray->zhat;
	k1_hat.hat();

	Radial_hat.cor[0] = k.sin_theta*k.cos_phi;
	Radial_hat.cor[1] = k.sin_theta*k.sin_phi;
	Radial_hat.cor[2] = k.cos_theta;
	Radial_hat.Len();


	double sin_th1 = Norm_Cross(&Radial_hat,&k1_hat,&w_hat); //trig
for snells law...verify w hernan
	double sin_th2 = sin_th1/ref_index;
	double cos_th1 = sqrt(1-sin_th1*sin_th1);
	double cos_th2 = sqrt(1-sin_th2*sin_th2);

	if(front_radius>0)
	{
		w_hat.cor[0] = k1_hat.cor[0] + Radial_hat.cor[0] * cos_th1;
		w_hat.cor[1] = k1_hat.cor[1] + Radial_hat.cor[1] * cos_th1;
		w_hat.cor[2] = k1_hat.cor[2] + Radial_hat.cor[2] * cos_th1;
		w_hat.hat();

		k2_hat.cor[0] = sin_th2 * w_hat.cor[0] - cos_th2 *
Radial_hat.cor[0];
		k2_hat.cor[1] = sin_th2 * w_hat.cor[1] - cos_th2 *
Radial_hat.cor[1];
		k2_hat.cor[2] = sin_th2 * w_hat.cor[2] - cos_th2 *
Radial_hat.cor[2];
	}
	if(front_radius<0)
	{
		w_hat.cor[0] = k1_hat.cor[0] - Radial_hat.cor[0] * cos_th1;
		w_hat.cor[1] = k1_hat.cor[1] - Radial_hat.cor[1] * cos_th1;
		w_hat.cor[2] = k1_hat.cor[2] - Radial_hat.cor[2] * cos_th1;
		w_hat.hat();

		k2_hat.cor[0] = sin_th2 * w_hat.cor[0] + cos_th2 *
Radial_hat.cor[0];
		k2_hat.cor[1] = sin_th2 * w_hat.cor[1] + cos_th2 *
Radial_hat.cor[1];
		k2_hat.cor[2] = sin_th2 * w_hat.cor[2] + cos_th2 *
Radial_hat.cor[2];
	}
```

```
	k2_hat.hat();
	double x2,y2,z2,q2;
	q2 = k.L * k1_hat.cor[2]/k2_hat.cor[2];

	x2 = k.L * k1_hat.cor[0] + temp_ray->x - q2 * k2_hat.cor[0];
	y2 = k.L * k1_hat.cor[1] + temp_ray->y - q2 * k2_hat.cor[1];
	z2 = 0;

	temp_ray->x=x2;
	temp_ray->y=y2;
	temp_ray->z=z2;
	temp_ray->xhat=k2_hat.cor[0];
	temp_ray->yhat=k2_hat.cor[1];
	temp_ray->zhat=k2_hat.cor[2];

	return true;
}

bool Lens_Surfaces::Refract_back(Ray *temp_ray)
{
	sph_cords k;
	k.L=k.sin_theta=k.cos_theta=k.sin_phi=k.cos_phi=0;
	// calculate the point of impact of a ray with the lens surface
	if(!l_b(temp_ray, &k))
		return false;
	if(!cos_theta_b(temp_ray, &k))
		return false;
	if(!sin_theta_b(temp_ray, &k)) // use this stuff to verify the
radial hat vector then comment out
		return false;
	if(!cos_phi_b(temp_ray, &k))
		return false;
	if(!sin_phi_b(temp_ray, &k))
		return false;

	Euc_Vect k1_hat(3);
	Euc_Vect Radial_hat(3);
	Euc_Vect w_hat(3);
	Euc_Vect k2_hat(3);

	k1_hat.cor[0] = temp_ray->xhat;
	k1_hat.cor[1] = temp_ray->yhat;
	k1_hat.cor[2] = temp_ray->zhat;
	k1_hat.hat();  //////////////

	Radial_hat.cor[0] = k.sin_theta*k.cos_phi;
	Radial_hat.cor[1] = k.sin_theta*k.sin_phi;
	Radial_hat.cor[2] = k.cos_theta;
	Radial_hat.Len();


	double sin_th1 = Norm_Cross(&Radial_hat,&k1_hat,&w_hat); //trig
for snells law...verify w hernan
```

```
	double sin_th2 = sin_th1*ref_index;
	double cos_th1 = sqrt(1-sin_th1*sin_th1);
	double cos_th2 = sqrt(1-sin_th2*sin_th2);

	if(back_radius<0)
	{
		w_hat.cor[0] = k1_hat.cor[0] + Radial_hat.cor[0] * cos_th1;
		w_hat.cor[1] = k1_hat.cor[1] + Radial_hat.cor[1] * cos_th1;
		w_hat.cor[2] = k1_hat.cor[2] + Radial_hat.cor[2] * cos_th1;
		w_hat.hat();

		k2_hat.cor[0] = sin_th2 * w_hat.cor[0] - cos_th2 *
Radial_hat.cor[0];
		k2_hat.cor[1] = sin_th2 * w_hat.cor[1] - cos_th2 *
Radial_hat.cor[1];
		k2_hat.cor[2] = sin_th2 * w_hat.cor[2] - cos_th2 *
Radial_hat.cor[2];
	}
	if(back_radius>0)
	{
		w_hat.cor[0] = k1_hat.cor[0] - Radial_hat.cor[0] * cos_th1;
		w_hat.cor[1] = k1_hat.cor[1] - Radial_hat.cor[1] * cos_th1;
		w_hat.cor[2] = k1_hat.cor[2] - Radial_hat.cor[2] * cos_th1;
		w_hat.hat();

		k2_hat.cor[0] = sin_th2 * w_hat.cor[0] + cos_th2 *
Radial_hat.cor[0];
		k2_hat.cor[1] = sin_th2 * w_hat.cor[1] + cos_th2 *
Radial_hat.cor[1];
		k2_hat.cor[2] = sin_th2 * w_hat.cor[2] + cos_th2 *
Radial_hat.cor[2];
	}
	k2_hat.hat();
	double x2,y2,z2,q2;
	q2 = k.L * k1_hat.cor[2]/k2_hat.cor[2];

	x2 = k.L * k1_hat.cor[0] + temp_ray->x - q2 * k2_hat.cor[0];
	y2 = k.L * k1_hat.cor[1] + temp_ray->y - q2 * k2_hat.cor[1];
	z2 = 0;

	temp_ray->x=x2;
	temp_ray->y=y2;
	temp_ray->z=z2;
	temp_ray->xhat=k2_hat.cor[0];
	temp_ray->yhat=k2_hat.cor[1];
	temp_ray->zhat=k2_hat.cor[2];

	return true;
}

//*************************************
```

```
//EucVect.h

#define EucVect_h

#include "math.h"

class Euc_Vect
{
public:
	int dim;
	double * cor;
	double length;

	Euc_Vect(int dim);
	double Len();
	double hat();
	~Euc_Vect();
};


double Cross(Euc_Vect *A, Euc_Vect *B, Euc_Vect *C);
double Dot(Euc_Vect *A, Euc_Vect *B, Euc_Vect *C);
double Norm_Cross(Euc_Vect *A, Euc_Vect *B, Euc_Vect *C);
double Norm_Dot(Euc_Vect *A, Euc_Vect *B, Euc_Vect *C);
```

```
//EucVect.cpp

#include "stdafx.h"
#include "EucVect.h"


Euc_Vect::Euc_Vect(int N)
{
	dim = N;
	cor = new double[dim];
	length =0;
}
Euc_Vect::~Euc_Vect()
{
	delete[] cor;
}

double Cross(Euc_Vect *A, Euc_Vect *B, Euc_Vect *C)
{
	C->cor[0] = A->cor[1] *B->cor[2]-A->cor[2]*B->cor[1];
	C->cor[1] = -A->cor[2] *B->cor[0]+A->cor[0]*B->cor[2];
	C->cor[2] = A->cor[0] *B->cor[1]-A->cor[1]*B->cor[0];

	return sqrt(C->cor[0]*C->cor[0]+C->cor[1]*C->cor[1]+C->cor[2]*C-
>cor[2]);
}
double Dot(Euc_Vect *A, Euc_Vect *B, Euc_Vect *C)
{
	C->cor[0] = A->cor[0]*B->cor[0];
	C->cor[1] = A->cor[1]*B->cor[1];
	C->cor[2] = A->cor[2]*B->cor[2];

	return C->cor[0] + C->cor[1]+ C->cor[2];
}
double Norm_Cross(Euc_Vect *A, Euc_Vect *B, Euc_Vect *C) //returns
sin(theta_AB)
{
	A->Len();
	B->Len();
	C->cor[0] = A->cor[1] *B->cor[2]-A->cor[2]*B->cor[1];
	C->cor[1] = A->cor[2] *B->cor[0]-A->cor[0]*B->cor[2];
	C->cor[2] = A->cor[0] *B->cor[1]-A->cor[1]*B->cor[0];

	return sqrt(C->cor[0]*C->cor[0]+C->cor[1]*C->cor[1]+C->cor[2]*C-
>cor[2])/(A->length*B->length); //add sign info to tell whether its a
clockwise vs counterclockwise product...
}
double Norm_Dot(Euc_Vect *A, Euc_Vect *B, Euc_Vect *C) // returns
cos(theta_AB)
{
		A->Len();
		B->Len();
```

```
	C->cor[0] = A->cor[0]*B->cor[0];
	C->cor[1] = A->cor[1]*B->cor[1];
	C->cor[2] = A->cor[2]*B->cor[2];

	return (C->cor[0] + C->cor[1] + C->cor[2])/(A->length*B->length);
}

double Euc_Vect::Len()
{
	length = sqrt(cor[0]*cor[0]+cor[1]*cor[1]+cor[2]*cor[2]);
	return length;
}

double Euc_Vect::hat()
{
	if(Len()==0) return 0;
	cor[0]/= length;
	cor[1]/= length;
	cor[2]/= length;
}
```

```
//Trace.h

#define Trace_h

#include "Lens_System.h"
#include "EucVect.h"

#define FIBER_RADIUS 125e-6
#define PI 3.14159265358979323846264338327795
#define THETA 11
#define N_A 0.0908

int Launch(Ray * temp_ray);
bool get_ray(Ray * temp_ray);
bool reject_ray(Ray * temp_ray);
bool Fiber_Intersect(Ray* temp_ray, double *x,double *y);
//************************

bool Trace(Ray * temp_ray, Define_Lens_System * Lens_Sys);
bool detect_ray(Ray *temp_ray, double z);
bool propigate(Ray *temp_ray,double z);
```

```
//Trace.cpp
#include "stdafx.h"
#include "Trace.h"

int Launch(Ray * temp_ray)
{
	int i=0;
	while(!get_ray(temp_ray))
		i++;
	return i;
 }
////////////////////////////////////////

//**************************************
bool get_ray(Ray * temp_ray)
{
	Range x, y, z, theta, phi;
	x.min=y.min=z.min=theta.min=phi.min=x.max=y.max=z.max=theta.max=p
hi.max=0;
	x.max=FIBER_RADIUS;
	y.max=FIBER_RADIUS;
	x.min=-FIBER_RADIUS;
	y.min=-FIBER_RADIUS;
	theta.max= 2*PI*THETA/360.0;
	phi.max= 2*PI;
	get_random_ray(temp_ray,x, y, z, theta, phi);
	return reject_ray(temp_ray);
}

bool reject_ray(Ray * temp_ray)
{
	//rejects the candidate ray if the angle it makes with the
surface normal is too great
	double x,y;
	x=y=0;

	double A,B,C,L;
	A = (temp_ray->xhat*temp_ray->xhat+temp_ray->yhat*temp_ray-
>yhat);
	if(A==0)
		return true;
	B = 2*(temp_ray->xhat*temp_ray->x+temp_ray->yhat*temp_ray->y);
	C = temp_ray->x*temp_ray->x+temp_ray->y*temp_ray->y-
FIBER_RADIUS*FIBER_RADIUS;
	if(C>0)
		return false;
	double disc=B*B-4*A*C;
	if(disc<0)
		return false;
	L = ( -B-sqrt(disc) ) / (2*A);

	Euc_Vect T_R(3);
	Euc_Vect R(3);
```

```
	Euc_Vect N(3);

	R.cor[0] = L*temp_ray->xhat+temp_ray->x;
	R.cor[1] = L*temp_ray->yhat+temp_ray->y;
	R.cor[2] = 0;
	T_R.cor[0] = temp_ray->xhat;
	T_R.cor[1] = temp_ray->yhat;
	T_R.cor[2] = temp_ray->zhat;

	double TRxR = Norm_Cross(&T_R,&R,&N);
	TRxR = 1-TRxR*TRxR;
	if( TRxR <= N_A*N_A)
		return true;
	else
		return false;
}

bool Fiber_Intersect(Ray *temp_ray,double *x,double *y)
{
	double A,B,C,L;
	A = (temp_ray->xhat*temp_ray->xhat+temp_ray->yhat*temp_ray-
>yhat);
	if(A==0)
		return true;
	B = 2*(temp_ray->xhat*temp_ray->x+temp_ray->yhat*temp_ray->y);
	C = temp_ray->x*temp_ray->x+temp_ray->y*temp_ray->y-
FIBER_RADIUS*FIBER_RADIUS;
	double disc=B*B-4*A*C;
	if(disc<0)
		return false;
	L = ( -B-sqrt(disc) ) / (2*A);

	Euc_Vect T_R(3);
	Euc_Vect R(3);
	Euc_Vect N(3);

	R.cor[0] = L*temp_ray->xhat+temp_ray->x;
	R.cor[1] = L*temp_ray->yhat+temp_ray->y;
	R.cor[2] = 0;
	T_R.cor[0] = temp_ray->xhat;
	T_R.cor[1] = temp_ray->yhat;
	T_R.cor[2] = temp_ray->zhat;

	double TRxR = Norm_Cross(&T_R,&R,&N);
	TRxR = sqrt(1-TRxR*TRxR);
	if( TRxR <= N_A)
		return true;
	else
		return false;
}
//************************

bool detect_ray(Ray *temp_ray, double z)
```

```
{
	double x,y,q;
	q = z / temp_ray->zhat;
	x = temp_ray->xhat*q+temp_ray->x;
	y = temp_ray->yhat*q+temp_ray->y;
	double test = sqrt(x*x+y*y);
	if(test > FIBER_RADIUS)
		return false;
	temp_ray->x = x;
	temp_ray->y = y;
	return Fiber_Intersect(temp_ray,&x,&y);
}


//***************************************
bool Trace(Ray * temp_ray, Define_Lens_System * Lens_Sys)
{

	for( int i=0; i< Lens_Sys->Num_Lens;i++)
	{
		if(!Lens_Sys->Lens[i].Refract_front(temp_ray))
			return false;
		if(!Lens_Sys->Lens[i].Refract_back(temp_ray))
			return false;
	}
	return true;
}

bool propigate(Ray *temp_ray, double z)
{
	double q, x, y;
	q = z/temp_ray->zhat;
	x = q*temp_ray->xhat;
	y = q*temp_ray->yhat;

	if ( (z - temp_ray->z) >0)
	{
		temp_ray->x += x;
		temp_ray->y += y;
		temp_ray->z += z;
		return true;
	}
	else
		return false;
}
```

```
//Ray.h
#define Ray_h

class Ray{
public:
      Ray(){x=y=z=xhat=yhat=zhat=theta=phi=0;};
      void copy(Ray *temp_ray){x=temp_ray->x;y=temp_ray->y;z=temp_ray-
>z;xhat=temp_ray->xhat;yhat=temp_ray->yhat;zhat=temp_ray-
>zhat;theta=temp_ray->theta;phi=temp_ray->phi;}
      double xhat,yhat,zhat; //this is k_hat
      double x,y,z; // origin of ray for my purposes it is p*h_hat
      double theta, phi; // these specify k_hat
  //k1=l*k_hat-p*h_hat
};
struct Range{
      double min,max;
};

void get_random_ray(Ray * temp_ray, Range x, Range y, Range z, Range
theta, Range phi);
```

```
//Ray.cpp

#include "stdafx.h"
#include "Ray.h"
#include "stdlib.h"
#include "time.h"
#include "math.h"

#define PI 3.14159265358979323846264338327795

void get_random_ray(Ray * temp_ray, Range x, Range y, Range z, Range
theta, Range phi)
{
	if(x.min!= x.max)
	{
		double q = (double) (RAND_MAX);
		double ran = (double)( rand());
			ran = ((double)ran/(double) RAND_MAX);
		ran =ran* x.max;
		temp_ray->x=ran;
		ran = (double)  (rand());
		ran = ran/(double) (RAND_MAX);
		ran *= 2 * PI;
		temp_ray->y = temp_ray->x * sin(ran);
		temp_ray->x *= cos(ran);
	}
	else {temp_ray->x=x.min;}
	if(y.min==y.max)
		temp_ray->y=y.max;
	if(z.min!=z.max)
	{
		double ran = ((double) rand()/(double) RAND_MAX);
		ran =ran*(z.max-z.min)+ z.min;
		temp_ray->z=ran;
	}
	else {temp_ray->z=z.min;}
	if (theta.min!=theta.max)
	{
		double ran = ((double) rand()/(double) RAND_MAX);
		ran = ran*(theta.max-theta.min)+theta.min;
		temp_ray->theta=ran;
		temp_ray->xhat = sin(ran);
		temp_ray->yhat = sin(ran);
		temp_ray->zhat = cos(ran);
	}
	else {
		temp_ray->theta=theta.min;
		temp_ray->xhat = sin(temp_ray->theta);
		temp_ray->yhat = sin(temp_ray->theta);
		temp_ray->zhat = cos(temp_ray->theta);
	}
	if(phi.min!=phi.max)
	{
```

```
            double ran = ((double) rand()/(double) RAND_MAX);
            ran =ran*(phi.max-phi.min)+phi.min;
            temp_ray->phi=ran;
            temp_ray->xhat*=cos(ran);
            temp_ray->yhat*=sin(ran);
      }
      else {
            temp_ray->phi=phi.min;
            temp_ray->xhat*=cos(temp_ray->phi);
            temp_ray->yhat*=sin(temp_ray->phi);
      }
}
```

Appendix C: *Sample Code from Particle Counter*

This code was used to count the particles in the TEM images. To function, this code requires many libraries that are not shown but nevertheless can give a flavor for the type of processes developed for that application. A reader attempting to run the algorithm presented here would need to develop their own interface.

```
#include <vcl.h>
#pragma hdrstop

#include "Unit1.h"
//---------------------------------------------------------------------------
#pragma package(smart_init)
#pragma link "Plot"
#pragma resource "*.dfm"
TForm1 *Form1;
//---------------------------------------------------------------------------
__fastcall TForm1::TForm1(TComponent* Owner)
  : TForm(Owner)
{
}
//---------------------------------------------------------------------------
bool OpenFile()
{
   if (Form1->OpenPictureDialog1->Execute() && CheckImage())
   {
      Form1->Image1->Refresh();
      return true;
   }
   return false;
}

/////**********************????CHECK_IMAGE???**************************
**///////
////*****************************BUTTON_1*********************************
*****////

bool CheckImage()
{
```

```
   if (!CheckExtension()) return false;

   return true;
}
//////*******************????CHECK_EXTENSION????************************
**///////
////*****************************BUTTON_1*********************************
*****////
bool CheckExtension()
{
   filename = Form1->OpenPictureDialog1->FileName;

   AnsiString ext = filename.SubString(filename.Length() - 2, 3);
   if (ext.AnsiCompareIC("bmp") == 0) Form1->Image1->Picture-
>LoadFromFile(filename);
   else if (ext.AnsiCompareIC("jpg") == 0)
   {
      TJPEGImage *jp = new TJPEGImage();
      jp->LoadFromFile(filename);
      Form1->Image1->Picture->Bitmap->Assign(jp);
      delete jp;
   }
   else
   {
      Application->MessageBox("Unsupported File Type", "Error Opening File",
MB_OK);
      return false;
   }

   return true;
}
/////**********************INITIALIZE_IMAGE_MEMORY*********************
*******////
////*****************************BUTTON_1*********************************
*****////
void Initialize_Image_Memory()
{
int TEMsize = MAX;
if(image!=NULL)
{
  if(imagebk!=NULL)
    for(int i=0;i<LastMAX;i++)
      delete[] imagebk[i];
```

```
  delete [] imagebk;
  imagebk=NULL;
  for(int i=0; i<LastMAX;i++)
    delete[] image[i];
  image = NULL;
}
dotlist.Clear();
rowavg.Clear();
colavg.Clear();
spotnum=0;
q=0;

Vect<double> tmprow(TEMsize);
ZeroMemory(tmprow.data,sizeof(double)*TEMsize);
rowavg.Pass_Data(&tmprow);
Vect<double> tmpcol(TEMsize);
ZeroMemory(tmpcol.data,sizeof(double)*TEMsize);
colavg.Pass_Data(&tmpcol);
image = new double*[TEMsize]; //check delete
LastMAX=MAX;
for(unsigned i=0;i< TEMsize;i++) {
 image[i]=new double[TEMsize];
 for(unsigned j=0;j<TEMsize;j++)  {
    image[i][j]=256-Form1->Image1->Canvas->Pixels[i][j]%256;
    rowavg.data[j]+=image[i][j]/((float)(TEMsize));
 }
}
}

////**************************NO_FUNCTIONS_FOR_BUTTON_2*************
*********////
////**************************NO_FUNCTIONS_FOR_BUTTON_2*************
*********////

////*****************************IMAGE_BACUP_RESTORE*****************
********////
////*****************************BUTTON_3*******************************
*****////
void image_backup_restore()
{
int TEMsize=MAX;

if(imagebk==NULL)
```

```
{
  imagebk=new double*[TEMsize];
  for(int i =0;i<TEMsize;i++)
  {
    imagebk[i]=new double[TEMsize];
    CopyMemory(&imagebk[i][0],&image[i][0],sizeof(double)*TEMsize);
  }
}
else
{
  for(int i =0;i<TEMsize;i++)
    CopyMemory(&image[i][0],&imagebk[i][0],sizeof(double)*TEMsize);
}
}

////**********????MASK_INITIALIZED?????**********
****////
////**********BUTTON_4**********
*****////
bool mask_initialized(int &count)
{
if (image == NULL) //no image loaded!!!
      return FALSE;
int TEMsize=MAX;
count=0;   //set all memory to defalut null values
dotlist.Clear();
if(mask.data != NULL)   {
  mask.Clear();
  q=0;
  spotnum=0;
}
Matrix<bool> tmpmask(TEMsize,TEMsize);// allocate and initialize working memory
for(int i =0; i<TEMsize;i++)
  for(int j=0;j<TEMsize;j++)
    tmpmask.data[i][j]=FALSE;
mask.Pass_Data(&tmpmask); ///initialize mask

for(int i=0;i< TEMsize;i++){// load mask data according to local threshold conditions
 for(int j=0;j<TEMsize;j++)
    if(rowavg.data[j]+cut*stdev<image[i][j] && colavg.data[i]+cut*stdev<image[i][j])  {
      count++;
      mask.data[i][j]=TRUE;
    }
```

```
}
return TRUE; ///mask initialization successfull
}

////**************************BUILD_DOTLIST*************************
*****////
////**********************BUTTON_4*************************************
*****////
void build_dotlist(int &count)
{
int TEMsize=MAX;
int OUT_OF_RANGE=-1;

{
if(dotlist.data==NULL)
      dotlist.Clear();
Vect<spotdot> tmpdotlist(count);
ZeroMemory(tmpdotlist.data,sizeof(spotdot)*count);
dotlist.Pass_Data(&tmpdotlist);
totaldots=count;
}

int boxres = Form1->Edit4->Text.ToInt();

for(int i=0;i<count;i++)
  dotlist.data[i].spotnumber=OUT_OF_RANGE;

for(int i=boxres;i<TEMsize;i++)   {  //build a list of candidate nanoparticles or spots
(dot~=pixle)
  for(int j=boxres;j<TEMsize;j++)   {
    if(mask.data[i][j])      {
      int tmpdotcount=q;
      spotnum++;
      dotwalk(j,i);
      tmpdotcount=dotlist.data[tmpdotcount].dotcount=q-tmpdotcount;
      if(tmpdotcount>1)
        dotlist.data[q-1].dotcount=tmpdotcount;
    }
  }
}
for(int i=0;i<count;i++)
  if(dotlist.data[i].dotcount==0)
```

```
    dotlist.data[i].dotcount=dotlist.data[i-1].dotcount;  //finished building list of candidate
nanoparticles
}

////**************************COUNT_SPOTS*****************************
******////
////************************BUTTON_4**********************************
*****////
int count_spots()
{
int OUT_OF_RANGE =-1;
int RES=Form1->Edit5->Text.ToInt();  //sets a detection threshold i.e. too small = below
microsope resolution
int MAXRES=Form1->Edit9->Text.ToInt(); //sets a detection threshold i.e. too big =
micro-particle or large agglomerate
int spots =0;
for(unsigned i=0;i<dotlist.size;i+=dotlist.data[i].dotcount)
{
  if(dotlist.data[i].dotcount>RES && dotlist.data[i].dotcount<MAXRES) //asks if
candidate np is within acceptable size range
  {
    dotlist.data[i].spotnumber=spots; // adds the spot number to the dot list
    for(unsigned k=i;k<i+dotlist.data[i].dotcount;k++)
      dotlist.data[k].spotnumber=spots;
    spots++;  // advances the count of np's
  }
  else
  { //if the proposed spot is not within the range to be considered a nanoparticle it is
labled OUT_OF_RANGE to streamline later logic
    for(unsigned k=i;k<i+dotlist.data[i].dotcount;k++)
      dotlist.data[k].spotnumber=OUT_OF_RANGE;
  }
}
return spots;
}
////**************************HILIGHT_NPS*****************************
****////
////************************BUTTON_4**********************************
*****////
void Highlite_Nps()
{
int OUT_OF_RANGE=-1;
```

```
for(unsigned i=0;i<dotlist.size;i++) // highlights candidate np's within appropreate size
range
  if(dotlist.data[i].spotnumber!=OUT_OF_RANGE)
    Form1->Image1->Canvas-
>Pixels[dotlist.data[i].y][dotlist.data[i].x]=(dotlist.data[i].spotnumber%256)+(255-
dotlist.data[i].spotnumber%256)*256*256; //black n white
(dotlist[i].spotnumber%256)+(dotlist[i].spotnumber)*256+(dotlist[i].spotnumber%256)*
256*256;
Form1->Image1->Width=1024;
Form1->Image1->Height=1024;
Form1->Image1->Refresh();
Form1->Image1->Repaint();
}

////**************************BUILD_NPDIST*******************************
*****////
////************************BUTTON_4****BUTTON_5***********************
*******////
void build_NPdist(Vect<double> &dist)
{
int j=0;
int  OUT_OF_RANGE=-1;
double cal = Form1->Edit10->Text.ToDouble(); //sets length scale pixles/micron given
by the microscope
for(unsigned i=0;i<dotlist.size;i+=dotlist.data[i].dotcount){
  if(dotlist.data[i].spotnumber!=OUT_OF_RANGE) {
      dist.data[j]=sqrt(dotlist.data[i].dotcount/(cal*cal*PI))*1000;
      j++;
  }
}
}
////**************************PLOT_HIST**********************************
****////
////************************BUTTON_4***********************************
*****////
void plot_hist(Histogram<double> &Nps)
{
Vect<double> npsize(Nps.Hist.size);
Vect<double> Y(Nps.Hist.size);  //plothist();
for(unsigned i=0;i<Nps.Hist.size;i++)
      Y.data[i]=(double)(Nps.Hist.data[i]);
for(int i=0;i<Nps.Hist.size;i++)
  npsize.data[i]= Nps.min+Nps.step*i;
```

```
Form1->Plot2->Clear();
Form1->Plot2->Draw<double>(npsize.data,Y.data,npsize.size);

Form1->Memo1->Clear();
for (unsigned i =0; i< Nps.Hist.size; i++)
  Form1->Memo1->Lines-
>Add(AnsiString(npsize.data[i])+"\t"+AnsiString(Nps.Hist.data[i]));
}
////*****************************PLOT_GAUSS*****************************
*****////
////************************BUTTON_4*************************************
*****////
void plot_gauss(Histogram<double> &Nps)
{
Vect<double> npsize(Nps.Hist.size);
for(int i=0;i<Nps.Hist.size;i++)
  npsize.data[i]= Nps.min+Nps.step*i;

Vect<double> np_gauss(Nps.Hist.size); //plotgauss;

for (unsigned i =0; i< Nps.Hist.size; i++)
{
  np_gauss.data[i]= (double)(Nps.peak_count)*exp(-0.5*(npsize.data[i]-
Nps.mean)*(npsize.data[i]-
Nps.mean)/((Nps.stddev)*(Nps.stddev)));//npmax/(1+(npsize[i]-max)*(npsize[i]-
max)/((sizdev-1.5)*(sizdev-1.5)));
}
Form1->Plot2->LineColor=clBlue;
Form1->Plot2->Draw<double>(npsize.data,np_gauss.data,npsize.size);
Form1->Plot2->LineColor=clRed;
}


//---------------------------------------------------------------------------//
void __fastcall TForm1::Button1Click(TObject *Sender)
{

if(!OpenFile())
      return;
Initialize_Image_Memory();

unsigned TEMsize=MAX;
```

```
float sum;
double min, max;

cut=Form1->Edit3->Text.ToDouble();
sum=stdev=0;

Form1->Image1->Width=1024;
Form1->Image1->Height=1024;
Form1->Image1->Refresh();
Form1->Image1->Repaint();
{

min=256;
max=0;
for(unsigned i=0;i<TEMsize;i++)
{
  for(unsigned j=0;j<TEMsize;j++)
  {
    image[i][j]=image[i][j]-rowavg.data[j];
    if(image[i][j]>max)
      max=image[i][j];
    if(image[i][j]<min)
      min=image[i][j];
  }
}

double range = max-min;
for(unsigned i=0;i<TEMsize;i++)
{
  for(unsigned j=0;j<TEMsize;j++)
  {
    image[i][j]=255*(image[i][j]-min)/range;
    colavg.data[i]+=image[i][j]/((float)(TEMsize));
    Form1->Image1->Canvas->Pixels[i][j]=(int)(image[i][j]);
  }
}

min=256;
max=0;
for(unsigned i=0;i<TEMsize;i++)
{
  for(unsigned j=0;j<TEMsize;j++)
  {
```

```
      image[i][j]=image[i][j]-colavg.data[i];
      if(image[i][j]>max)
        max=image[i][j];
      if(image[i][j]<min)
        min=image[i][j];
    }
  }

  ZeroMemory(rowavg.data,sizeof(double)*TEMsize);
  ZeroMemory(colavg.data,sizeof(double)*TEMsize);
  range = max-min;
  for(unsigned i=0;i<TEMsize;i++)
  {
    for(unsigned j=0;j<TEMsize;j++)
    {
      image[i][j]=255*(image[i][j]-min)/range;
      rowavg.data[j]+=image[i][j]/((float)(TEMsize));
      colavg.data[i]+=image[i][j]/((float)(TEMsize));
      Form1->Image1->Canvas->Pixels[i][j]=(int)(image[i][j]);
    }
  }
  }

  Form1->Image1->Width=1024;
  Form1->Image1->Height=1024;
  Form1->Image1->Refresh();
  Form1->Image1->Repaint();

  }
  //---------------------------------------------------------------------------
  void __fastcall TForm1::Button2Click(TObject *Sender)
  {
    if(!Filter)
    {
      Form1->Button2->Caption="Hide Filter";
      Filter = TRUE;
      return;
    }

    if(Filter)
    {
      Form1->Button2->Caption="Show Filter";
      Filter = FALSE;
```

```
    return;
  }
}
//---------------------------------------------------------------------------

void __fastcall TForm1::Button3Click(TObject *Sender)
{
if(image ==NULL)
  return;
image_backup_restore();

int TEMsize=MAX;

//int count=0;
int res=Form1->Edit4->Text.ToInt(); //junk filter                              //box
for(int i=res;i< TEMsize-res;i++)
{
  float tmp = 0;
  for(int j=res;j<TEMsize-res;j++)
  {
    tmp=0;
    for(int x=0-res;x<=res;x++)
      for(int y=0-res;y<=res;y++)
        tmp+=image[i+x][j+y];
    image[i][j]=tmp/((2*res+1)*(2*res+1));
  }
}

Form1->Image1->Width=1024;
Form1->Image1->Height=1024;
Form1->Image1->Refresh();
Form1->Image1->Repaint();


//------------------------fft filter lowpass
  int MDreclen = TEMsize;                    //fft
  Vect<double> fftdata(2*MDreclen);       //fft
  double fftsum=0;                          //fft
  double tot;                               //fft

  Vect<double> index(TEMsize);
  for(int i=0;i<TEMsize;i++)
    index.data[i]=i;
```

```
                                        //fft
for(int k=0;k<MDreclen;k++)                 //fft
{                                       //fft

  for(int i=0;i<MDreclen;i++)
    fftsum+=image[k][i];                //fft
  tot = fftsum;
  Plot1->LineColor=clRed;
  Plot1->Clear();
  Form1->Plot1->Draw<double>(index.data,&image[k][0],TEMsize);

                                        //fft
  for(int i=0;i<MDreclen;i++)
    image[k][i]/=fftsum;
                                        //fft
 // Plot1->Draw<double>(MDrecord,MDreclen);       //fft

  for(int i=0;i<MDreclen;i++)
  {                                     //fft
    fftdata.data[2*i]= image[k][i];
    fftdata.data[2*i+1]=0;
  }                                       //fft
/*   for(int i=0;i<MDreclen;i++) //gaussian test function
  {
      fftdata[2*i]= 1/sqrt(PI)*exp(-(double)(i-1024)*(double)(i-1024)/200);
      fftdata[2*i+1]=0;
  }*/
                                        //fft
  fft(fftdata.data-1, MDreclen, 1);             //fft

  int low = 2*Edit1->Text.ToInt();
  int high = Edit2->Text.ToInt();               //fft
  for(int i=low;i<2*MDreclen;i++)
    fftdata.data[i]=fftdata.data[i]*exp(-1.0*((double)(high)/1000.0)*((double)(i-
low)))/(1+exp(-1.0*((double)(high)/1000.0)*((double)(i-low))));

  fft(fftdata.data-1, MDreclen, -1);
  fftsum=0;                             //fft
  for(int i=0; i<MDreclen;i++)
    fftsum+=(image[k][i]=fftdata.data[2*i]);
  for(int i=0;i<MDreclen;i++)                   //fft
  image[k][i]/=(fftsum/tot);                    //fft
```

```
for(int j=0;j<TEMsize;j++)
  Form1->Image1->Canvas-
>Pixels[k][j]=(int)(image[k][j])+256*(int)(image[k][j])+(int)(image[k][j])*256*256;

if(Filter)
{

  Plot1->LineColor=clBlue;
  Form1->Plot1->Draw<double>(index.data,&image[k][0],TEMsize);
  Plot1->LineColor=clGreen;
  Form1->Plot1->Draw<double>(index.data,rowavg.data,TEMsize);
  Form1->Plot1->Draw<double>(index.data,colavg.data,TEMsize);
  Form1->Plot1->PlotImage->Refresh();
  Form1->Plot1->PlotImage->Repaint();

  Form1->Image1->Width=1024;
  Form1->Image1->Height=1024;
  Form1->Image1->Refresh();
  Form1->Image1->Repaint();
}

}

avg=0;
for(int i=0;i< TEMsize;i++)
{
 for(int j=0;j<TEMsize;j++)
 {
    rowavg.data[j]+=image[i][j];
    colavg.data[i]+=image[i][j];
    avg+=image[i][j];
 }
}
avg/=((float)(TEMsize)*(float)(TEMsize));
for(int j=0;j<TEMsize;j++)
{
  rowavg.data[j]/=((float)(TEMsize));
  colavg.data[j]/=((float)(TEMsize));
}

for(int i=0;i< TEMsize;i++)
{
```

```
  for(int j=0;j<TEMsize;j++)
  {
    float tmp=(rowavg.data[j]-image[i][j])*(rowavg.data[j]-image[i][j]);
    stdev+=tmp;
  }
}

stdev=sqrt(stdev/(TEMsize*TEMsize-1));

}

//---------------------------------------------------------------------------

void __fastcall TForm1::Button4Click(TObject *Sender)
{
int TEMsize = MAX;
int count=0;

if(!mask_initialized(count)) //makes a list (dotlist) of all above threshold pixiles
      return;

build_dotlist(count);         //calls dotwalk on above threshold pixles
int spots=count_spots();       // counts number of nanoparticles
Highlite_Nps();

Vect<double> npdist(spots);
ZeroMemory(npdist.data,sizeof(double)*spots);
build_NPdist(npdist);         // list of NP radii indexed by spotnum

int bins = Form1->Edit14->Text.ToInt();
Histogram<double> Nps(npdist,0,0,bins);  //add histogram statistics struct
NPs.stats.{mean,median,mode,stdev,peak,counts etc...}

Form1->Edit6->Text=spots;
Form1->Edit7->Text=Nps.mean; //mean radius
Form1->Edit8->Text=Nps.stddev; //standard deviation of particle radii
Form1->Edit11->Text=Nps.min;
Form1->Edit12->Text=Nps.max;
Form1->Edit13->Text=Nps.peak_count;
Form1->Edit17->Text=Nps.mode; //!!max radius dont confuse w npmax which is the
max nanoparticle count in any radiusbin!!!!!

double pcntVol=0;
```

```
double thickness=Form1->Edit15->Text.ToInt();
double cal = Form1->Edit10->Text.ToDouble(); //sets length scale pixles/micron given
by the microscope
pcntVol=100*spots*(4/3)*PI*Nps.mean/1000*Nps.mean/1000*Nps.mean/1000*(cal/TE
Msize)*(cal/TEMsize)/thickness;
Form1->Edit16->Text=pcntVol;

plot_hist(Nps);
plot_gauss(Nps);
}

//---------------------------------------------------------------------------
void __fastcall TForm1::Button5Click(TObject *Sender)
{
if(image == NULL)
  return;
if(dotlist.data == NULL)
  return;


spotdot **spotindex;
int totalspots=spotnum;
spotindex=new spotdot *[totalspots];

int OUT_OF_RANGE=-1;
int spots=0;
{
int j=0;
for(int i=0;i<totaldots;i+=dotlist.data[i].dotcount) //makes a list of indexed spots
{                                        //that we have already counted
  if(dotlist.data[i].spotnumber!=OUT_OF_RANGE)
  {
    spotindex[j]=&dotlist.data[i];
    j++;
  }
}
spots=j;
}

Vect<double> npdist(spots);
ZeroMemory(npdist.data,sizeof(double)*spots);
build_NPdist(npdist);         // list of NP radii indexed by spotnum
```

```
int bins = Form1->Edit14->Text.ToInt();
Histogram<double> Nps(npdist,0,0,bins);  //add histogram statistics struct
NPs.stats.{mean,median,mode,stdev,peak,counts etc...}


//finds all perimeter points AND interior VOIDs
for(int i=0;i<spots;i++)//determines whether a point in a spot is on the perimeter
{
  for(int j=0;j<spotindex[i][0].dotcount;j++)//loops over all dots in a spot
  {
    int k=0;
    while(k<spotindex[i][0].dotcount)//searches for potential neighbors
    {
       //only look at dots we've not already filled in...
      if(spotindex[i][j].r==NULL || spotindex[i][j].ru==NULL ||
spotindex[i][j].u==NULL || spotindex[i][j].ul==NULL || spotindex[i][j].l==NULL ||
spotindex[i][j].dl==NULL || spotindex[i][j].d==NULL || spotindex[i][j].dr==NULL)
      {
        int x=spotindex[i][j].x;  //we are interogating the x and y position
        int y=spotindex[i][j].y;  //of the jth point.
        int xk=spotindex[i][k].x; //By checking whether the kth point is a
        int yk=spotindex[i][k].y; //neighbor of the jth point.
        if(xk-x>=-1 && xk-x<=1 && yk-y>=-1 && yk-y<=1)//is k a neighbor point?
        {
          int xswitch=((xk-x)+1)*3+1;//gives me 1,4,7 for (xk-x)=-1,0,1 respectively.
                          //xk-x=-1 is l, =1 is r.
          int yswitch=yk-y;
          switch(xswitch+yswitch)
          {
            case 0: //xk=x-1, yk=y-1 dl, ru
              spotindex[i][j].dl=&spotindex[i][k];
              spotindex[i][k].ru=&spotindex[i][j];
              break;
            case 1: //xk=x-1, yk=y, r
              spotindex[i][j].l=&spotindex[i][k];
              spotindex[i][k].r=&spotindex[i][j];
              break;
            case 2: //xk=x-1, yk=y+1 ul, dr
              spotindex[i][j].ul=&spotindex[i][k];
              spotindex[i][k].dr=&spotindex[i][j];
              break;
            case 3: //xk=x, yk=y-1 u, d
              spotindex[i][j].d=&spotindex[i][k];
```

```
                spotindex[i][k].u=&spotindex[i][j];
                break;
              case 4: //xk=x, yk=y c
                spotindex[i][j].c=&spotindex[i][j];
                break;
              case 5: //xk=x, yk=y+1 u, d
                spotindex[i][j].u=&spotindex[i][k];
                spotindex[i][k].d=&spotindex[i][j];
                break;
              case 6: //xk=x+1, yk=y-1 dr, ul
                spotindex[i][j].dr=&spotindex[i][k];
                spotindex[i][k].ul=&spotindex[i][j];
                break;
              case 7: //xk=x+1, yk=y r, l
                spotindex[i][j].r=&spotindex[i][k];
                spotindex[i][k].l=&spotindex[i][j];
                break;
              case 8: //xk=x+1, yk=y+1 ur, dl
                spotindex[i][j].ru=&spotindex[i][k];
                spotindex[i][k].dl=&spotindex[i][j];

            }
          }
        }
        k++;
      }
    }
}

int totperim=0;
int perim_ct=0;
int currentspot=0;

for(int i=0;i<spots;i++)//determines whether a point in a spot is on the perimeter
  for(int j=0;j<spotindex[i][0].dotcount;j++)
  {
    if(spotindex[i][j].r==NULL || spotindex[i][j].ru==NULL || spotindex[i][j].u==NULL
|| spotindex[i][j].ul==NULL || spotindex[i][j].l==NULL || spotindex[i][j].dl==NULL ||
spotindex[i][j].d==NULL || spotindex[i][j].dr==NULL)
      totperim++;//counts the total number of perimeter points in all spots
  }

spotdot **perimindex;
```

```
perimindex=new spotdot*[totalspots];

spotdot *perimdots;
perimdots = new spotdot[totperim];

int pcount=0;
int tmpspot=0;
int k=0;
for(int i=0;i<spots;i++)
{
  int j=0;
  while(j<spotindex[i][0].dotcount)
  {
    if(spotindex[i][j].r==NULL || spotindex[i][j].ru==NULL || spotindex[i][j].u==NULL
|| spotindex[i][j].ul==NULL || spotindex[i][j].l==NULL || spotindex[i][j].dl==NULL ||
spotindex[i][j].d==NULL || spotindex[i][j].dr==NULL)
    {
      CopyMemory(&perimdots[k], &spotindex[i][j],sizeof(spotdot));
      k++;
      pcount++;
    }
    j++;
  }
  perimindex[i]=&perimdots[k-pcount];
  perimindex[i][0].dotcount=pcount;
  for(int l=0;l<pcount;l++)
    perimindex[i][l].dotcount=pcount;
  pcount=0;
}

for(int i=0;i<spots;i++)
  for(int j=0;j<perimindex[i][0].dotcount;j++)
    perimindex[i][j].dotcount=perimindex[i][0].dotcount;

for(int i=0;i<spots;i++)
{
  int diff=perimwalk(perimindex[i]);
  if(diff!=0)
    for(int j=0;j<perimindex[i][0].dotcount;j++)
    {
        perimindex[i][j].doughnut=TRUE;
        Form1->Image1->Canvas-
>Pixels[perimindex[i][j].y][perimindex[i][j].x]=clGreen;
```

```
          Form1->Image1->Refresh();
          Form1->Image1->Repaint();
      }
   else
      for(int j=0;j<perimindex[i][0].dotcount;j++)
      {
          perimindex[i][j].doughnut=TRUE;
          Form1->Image1->Canvas-
>Pixels[perimindex[i][j].y][perimindex[i][j].x]=clYellow;
          Form1->Image1->Refresh();
          Form1->Image1->Repaint();
      }

}
////////////////////////////////
//---------------------------------------------------------------------------
void GetRGBValues(int x, int y, int *r, int *g, int *b)
{
    int color;
    color = Form1->Image1->Canvas->Pixels[x][y];
    *r = color % 256;
    color /= 256;
    *g = color % 256;
    color /= 256;
    *b = color % 256;
}


spotdot *dotwalk(int x, int y) //only works for a left to right top to bottom scan pattern in
calling loop
{
   int i=q;
   q++;
   if(x==0 || y==0 || x==MAX-1 || y==MAX-1)
   {
      mask.data[y][x]=FALSE;
      dotlist.data[i].x=x;
      dotlist.data[i].y=y;
      dotlist.data[i].spotnumber=spotnum;
      return &dotlist.data[i];
   }
   if(mask.data[y][x-1])//x-1
   {
```

```
  mask.data[y][x]=FALSE;
  dotlist.data[i].l=dotwalk(x-1,y);
}
if(mask.data[y-1][x-1])
{
  mask.data[y][x]=FALSE;
  dotlist.data[i].dl=dotwalk(x-1,y-1);
}
if(mask.data[y-1][x])
{
  mask.data[y][x]=FALSE;
  dotlist.data[i].d=dotwalk(x,y-1);
}
if(mask.data[y-1][x+1])
{
  mask.data[y][x]=FALSE;
  dotlist.data[i].dr=dotwalk(x+1,y-1);
}
if(mask.data[y][x+1])
{
  mask.data[y][x]=FALSE;
  dotlist.data[i].r=dotwalk(x+1,y);
}
if(mask.data[y+1][x+1])
{
  mask.data[y][x]=FALSE;
  dotlist.data[i].ru=dotwalk(x+1,y+1);
}
if(mask.data[y+1][x])
{
  mask.data[y][x]=FALSE;
  dotlist.data[i].u=dotwalk(x,y+1);
}
if(mask.data[y+1][x-1])
{
  mask.data[y][x]=FALSE;
  dotlist.data[i].ul=dotwalk(x-1,y+1);
}
mask.data[y][x]=FALSE;
dotlist.data[i].x=x;
dotlist.data[i].y=y;
dotlist.data[i].spotnumber=spotnum;
return &dotlist.data[i];
```

```
}

int perimwalk(spotdot *perim)
{//returns number of perimeter points not on the boundary
  int x=0;
  int y=0;
  int index=0;
  for(int i=0; i<perim[i].dotcount; i++)
    if(perim[i].x>x)
    {
      x=perim[i].x;
      index=i;
    }
  y=perim[index].y;
  spotdot curentdot;
  curentdot=perim[index];
  int checksum=0;
  int *cksum=&checksum;
//perimstep() returns the number of dots on outermost boundary.
  perimstep(perim[index],perim[index],cksum);
  return (perim[index].dotcount-checksum);
}

perimstep(spotdot perim,spotdot start, int *checksum)
{
  if(perim.r==NULL || perim.ru==NULL || perim.u==NULL || perim.ul==NULL ||
perim.l==NULL || perim.dl==NULL || perim.d==NULL || perim.dr==NULL)
  {
    if((*checksum) == perim.dotcount)
      return 0;
    if(&perim == &start)
      return 0;
    (*checksum)++;
    if(perim.r!=NULL)
      perimstep(*(perim.r),start,checksum);
    if(perim.ru!=NULL)
      perimstep(*(perim.ru),start,checksum);
    if(perim.u!=NULL)
      perimstep(*(perim.u),start,checksum);
    if(perim.ul!=NULL)
      perimstep(*(perim.ul),start,checksum);
    if(perim.l!=NULL)
      perimstep(*(perim.l),start,checksum);
```

```
    if(perim.dl!=NULL)
      perimstep(*(perim.dl),start,checksum);
    if(perim.d!=NULL)
      perimstep(*(perim.d),start,checksum);
    if(perim.dr!=NULL)
      perimstep(*(perim.dr),start,checksum);
  }
}

//---------------------------------------------------------------------------



void __fastcall TForm1::Button6Click(TObject *Sender)
{
  if(!Filter)
  {
    Form1->Button6->Caption="1um";
    Form1->Edit5->Text=8;
    Form1->Edit9->Text=1000;
    Form1->Edit10->Text=169.47;
    Filter = TRUE;
    return;
  }

  if(Filter)
  {
    Form1->Button6->Caption="100nm";
    Form1->Edit5->Text=80;
    Form1->Edit9->Text=10000;
    Form1->Edit10->Text=859.45;
    Filter = FALSE;
    return;
  }

}
//---------------------------------------------------------------------------


void __fastcall TForm1::Image1MouseDown(TObject *Sender,
    TMouseButton Button, TShiftState Shift, int X, int Y)
{
/* Switch(Locate_Click())
```

```
   {
    case IMAGE
    {
       Get_NP();//highlights NP and boundary and displays its stats in NP pannell
    }
    case HIST
    {
       Get_Bin(); //highlights all NPs and their boundaries in the sellected Bin and supports
stats toggle in NP pannell
    }
   };

*/
   int s=1;
   if (X==Y)
       s++;
}
//---------------------------------------------------------------------------
```

```
//The header file for the above code
//---------------------------------------------------------------------------
#ifndef Unit1H
#define Unit1H
//---------------------------------------------------------------------------
#include <Classes.hpp>
#include <Controls.hpp>
#include <StdCtrls.hpp>
#include <Forms.hpp>
#include <Dialogs.hpp>
#include <ExtDlgs.hpp>
#include <ExtCtrls.hpp>
#include <graphics.hpp>
#include <jpeg.hpp>
#include <math.h>
#include "Plot.h"
#include <Graphics.hpp>
#include "cRVect.h"
#define PI 3.14159265358979323846264338327 95
//---------------------------------------------------------------------------
class TForm1 : public TForm
{
__published:    // IDE-managed Components
  TOpenPictureDialog *OpenPictureDialog1;
  TButton *Button1;
  TImage *Image1;
  TImage *Image2;
  TPlot *Plot1;
  TEdit *Edit1;
  TEdit *Edit2;
  TLabel *Label1;
  TLabel *Label2;
  TLabel *Label3;
  TEdit *Edit3;
  TLabel *Label4;
  TEdit *Edit4;
  TEdit *Edit5;
  TLabel *Label5;
  TEdit *Edit6;
  TLabel *Label6;
  TEdit *Edit7;
  TLabel *Label7;
  TEdit *Edit8;
```

```
  TLabel *Label8;
  TPlot *Plot2;
  TImage *Image3;
  TEdit *Edit9;
  TLabel *Label9;
  TEdit *Edit10;
  TLabel *Label10;
  TEdit *Edit11;
  TEdit *Edit12;
  TLabel *Label11;
  TLabel *Label12;
  TEdit *Edit13;
  TLabel *Label13;
  TButton *Button2;
  TEdit *Edit14;
  TLabel *Label14;
  TLabel *Label15;
  TEdit *Edit15;
  TLabel *Label16;
  TEdit *Edit16;
  TEdit *Edit17;
  TLabel *Label17;
  TButton *Button3;
  TButton *Button4;
  TButton *Button5;
  TMemo *Memo1;
  TButton *Button6;
  TLabel *Label18;

  void __fastcall Button1Click(TObject *Sender);
  void __fastcall Button2Click(TObject *Sender);
  void __fastcall Button3Click(TObject *Sender);
  void __fastcall Button4Click(TObject *Sender);
  void __fastcall Button5Click(TObject *Sender);
  void __fastcall Button6Click(TObject *Sender);
      void __fastcall Image1MouseDown(TObject *Sender,
       TMouseButton Button, TShiftState Shift, int X, int Y);
private:          // User declarations
public:           // User declarations
  __fastcall TForm1(TComponent* Owner);

};
//---------------------------------------------------------------------------
```

```
extern PACKAGE TForm1 *Form1;

AnsiString filename;
bool OpenFile();
bool CheckImage();
bool CheckExtension();
void GetRGBValues(int x, int y, int *r, int *g, int *b);
bool mask_initialize(int &count);
void build_dotlist();
int count_spots();
void Highlite_Nps();
void build_NPdist(Vect<double> &dist);
void plot_hist(Histogram<double> &Nps);
void plot_gauss(Histogram<double> &NPs);
void image_backup_restore();

Matrix<bool> mask;
double **image=NULL;
double **imagebk=NULL;
Vect<double> rowavg, colavg;
double avg,stdev,cut;

bool Filter = FALSE;
bool Defaults=FALSE;
struct spotdot {
  int x;
  int y;
  int spotnumber;
  int dotcount;
  spotdot *r,*ru,*u,*ul,*l,*dl,*d,*dr,*c;
  bool doughnut;
};


Vect<spotdot> dotlist;
int q=0;   //counts dotlist entrie in dotlist global to save overhead in dotwalk calls
int spotnum=0; //counts the current spot for dotwalk global to save overhead
int totaldots=0;
unsigned MAX=1024;
int LastMAX=0;  //picture resolution must be square and an integral power of 2

spotdot *dotwalk(int x, int y); //gathers all spatially contiguous dots into spots
int perimwalk(spotdot *perim);//returns number of perimeter points not on the boundary
```

```
perimstep(spotdot perim,spotdot start, int *checksum);

#define SWAP(a,b) tempr=(a);(a)=(b);(b)=tempr
void fft(double *data,unsigned nn, int isign);
//--------------------------------------------------------------------------
#endif
```

Appendix D: *Chamber Drawings*

Included in the following pages are the mechanical drawings of the chamber designed and built to collect the most important of the samples in this work. Some alterations to the design were necessary to facilitate the machining process. Some of these modifications were not incorporated into the drawings. However, they still represent a very complete description of the chamber. .

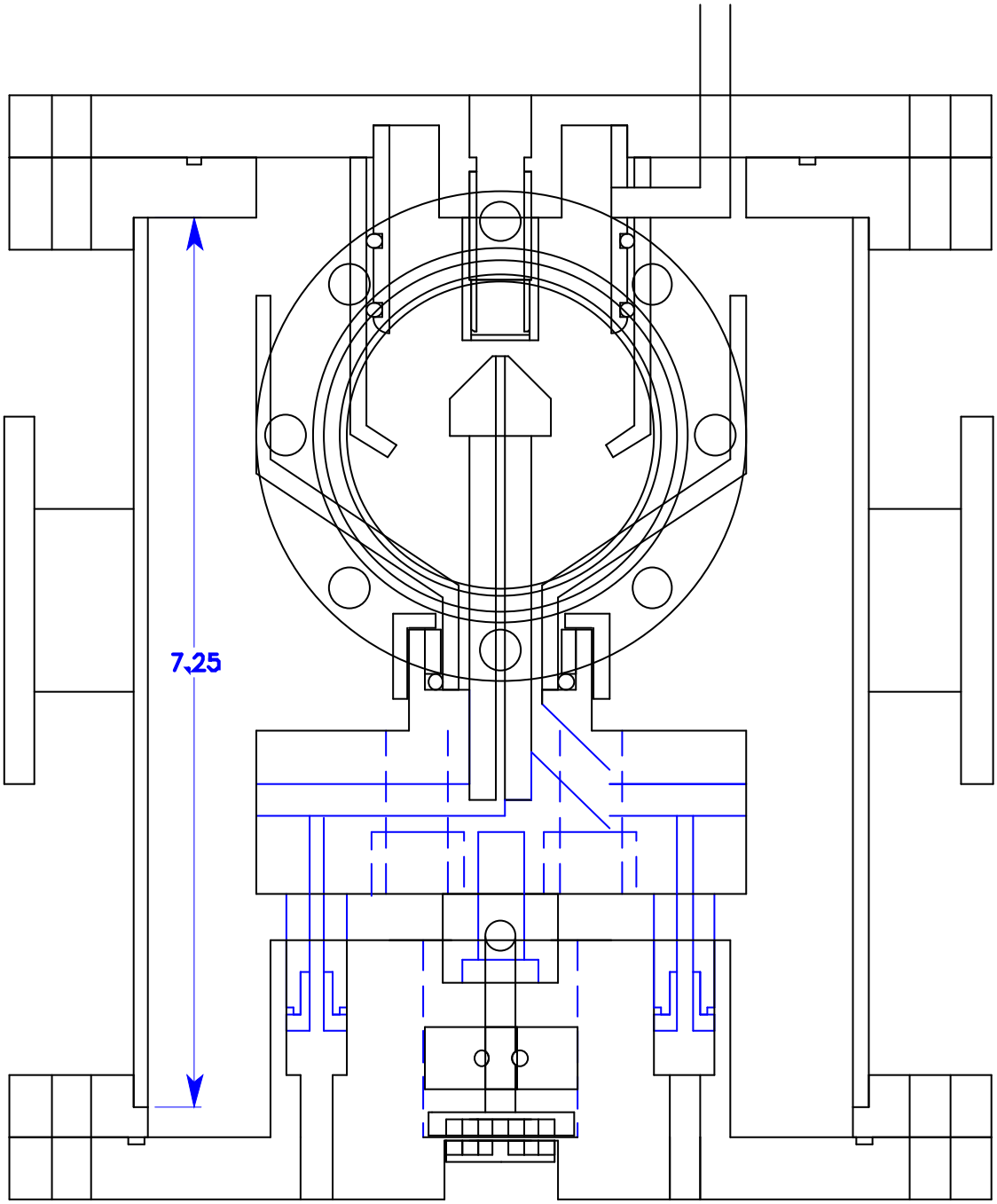
7.25

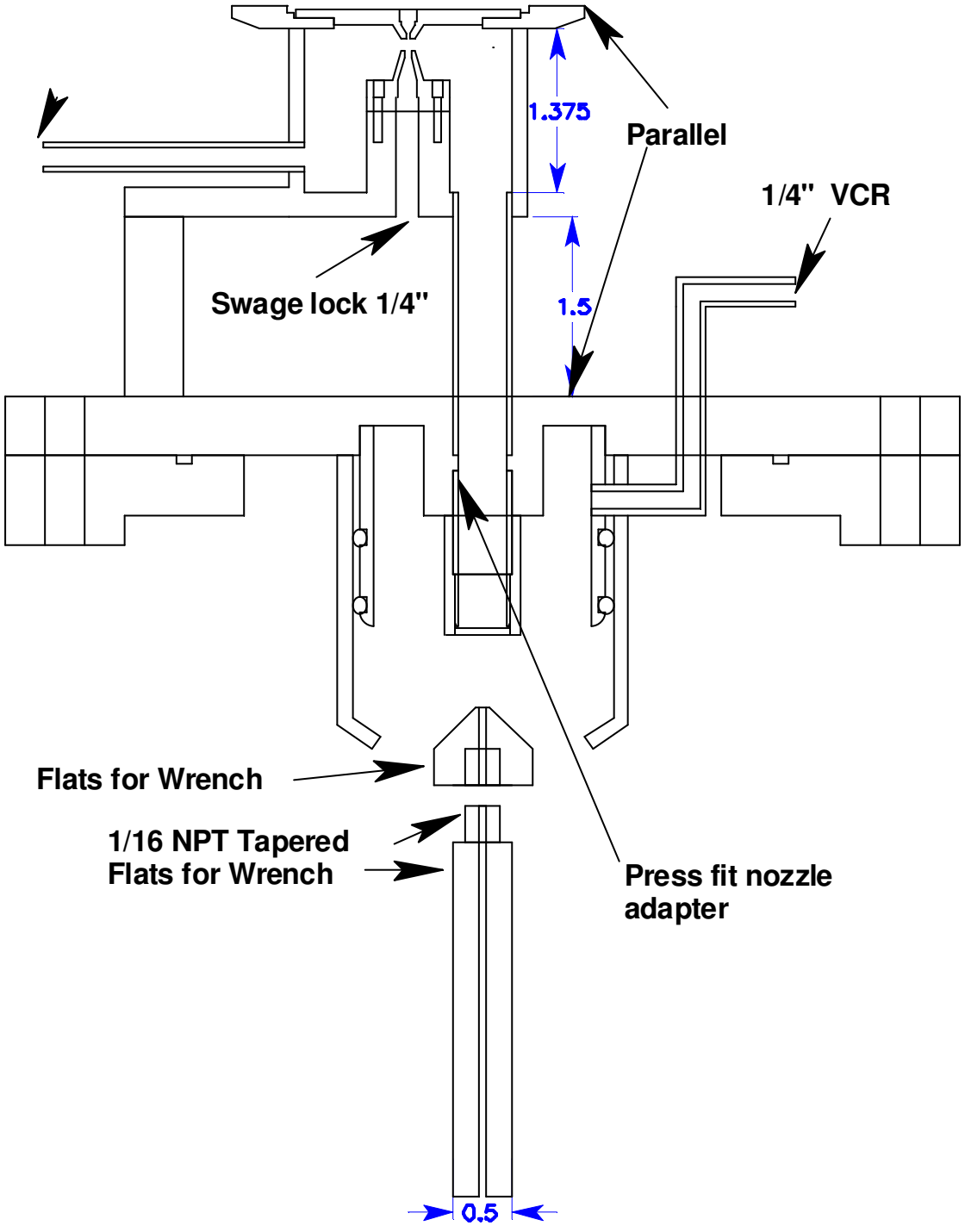
1.375
Parallel
1/4" VCR
Swage lock 1/4"
1.5
Flats for Wrench
1/16 NPT Tapered
Flats for Wrench
Press fit nozzle
adapter
0.5

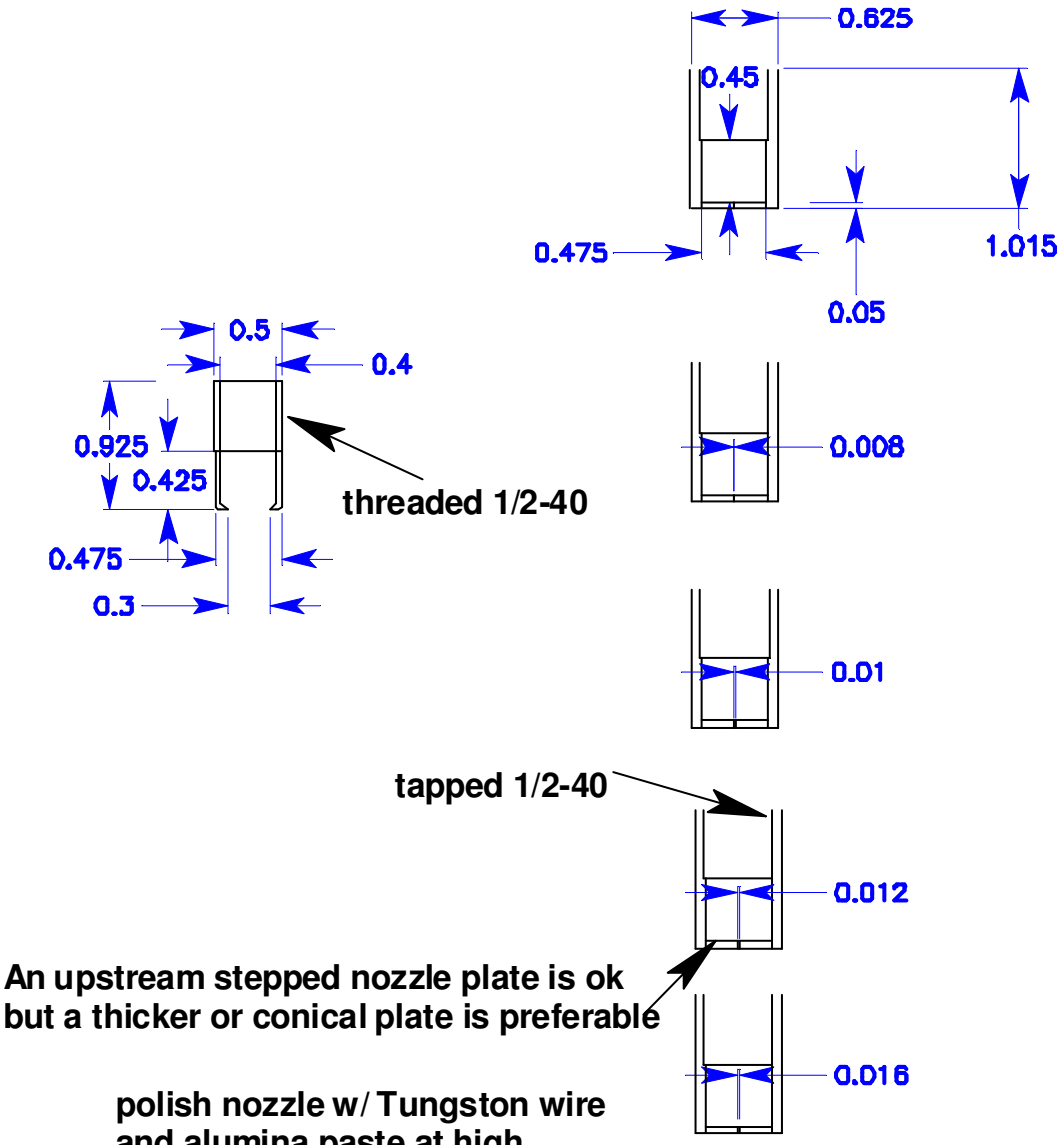

An upstream stepped nozzle plate is ok but a thicker or conical plate is preferable

polish nozzle w/ Tungston wire and alumina paste at high speed for finish

nozzle dimension not critical use nearest conveinent wire diameter

Top Flange Non rotatable w dowel pins

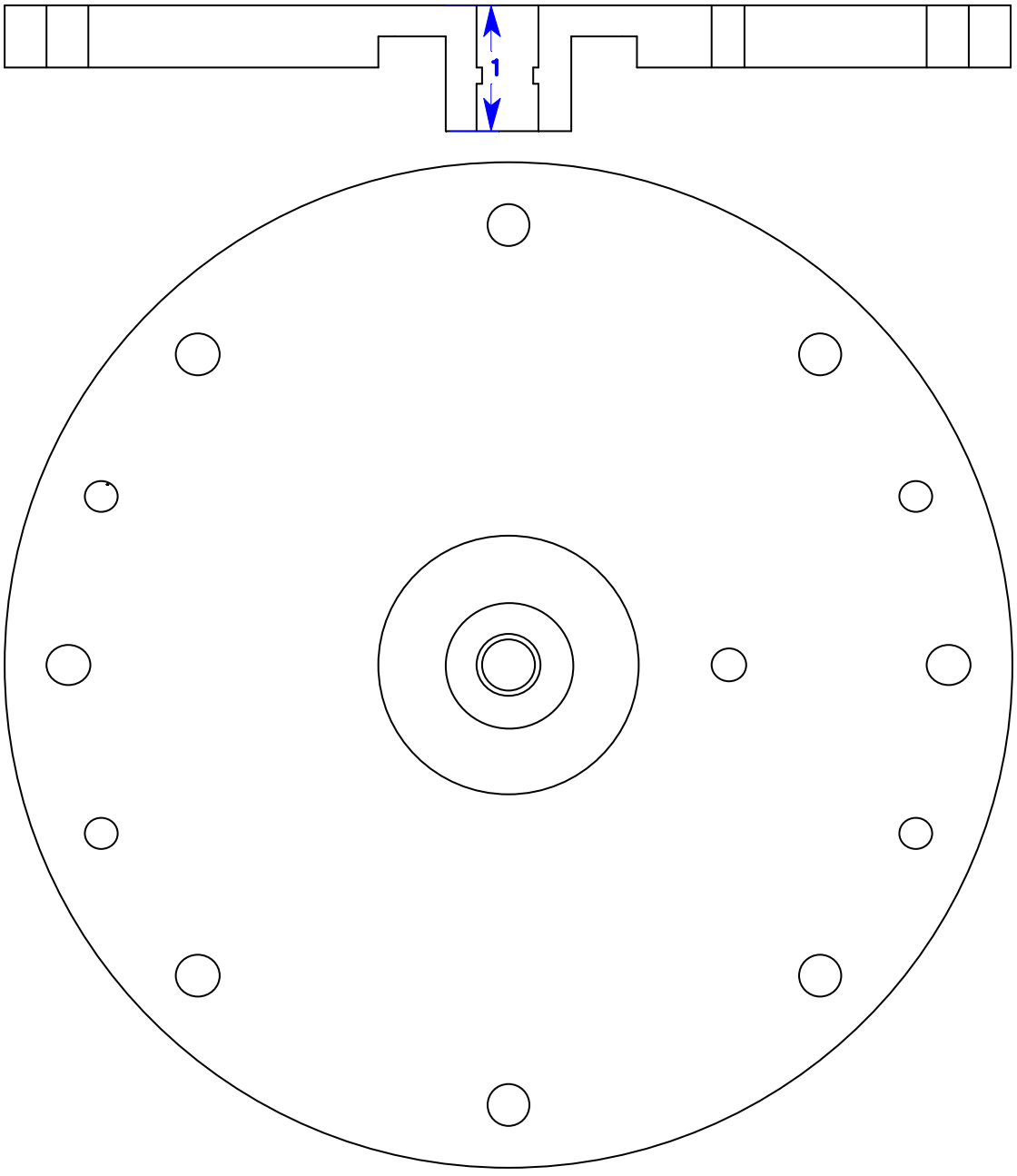

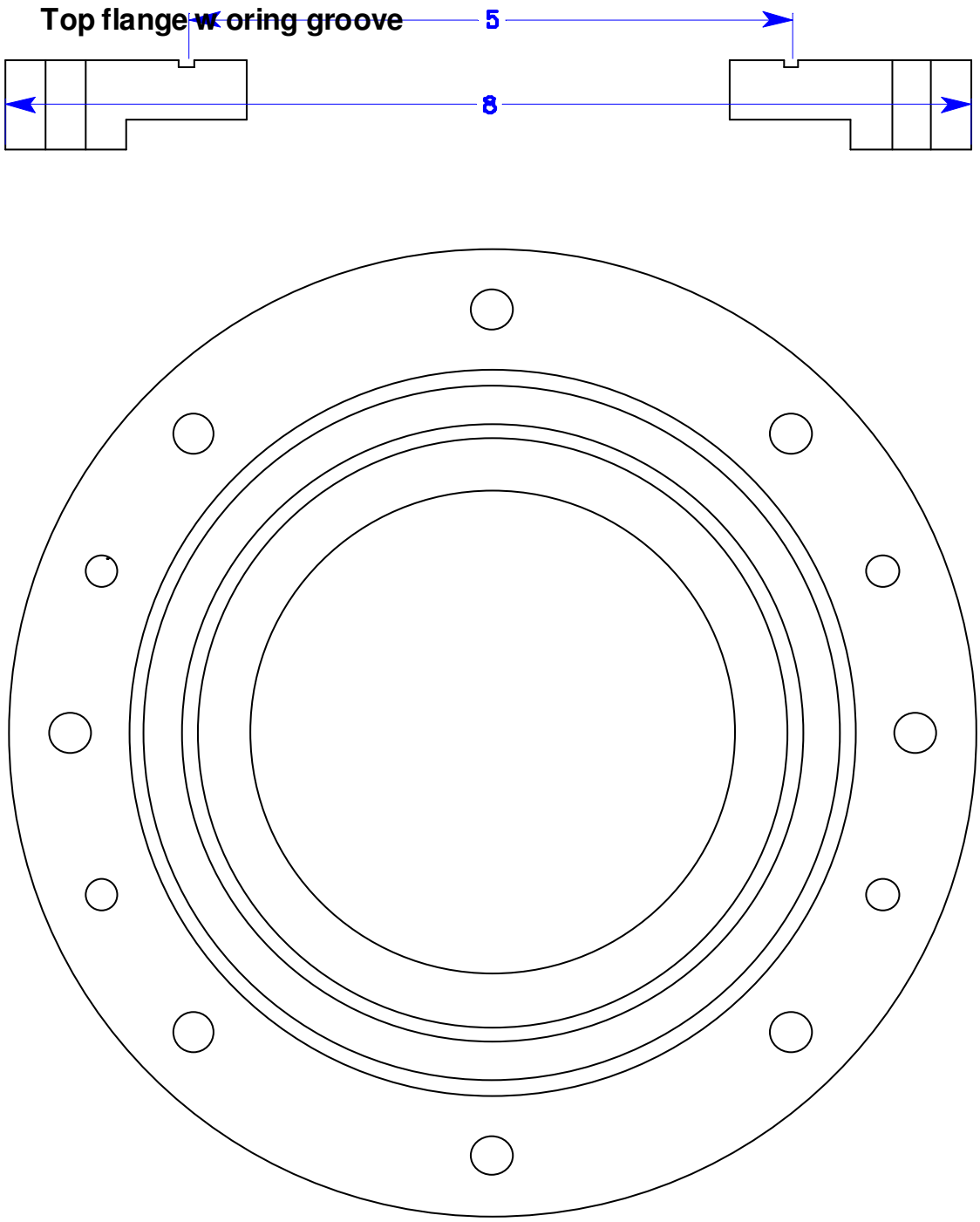
Top flange w oring groove
5
8

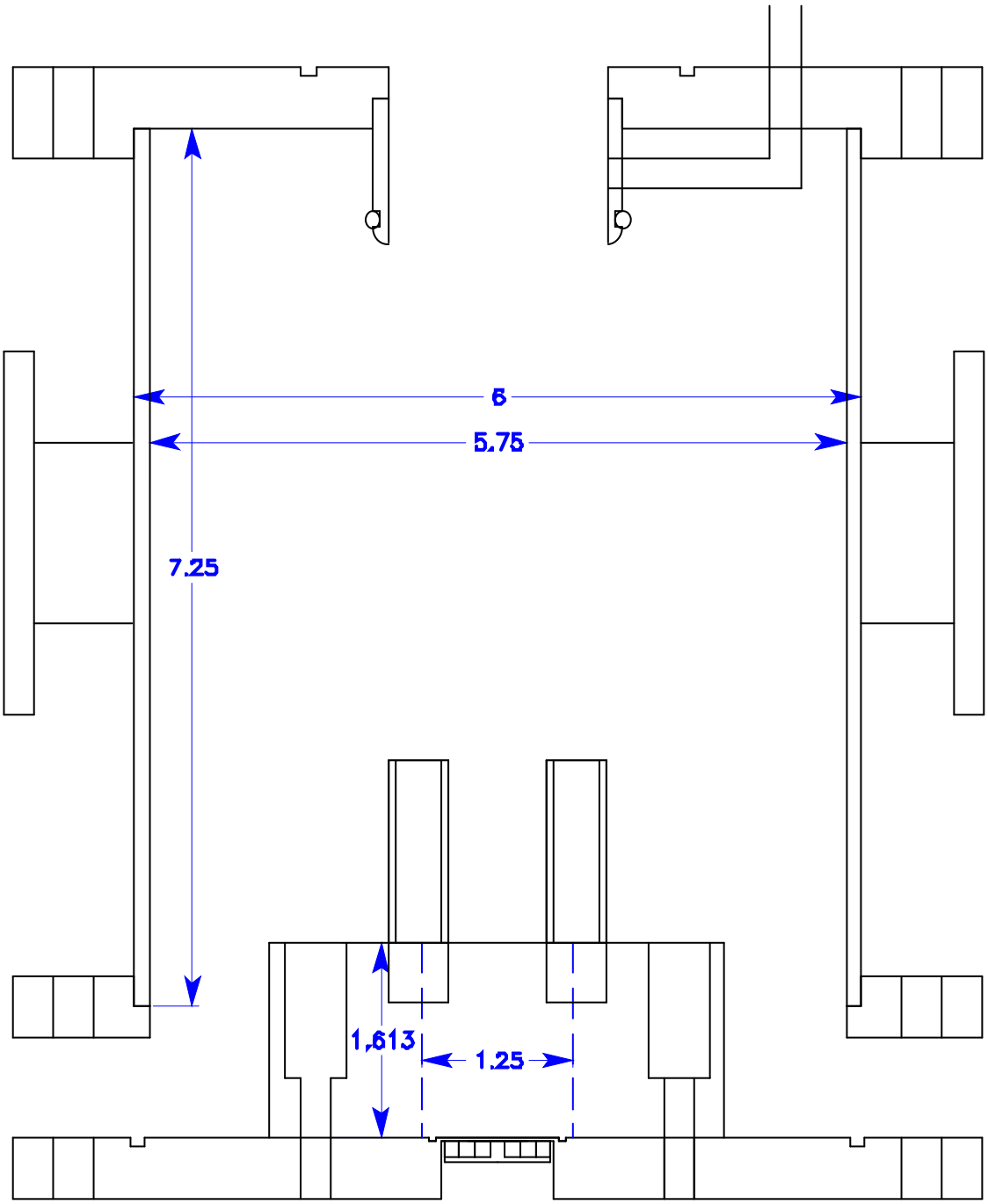
6
5.75
7.25
1.613
1.25

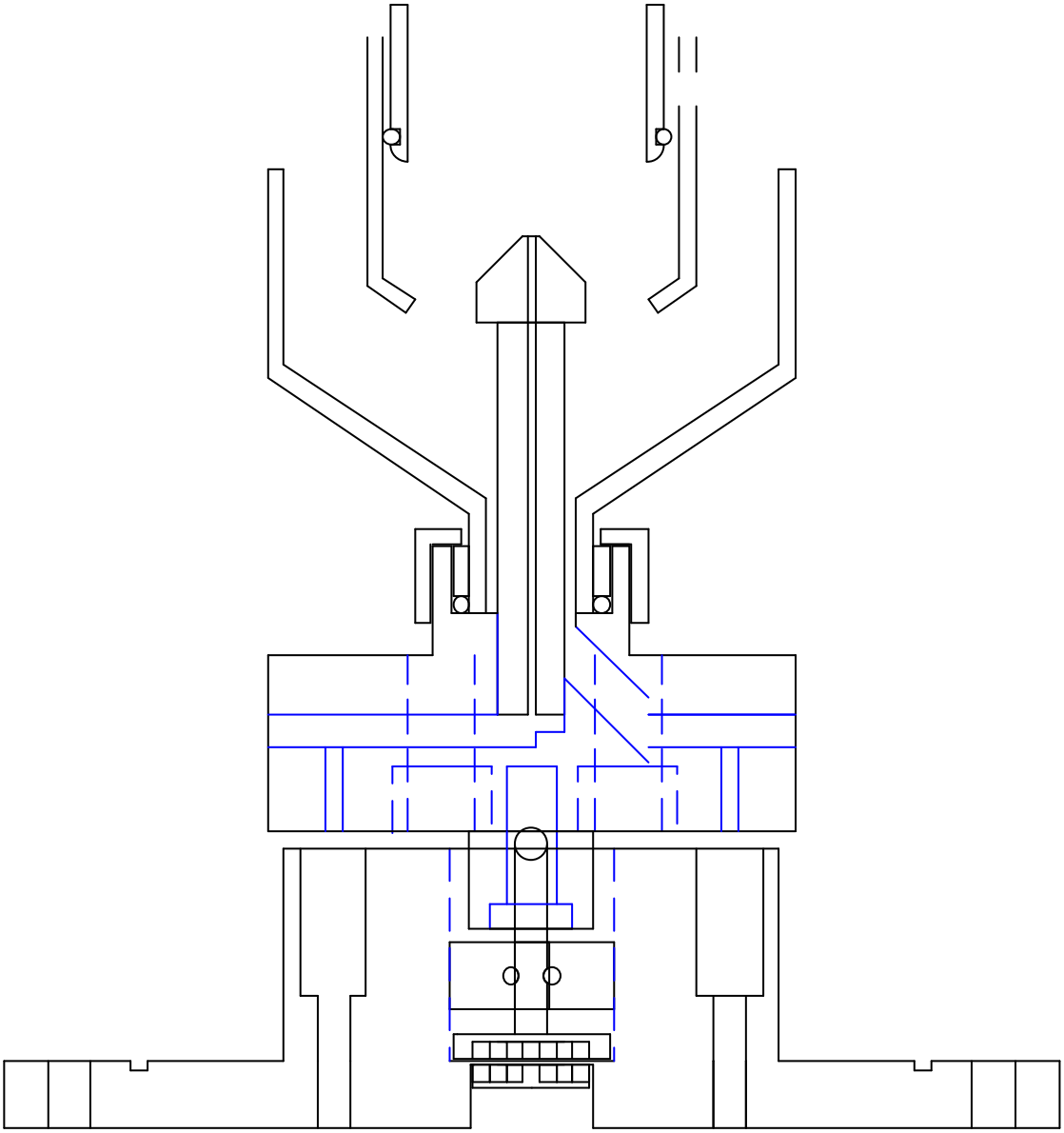

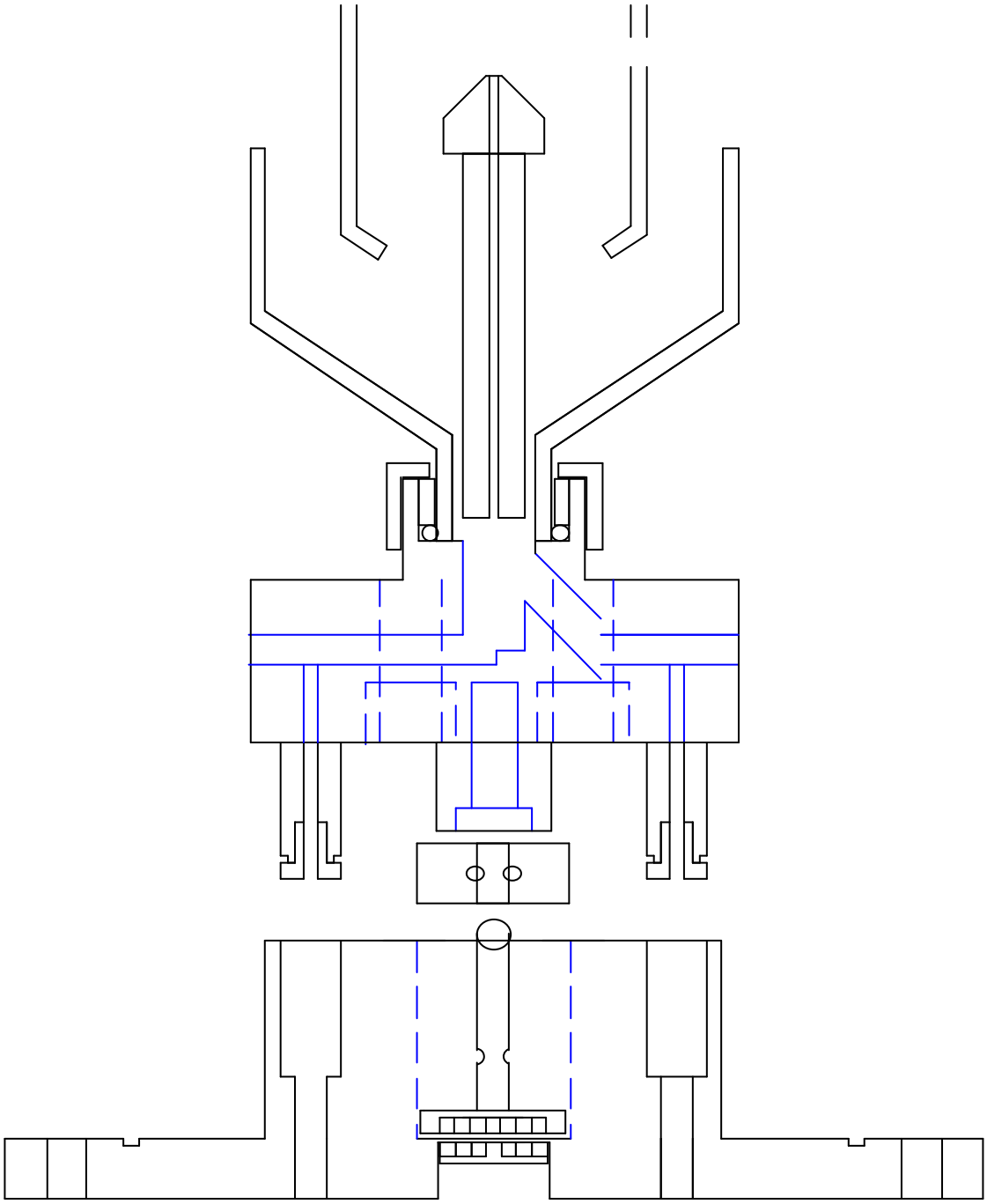

Translator Collector Sub-assembly

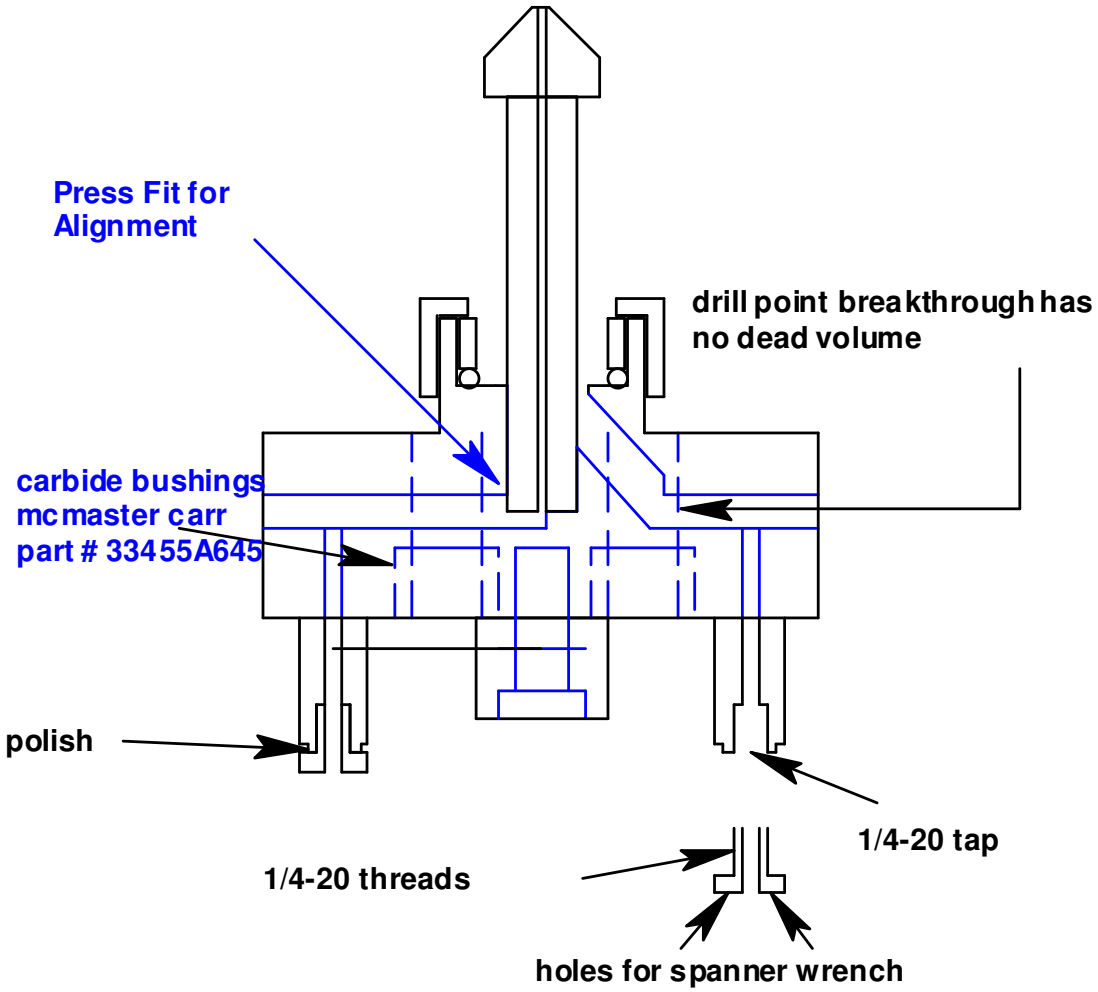

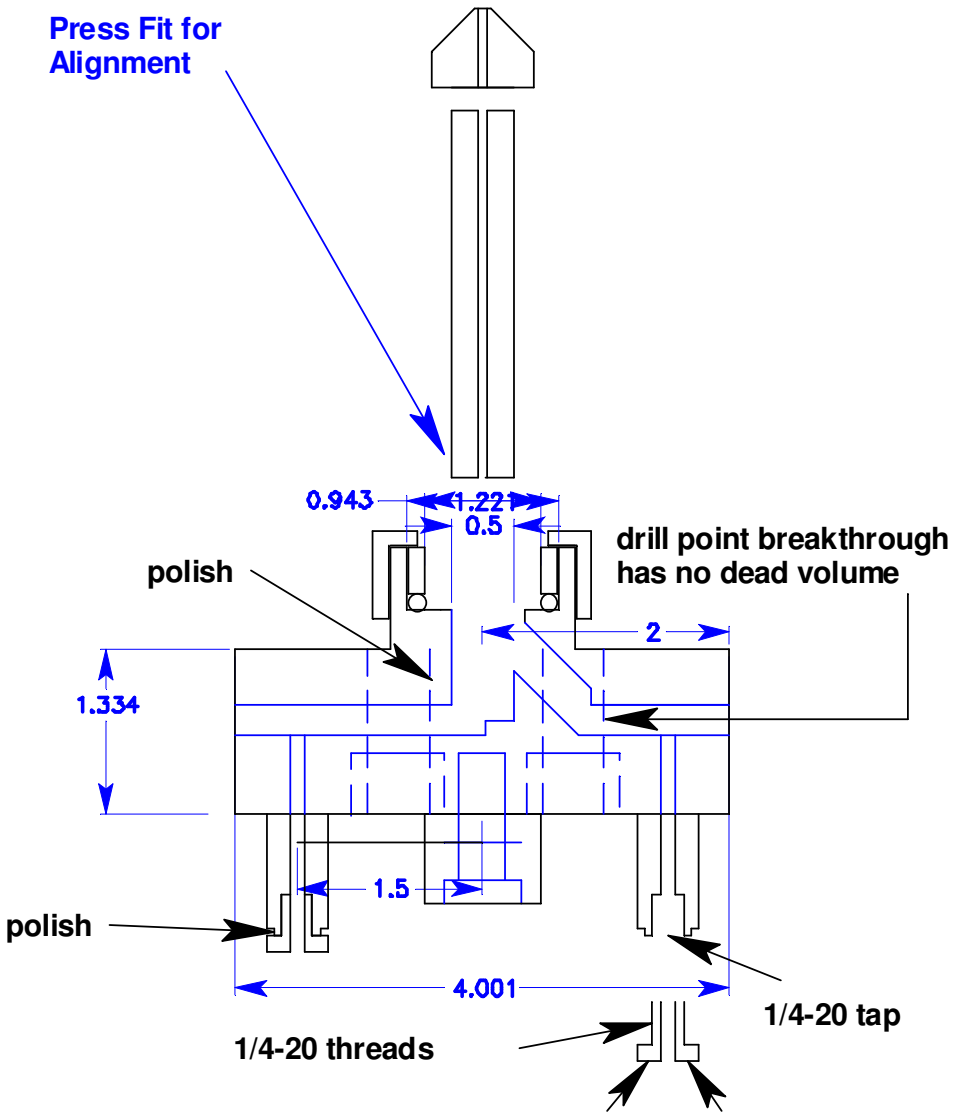
Press Fit for
Alignment
0.943
1.22
0.5
drill point breakthrough
has no dead volume
polish
2
1.334
1.5
polish
4.001
1/4-20 tap
1/4-20 threads

Title: Nano Particle Colltction Chamber
Subassembley: Bottom Flange- Translation Collector
Part (# of pcs): Nozzle (9)
Scale: 1:1
Name: Robert Morgan
Group: Ditmire
Material: Type 316 Stainless

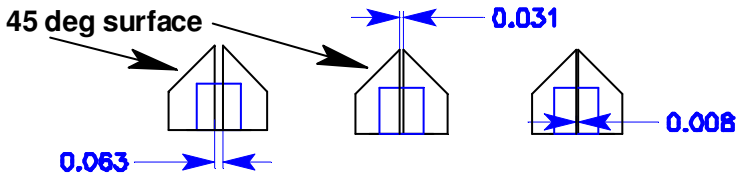

55 deg surface

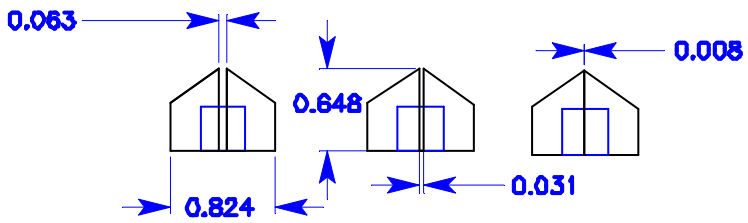

70 deg surface

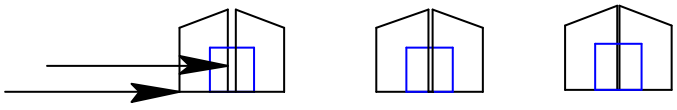

1/16 NPT Tapered Flats for Wrench

Title: Nano Particle Colltction Chamber
Subassembley: Bottom Flange- Translation Collector
Part (# of pcs): Stem (1)
Scale: 1:1
Name: Robert Morgan
Group: Ditmire
Material: Type 316 Stainless

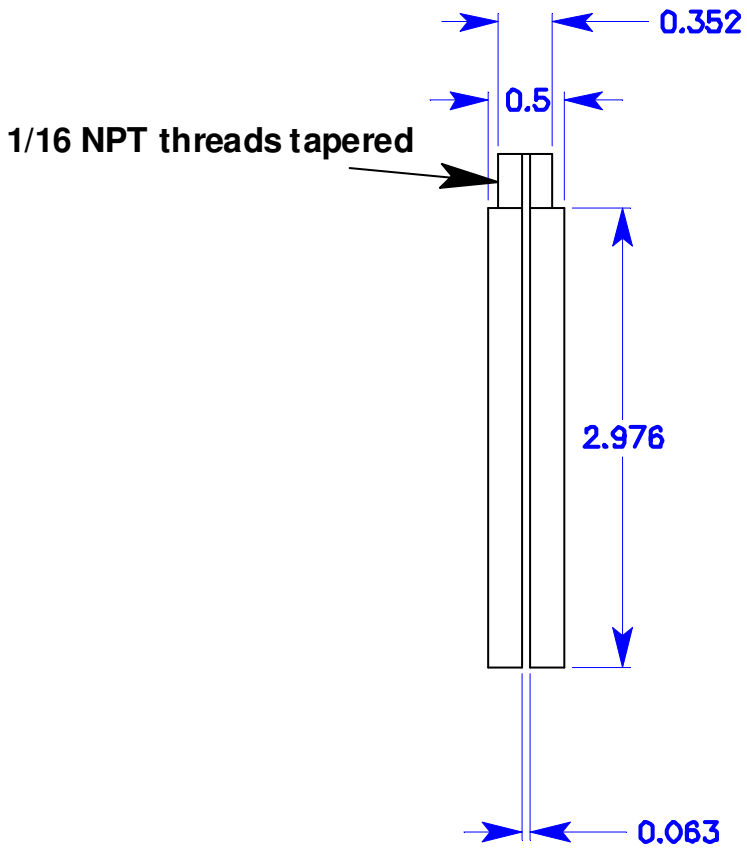

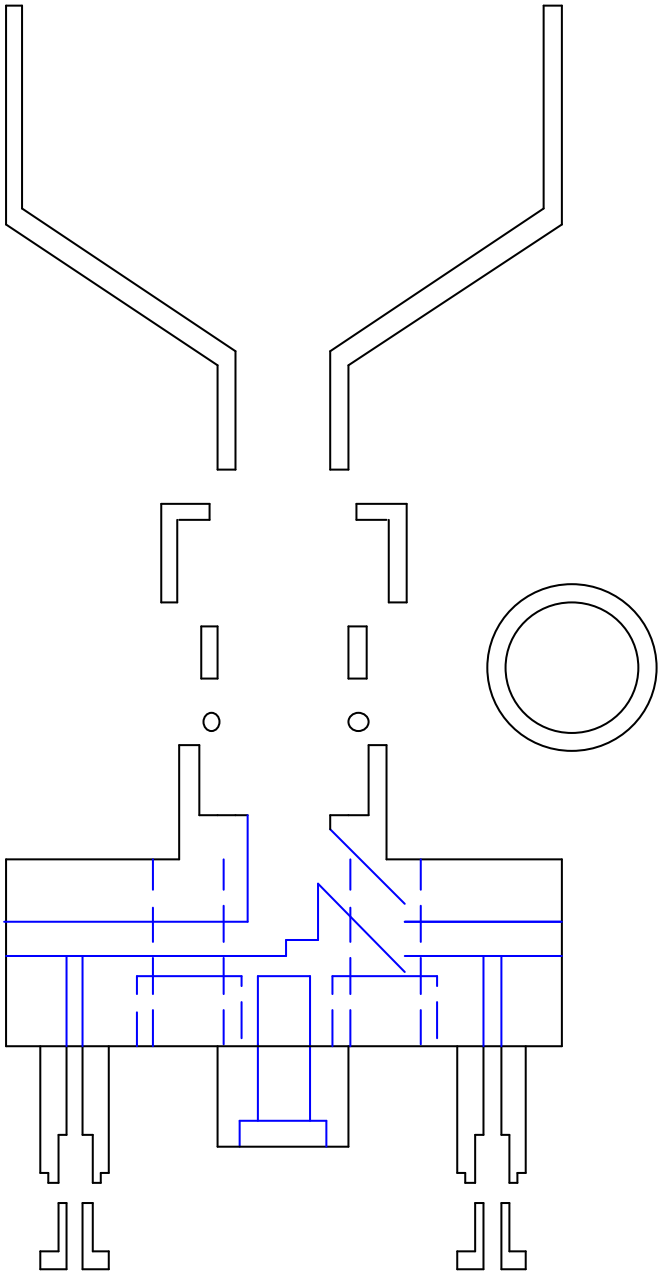

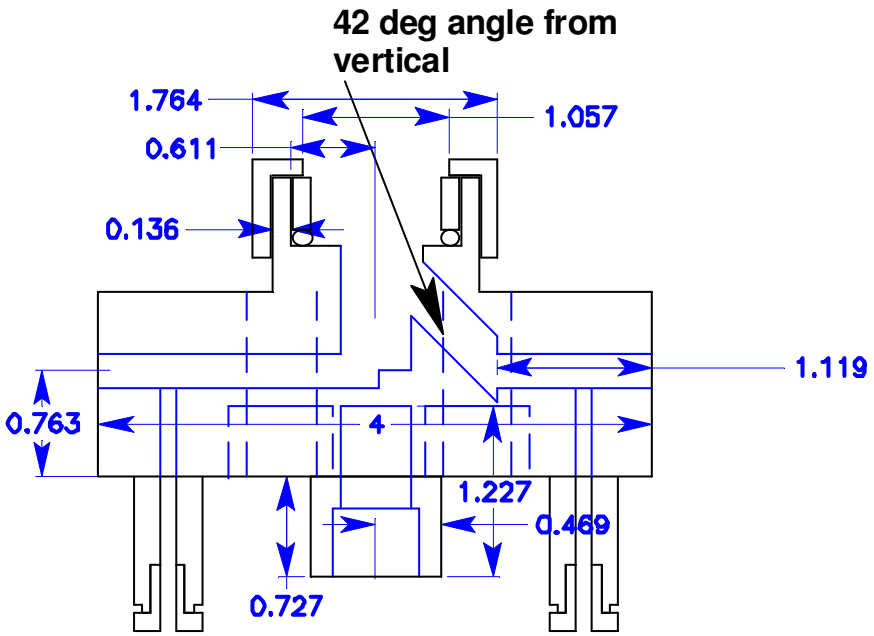
42 deg angle from vertical
1.764
1.057
0.611
0.136
1.119
0.763
4
1.227
0.469
0.727

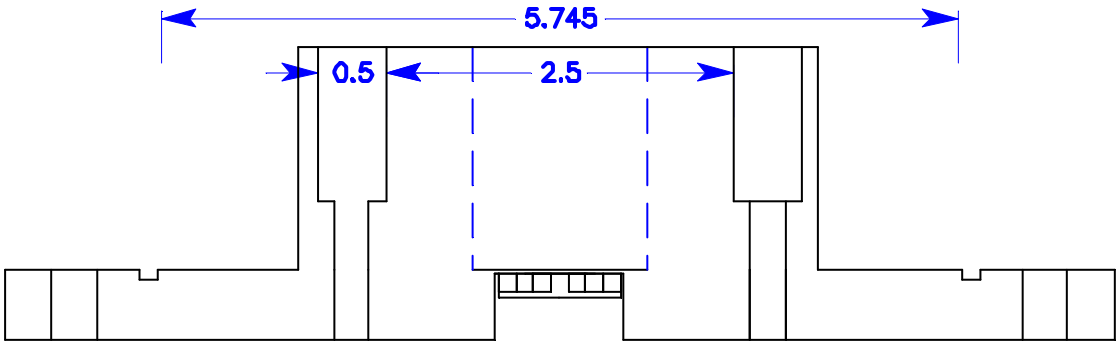
5.745
0.5
2.5

Title: Nano Particle Colltction Chamber
Subassembley: Bottom Flange- Translation Collector
Part (# of pcs): Cap (1)
Scale: 1:1
Name: Robert Morgan
Group: Ditmire
Material: Type 316 Stainless

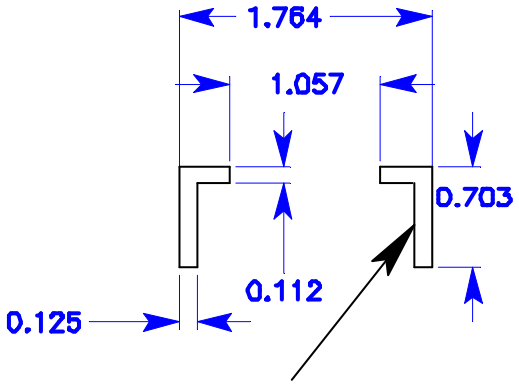

threaded to match mainfold

Translator Collector Sub-assembly

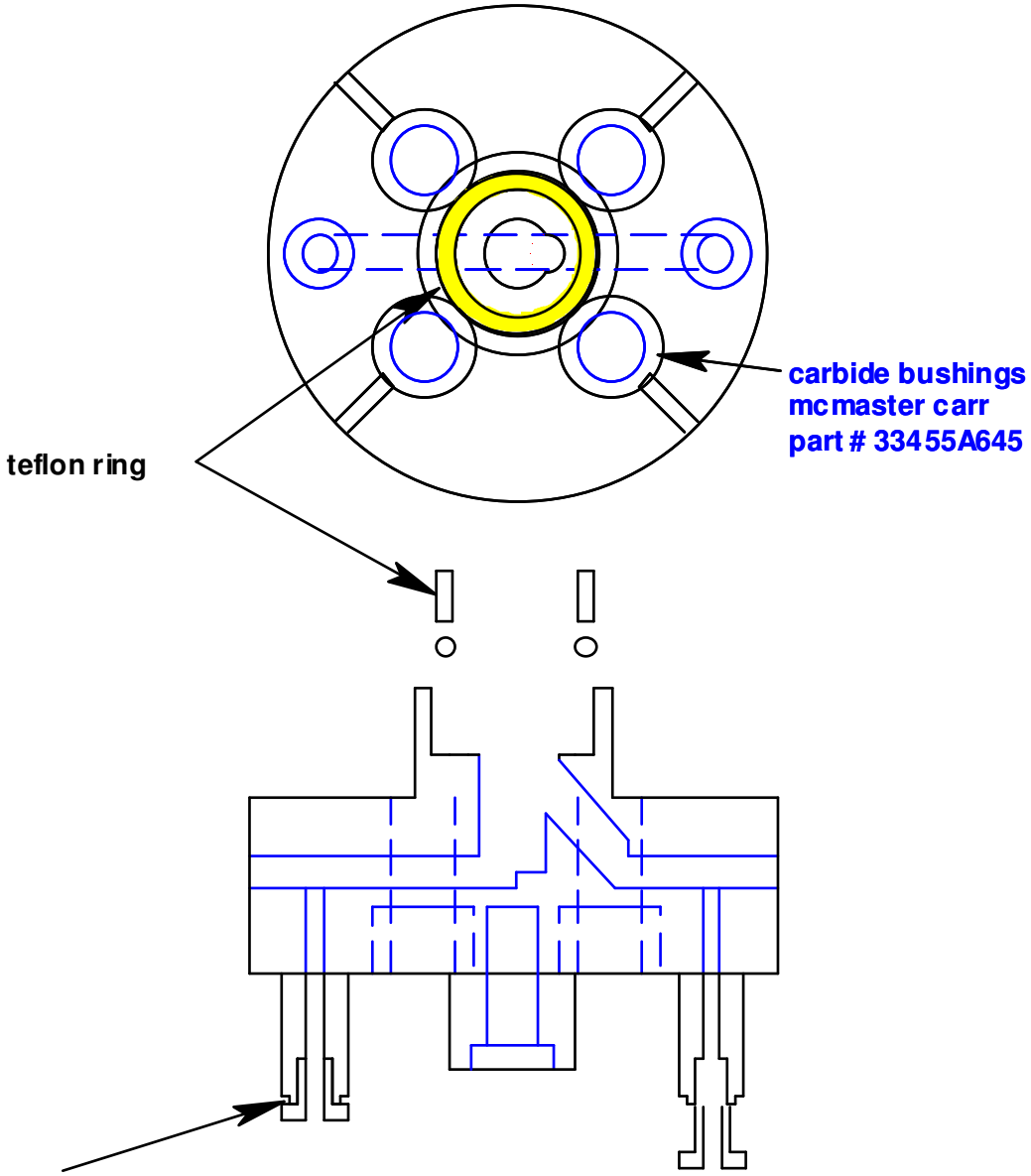

Title: Nano Particle Colltction Chamber
Subassembley: Bottom Flange- Translation Collector
Part (# of pcs)x(# of copies): Seal Legs (2)x(2)
Scale: 1:1
Name: Robert Morgan
Group: Ditmire
Material: Type 316 Stainless

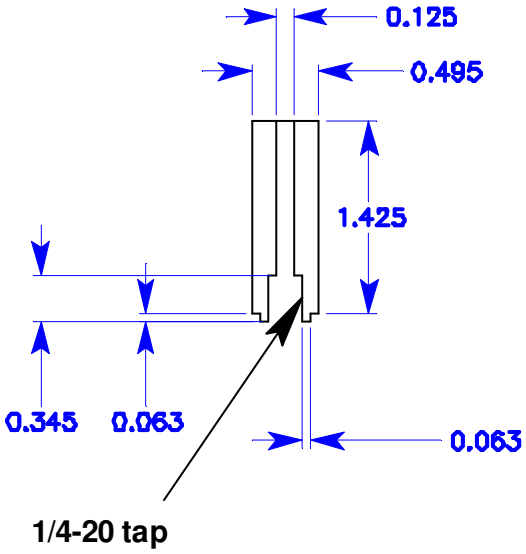

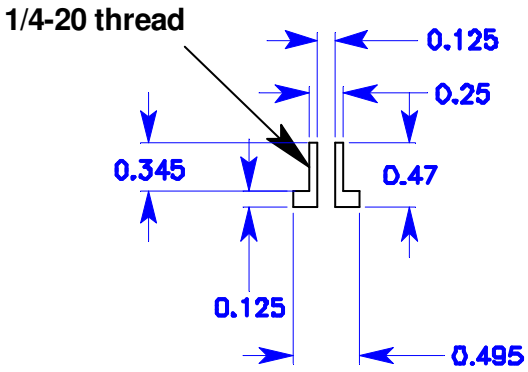

for gland dimensions see attached seal specs for mc master carr part # 13125k66,76

Title: Nano Particle Colltction Chamber
Subassembley: Bottom Flange- Translation Collector
Part (# of pcs): Teflfon Ring (1)
Scale: 1:1
Name: Robert Morgan
Group: Ditmire
Material: Teflon

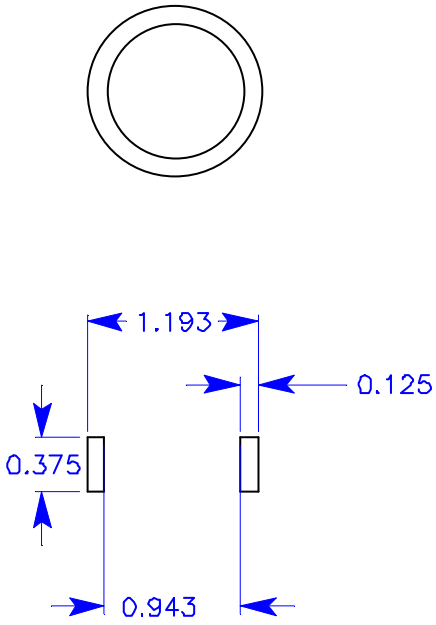

Title: Nano Particle Collection Chamber
Subassembley: Bottom Flange- Translation Collector
Part (# of pcs): Fluid Manifold (1)
Scale: 1:1
Name: Robert Morgan
Group: Ditmire
Material: Type 316 Stainless

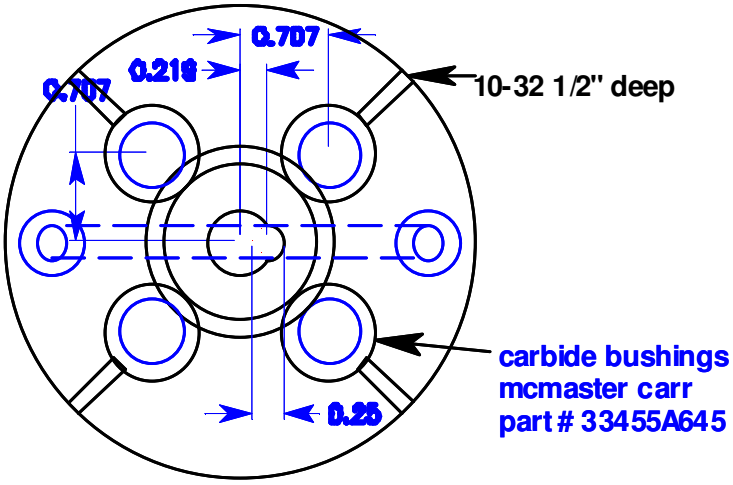

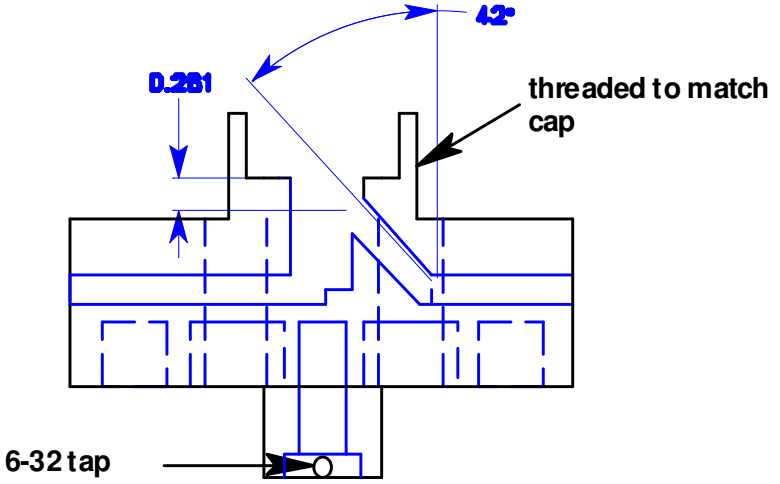

Title: Nano Particle Collection Chamber
Subassembley: Bottom Flange- Translation Collector
Part (# of pcs): Fluid Manifold (1)
Scale: 1:1
Name: Robert Morgan
Group: Ditmire
Material: Type 316 Stainless

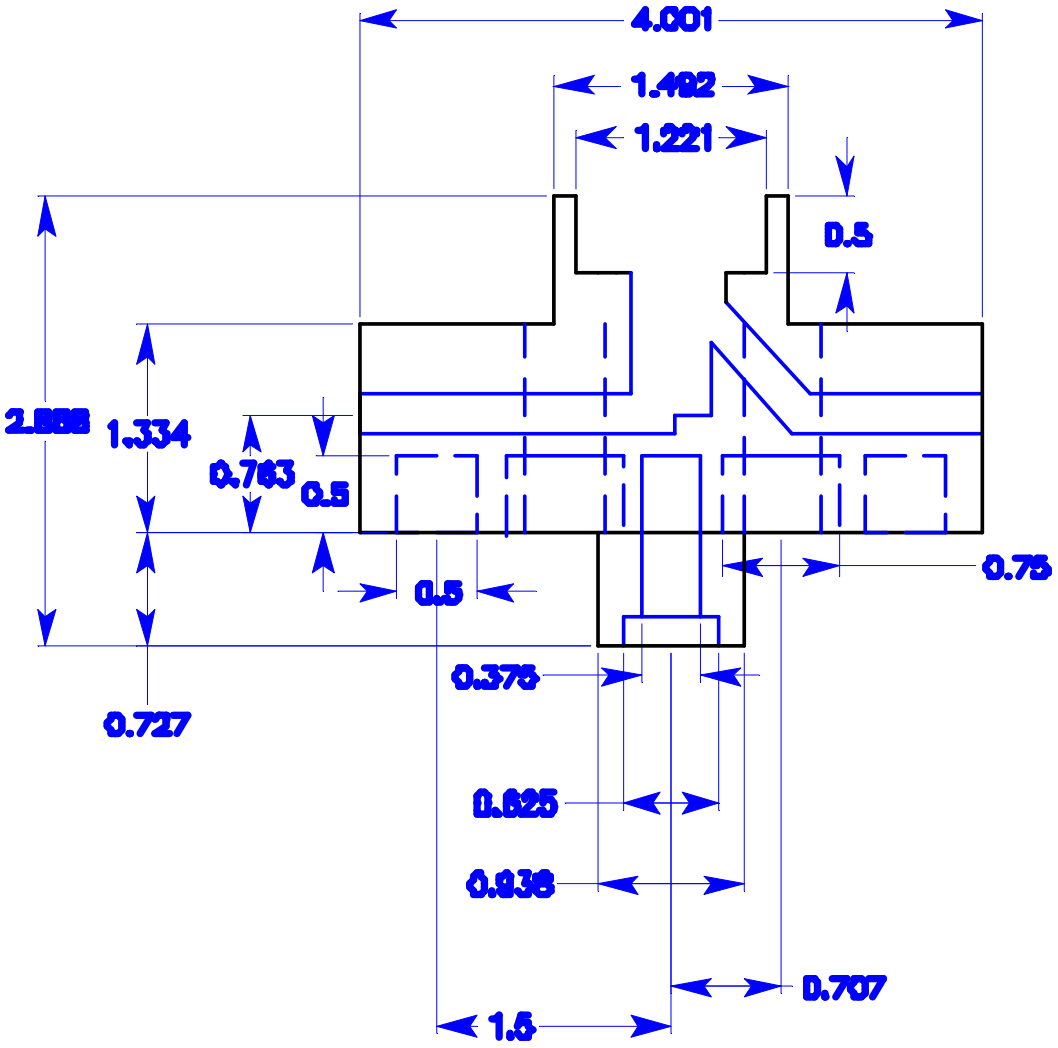

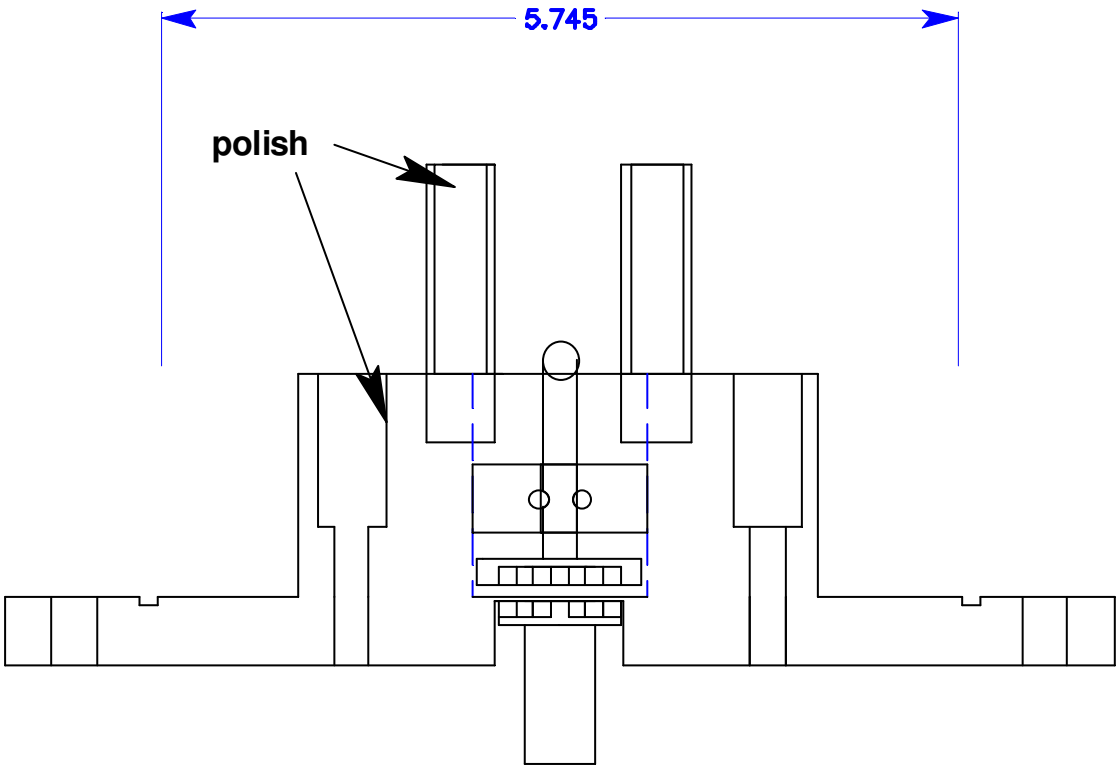
5.745
polish

Title: Nano Particle Colltction Chamber
Subassembley: Bottom Flange- Bottom Flange
Part (# of pcs): Magnent holder (already made see T.C.)
Scale: 1:1
Name: Robert Morgan
Group: Ditmire
Material: Type 316 Stainless

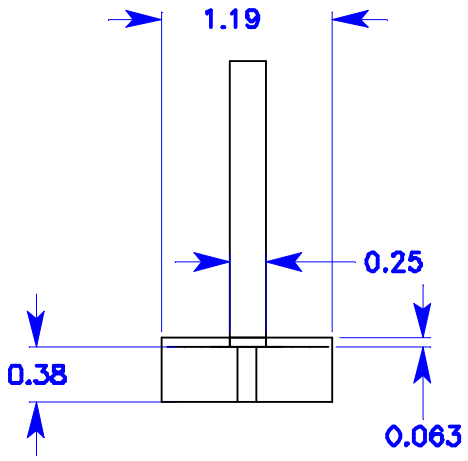

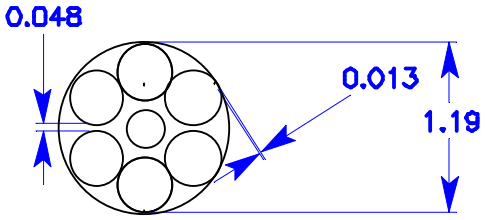

2 rings with 16 1/8" holes 0.5" radius and 0.375" radius
1 ring with 8 1/8" holes 0.25" radius
1 ring with 4 1/8" holes at 0.125" radius

Top View of Base w.o. Flange shown

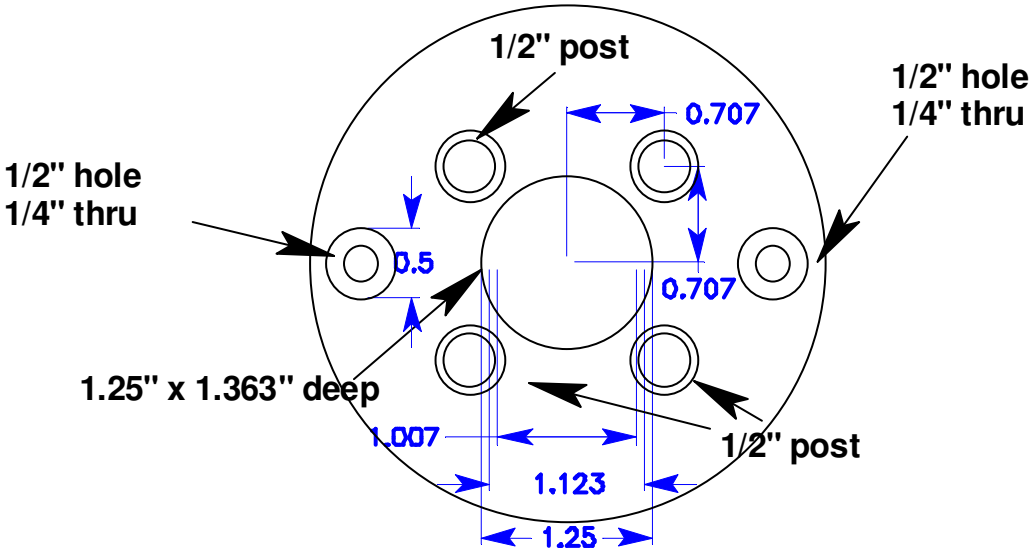

Side View of Flange w/ Flange Shown

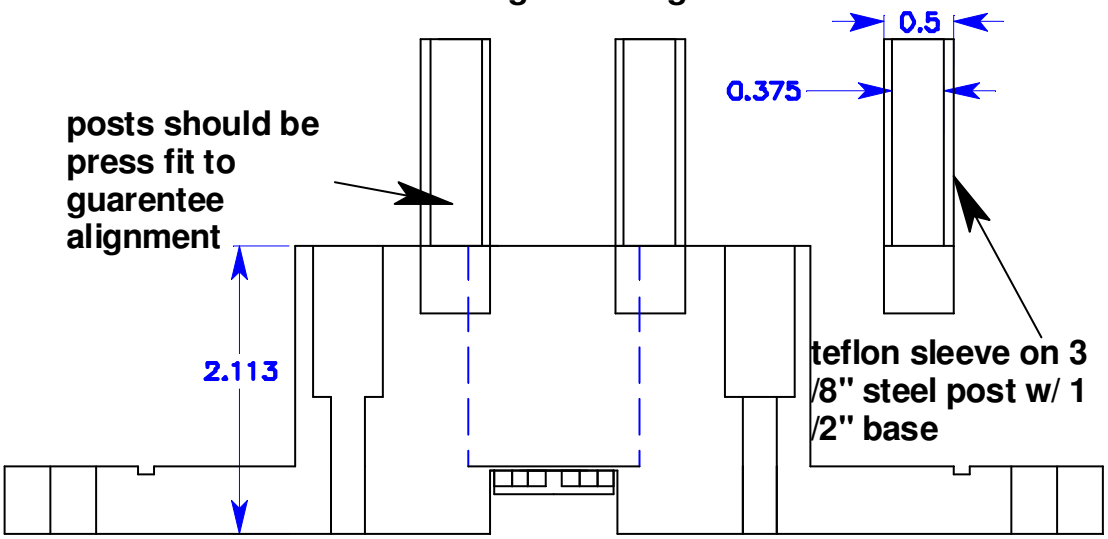

Bottom Flange Sub-assembly

Side View of Flange w/ Flange Shown

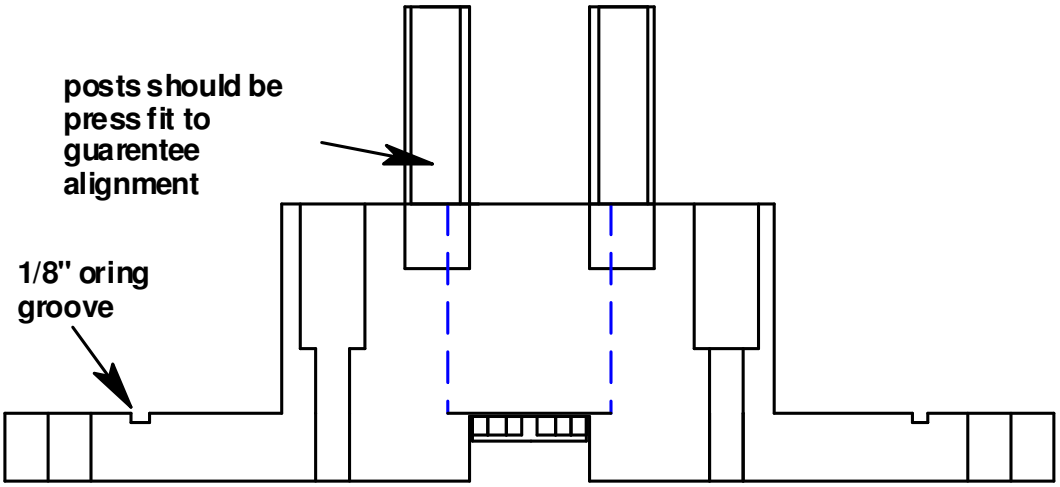

Title: Nano Particle Colltction Chamber
Subassembley: Bottom Flange- Bottom Flange
Part (# of pcs)x(# of copies): Guide Post (2)x(4)
Scale: 1:1
Name: Robert Morgan
Group: Ditmire
Material: Type 316 Stainless and Delron

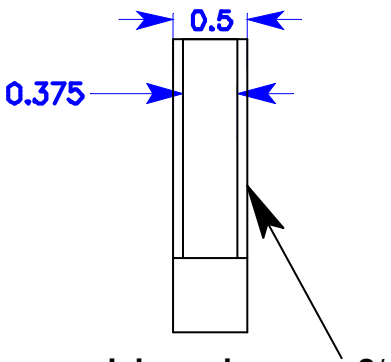

delron sleeve on 3/ 8" steel post w/ 1/ 2" base

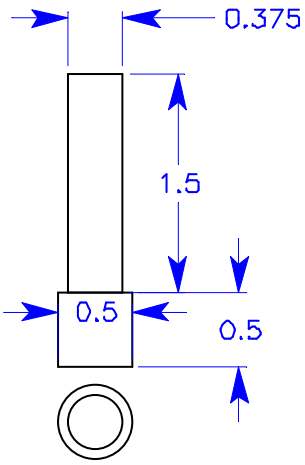

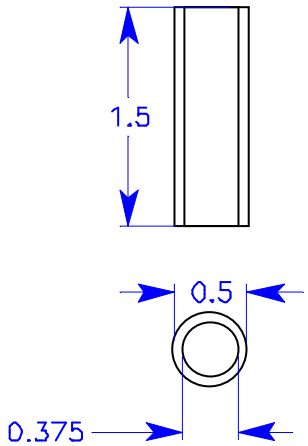

Delron Sleeve

Title: Nano Particle Colltction Chamber
Subassembley: Bottom Flange- Bottom Flange
Part (# of pcs): Bottom Flange(1)
Scale: 1:1
Name: Robert Morgan
Group: Ditmire
Material: Type 316 Stainless

Side View of Flange w/ Flange Shown

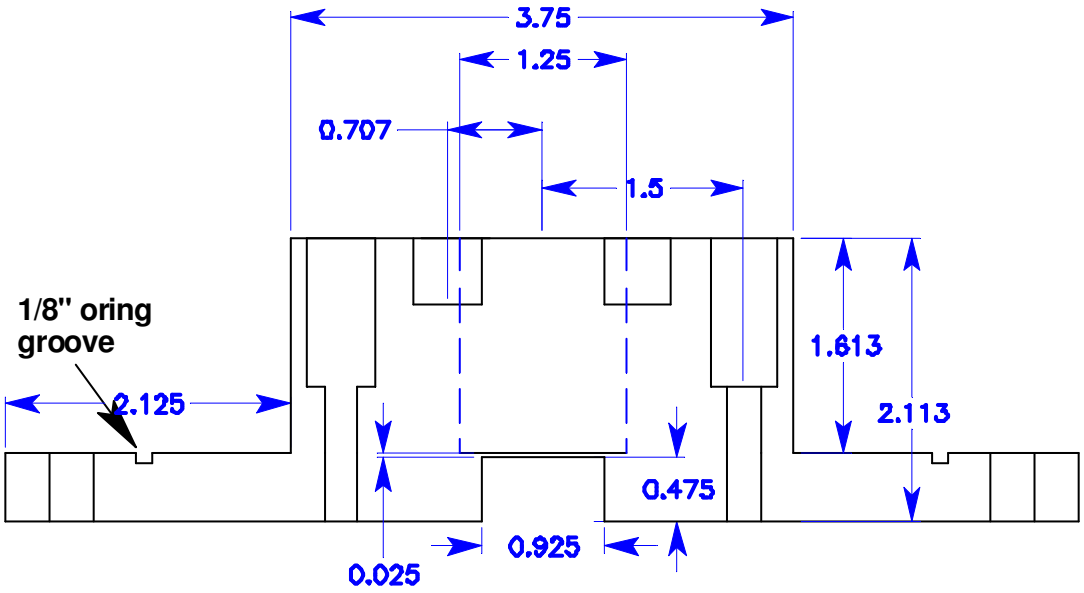

Title: Nano Particle Colltction Chamber
Subassembley: Bottom Flange- Bottom Flange
Part (# of pcs): Bottom Flange(1)
Scale: 1:1
Name: Robert Morgan
Group: Ditmire
Material: Type 316 Stainless

Top View of Base w.o. Flange shown

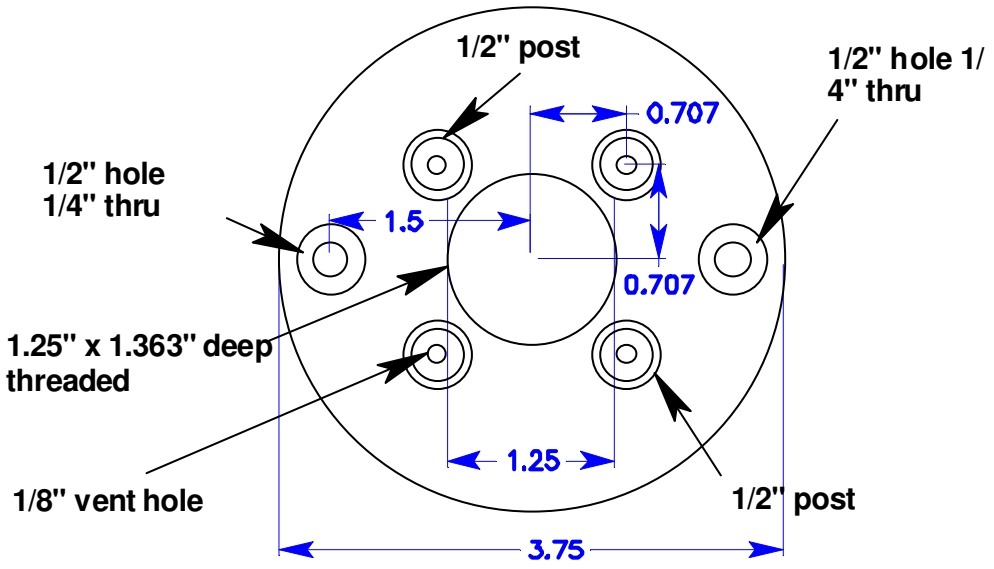

bottom flange with oring groove and dowell pins

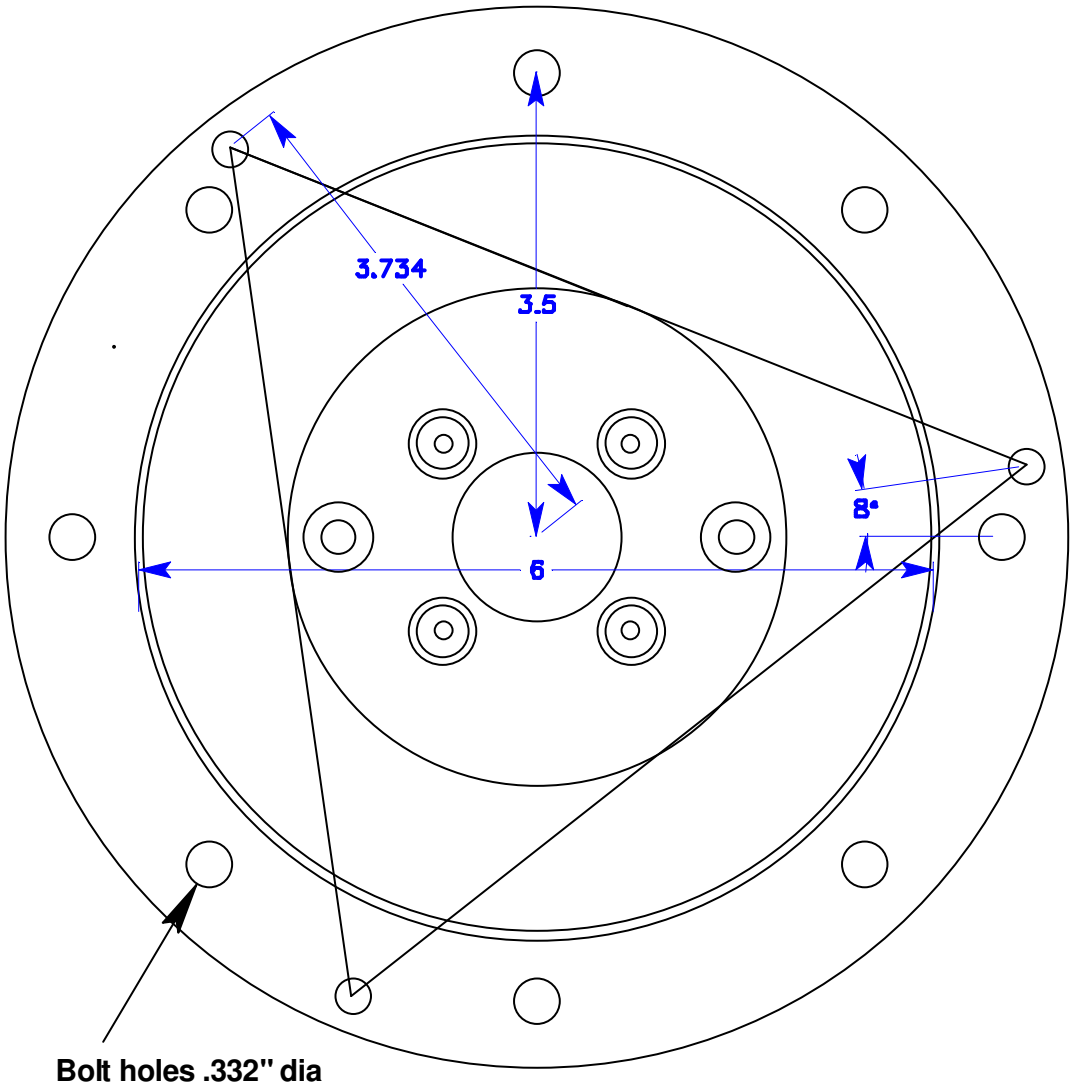

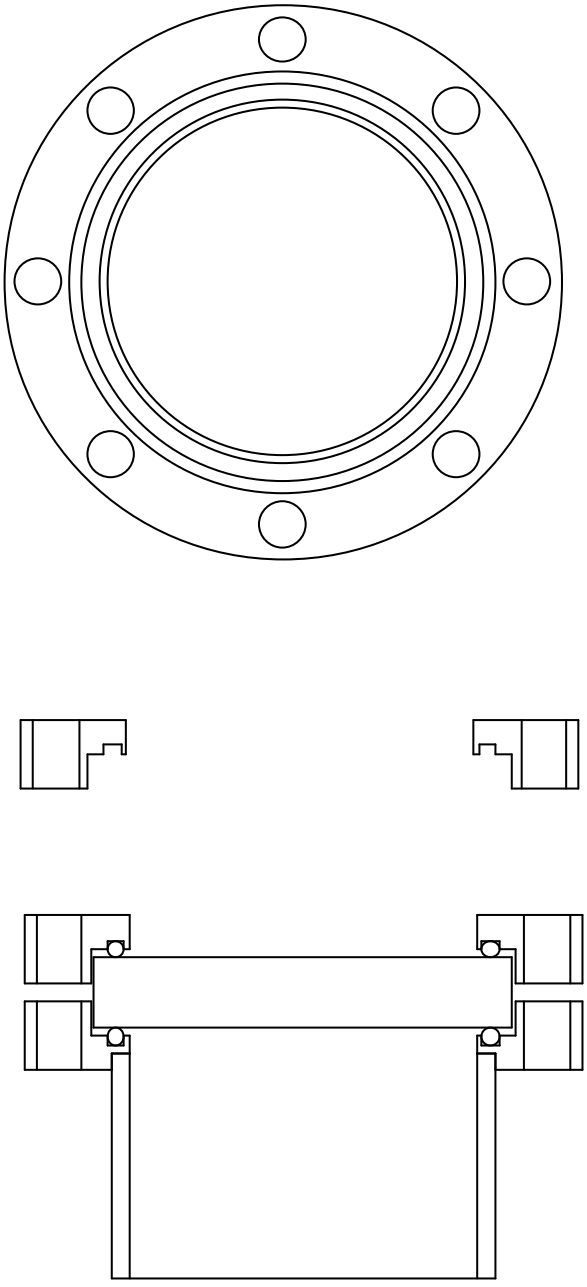

bottom flange with oring groove and dowell pins

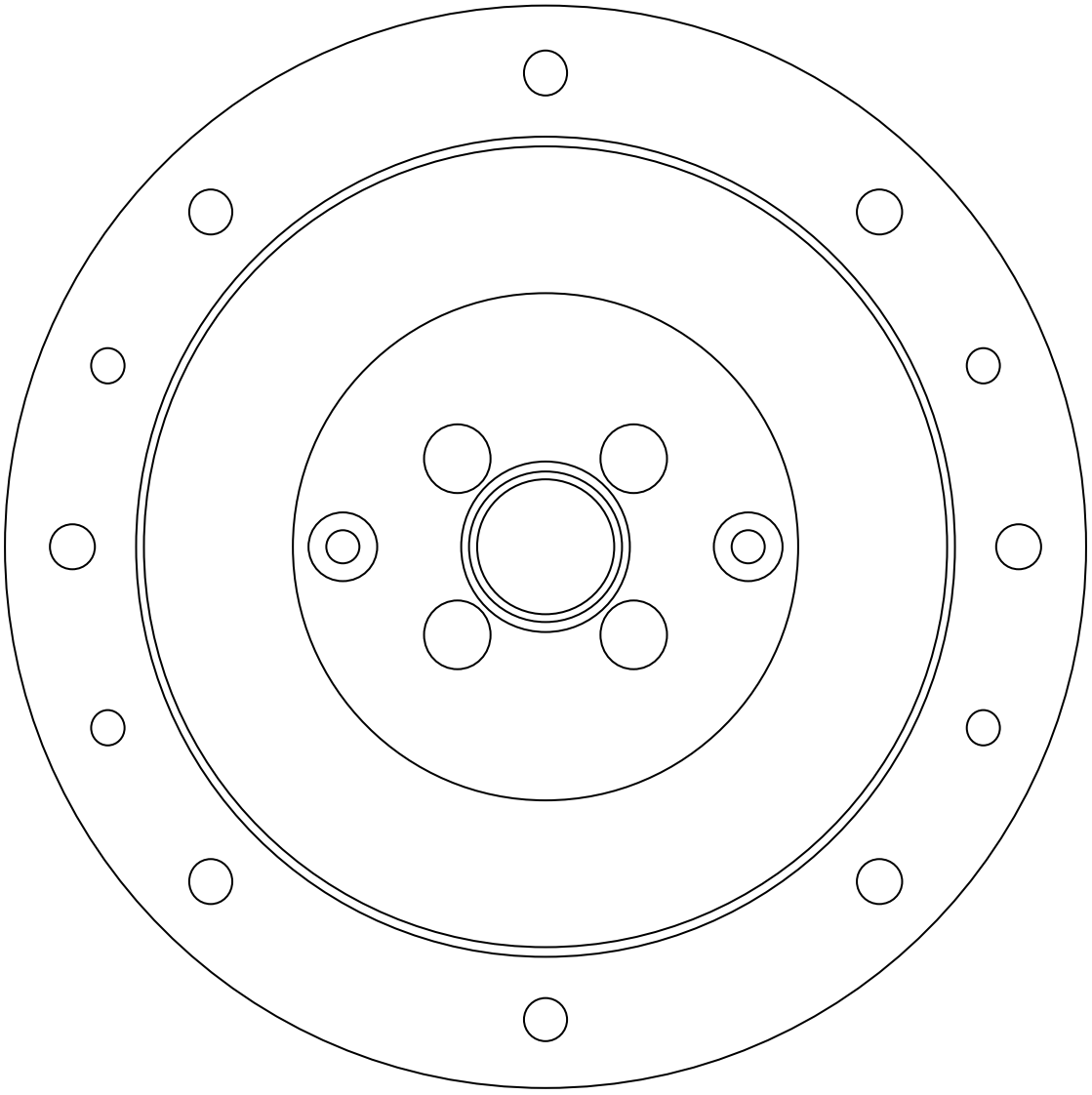

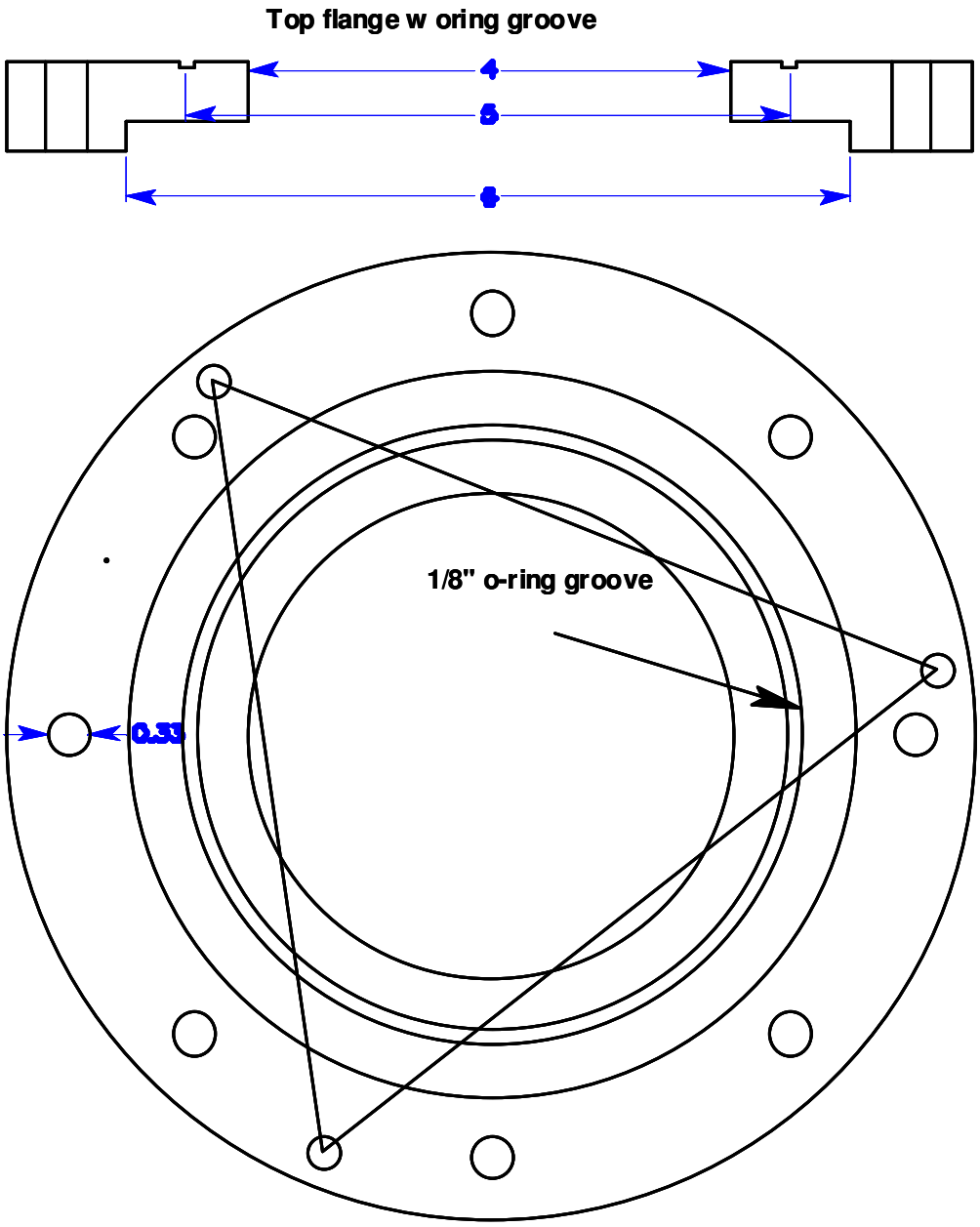
Top flange w oring groove
4
5
6
1/8" o-ring groove
0.33

Title: Nano Particle Colltction Chamber
Subassembley: Chamber Assembly - Window Flange win side
Part (# of pcs)x(# of copies): Guide Post (1)x(2)
Scale: 1:1
Name: Robert Morgan
Group: Ditmire
Material: Type 316 Stainless

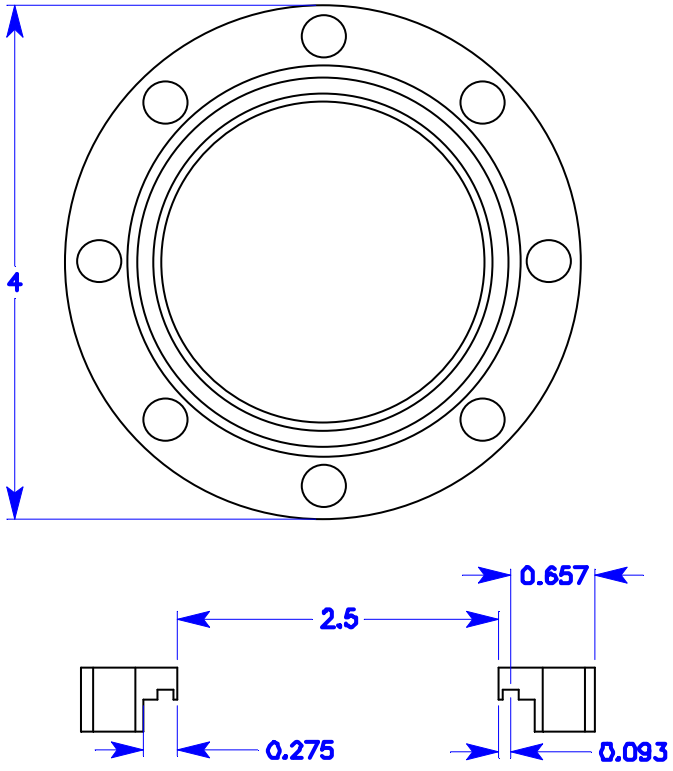

Title: Nano Particle Collteion Chamber
Subassembley: Chamber Assembly - Window Flange tube side
Part (# of pcs)x(# of copies): Guide Post (1)x(2)
Scale: 1:1
Name: Robert Morgan
Group: Ditmire
Material: Type 316 Stainless

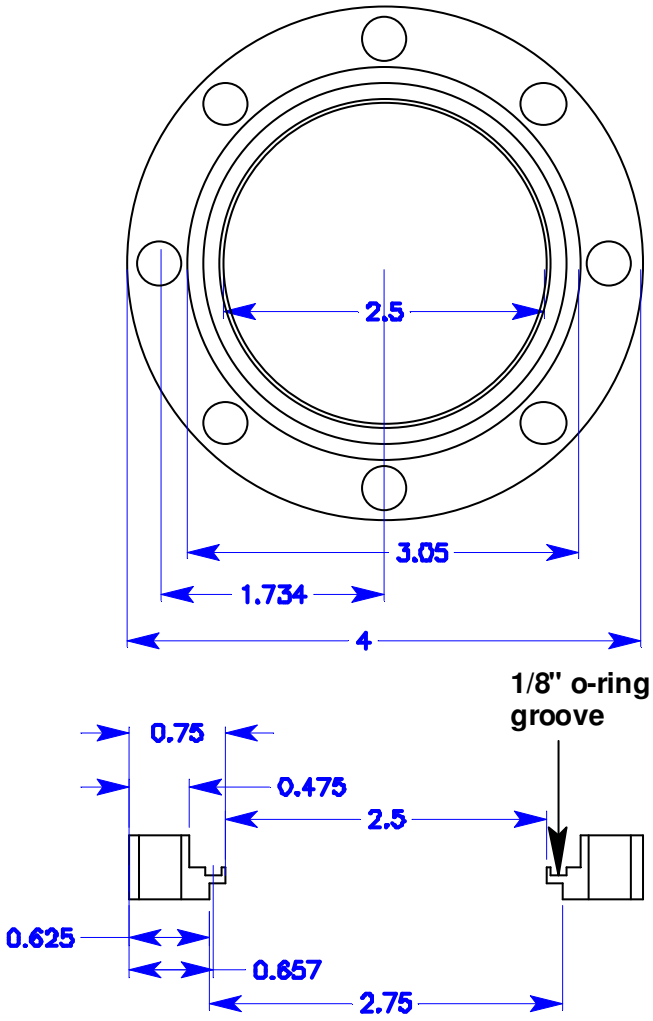

Chamber Assembly Welded

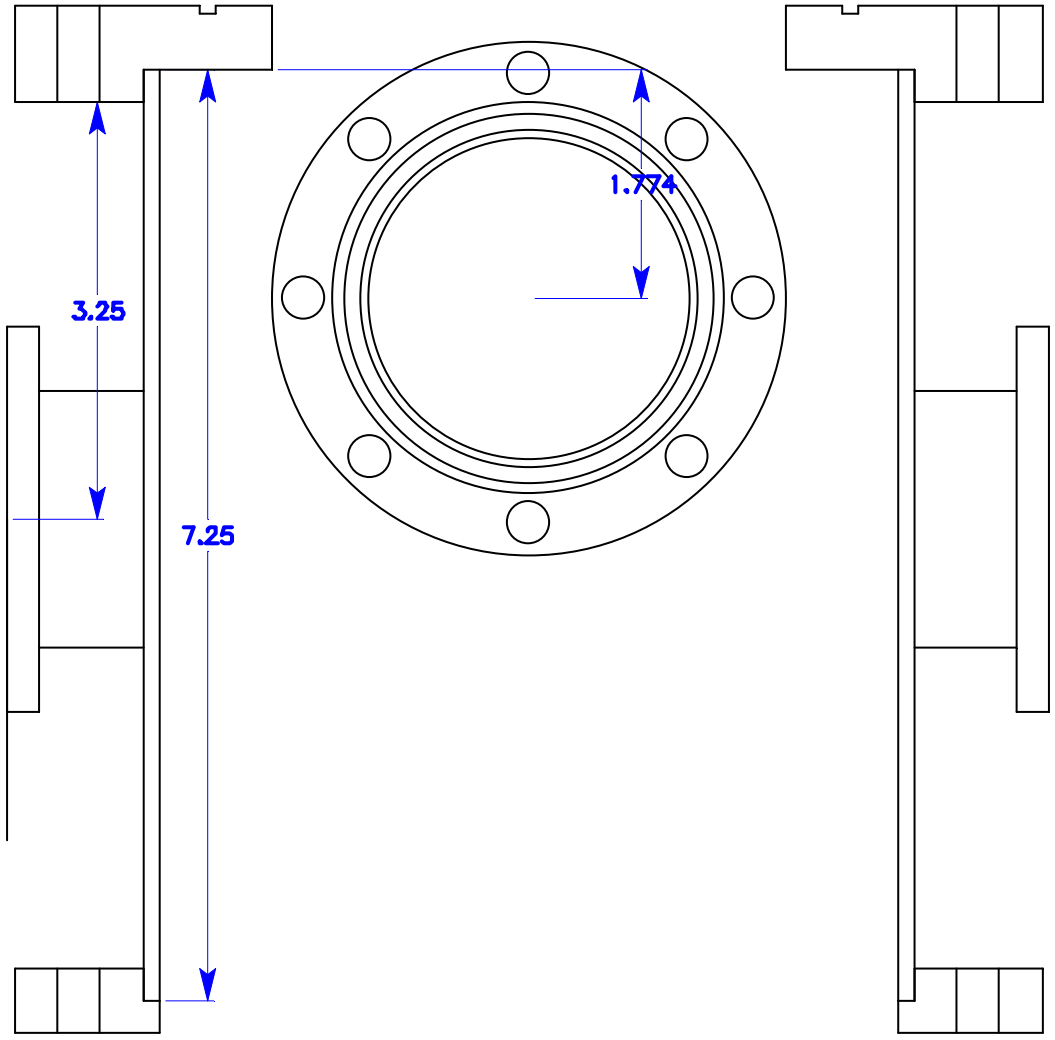

Window Assembly Tube Welded

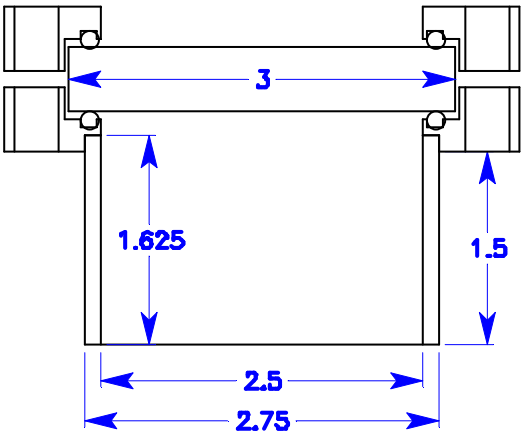

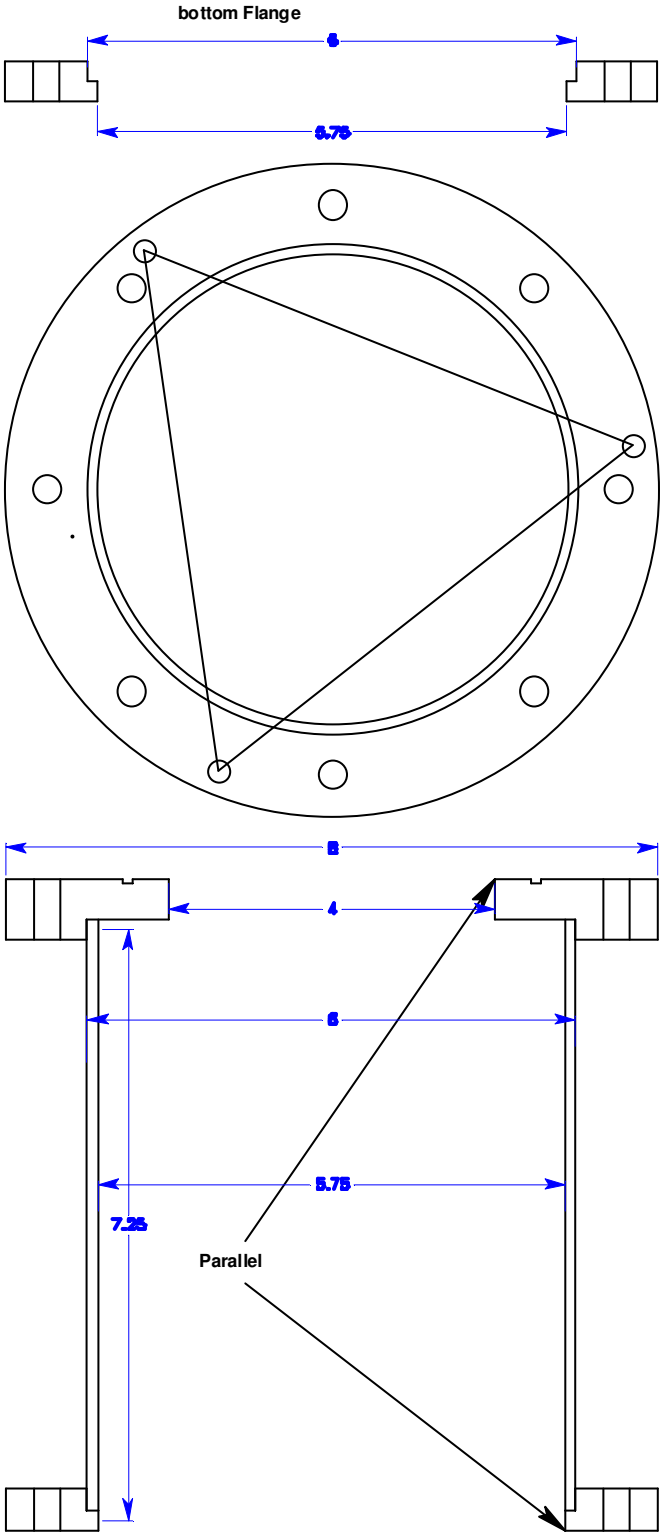
bottom Flange
6
6.75
8
4
6
5.75
7.25
Parallel

References

[1] W. Koechner, Solid State Laser Materials 5th ed., (Springer, 1999), Ch 11.

[2] J. Campbell, T. Suratwala, Nd-doped phosphate glasses for high-energy/high-peak-power lasers, J. Non-Cryst. Solids, 263&264:318 (2000).

[3] Figure reprinted from reference 2 with permission from Elsiver.

[4] A. Siegman, Lasers, (University Science Books, 1986), Ch 6 and 7.

[5] W. Koechner, Solid State Laser Materials 5th ed., (Springer, 1999), Ch 3 and.

[6] A. Siegman, Lasers, (University Science Books, 1986), Ch 19 and 17.

[7] F. Wani, M. Endo, T. Fujioka, High-pressure, high-efficiency operation of a chemical oxygen-iodine laser, Appl. Phys. Lett. 75(20):3081 (1999).

[8] A. Siegman, Lasers, (University Science Books, 1986), Ch 19 and 21.

[9] W. Koechner, Solid State Laser Materials 5th ed., (Springer, 1999), Ch7.

[10] S. Timoshenko J. Goodier Theory of Elasticity 3rd ed., (McGraw Hill, 1982).

[11] W. Koechner, Solid State Laser Materials 5th ed., (Springer, 1999), Ch6.

[12] From a 2005 Conversation with Dr. Zwiebeck, a scientist at General Atomics working on high average power laser development.

[13] J. Jackson, Classical Electrodynamics, 3rd ed. (Wiley, 1999), Ch 10.

[14] M. Saani, T. Ghodselahi, K. Esfarjani, Strain-induced instability of spherical nanodiamond hydrocarbons: effect of surface CHn and charging, Phys. Rev. B, 79,125429:1 (2009).

[15] Z. Shan, G. Adesso, A. Cabot, M. Sherburne, S. Asif, O. Warren, D. Chrzan, A. Minor, A. Alivisatos, Ultrahigh stress and strain in hierarchically structured hollow nanoparticles, Nature Mater., 7:947 (2008).

[16] Q. Li, L. Gao, D. Yan, The crystal structure and spectra of nano-scale YAG:Ce3+, Mater. Chem. Phys., 64:41 (2000).

[17] A. Barnes, Surface Chemistry Studies of Phosphate Glasses, UMI 3096930 (2003).

[18] B. Bunker, G. Arnold, J. Wilder, Phosphate Glass Dissolution in Aqueous Solutions, J. Non-Crystalline Solids 64:291 (1984).

[19] R.C. Powell, Physics of Solid State Laser Materials, (Springer-Verlag, 1998), ch 4.

[20] W. Koechner, Solid State Laser Materials 5th ed., (Springer, 1999), Ch 2.

[21] J. Vetrovec, R. Shah, T. Endo, A, Koumvakalis, K. Masaters, W. Wooster, K. Widen, S. Lassovsky, Progress in the development of solid-state disk laser, conference proceedings SPIE LASE 2004 preprint, San Jose Ca, 2004, Vol 5332 (2004).

[22] J. Vetrovec, R. Rice, R. Shah, T, Tran, L. Schirber, Concept designs for solid-state high-energy laser, conference proceedings SSDLTR HPLS-8 (2004).

[23] R.C. Powell, Physics of Solid State Laser Materials, (Springer-Verlag, 1998), Ch 8 and 9.

[24] A. Siegman, Lasers, (University Science Books, 1986).

[25] M. Hudson, Calculation of the maximum optical coupling efficiency into multimode optical waveguides, Appl. Opt., 13,5:1029 (1974).

[26] J. Baker, D. Payne, Expanded-beam connector design study, Appl. Opt., 20,16:2861 (1981).

[27] M. Digonnet, C. Gaeta, Theoretical analysis of optical fiber laser amplifiers and oscillators, Appl. Opt., 24,3:333 (1985).

[28] M. Born, E. Wolf, Principles of Optics: Electromagnetic Theory of Propagation, Interference and Diffraction of Light 7th ed, (Cambridge Univ. Press, 2002).

[29] B. Judd, An analysis of the fluorescence spectrum of Neodymium Chloride, Proc. Royal Soc. London Series A, Math. Phys. Sci., 251,1264:134 (1959).

[30] Design and testing of a large-aperture, high-gain Brewster's-angle, zig-zag Nd:glass slab amplifier, edited by M. Skeldon, LLE Rev., 68:209.

[31] W. Nichols, J. Keto, D. Henneke, J. Brock, G. Malyavanatham, M. Becker, H. Glicksman, Large-scale production of nanocrystals by laser ablation of micro-particles in a flowing aerosol, Appl. Phys. Lett., 78,8:1128 (2001).

[32] J. Lee, M. Becker, J. Keto, Dynamics of laser ablation of micro-particles prior to nanoparticle generation, J. Appl. Phys., 89,12:8146 (2001).

[33] S. Ude, J. de la Mora, Hypersonic impaction with molecular mass standards, J. Aerosol Sci., 34:1245 (2003).

[34] L. Landau, E. Lifshitz, Fluid Mechanics 2nd ed, Butterworth Heinemann (1987).

[35] C. Huang, W. Nichols, D. O'Brien, M. Becker, D. Kovar, J. Keto, Supersonic jet deposition of silver nanoparticle aerosols: Correlations of impact conditions and film morphologies, J. Appl. Phys., 101: 064902 (2007).

[36] I. Loscertales, Mass diameter versus aerodynamic diameter of nanoparticles. Implications on the calibration curve of an inertial impactor, J. Aerosol Sci., 31,8:923 (2000).

[37] V. Marple, B. Liu, Characteristics of laminar jet impactors, Environ. Sci. Technol., 8,7:648 (1974).

[38] V. Marple, C. Chien, Virtual impactors: a theoretical study, Environ. Sci. Technol., 14,8:976 (1980).

[39] P. Biswas, R. Flagan, High velocity inertial impactors, Environ. Sci. Technol., 18:611 (1984).

[40] J. de la Mora, A. Schmidt-Ott, Performance of a hypersonic impactor with silver particles in the 2 nm range, J. Aerosol Sci., 24,3:409 (1993).

[41] C. Cercignani, Rarefied Gas Dynamics, (Cambridge Univ. Press, 2000), ch 8.

[42] H. Tammet, Size and mobility of nanometer particles, clusters, and ions, J. Aerosol Sci., 26,3:459 (1995).

[43] F. de la Mora, S. Hering, N. Rao, P. McMurry, Hypersonic impaction of ultrafine particles, J. Aerosol Sci., 21:169 (1990).

[44] J. Moore, C. Davis, M. Coplan, Building Scientific Apparauts 3rd ed., (Westview Press, 2002).

[45] THOR laser was 20 TW 38 fs Ti:sapphire laser operaed by Prof. Ditmire from 2000-2009. This experiment used lower power beams from this system to probe the fluorescence of the colloids produced during the early stages of this work.

[46] R. Altkorn, I. Koev, R. Van Duyne, M. Litorja, Low-loss liquid-core optical fiber for low-refractive-index liquids: fabrication, characterization, and application in Raman spectroscopy, Appl. Opt., 36,34:8992 (1997).

[47] R. Byrne, E. Kaltenbacher, Comment, Limnol. Oceanogr., 46,3:740 (2001).

[48] W. van Etten, W. Lambo, P. Simons, Loss in multimode fiber connections with a gap, Appl. Opt., 24,7:970 (1985).

[49] J. Baker, D. Payne, Expanded-beam connector design study, Appl. Opt., 20,16:2861 (1981).

[50] M. Digonnet, C. Gaeta, Theoretical analysis of optical fiber laser amplifiers and oscillators, Appl. Opt., 24,3:333 (1985).

[51] D. Chandler, Z. Majumdar, G. Heiss, R. Clegg, Ruby crystal for demonstrating time- and frequency-domain methods of fluorescence lifetime measurements, J. Fluoresc., 16:793 (2006).

[52] L. Hersh, E. Onyiriuka, W. Hertl, Amine-reactive surface chemistry of zinc phosphate glasses, J. Mater. Res., 10,8:2120 (1995).

[53] D. Henneke, G. Malyavanatham, D. Kovar, D. O'Brien, M. Becker, W. Nichols, J. Keto, Stabilization of silver nanoparticles in nonanoic acid: A temperature

activated conformation reaction observed with surface enhanced Raman spectroscopy, J. Chem. Phys., 119,13:6802 (2003).

[54] R. Nyquist, Interpreting Infrared Raman and Nuclear Magnetic Resonance Spectra 1st ed., Academic Press, (2001).

[55] R.C. Powell, Physics of Solid State Laser Materials, (Springer-Verlag, 1998), ch 8.

[56] C. Brecher, L. Riseberg, Line-narrowed fluorescence spectra and site-dependent transition probabilities of Nd3+ in oxide and fluoride glasses, Phys. Rev. B, 18,10:5799 (1978).

[57] L. Merckle, R. Powell, Energy transfer among Nd3+ ions in garnet crystals, Phys. Rev. B, 20,1:75 (1979).

[58] M. Yamane, Y. Asahara, Glasses for Photonics, (Cambridge Univ. Press, 2000).

[59] R.C. Powell, Physics of Solid State Laser Materials, (Springer-Verlag, 1998), Ch 2 and 3.

[60] G. Burdick, C. Jayasankar, F. Richardson, Energy-level and line-strength analysis of optical transitions between Stark levels in Nd3+:Y3Al5O12, Phys. Rev. B, 50,22:16 309 (1994-II).

[61] S.E. Stokowski, Laser glass: an engineered material, Lawrence Livermore National Laboratory Report,UCRL-96331, (1987), p. 1.

[62] H. Toratani, PhD thesis, Kyoto University, Kyoto,Japan, 1989.

[63] S. Payne, M.L. Elder, J.H. Campbell, G.D. Wilke, M.J.,Weber, in: A.J. Bruce, B.V. Hiremath (Eds.), Solid-State,Optical Materials, vol. 28, American Ceramic Society,Westerville, OH, (1991), p. 253.

[64] J.H. Campbell, SPIE CR 64 (1996) 3.

[65] Y. Jiang, S. Jiang, Y. Jiang, J. Non-Cryst. Solids 112:268 (1989).

[66] S.A. Payne, G.D. Wilke, L.K. Smith, W.F. Krupke, Opt. Commun. 111:263 (1994).

[67] L.D. Merkel, R.C. Powell, Phys. Rev. B 20,1: 75 (1979).

[68] K. Urman, J. Otaigbe, Novel phosphate glass/polyamide 6 hybrids: miscibility, crystallization kinetics, and mechanical properties, Wiley Intersci., online:441 (2005).

[69] J.J. Sakurai, Modern Quantum Mechanics, (Adison Westley Longman, 1994), Ch 5.

[70] S. Payne, L. Chase, L. Smith, W. Kway, W. Krupke, Infrared cross-section measurements for crystals doped with Er3+, Tm3+, and Ho3+, IEEE J. Quant. Elec., 28,11:2619 (1992).

[71] W. Krupke, Induced-emission cross sections in Neodymium laser glasses, IEEE J. Quant. Elec., QE-10,4:450 (1974).

Vita

Robert Douglas Morgan attended Tom C. Clark High School in San Antonio, Texas. He graduated from Stanford University in 2001 with a Bachelor of Science with Departmental Honors in Physics and a minor in Mathematics. He entered the Graduate School at the University of Texas at Austin in 2002.

Email: crob23@mail.utexas.edu

This dissertation was typed by the author.